Arnold Schwarzenegger
Governor

PHYSICAL/STATISTICAL AND MODELING DOCUMENTATION OF THE EFFECTS OF URBAN AND INDUSTRIAL AIR POLLUTION IN CALIFORNIA ON PRECIPITATION AND STREAM FLOWS

PIER FINAL PROJECT REPORT

Prepared For:
California Energy Commission
Public Interest Energy Research Program

Prepared By:
Woodley Weather Consultants
The Hebrew University of Jerusalem

March 2007
CEC-500-2007-019

California Climate Change Center
Report Series Number 2007-005

Prepared By:
Woodley Weather Consultants
Dr. William L. Woodley
Littleton, Colorado

The Hebrew University of Jerusalem
Dr. Daniel Rosenfeld, Dr. Alexander Khain,
Dr. Barry Lynn, and Mr. Amir Givati
Jerusalem, Israel

Commission Contract No.: 500-02-004
Commission Work Authorization No.: MR-032

Prepared For:
Public Interest Energy Research (PIER) Program
California Energy Commission

Beth Chambers
Contract Manager

Kelly Birkinshaw
Program Area Lead
Energy-Related Environmental Research

Laurie ten Hope
Office Manager
Energy System Research

Martha Krebs
Deputy Director
ENERGY RESEARCH & DEVELOPMENT DIVISION

B.B. Blevins
Executive Director

DISCLAIMER

This report was prepared as the result of work sponsored by the California Energy Commission. It does not necessarily represent the views of the Energy Commission, its employees or the State of California. The Energy Commission, the State of California, its employees, contractors and subcontractors make no warrant, express or implied, and assume no legal liability for the information in this report; nor does any party represent that the uses of this information will not infringe upon privately owned rights. This report has not been approved or disapproved by the California Energy Commission nor has the California Energy Commission passed upon the accuracy or adequacy of the information in this report.

Acknowledgments

The authors are grateful to their colleagues working with them on this PIER project, who supported them with observational data and who consulted with them in technical and model problems. The authors express their deep gratitude to Dr. J. Dudhia for consulting related to utilization of the Weather Research Forecast (WRF) model and implementation of the spectral (bin) microphysics (SBM) in WRF. The authors are indebted particularly to the Public Interest Energy Research (PIER) Program of the California Energy Commission (Energy Commission) for its support of the study. The authors especially thank Mr. Guido Franco of PIER for his support and advice. This study was supported also by NSF (Grant #0503152) and by the Israel Water Company (Grant 162/03).

Please cite this report as follows:

Woodley Weather Consultants. 2007. *Physical/Statistical and Modeling Documentation of the Effects of Urban and Industrial Air Pollution in California on Precipitation and Stream Flows.* California Energy Commission, PIER Energy-Related Environmental Research Program. CEC-500-2007-019.

Preface

The Public Interest Energy Research (PIER) Program supports public interest energy research and development that will help improve the quality of life in California by bringing environmentally safe, affordable, and reliable energy services and products to the marketplace.

The PIER Program, managed by the California Energy Commission (Energy Commission), conducts public interest research, development, and demonstration (RD&D) projects to benefit California's electricity and natural gas ratepayers. The PIER Program strives to conduct the most promising public interest energy research by partnering with RD&D entities, including individuals, businesses, utilities, and public or private research institutions.

PIER funding efforts are focused on the following RD&D program areas:

- Buildings End-Use Energy Efficiency
- Energy-Related Environmental Research
- Energy Systems Integration
- Environmentally Preferred Advanced Generation
- Industrial/Agricultural/Water End-Use Energy Efficiency
- Renewable Energy Technologies
- Transportation

In 2003, the California Energy Commission's Public Interest Energy research (PIER) Program established the **California Climate Change Center** to document climate change research relevant to the states. This Center is a virtual organization with core research activities at Scripps Institution of Oceanography and the University of California, Berkeley, complemented by efforts at other research institutions. Priority research areas defined in PIER's five-year Climate Change Research Plan are: monitoring, analysis, and modeling of climate; analysis of options to reduce greenhouse gas emissions, assessment of physical impacts and of adaptation strategies, and analysis of the economic consequences of both climate change impacts and the efforts designed to reduce emissions.

The California Climate Change Center Report Series details ongoing Center-sponsored research. As interim project results, the information contained in these reports may change; authors should be contacted for the most recent project results. By providing ready access to this timely research, the Center seeks to inform the public and expand dissemination of climate change information; thereby leveraging collaborative efforts and increasing the benefits of this research to California's citizens, environment, and economy.

Physical/Statistical and Modeling Documentation of the Effects of Urban and Industrial Air Pollution in California on Precipitation and Stream Flows is the final report for the Physical/Statistical and Modeling Documentation of the Effects of Urban and Industrial Effects of Urban and Industrial Air Pollution in California project (contract number 500-02-004, work authorization number MR-032) conducted by Woodley Weather Consultants and The Hebrew University of Jerusalem.

For more information on the PIER Program, please visit the Energy Commission's website www.energy.ca.gov/pier/ or contract the Energy Commission at (916) 654-5164.

Table of Contents

Preface iii

Abstract xv

Executive Summary 1

1.0 Introduction 5

2.0 The Effects of Pollution on Clouds and Precipitation 7

2.1. Physical Evidence 7

2.2. Statistical Evidence 13

2.3. Physical/Statistical Summary 17

3.0 Proposal Goal and Objectives 21

4.0 The Hydrological Analyses 27

4.1. Introduction 27

4.2. Historical Relationships between Precipitation and Stream Flow in the Sierra Nevada and the Coastal Range 28

4.3. Establishing Runoff Relationships 28

4.4. Downwind versus Upwind Sierra Runoff Relationships 32

4.5. Runoff Relationships in Relatively Pristine vs. Polluted Areas 35

4.6. Precipitation and Runoff Relationships in Washington State 36

4.7. Climate Indices as an Alternative Explanation for the Decreasing Ro 39

4.8. The Effects of the PDO on the Runoff / Precipitation Ratio 41

4.9. Conclusions 43

5.0 Determining the Relationship between Air Pollution and Cloud Structure and Precipitation-Forming Processes 45

5.1. Satellite-Inference of Cloud Effective Radius in California 45

5.1.1. Methodology 46

5.1.2. Results 48

5.2. Aircraft Validation of the Satellite Inferences of Cloud Microstructure 57

6.0 Numerical Simulation of Cloud Processes Under Polluted and Non-Polluted Conditions 63

6.1. Objectives of the Numerical Study 63

6.2. The Choice of Numerical Model 63

6.3. Simulations with the 3-D MM5-SBM Model 66

6.4. Two-Dimensional Simulations with Spectral (bin) Microphysics (SBM) 72

6.4.1. Modification of Model Microphysics 72
6.4.2. Results of Basic 2-D Simulations 76
6.4.3. Sensitivity Studies 81
6.5. Comparison of the SBM Results with Those from Bulk Parameterization 82
6.6. Discussion and Conclusions 84
7.0 Overall Report Summary 87
8.0 References 89
9.0 Glossary 97

Appendix A. The Satellite Methodology Used in the Research Effort

Appendix B. Results of Supplemental Analyses for Objective 1: Hydrological Stream Flow Analysis

Appendix C. Effects of Aerosols on Precipitation from Orographic Clouds

Appendix D. Aerosol Properties and Trends in Relation to Changes in Precipitation over Elevated Terrain in the Western United States

List of Figures

Figure 1. Satellite visualization of NOAA/AVHRR images, showing the microstructure of clouds with streaks of visibly smaller drops due to ingestion of pollution, for three cases over three continents, originating from known pollution sources, marked by white numbered asterisks. The yellow streaks in panel A (about 300 x 200 km) originate from the urban air pollution of Istanbul (*1), Izmit (*2), and Bursa (*3), on 25 December 1998 at 12:43 Universal Time (UT). Panel B (about 150 x 100 km) shows the impact of the effluents from the Hudson Bay Mining and Smelting compound at Flin Flon (*4), Manitoba, Canada (54:46N 102:06W), on 4 June 1998 at 20:19 UT. Panel C (about 350 x 450 km) shows pollution tracks over South Australia on 12 August 1997 at 05:26 UT, originating from Port Augusta power plant (*5), Port Pirie lead smelter (*6), Adelaide port (*7), and the oil refineries (*8). All images are oriented with north at the top. The images are color composites, where the red is modulated by the visible solar reflectance, blue by the thermal infrared (IR), and green is modulated by the solar reflectance component of the 3.7 μm solar reflectance, where larger (greener) reflectance means smaller droplets. This red-green-blue composition determines the color of the clouds, where red represents clouds with large drops, and yellow represents clouds with small drops. The blue background is the ground surface below the clouds. A full description of the color pallets and their meaning is provided in Rosenfeld and Lensky (1998). 8

Figure 2. Similar to Figure 1. This figure is a satellite visualization of a TRMM VIRS image of Southeast Australia, with precipitation areas overlaid as white patches on the image. The white patches denote precipitation echoes, as observed by the TRMM Precipitation Radar (PR). The two parallel lines delimit the PR swath of 230 km. The swath is oriented from west (left of the image) to east. The image shows pollution plumes in the clouds over southeastern Australia, from 21 October 1998, 04:44 UT. The lines AB and CD show the locations of the vertical cross sections shown in Figure 5. 10

Figure 3. Analysis of the T-r_e relations, where T is the temperature and r_e is the cloud particle effective radius, for the clouds in the seven boxes in Figure 2. Plotted are the 15% (long dashed line), 50% (solid line), and 85% (short dashed line) percentiles of the r_e for each 1° interval. The black lines correspond to the polluted boxes. The vertical green line marks the 14 μm precipitation threshold. A full description of the meaning of the T-r_e charts is provided in Rosenfeld and Lensky 1998). 11

Figure 4. Vertical profiles of the precipitation echo intensities, as measured by the TRMM Precipitation Radar for the various boxes in Figure 2. The peak near 2 km corresponds to enhanced echoes from snowmelt just below the 0^oC isotherm. Box 2 had no detectable precipitation. Boxes 4 and 7 are outside of the radar swath. 12

Figure 5. Vertical cross-section along the lines AB and CD in Figure 2. The dark gray areas represent clouds. The vertical extent of the clouds is converted from the VIRS measured top temperatures. The colors represent the precipitation reflectivity, in dBZ, as measured by the TRMM radar. The white line is the brightness temperature of the TRMM Microwave

Imager 85 GHz vertical polarization (T_{85}), plotted at the altitude of that temperature. Lower T_{85} (represented as larger height of the white line) in non-precipitating clouds means larger cloud water content. Please note that the T_{85} and actual cloud top temperature have different physical meanings. 12

Figure 6. Long-range trends of (A) the annual precipitation measured in San Diego, and in (B) the downwind hilly station of Cuyamaca at an elevation of 1550 m; (C) the correlation between these two stations; and (D) the annual ratio of precipitation (Ro) measured between them. The stations with the longest record in California are presented here. Note the sharp decrease in Ro with time in this area, which is affected by urban air pollution. *Ending/starting ratio* means the ratio at the beginning of the time series compared to the ratio at the end, as calculated from the regression line at these times. *R* means the linear correlation coefficient, and *P* is the statistical significance that corresponds to the t test statistic from Student's t test. 15

Figure 7. Same as Figure 6, but for (A) the relatively clean area in Northern California at Ukiah and (B) the downwind hilly station of Lake Spaulding at an elevation of 1717 m. (C) The annual precipitation of the two stations is well correlated. Both stations show increases in precipitation over the period of record. Note (D) the lack of a trend in the ratio between the hilly and upwind lowland stations. 16

Figure 8. Topographic cross section showing the effects of urban air pollution on precipitation as the clouds move from west to east from the coast to the Sierra Nevada Mountains and to the eastern slopes. The boxes show the amount of the annual precipitation (mm/year) in each topographic location and the numbers above them show the loss or gain of precipitation (mm/year) at each site. Maritime air (in zone 1) is polluted over coastal urban areas (in zones 2 and 3), but no precipitation decrease occurs. The polluted air rises over mountains downwind and forms new polluted clouds (in zone 4), resulting in decreases of 15%–20% (losses of 220 mm/year) in the ratio between the western slopes to the coastal and plain areas. The clouds reach to the high mountains (in zone 5). All the precipitation is snow, and there is a slight decrease of 5% to 7% (a loss of 65 mm/year) in the ratio between the summits to the plains areas. The clouds move to the high eastern slopes of the range (in zone 6), where there is an increase of 14% (gain of 66 mm/year) in the ratio between the eastern slopes to the plains. According to Table 1, the net loss is dominant..... 18

Figure 9. Processed satellite image at 2050 UT (1250 PST) on 7 December 2003. The T-r_e analyses for the areas shown in the colorized image appear in the insets on the right. The median plot is at the interface of the yellow and green lines. The threshold for precipitation is the vertical white line at 15 μm. The short vertical colored lines on the left are the microphysical zones discussed in Appendix A. 22

Figure 10. The same as for Figure 9, except the inset T-r_e plots are for areas 9 through 16..... 23

Figure 11. Same as Figure 9, except the inset T-r_e plots are for areas 16 through 24..... 24

Figure 12.The correlation between (A) the American river (at Folsom) and the annual precipitation at the rain gauges of Pacific House (3400 ft, lat: 38.765, long: 120.500), and (B) the Russian river (at Healdsburg) and the precipitation in Ukiah (633 ft, lat: 39.15, long: -123.20l). 28

Figure 13. Map of the locations of analyzed flows for the Sierra and coastal range rivers, and the main results of the trends of the ratio between them. The methodology for calculating the trends between the Sierra to the coastal rivers is shown in Figure 14 for the pair of American and Russian Rivers, in the nine-panel graph below. Note the good precipitation-flow relationships, which make the response of the hilly river flow linearly related to the change in the orographic enhancement factor of the precipitation. 29

Figure 14. Correlation between (A) the Russian River and rain gauges in the basin, (D) the American River and rain gauges in the basin, and (G) the American vs. the Russian rivers. The middle columns of the panel display the annual precipitation at clusters of rain gauges at (B) the Russian basin, (E) the American river, and (H) the ratio between them. The right column displays the flow in (C) the Russian River, (F) the American River, and(I) the ratio between them. 30

Figure 15. The ratio between (A) Merced to precipitation in Merced, (B) San Joaquin River to precipitation at Big Sur, and (C) San Joaquin River to precipitation at Fresno 31

Figure 16. Stable trend for the 100-year ratio between (A) the San Joaquin river to the Arroyo Seco, and also for (B) the period 1905–1945, and (C) the decreasing trend for the period between 1945–2003. 32

Figure 17. The ratio of annual precipitation between rain gauges on the eastern vs. the western Sierra slopes in a relatively polluted area (Woodfords vs. Pacific House gauges) and in a relatively pristine area in Northern California (Boca vs. Bowman gauges) Source: Givati and Rosenfeld (2004) 33

Figure 18. The ratio between western vs. eastern Sierra slopes for the periods of 1905–2003 (panels A and C) and 1945–2003 (panels B and D) for the Stanislaus River vs. the West Walker River,(A and B) and the Mokelumne River vs. the West Walker River (C and D) ... 34

Figure 19. The ratio between the American river, the Cosumnes and the Mokelumne rivers (western slopes) vs. the West Walker River (eastern slopes) 35

Figure 20. Trends, correlation, and the ratio between the American and the Feather rivers 36

Figure 21. The locations of hilly (red) and plains (blue) rain gauges in a relatively pristine area and a polluted area in Washington state 37

Figure 22. The ratio of annual precipitation in a relatively pristine area, the Olympic peninsula, Washington : (A) Wishka versus Aberdeen, and the ratio in a relatively polluted area between (B): Palmer versus Seattle 37

Figure 23. The locations of Quinault River (in the Olympic peninsula), and the Cedar River (downwind of Seattle, Washington) 38

Figure 24. The correlation (A) and ratio (B) between the annual stream flow in the Cedar River downwind of Seattle to the annual stream flow in the Quinault River in the relatively pristine Olympic peninsula 39

Figure 25. Winter values (October–April) of the PDO and SOI indexes. Note the three phases of the PDO: a positive phase from 1900–1944, a negative phase from 1945–1975, and another positive phase since 1976. 40

Figure 26. The ratio between runoff at the San Joaquin River and precipitation in Crane Valley versus the PDO winter positive values 42

Figure 27. The ratio between precipitation at Crane Valley (Sierra) to precipitation at Big Sur (coastal range) during negative and positive PDO phases 42

Figure 28. A map of the regions in which the cloud properties were characterized. The area numbers appear with a # sign before them. The corners of the regions are denoted by the name of the nearest geographical landmark. The middle number denotes the number of cases meeting the selection criteria in each region, and the averaged r_e of these cases is the right number within each area. 47

Figure 29. Median effective radii vs. temperature under light and variable 700 mb winds for five coast and five Sierra areas as shown in Figure 28. The number of cases appears above each bar. 49

Figure 30. Median effective radii vs. temperature under moderate 700 mb southwest winds for five coast and five Sierra areas as shown in Figure 28. The number of cases appears above each bar. 55

Figure 31. Median effective radii vs. temperature under moderate northwesterly winds at 700 mb for the five coastal and five Sierra areas shown in Figure 28. The number of cases appears above each bar. 56

Figure 32. Median effective radii vs. temperature for strong westerly winds at 700 mb for the five paired coast and Sierra areas, as shown in Figure 28. The number of cases appears above each bar. 57

Figure 33. Scatter plot of the median effective radii determined by aircraft (Aircraft r_e) for individual cloud passes vs. the median effective radii inferred from the multi-spectral satellite imagery (Satellite median r_e) for the altitudes and temperatures of the aircraft cloud passes for clouds within boxes that contain the cloud passes. The comparisons were made for data obtained on February 7 and March 4, 2005. 59

Figure 34. Cloud drop number concentrations as a function of the CCN concentration at a supersaturation of 0.5%. Each point represents the median (blue) and maximum (red)

droplet concentrations for one cloud pass. The best-fit equations and corresponding correlations are as shown. 60

Figure 35. The effective diameter of the cloud drops normalized for the cloud liquid water content by the expression Deff / $LWC^{0.333}$, as a function of the CCN concentrations for each cloud pass 61

Figure 36. Scatter plot of the cloud depth (in meters) necessary for the in-cloud droplet sizes to reach the precipitation threshold of 24 μm versus the maximum CCN concentrations measured beneath each subject cloud 62

Figure 37. Satellite picture of cloudiness observed on 7 December 2003 66

Figure 38. The nested grid system used in the simulations with the MM5-SBM model. (A) the triply nested grid system with the finest grid resolution at 3 km; (B) the nested grid system consisting of four grids, with the finest grid resolution at 1 km. 67

Figure 39. (A) Accumulated rain amounts in mm in the M- and C-runs, (B) difference in millimeters 68

Figure 40. Accumulated precipitation in the M- and C-cases in simulations with "full microphysics" included within the time period 19–23 hours into the simulation 69

Figure 41. The ratio (PM-PC)/PM (in %) obtained in the 1-km resolution simulation at different time instances. PM-accumulated precipitation under maritime (clean) air; PC-accumulated rain in C-case (polluted air). The dashed line shows the location of the main ridge. 70

Figure 42. Cross-sections in the fields of liquid water content (QL), rain water (QRAIN), graupel (QGRAUPEL) and snow (QSNOW) contents obtained in the 1-km resolution simulation at 20 h into the simulation. The topography profile is presented for the sake of convenience. 71

Figure 43. DSDs obtained using the traditional K-O scheme and a new three-moment scheme along the axis of the simulated pyro-cloud (left) and the green-ocean cloud (right). The DSDs calculated using the three-moment scheme are narrower than those calculated using the K-O scheme. 73

Figure 44. East to west cross sections of droplet concentration, CWC, and rainwater contents (RWC) simulated with the old (two-point) and a new (three-point) remapping schemes 74

Figure 45. The same as Figure 44, but for ice hydrometeors 75

Figure 46. Spatial distributions of accumulated precipitation in M- and C-cases when the old (two-point) and new (three-point) schemes were used. 76

Figure 47. West-to-east cross-sections of cloud droplet concentrations simulated with MAR-Control (left) and Con-Control (right) at 3 hours 77

Figure 48. West-to-east cross-sections of CWC simulated with MAR-Control (left) and Con-Control (right) at 3 hours 77

Figure 49. Same as Figure 48, but for rain water mass 78

Figure 50. Same as Figure 48, but for ice crystal mass (dendrites, columns, and plates) 78

Figure 51. Same as Figure 48, but for snow mass 79

Figure 52. Accumulated precipitation on the mountain slope for three hours, for both Mar-Control and Con-Control The green line is the height of the terrain. 79

Figure 53. Accumulated precipitation in simulations with spectral bin microphysics and bulk microphysics parameterization developed by Thompson et al. (2006) The units for the Nt c values are cm^{-3}. 83

List of Tables

Table 1. The approximate budget of precipitation change in the section with suppressed precipitation across the longitudinal zones of the Sierra Nevada, as defined in Figure 8. The change in precipitated water volume is calculated for a 1 km-wide strip across the mountains. 17

Table 2. Multiple linear regression results showing the significances of three independent variables: The PDO, the SOI, and the years over which Ro is calculated vs. the dependent variable—individual precipitation of rain gauges in California. 41

Table 3. Multiple linear regression results showing the significances of three independent variables: The PDO, the SOI and years, vs. the dependent variable, the ratio of precipitation between the rain gauge pairs, which is the orographic enhancement factor... 41

Table 4. Summary of the median effective radius calculations for areas in the Sierra Nevada, with 700 mb winds. The first and second rows show wind vectors U (eastward) and V (northward) and their wind velocities (upper number to lower number), in m s-1. The next five rows represent the five ranges of the Sierra Nevada from north to south, with the area numbers corresponding to the areas in Figure 28. The first number in each wind/temperature block is the number of cases that met the selection criteria for each region, and the number to its immediate right is the effective radius of all the cases at the listed T, for cloud base warmer than 0°C. 50

Table 5. The same as Table 4, but for the coastal range, 700 mb winds. Areas are listed from north to south. 51

Table 6. The same as Table 4, but for the coastal ocean, 700 mb winds. Areas are listed from north to south. 52

Table 7. The same as Table 5, but for the coastal range with 850 mb winds. Areas are listed from north to south. 53

Table 8. The same as Table 6, but for the coastal ocean, 850 mb winds. Areas are listed from north to south. 54

Table 9. Accumulated precipitation (in mm) obtained up to the hour shown. The data were averaged from 150 to 350 km in the simulation domain. 81

Abstract

This research achieved insights into the documented impacts of urban and industrial air pollution on orographic clouds and precipitation (and the resulting stream flows) over the California Sierra Nevada, downwind of the pollution sources. The pollution aerosols are submicron cloud condensation nuclei (CCN) that are incorporated into the orographic clouds, thereby slowing the coalescence of raindrops and riming on ice precipitation and delaying the conversion of cloud water into precipitation. The net rain-volume losses in the polluted central and southern California Sierra Nevada are estimated at 4×10^9 cubic meters (m^3) of water per year.

This project's accomplishments are threefold. First, it demonstrated through hydrological analyses that the negative effect of pollutants on mountain precipitation also results in stream flow losses. Second, quantitative analyses of cloud structure using multi-spectral satellite imagery showed that the cloud precipitation-forming processes are being suppressed in the same Sierra Nevada regions that are experiencing losses in precipitation and stream flows. Third, the results of numerical modeling simulations showed good agreement with precipitation and stream flow analyses based on observations that submicron CCN pollution can alter Sierra precipitation.

This study's finding that aerosols have been suppressing precipitation in high-elevation areas in California for many years carries significant implications for the state's water supply.

Keywords: Precipitation, pollution, aerosols, mountain stream flows, numerical modeling, clouds, satellite imagery, hydrology

Executive Summary

Introduction

Most climate change investigations focus on the role of greenhouse gases in global warming and on the role of minute particles in the atmosphere (atmospheric aerosols) that cool the atmosphere by reflecting some of the incoming solar radiation back to space. Atmospheric aerosols were thought to counterbalance global warming; however, this is not their only role. Recent research, funded by the California Energy Commission with Dr. Daniel Rosenfeld and Dr. William Woodley along with their research team, focused on California-specific analysis that indicates atmospheric aerosols can also impede rain and snow formation in the Sierra Nevada Mountains.

This study showed that high concentrations of extremely small (submicron) cloud condensation nuclei (CCN) aerosols (on which atmospheric water can form) slow the formation of raindrops and ice, which delays the conversion of cloud water into precipitation. This effect is exhibited in different ways in clouds – either strengthening deep convective clouds or suppressing the amount of precipitation from shallow clouds around mountains (orographic clouds). These short-lived orographic clouds are the most common in the winter on the west coast and are formed as air is forced upward when passing over barriers such as mountains. California's annual precipitation losses over the mountains are projected at 10 to 25 percent, presumably because of the pollution aerosols that are transported from urban and industrial areas.

Project Purpose

The increasing loss of Sierra precipitation over the last 50 years was documented earlier in published studies by the research team. According to the California Energy Commission, California depends on in-state hydroelectric power generation for approximately 15 percent of its total electricity supplies, and a loss or decline of this generation would be significant. The original research also suggests that as rainfall declines, California's water supply, especially for agriculture, could be impacted. These losses have not noticeably affected California's water supply because until now they have been masked in many places by an increasing trend of statewide precipitation.

This project builds on the previous work done by the research team and focuses on whether 1) the obvious precipitation losses results in reduced mountain streams flows and 2) modeling the aerosol effects on clouds and precipitation could identify the processes that produce mountain precipitation losses.

Project Goal and Objectives

This research effort documented the effect of aerosols on precipitation patterns in the Sierra Nevada and other high elevation areas in California by better understanding the damaging impacts of human-made aerosols on clouds, precipitation and stream flows in mountainous terrain downwind from pollution sources.

The research focused on three major project objectives:

• Combine previous rainfall analysis with available stream flow data to determine the effect of the precipitation changes on water availability in various Sierra drainage basins.

• Use National Oceanic and Atmospheric Administration/Advanced Very High Resolution Radiometer daylight satellite overpasses to identify where the aerosol effects are apparent to determine the relationship between air pollution and cloud structure and precipitation-forming processes.

• Conduct simulations of cloud processes under polluted and non-polluted conditions to clarify their impact on cloud structure and precipitation.

Project Results

For the first time, researchers quantified the losses of stream flows at approximately 15 to 35 percent of the annual stream flow volumes in major Sierra Nevada rivers that are downwind from urban areas. The percentage of reduced precipitation on the western or upside of a mountain correlates to similar precipitation increases on the much drier or eastern down-slope side of the mountain crest. The evidence shows that over the last 50 years, the runoff is declining in the more polluted central and southern Sierra mountain areas; however, there is no similar evidence for runoff losses in the relatively pristine rivers in northern Sierra Nevada. These results agree with an analysis of rain gauge records and suggest that human-caused air pollution has a major impact on orographic precipitation and on stream flow volumes, which are responsible for most of California's water supplies. The research also found that no alternative explanations, such as long-term trends in cross-mountain moisture changes or climatic fluctuations were probable.

Using aircraft and satellite data that provided "pollution tracks" in cloud tops, researchers studied any possible relationships between pollution aerosols, and cloud structures and the precipitation-forming processes. Cloud-tops with volumes of small droplets or particles develop precipitation slowly – presumably because of pollution impacts and temperature. The research team found strong evidence that cloud microstructures had been altered, making them unable to form precipitation-sized drops and ice particles, which reduced precipitation and stream flow in the central and southern Sierra but not in the northern Sierra.

Finally the researchers used two- and three-dimensional model simulations in the same study areas to investigate the effects of aerosols on clouds. They found the clouds in those areas downwind of the urban zones had increased concentrations of pollutants that led to more and smaller droplets that move to higher levels in the cloud-tops without producing large raindrops. The clouds moved over the central and southern Sierra depositing less precipitation on the western or California side.

Conclusion

This cutting edge research effort showed that increased aerosol pollution from urban areas over the last 50 years has reduced rain and snow formation in the central and southern Sierra Nevada Mountains. This decreasing water runoff directly impacts in-state hydroelectric generation and that California's water supplies, especially for agriculture, could be jeopardized.

It is important to pursue additional research to better understand the impact of aerosols on future rain and snow levels in the Sierra Nevada.

1.0 Introduction

There is increasing international concern about the effects of human activity on the environment, air quality, the amount and quality of water resources, and weather and climate change. Most investigations of climate change have focused on the role of greenhouse gases (GHGs) in global warming and on the role of atmospheric aerosols in cooling the atmosphere by reflecting some of the incoming solar radiation back to space. Thus, atmospheric aerosols are thought to serve as a counterbalance to the hypothesized global warming due to the GHG; however, this is not their only role. The precipitation forming processes in clouds depend to a large extent on the presence of aerosols—namely cloud condensation nuclei (CCN) and ice nuclei (IN). The large concentrations of small CCN in the smoke from burning vegetation nucleate many small cloud droplets (Hobbs and Radke 1969; Kaufman and Fraser 1997), which coalesce very inefficiently into raindrops (Squires 1958; Jonas and Mason 1974). Although suspected for many years (Warner 1968; Rosenfeld and Lensky 1998), conclusive evidence that smoke from burning vegetation suppresses precipitation was obtained using the observations of the Tropical Rainfall Measuring Mission (TRMM 1997) satellite (Rosenfeld 1999).

Much less is known, however, about the impact of aerosols from urban and industrial air pollution on precipitation. It was assumed initially that such anthropogenic aerosols inhibit precipitation, as is the case with the smoke from burning vegetation (Gunn and Phillips 1957). However, later reports of enhanced rainfall downwind of paper-mills (Eagen et al. 1974) and over major urban areas (Braham 1981) suggested that giant CCN caused enhancement of precipitation (Johnson 1982), but attempts to correlate the urban-enhanced rainfall to the air pollution sources failed to show any relationship (Gatz 1979). Another explanation for the urban rain enhancement invoked the heat-island effect and increased friction, both of which would tend to increase the surface convergence, resulting in more cloud growth and rainfall over and downwind of the urban areas (Jauregui and Romales 1996). Furthermore, the recent suggestion by Cerveny and Balling (1998) that air pollution might enhance precipitation on the large scale in northeastern America, and the accompanying speculative explanations, demonstrate how little is known about the subject. This is changing as detailed herein. The preponderance of the evidence now suggests that CCN pollution acts to decrease precipitation, particularly on the west coasts of continents where most of the rainfall comes from relatively shallow clouds that are more susceptible to the effects of pollution.

2.0 The Effects of Pollution on Clouds and Precipitation

2.1. Physical Evidence

Space-borne (Coakley et al. 1987) and in situ aircraft (Radke et al. 1989) measurements of ship tracks in marine stratocumulus clouds provided the first evidence that the effluent from ship stacks change cloud microstructure such that their water is redistributed into a larger number of smaller droplets. Albrecht (1989) suggested that the drizzle, which normally occurs in marine stratocumulus clouds in clean air, would be inhibited in clouds with reduced droplet size, thereby increasing the cloud water content and longevity. Extrapolation to clouds that are sufficiently thick for raining (that is, at least 2 kilometers (km) from base to top) would mean that the effluents have the potential to suppress precipitation over ocean and over land. However, pollution tracks in any clouds over land were not reported in previous studies. Application of the imaging scheme of Rosenfeld and Lensky (1998) to the Advanced Very High Resolution Radiometer (AVHRR) onboard the National Oceanic and Atmospheric Administration (NOAA) orbiting weather satellites revealed numerous "ship-track" like features in clouds over land, emanating from major urban and industrial pollution sources. Illustrations of such tracks from Turkey (Figure 1A), Canada (Figure 1B), and Australia (Figure 1C) are shown above. Because the tracks clearly originate from pollution sources, they will be called hereinafter "pollution tracks."

The pollution tracks in Turkey (Figure 1A) originate from several sources in and near the cities of Istanbul, Izmit, and Bursa.

The pollution track in Canada (Figure 1B) originates from Flin-Flon, Manitoba, the home of the Hudson Bay Mining and Smelting Company. That location has been a frequent source for such tracks. Other sources in Canada have been observed, but are not reported here.

Study of the pollution tracks emanating from the region of Adelaide, South Australia, is especially interesting. They received special attention because of their intensity and frequent occurrence. These pollution tracks were identified in the clouds of all 47 AVHRR images on different days that were examined in which stratocumulus and cumulus clouds with tops warmer than about -12°C existed over the region. The pollution tracks in Figure 1C coincide with these major industrial and urban areas:

- Port Augusta (marked as PA in Figure 1C) has a 520 megawatt power plant operating on brown coal, providing electricity to the mines in the vicinity and to the adjacent large steel industry in Whyalla. Port Pirie (PP) is the home of the world's largest lead smelter and refinery.
- Adelaide (AD) has industry for processing minerals mined in the vicinity. Among these is Australia's largest cement plant, located on the Port Adelaide River. A major oil refinery and a power plant are located 20 km to the south of the city, near the origin of the strongest pollution track in Figure 1C.

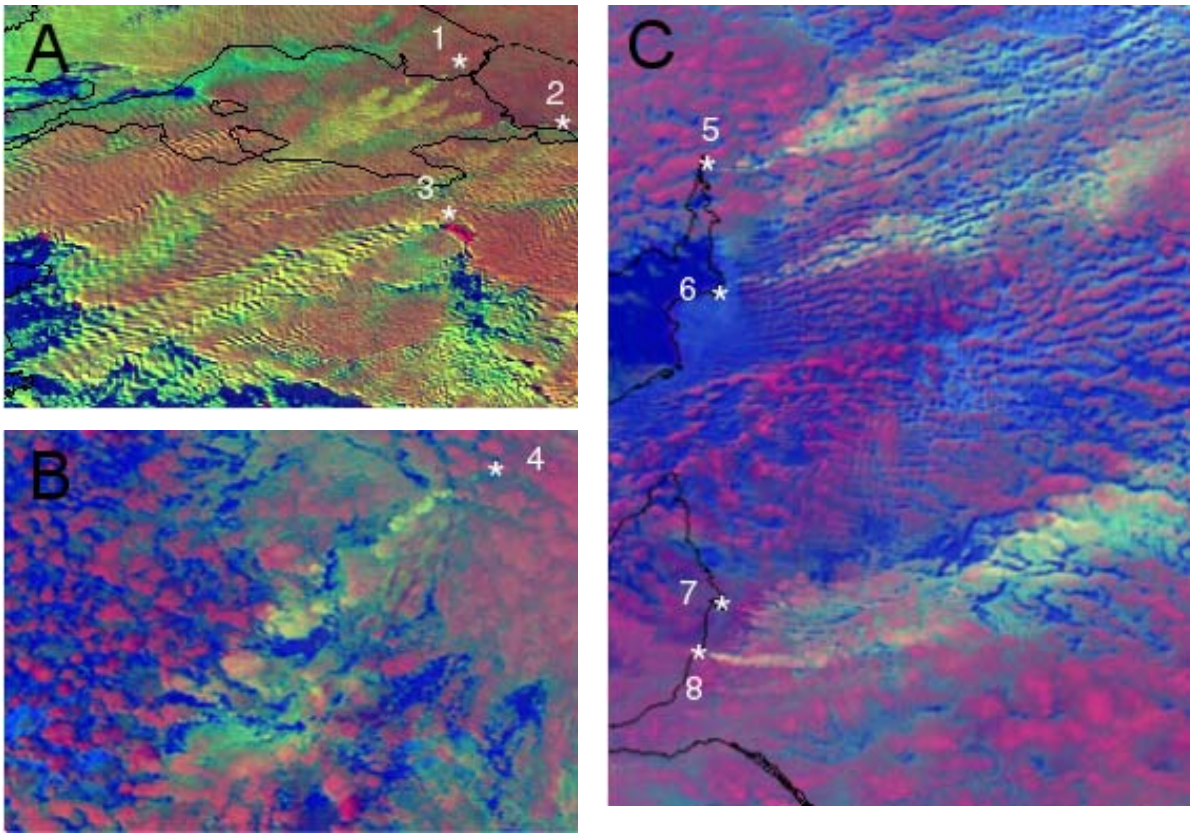

Figure 1. Satellite visualization of NOAA/AVHRR images, showing the microstructure of clouds with streaks of visibly smaller drops due to ingestion of pollution, for three cases over three continents, originating from known pollution sources, marked by white numbered asterisks. The yellow streaks in panel A (about 300 x 200 km) originate from the urban air pollution of Istanbul (*1), Izmit (*2), and Bursa (*3), on 25 December 1998 at 12:43 Universal Time (UT). Panel B (about 150 x 100 km) shows the impact of the effluents from the Hudson Bay Mining and Smelting compound at Flin Flon (*4), Manitoba, Canada (54:46N 102:06W), on 4 June 1998 at 20:19 UT. Panel C (about 350 x 450 km) shows pollution tracks over South Australia on 12 August 1997 at 05:26 UT, originating from Port Augusta power plant (*5), Port Pirie lead smelter (*6), Adelaide port (*7), and the oil refineries (*8). All images are oriented with north at the top. The images are color composites, where the red is modulated by the visible solar reflectance, blue by the thermal infrared (IR), and green is modulated by the solar reflectance component of the 3.7 μm solar reflectance, where larger (greener) reflectance means smaller droplets. This red-green-blue composition determines the color of the clouds, where red represents clouds with large drops, and yellow represents clouds with small drops. The blue background is the ground surface below the clouds. A full description of the color pallets and their meaning is provided in Rosenfeld and Lensky (1998).

The 1998/1999 annual average effluents from the stack of the Port Augusta power plant were 43 kilograms per hour (kg hr^{-1}) of submicron ash particles with modal diameter of 0.14 μm past the electrostatic precipitator. The gaseous annual average effluents are 1108 kg hr^{-1} of sulfur dioxide (SO_2) and 1655 kg hr^{-1} of nitrogen oxides (NO_x) (emission data obtained from Flinders Power, Port Augusta, South Australia). Apparently part of the ash particles act as CCN at short

range, and chemical reactions of the gases produce additional CCN hundreds of km farther downwind of the pollution source, mainly in the form of sulfates.

The AVHRR data were used to retrieve the dependence of the indicated effective radius ($r_e = \langle r^3 \rangle / \langle r^2 \rangle$, where r is the radius of the cloud droplets in the measurement volume) on cloud temperature, T. The method of Rosenfeld and Lensky (1998) was used to derive the T-r_e relations for inference of the precipitation forming processes in the clouds.

The median r_e of the cloud tops in the pollution plumes (Figures 1A–1C) was considerably less than the precipitation threshold of 14 micrometers (μm) (Rosenfeld and Gutman 1994). Outside the plumes, however, r_e increased steeply with decreasing T to more than 25 μm, indicating that the cloud droplets in the general area were coalescing into precipitation. At the same time, little growth of r_e with decreasing T was indicated within the pollution plumes, indicating a lack of coalescence and, thus, suppressed precipitation.

These inferences were validated using the additional sensors onboard the TRMM satellite. The TRMM instruments used were:

- Visible and Infra Red Sensor (VIRS): Similar to the NOAA/AVHRR, but with a 2 km sub-satellite resolution instead of the 1.1 km resolution of the AVHRR. The VIRS is used to obtain the T-r_e relations, as is done with the NOAA/AVHRR.
- Precipitation radar (PR): 2.2 (centimeters, cm) radar, with a sub-satellite resolution of 250 meters (m) vertically by 4 km horizontally. The minimum detectable signal is about 17 dBZ,[1] equivalent to about 0.7 millimeters per hour (mm/hr). The PR is used to measure the precipitation that forms in the clouds.
- TRMM passive Microwave Imager (TMI): The 85 gigahertz (GHz) vertical polarization brightness temperature (T_{85}) is used here to detect the water in non-precipitating clouds.

  The TRMM measurements are validated by an extensive ground validation program (http://trmm-fc.gsfc.nasa.gov/index.html) with preliminary results showing variability of about 25% between rain gauges and TRMM rainfall over large areas, with some TRMM underestimate at the heavier rainfall (Oki et al. 1999). The simultaneous space-borne measurements of cloud microphysics (VIRS), cloud water (TMI), and precipitation (PR) makes it possible to relate the precipitation to cloud microstructure.

The TRMM overpass selected for analysis in this study is for 21 October 1998 at 04:41 UT during a time of strong pollution-track signatures in the clouds throughout southeastern Australia (Figure 2). Seven boxes within the image in Figure 2 were delimited for analyses of the dependence of r_e (Figure 3) and the PR reflectivities (Figure 4) as a function of T. Box 2 encloses a pollution plume, which is clearly visible by the yellow coloring indicating the small r_e of the cloud particles downwind of Adelaide. According to the T-r_e relations presented in Figure 3A, the clouds in the plume had little coalescence, had not glaciated, and were without precipitation; whereas the unpolluted clouds in boxes 1 and 3 in Figure 2 (which are not along

[1] The radar precipitation reflectivity [$mm^6 m^{-3}$] measured in decibels.

the flow, but rather side wind or cross wind to the flow in box 2) had strong coalescence and were precipitating. That inference is corroborated by the PR, which observed precipitation echoes in the clouds outside the plume, but not in the plume. The PR-measured rain intensities exceeded 10 mm/hr. Another large area of clouds with extremely small r_e existed in the Melbourne area and extended downwind to the northeast (box 4). The r_e increased gradually farther downwind but did not reach the precipitation threshold. Farther downwind and to the east of the plume (box 5) only a few isolated showers had formed in some of the clouds that reached the -9°C isotherm and barely exceeded the 14 μm precipitation threshold.

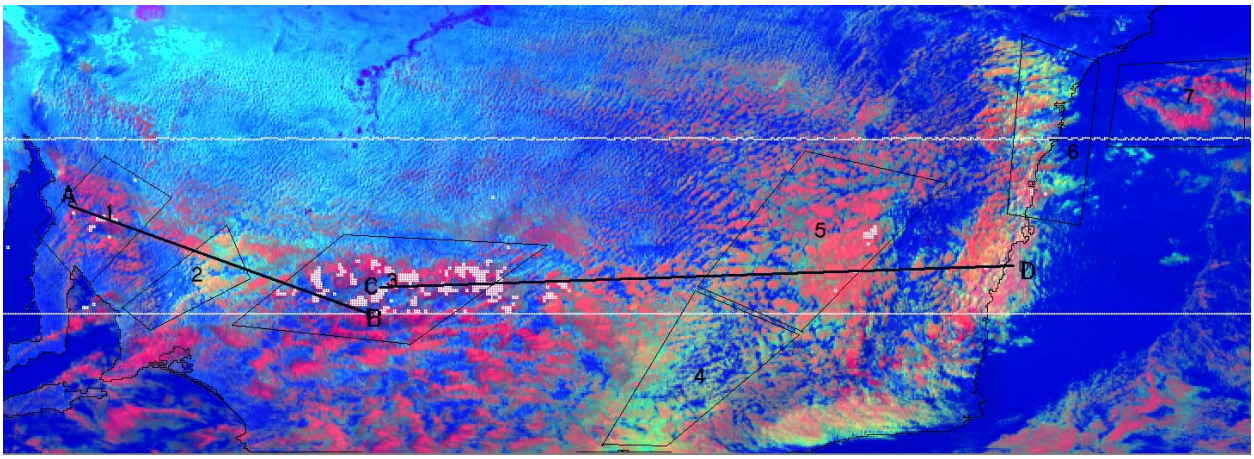

Figure 2. Similar to Figure 1. This figure is a satellite visualization of a TRMM VIRS image of Southeast Australia, with precipitation areas overlaid as white patches on the image. The white patches denote precipitation echoes, as observed by the TRMM Precipitation Radar (PR). The two parallel lines delimit the PR swath of 230 km. The swath is oriented from west (left of the image) to east. The image shows pollution plumes in the clouds over southeastern Australia, from 21 October 1998, 04:44 UT. The lines AB and CD show the locations of the vertical cross sections shown in Figure 5.

Clouds over the Sydney area (box 6) also had much-reduced r_e, apparently due to the pollution there. Clouds over the sea some 150 km away from Sydney (box 7) had much large r_e, indicative of strong coalescence and precipitation, apparently in the relatively pristine maritime air. The TMI-based TRMM rainfall algorithm identified those clouds as precipitating.

The vertical cross sections (Figure 5), cutting through the plumes, show no obvious differences in the cloud top heights and horizontal dimensions in and outside the areas of suppressed precipitation. Furthermore, the depression of the TMI measured T_{85} in the non-precipitating clouds indicates that lack of cloud water was not the reason for the lack of precipitation from these clouds.

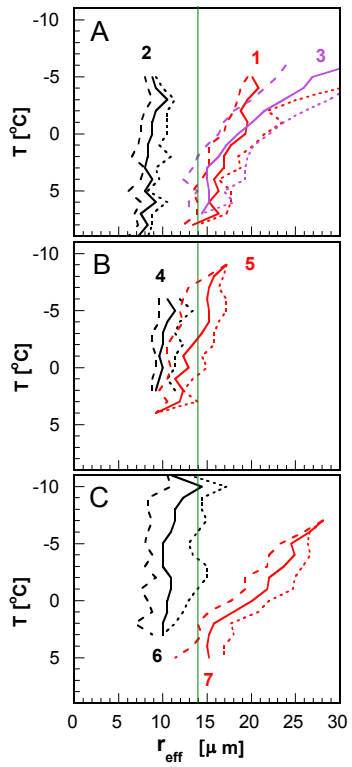

Figure 3. Analysis of the T-r_e relations, where T is the temperature and r_e is the cloud particle effective radius, for the clouds in the seven boxes in Figure 2. Plotted are the 15% (long dashed line), 50% (solid line), and 85% (short dashed line) percentiles of the r_e for each 1° interval. The black lines correspond to the polluted boxes. The vertical green line marks the 14 μm precipitation threshold. A full description of the meaning of the T-r_e charts is provided in Rosenfeld and Lensky 1998).

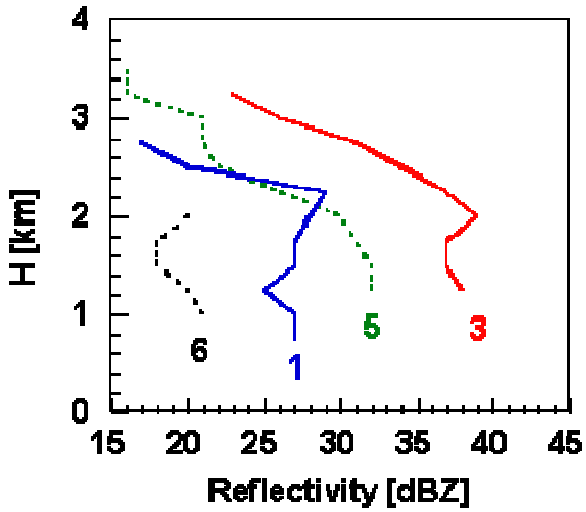

Figure 4. Vertical profiles of the precipitation echo intensities, as measured by the TRMM Precipitation Radar for the various boxes in Figure 2. The peak near 2 km corresponds to enhanced echoes from snowmelt just below the 0°C isotherm. Box 2 had no detectable precipitation. Boxes 4 and 7 are outside of the radar swath.

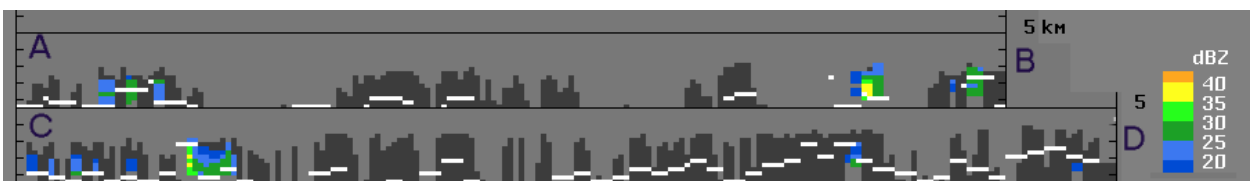

Figure 5. Vertical cross-section along the lines AB and CD in Figure 2. The dark gray areas represent clouds. The vertical extent of the clouds is converted from the VIRS measured top temperatures. The colors represent the precipitation reflectivity, in dBZ, as measured by the TRMM radar. The white line is the brightness temperature of the TRMM Microwave Imager 85 GHz vertical polarization (T_{85}), plotted at the altitude of that temperature. Lower T_{85} (represented as larger height of the white line) in non-precipitating clouds means larger cloud water content. Please note that the T_{85} and actual cloud top temperature have different physical meanings.

The vertical profile of the precipitation echoes, as measured by the PR, has a distinct maximum near the 0°C isotherm, between 2 and 2.5 km above sea level (Figure 4). This maximum is caused by the enhanced radar returns from melting snowflakes, known as the "bright band." The existence of the bright band shows that much of the precipitation was initiated as snow in the upper parts of the clouds. That means that the pollution suppressed the precipitation not only by inhibiting the coalescence of the cloud droplets into raindrops but also by preventing the formation of ice particles and cold precipitation-processes clouds. A likely explanation is that the pollution reduces the radius of the largest cloud droplets below the threshold of 12 μm, which is required for both primary and secondary ice generation in clouds (Mossop and Hallett 1974; Rangno and Hobbs 1994). In view of the observations that most of the winter precipitation events in the Snowy Mountains in Australia (east of box 4 in Figure 2) come from clouds with

tops between -4°C and -13°C, air pollution must be a significant factor in determining the precipitation amounts in the region. Interestingly, a decreasing trend of the snow cover in the Snowy Mountains was suspected for the period 1897–1991 (Harasymiw and McGee 1993). However, a trend analyses for 1910–1991 of snow, winter temperature, and total winter rainfall showed that the decreases in all three parameters were statistically insignificant (Duus 1992).

The satellite data provide evidence connecting urban and industrial air pollution to the reduction of the precipitation, pinpointing both the sources and the affected clouds. This has become possible with the newly acquired capabilities to observe both cloud microstructure and precipitation over large areas, using the TRMM satellite observations. It might be seen as strange that some of the most obvious pollution signatures occur in Australia, which is probably the least polluted inhabited continent. The pollution is evident best in Australia perhaps because it is seen against a background of relatively pristine clouds; whereas in most other places the clouds are already polluted on a very large scale. That might serve as a preliminary indication that human activity may be altering clouds and natural precipitation on virtually a global scale.

2.2. Statistical Evidence

Based on the physical evidence showing the suppressive effect of pollution on rainfall discussed above, Givati and Rosenfeld (2004) decided to examine precipitation records in regions in which the processed satellite imagery suggested would be affected negatively by pollution. The objective of their study was the first-ever quantification of the microphysical effect of air pollution aerosols on precipitation on a regional scale (tens to several hundreds of kilometers). Previous studies had shown qualitatively that urban and industrial air pollution suppresses precipitation-forming processes in convective clouds (Rosenfeld 1999, 2000). The pollution aerosols serve as small CCN that form large concentrations of small cloud droplets. This in turn suppresses the drop coalescence and the warm rain processes, as well as the ice precipitation (Rosenfeld 2000; Borys et al. 2003) and so prolongs the time required to convert the cloud water that exists in small drops into large hydrometeors that can precipitate. Borys et al. (2003) show that the addition of as little as 1 microgram per cubic meter (m^{-3}) of anthropogenic sulfate aerosols to a clean background can reduce the orographic snowfall rate in the Colorado Rocky Mountains by up to 50%. The suppression is stronger in shallower clouds with warmer top temperatures. Satellite observations showed that pollution can completely shut off precipitation from clouds that have temperatures at their tops > -10°C (Rosenfeld and Woodley 2003). Therefore, they expected to find the greatest rain suppression in regions that are dominated by relatively short living clouds with relatively warm tops downwind of major urban areas. Due to their short life, such clouds are more sensitive to slowing down of the conversion of cloud water to precipitation; whereas long living clouds would eventually convert their water into precipitation regardless of the conversion rate. The urban heat island has been documented previously as the main cause for precipitation enhancement in the warm season downwind of major urban areas (Changnon 1979; Changnon et al. 1991; Shepherd et al. 2002). Therefore, they had to select regions where the precipitation is dominated by clouds that are not thermally driven, preferably formed by orographic lifting over mountain ranges downwind of pollution sources during the cold season. California and Israel fit this description and were used for this

study. Annual rainfall data were used because almost all the precipitation in California and Israel occurs in the winter or in winter-like storms during the spring and autumn.

Ideally, the effect would be most pronounced downwind of coastal cities with hills inland that receive precipitation mainly during the winter from shallow convective clouds in maritime onshore flow. The main effect would, therefore, be the suppression of the orographic component of the precipitation, which would be manifested as a reduction in the orographic enhancement factor *Ro,* which is defined as the ratio between the precipitation amounts in the hills to the precipitation in the upwind lowlands. Such conditions are quite abundant, especially on the west coast of continents in the subtropics and mid-latitudes, where the precipitation over the hills is a major source for the scarce water there. This is the reason that the study analyzed historical records of precipitation from California and from Israel, as representative of these conditions.

The main analysis tool was the time series of Ro based on annual precipitation from rain gauges downwind and side wind of major urban areas. The underlying assumption was that small particulate air pollution emissions have increased with the growth of the urban areas, resulting in a decrease in Ro with time. The side wind Ro time series are not expected to show any trend with time, and so serve as controls.

Examples of the methodology are given in Figure 6 for San Diego versus Cuyamaca (a polluted region) and in Figure 7 for Ukiah versus Lake Spaulding (a more pristine area). The top two panels of each figure give the precipitation trend over the twentieth century for each station. The bottom left panels give the correlation analysis and the lower right panels give the trend analysis for the ratio (R_o) of inland to coastal annual precipitation. Note that the paired stations are well correlated, but that the trend of R_o is strongly negative for San Diego versus Cuyamaca and flat for Ukiah versus Lake Spaulding in the more pristine area. This pattern was typical for mountain versus coastal stations in highly populated areas, in agreement with expectations.

Figure 8 shows in a schematic cross section from west to east the precipitation changes the full width of the Sierras. It can be seen that the western slopes are the areas most sensitive to air pollution. The decrease in the orographic ratio between the coastal and plains areas to the upwind slopes is around 20% (which is statistically significant). This trend becomes weaker with elevation, and the opposite trend occurs on the eastern slopes of the Sierra Nevada.

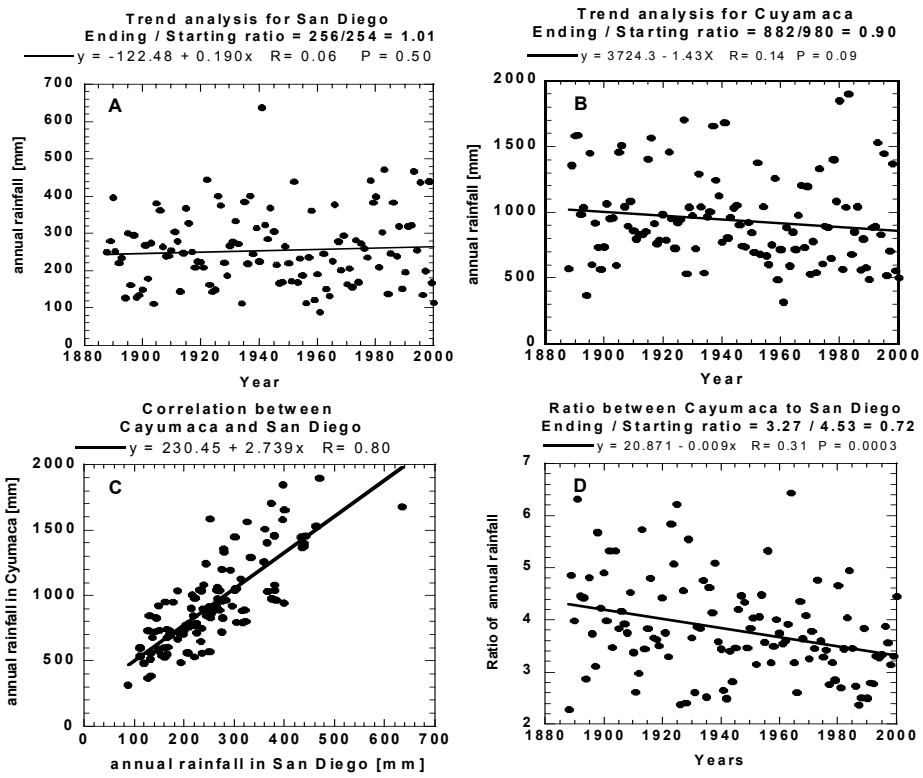

Figure 6. Long-range trends of (A) the annual precipitation measured in San Diego, and in (B) the downwind hilly station of Cuyamaca at an elevation of 1550 m; (C) the correlation between these two stations; and (D) the annual ratio of precipitation (Ro) measured between them. The stations with the longest record in California are presented here. Note the sharp decrease in Ro with time in this area, which is affected by urban air pollution. *Ending/starting ratio* means the ratio at the beginning of the time series compared to the ratio at the end, as calculated from the regression line at these times. *R* means the linear correlation coefficient, and *P* is the statistical significance that corresponds to the t test statistic from Student's t test.

It is important to determine the net gain or loss of precipitation along the whole cross section. This is calculated in Table 1 for a 1 km-wide strip across the average width of the Sierra Nevada with their respective rainfall changes, as defined in Figure 8. The reduction over the western slopes dominates the overall hydrological budget, incurring a large net loss of about 20 million m^3 for each 1 km segment of the mountain ranges. This means an overall loss of 4×10^9 m^3 $year^{-1}$ of precipitation water just for the 200 km-long section of the mountains that are located to the east of the line between Sacramento and Fresno. This calculation is highly oversimplified and merely provides an estimate of the magnitude of the problem. More exact calculations and their hydrological meaning, to be determined by relating precipitation to stream flows, are required. Further, these precipitation losses may not even be evident to water managers because of masking by the long-term increases in the overall upwind Sierra precipitation.

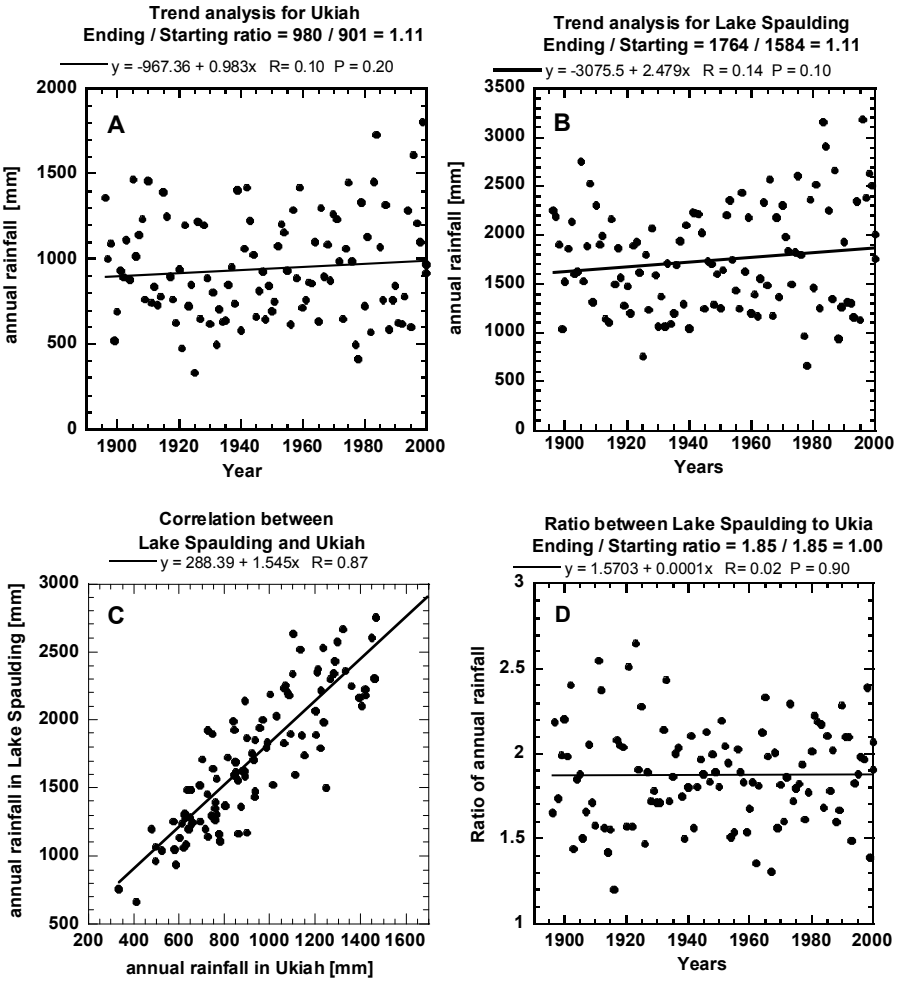

Figure 7. Same as Figure 6, but for (A) the relatively clean area in Northern California at Ukiah and (B) the downwind hilly station of Lake Spaulding at an elevation of 1717 m. (C) The annual precipitation of the two stations is well correlated. Both stations show increases in precipitation over the period of record. Note (D) the lack of a trend in the ratio between the hilly and upwind lowland stations.

This study analyzed only two geographical areas where the physical basis suggested that such an unfavorable redistribution of precipitation would occur and where the quality precipitation data at the hilly areas were available. Similar effects can be expected in other areas, such as the Snowy Mountains and Victorian Alps in Australia (Rosenfeld 2000), the Atlas Mountains, Mediterranean coastal hill ranges, Chile, Puerto Rico, and many more locations.

Table 1. The approximate budget of precipitation change in the section with suppressed precipitation across the longitudinal zones of the Sierra Nevada, as defined in Figure 8. The change in precipitated water volume is calculated for a 1 km-wide strip across the mountains.

Zone	Description	Heights (m above sea level)	Width (km)	Rainfall change (mm year^{-1})	Rainfall change (m^3)
4	Western slopes	500–2500	100	-220	-22×10^6
5	Divide	> 2500	50	-65	-3.25×10^6
6	Eastern slopes	> 2000	25	+66	$+1.65 \times 10^6$
Total					-23.60×10^6

Examination of the precipitation records over the twentieth century revealed that the detrimental effect of the pollution has not improved with time, despite the decreasing levels of standard measures of air pollution in California. This is explained by the constancy of the very small aerosols that account for the bulk of the CCN concentrations. A major source of very small (< 0.1 μm) aerosols, which are as efficient as CCN biomass smoke particles, is diesel engines (Lammel and Novakov 1995). A diesel car produces several orders of magnitude more such particles per mile than a gasoline car with the same fuel consumption (Pierson and Rachaczek 1984; Williams et al. 1989; Lowenthal et al. 1994; Weingartner et al. 1997; Maricq et al. 1999). The consumption of diesel fuel in transportation has been increasing in California at twice the pace of gasoline since 1980, and consequently the production of these small CCN aerosols, which are not reflected in any of the standard air quality measures. Furthermore, these small and numerous particles have the greatest potential for precipitation suppression. In contrast, the larger (> 1 μm) pollution particles could actually induce large drops and enhance precipitation, but these are the particles that have been most effectively eliminated from the emissions.

2.3. Physical/Statistical Summary

The physical analyses described in Section 2.1 make a strong case for the detrimental effects of pollution on cloud microphysical structure and rainfall. The effects can literally be seen in the multi-spectral satellite imagery.

In addition to the physical analyses, strong circumstantial evidence has provided a quantitative link of anthropogenic air pollution with the suppression of orographic precipitation downwind of the pollution sources by 15% to 25%, in the following ways:

- The decreasing trend of the mountain precipitation is linked to the period of urbanization and industrialization upwind; whereas similar analysis of the orographic rainfall in nearby more pristine areas showed no trends.

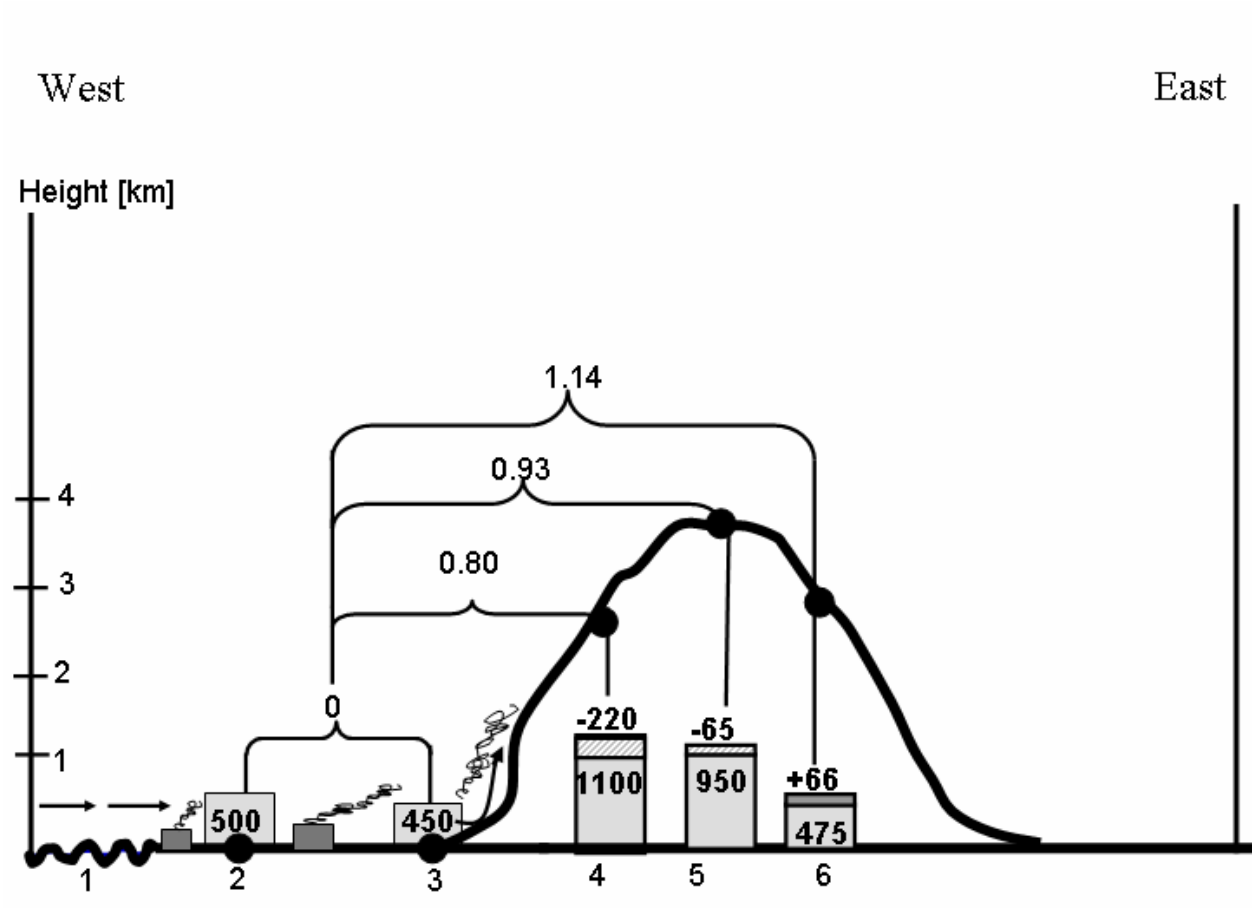

Figure 8. Topographic cross section showing the effects of urban air pollution on precipitation as the clouds move from west to east from the coast to the Sierra Nevada Mountains and to the eastern slopes. The boxes show the amount of the annual precipitation (mm/year) in each topographic location and the numbers above them show the loss or gain of precipitation (mm/year) at each site. Maritime air (in zone 1) is polluted over coastal urban areas (in zones 2 and 3), but no precipitation decrease occurs. The polluted air rises over mountains downwind and forms new polluted clouds (in zone 4), resulting in decreases of 15%–20% (losses of 220 mm/year) in the ratio between the western slopes to the coastal and plain areas. The clouds reach to the high mountains (in zone 5). All the precipitation is snow, and there is a slight decrease of 5% to 7% (a loss of 65 mm/year) in the ratio between the summits to the plains areas. The clouds move to the high eastern slopes of the range (in zone 6), where there is an increase of 14% (gain of 66 mm/year) in the ratio between the eastern slopes to the plains. According to Table 1, the net loss is dominant.

- The suppression occurs mainly in the relatively shallow clouds within the cold air masses of cyclones, which ingest the pollution from the boundary layer while ascending over the mountains.
- The suppression that occurs over the upslope side is coupled with similar percentage enhancement on the much drier downslope side of the hills, probably because more cloud water passes over the divide.

The main hydrological recharge zones of the water resources in the study areas overlap with the areas where large and statistically significant suppression of precipitation was measured, with water losses ranging between 15% and 25% of the annual precipitation. The downwind areas where compensatory enhancement occurs have much lower absolute amount of precipitation (about 25%) than the upslope side of the hills, and therefore the compensatory relative increases on the downwind side are manifested as much smaller amounts of added water compared to the losses in the upslope areas. For example, a net loss of precipitation water volume of about 4×10^9 m^3 (4 million kilotons) estimated over the mountains to the east of the line connecting Fresno and Sacramento. These are startling results for regions that occasionally experience severe water shortages. In addition to the obvious ramifications for water resources, climate impacts are also important and must be considered.

3.0 Proposal Goal and Objectives

The goal of the highly focused, exploratory research effort involving hydrological analyses, satellite-based cloud analyses, and numerical modeling, was to further document the detrimental effects of urban and industrial air pollution in California on clouds, precipitation, and stream flows in mountainous terrain downwind of the pollution sources. Accomplishing these tasks required the use of cutting-edge technology, methods, and models that are unique to the research team.

The research effort had three objectives: (1) to determine whether the documented losses in Sierra orographic precipitation are evident also in the Sierra stream flows, using hydrological stream flow analyses; (2) to quantify cloud microphysical structure through the analysis of multi-spectral satellite imagery, to determine whether the regions of precipitation loss are evident in the quantitative satellite analyses; and (3) to conduct numerical model simulations of the effect of CCN pollution aerosols on clouds and precipitation, for comparison with the results of objectives 1 and 2. The precipitation data already have been analyzed quite extensively, and the results are presented in Givati and Rosenfeld (2004) and summarized herein.

Instead of fine-tuning the precipitation analyses further, which would result in marginal additional insights, the rainfall analyses were combined with available stream flow data in addressing Objective 1 to determine the impact of the documented precipitation changes on water availability in the various Sierra drainage basins. The historical stability between precipitation amount and stream flow was established for each basin, because a high correlation between precipitation in the catchment and the stream flow is necessary in order to relate any potential changes in stream flow to changes in precipitation regardless of its cause. In addition, the relationship between precipitation and stream flow must be stable for the period of record to assess the stream flows' reaction to the anthropogenically induced precipitation changes.

Because the initial manifestation of the detrimental effect of air pollution on cloud precipitation-forming processes came through the analysis of a limited sample of multi-spectral satellite images, the next step in addressing Objective 2 was the analysis of a larger image sample. Specifically, all NOAA/AVHRR daylight satellite overpasses of California for three full rain seasons were analyzed. The analyses were partitioned as a function of wind direction and speed in order to specify the weather conditions under which the clouds are most susceptible to the suppressive effects of the pollution aerosols and the geographic areas of California that are most affected by the detrimental effects of the aerosols. Weather radar data were used in a few cases for validating the satellite inferences.

An example of what was to be done with three years of satellite imagery for California under the proposal is shown in Figures 9–11. (For satellite methodology details, please see Appendix A.) The analysis is for the image at 2050 UT (1250 PST) on 7 December 2004. All of California had been traversed by a strong cold front during the night and a westerly flow of cold unstable air was in place over California behind the front. Scattered to broken cloudiness was over much of California, with the exception of the mountains, where overcast conditions prevailed.

The T-r_e analyses for the areas shown in the colorized image appear in the insets on the right of each figure. The median plot is at the interface of the yellow and green lines. The threshold for precipitation is the vertical white line at 15 μm. Thus, the farther the plot is to the right the more likely that the clouds were producing precipitation. Conversely, if little to none of the plot crosses the white line corresponding to the precipitation threshold, it is unlikely that the clouds were producing precipitation. The short vertical colored lines on the left are the microphysical zones discussed in Appendix A.

Beginning in the north of the image, the clouds in areas 3 and 5 are mostly red and the inset plots suggest that the clouds were precipitating. As one progresses south, however, through areas 7 and 9, which are downwind of the San Francisco-Oakland urban area, the clouds are less red, with some yellow and green showing up. The inset plots for these areas are farther to the left of the 15 μm precipitation threshold, indicating that fewer of the clouds were precipitating and they were reaching the precipitation threshold at colder temperatures than in areas 3 and 5, which are downwind of relatively unpopulated areas.

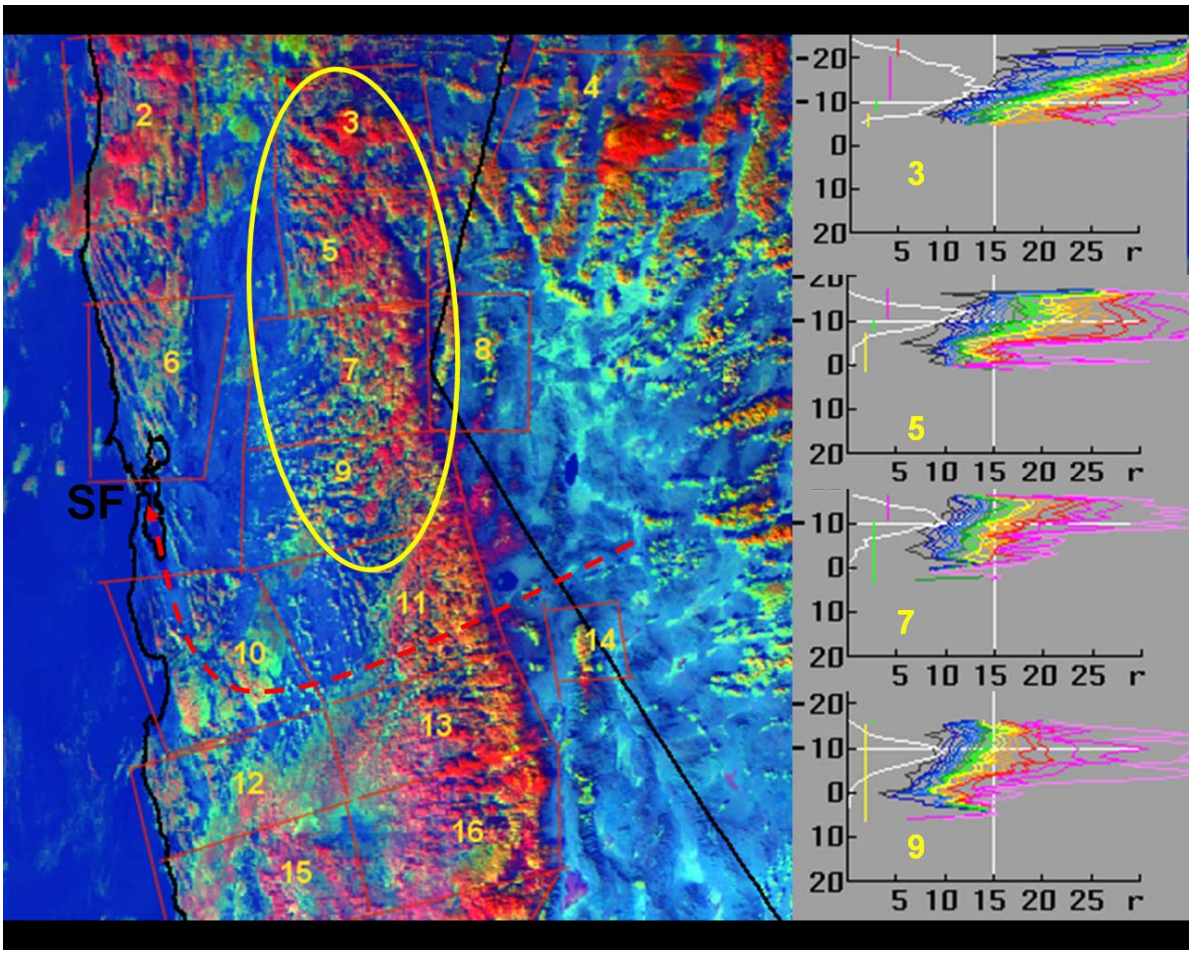

Figure 9. Processed satellite image at 2050 UT (1250 PST) on 7 December 2003. The T-r_e analyses for the areas shown in the colorized image appear in the insets on the right. The median plot is at the interface of the yellow and green lines. The threshold for precipitation is the vertical white line at 15 μm. The short vertical colored lines on the left are the microphysical zones discussed in Appendix A.

Continuing the southward progression through California in Figure 10, note that the inset plot is farthest to the left of the precipitation threshold in area 9 and that the plots move back to the right farther to the south. The plot for area 16, which is downwind of more sparsely populated areas in central California, is totally to the right of the precipitation threshold, with the exception of an excursion back to the left between -10°C and -15°C. This excursion is due to the presence of thin layer clouds obscuring the convective clouds underneath. Overall, there is a high probability that the clouds were precipitating.

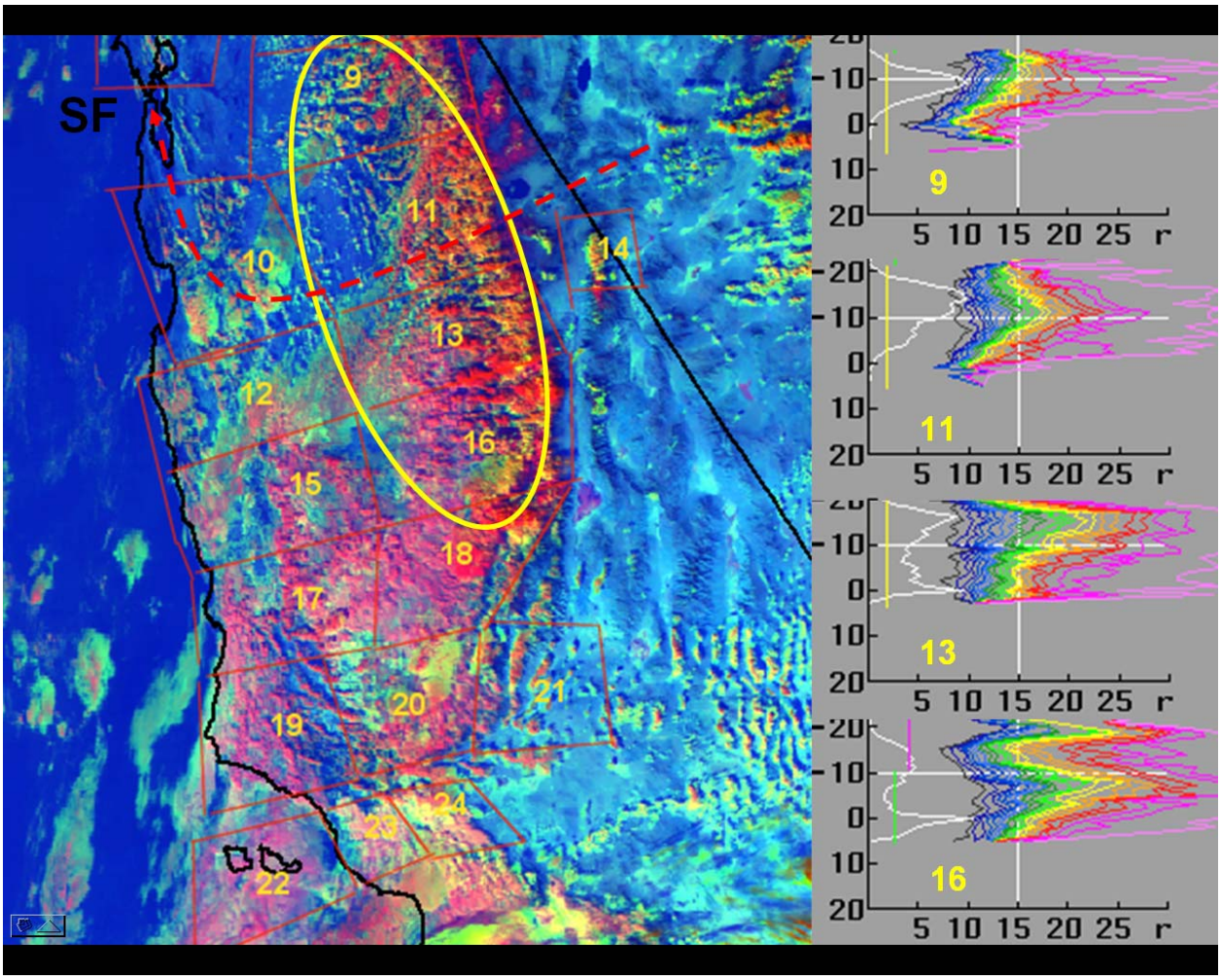

Figure 10. The same as for Figure 9, except the inset T-r_e plots are for areas 9 through 16

The southern portion of California is examined in Figure 11. The clouds in areas 16 and 18 show most of the inset plots to the right of the precipitation threshold and were likely precipitating. Farther south to the lee of Santa Barbara (area 20) and the Los Angeles metropolis (area 24) the plots move back to the left. The plot for area 24 for the mountains to the east of Los Angeles is well to the left of the vertical white line corresponding to the precipitation threshold. The analysis indicates that none of the clouds here was precipitating, suggesting that these clouds were highly polluted by tiny CCN aerosols.

This type of analysis was done under the contract for all days with polar-orbiter, multi-spectral, satellite overpasses for three California rainy seasons. The data were composited to identify which areas of California are likely most affected detrimentally by the pollution.

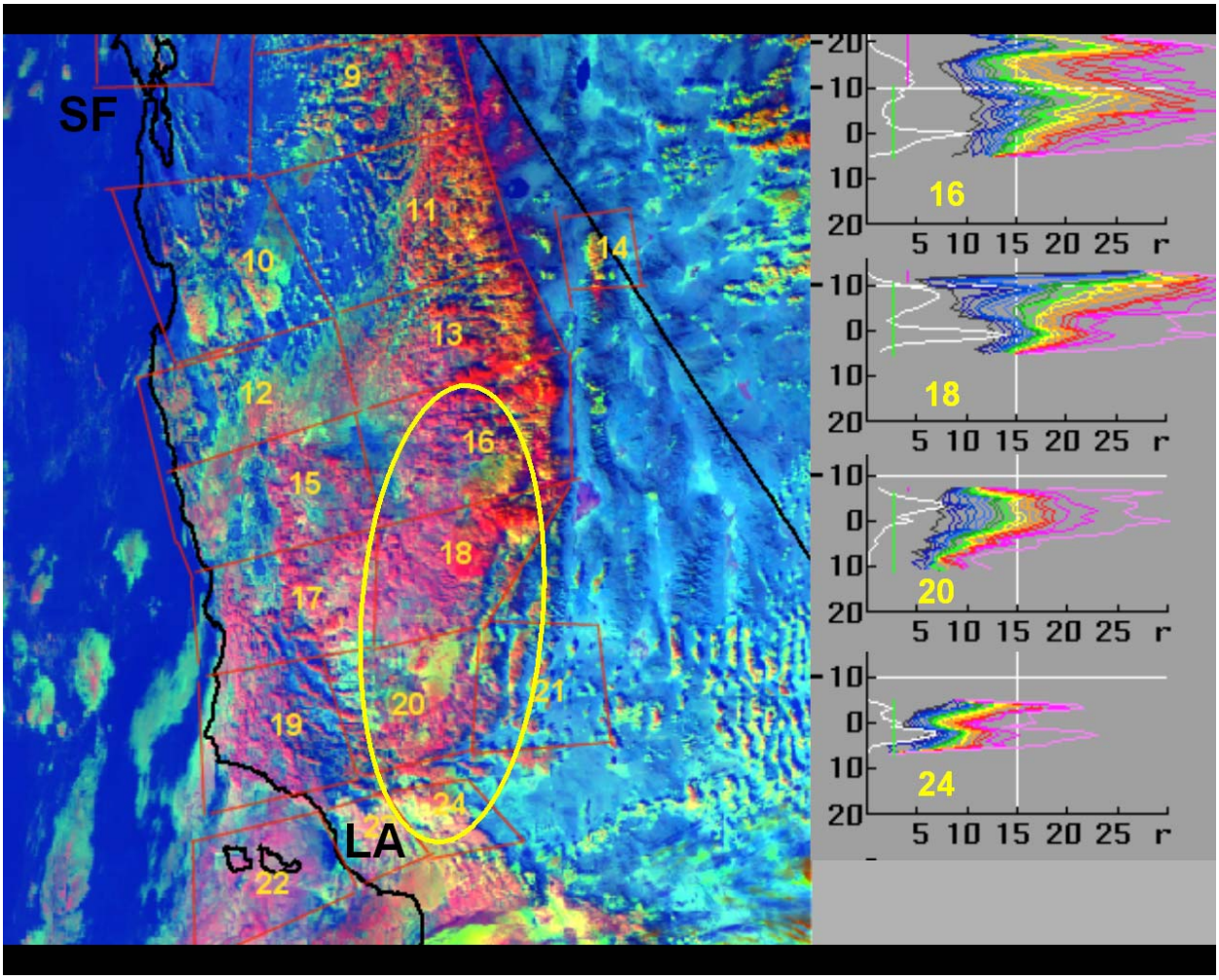

Figure 11. Same as Figure 9, except the inset T-r_e plots are for areas 16 through 24

The third objective of the research effort involved numerical model simulation of cloud processes under polluted and non-polluted conditions in order to specify the role of pollutants on cloud microstructure and precipitation. Accomplishing this required the incorporation of an explicit microphysical scheme and the topography of California into the dynamical framework of the Weather Research Forecast (WRF) mesoscale model, which is in wide use today. The integrated model was run for the case illustrated above. Comparisons were made between the conditions observed by satellite and radar with those simulated by the model. This was done to validate the model. This was followed by model runs with and without the effects of urban aerosols such that the differences provide an estimate of the net effect of pollution on precipitation.

The third objective of the research effort was the numerical simulation of the effects of pollutants on Sierra clouds and precipitation. Despite a significant improvement in model grid resolution and a decrease in initial condition uncertainty, the accurate prediction of precipitation amount and distribution still remains a difficult problem. One of the reasons for this situation is that state-of-the-art, cloud-resolving mesoscale models use bulk-parameterizations for description of microphysical processes. These schemes are non-sensitive to aerosols in the atmosphere, whose variation, as was shown in recent observational and numerical studies, has dramatic effects on precipitation. A novel mesoscale model with spectral (bin) microphysics (SBM) has been developed recently in the Hebrew University of Jerusalem. The model was constructed by implementation of the micro-physical package of the two-dimensional (2-D) Hebrew University Cloud Model (HUCM) initially into the well known Pennsylvania State University/National Center for Atmospheric Research mesoscale model (MM5) model and later in the WRF model. Both models include topography, surface fluxes of heat and moisture, as well as radiation. The MM5 model has been used for simulation of a mesoscale precipitating system that developed over Florida 27 July 1991 accompanied by a squall line formation. In parallel, similar simulations have been performed using all bulk-parameterization schemes, which are included in the current MM5 model. Simulations were performed using a nested grid system, with the finest resolutions of 1 and 3 km. The results showed that the SBM model produced a drastic improvement in the prediction of rain rate, rain amount, and spatial distribution of clouds as compared to bulk-parameterization schemes. While the SBM model correctly predicts the formation of both convective and stratiform clouds, all bulk parameterization schemes overestimate the intensity of convective clouds and strongly underestimate the coverage of stratiform clouds. Moreover, the SBM model showed significant sensitivity of precipitation amount and precipitation rate, as well as cloud structure, to atmospheric aerosols. The SBM mesoscale model developed can be used for analysis of sophisticated case studies of specific phenomena such as severe storms, winter storms, and others. It is specially designed to evaluate the effects of anthropogenic aerosols on precipitation amount and spatial redistribution of precipitation over complex terrain.

4.0 The Hydrological Analyses

4.1. Introduction

In addressing Objective 1—the hydrological analyses—researchers combined the precipitation data with available stream flow data, to determine the impact of precipitation changes on water availability in the various Sierra drainage basins. The basis for this study are the studies by Rosenfeld (1999; 2000), and recently by Givati and Rosenfeld (2004; 2005) and Rosenfeld and Givati (2006) that showed that urban and industrial air pollution has suppressed rain and snow. They quantified the precipitation losses over topographical barriers downwind of major coastal urban areas in California and other places in the western United States, which amounts to 15%–25% of the annual precipitation. The suppression occurs mainly in the relatively shallow orographic clouds within the cold air mass of cyclones. The suppression that occurs over the upslope side is coupled with similar percentage enhancement on the much drier downslope side of the hills such that there is a net overall loss of water.

As shown previously, Figure 8 summarizes in a schematic cross section the full phenomenon as it accrues in the relatively polluted part of the California Sierra Nevada downwind of Fresno. It can be seen that the western slopes are the most sensitive to the suppressive effect of the air pollution. The decrease in the orographic precipitation ratio between the mountainous areas and the coastal and plains areas upwind is around 20% (which is statistically significant). These precipitation losses become less with elevation with the opposite enhancement of precipitation on the eastern slopes of the Sierra Nevada.

Recent study by Rosenfeld and Givati (2006) quantified the effect of aerosols on precipitation not only in California but also farther inland through much of the western United States. Analyses of trends of the orographic winter precipitation enhancement factor (Ro) along the coastal mountain ranges of the western United States coast shows a pattern of decreasing ratio during the last century by as much as -24%. The decrease occurred from the southern border of California with Mexico to central California, to no decrease in Northern California and Oregon, and to a renewed decrease of Ro (-14%) in Washington to the east of the Puget Sound/Seattle area. Similar decreases occurred also well inland, over Arizona, New Mexico, Utah, and the Colorado Rockies.

Rosenfeld and Givati (2006) showed that both absolute precipitation amounts and Ro were affected by fluctuations in the atmospheric circulation patterns, such as those associated with the Pacific Decadal Oscillation (PDO) and the El Niño–Southern Oscillation Index (SOI). However, these climatic fluctuations cannot explain the observed trends in Ro. They also analyzed trends of aerosol measurements from the Interagency Monitoring of Protected Visual Environments (IMPROVE) aerosol monitoring network (available only since 1988) and showed that the negative trends in Ro are associated with elevated concentrations of fine aerosols ($PM_{2.5}$). The $PM_{2.5}$ showed stability or some increase in the areas where decreasing trends of Ro were noted. Strong decreasing trends of the coarse aerosols (PM_{10}–$PM_{2.5}$) were noted, especially in the areas with elevated levels of $PM_{2.5}$.

4.2. Historical Relationships between Precipitation and Stream Flow in the Sierra Nevada and the Coastal Range

The first step in this study was to establish the historical relationships between precipitation amount and stream flow for basins in the Sierra Nevada and for the coastal range. Strong linear correlations between the annual volumes of the flow and the annual precipitation were found. Figure 12 displays the correlation between (A) the annual flow volumes of the American River at Folsom and the annual precipitation at Pacific House in the Sierra Nevada, and (B) the correlation between the Russian River and the Ukiah rain gauge in the coastal range. Similar high correlations were found at other Sierra and coastal basins. Documentation is provided in Appendix B (Figures B1–B6 for rivers and rain gauges in the coastal range, and Figure B7 presents the location of those pairs).

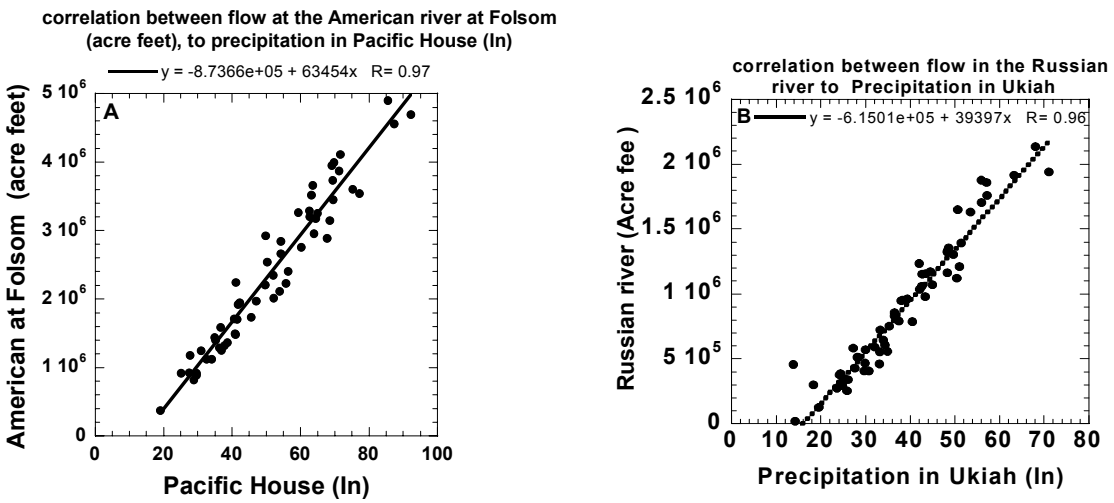

Figure 12.The correlation between (A) the American river (at Folsom) and the annual precipitation at the rain gauges of Pacific House (3400 ft, lat: 38.765, long: 120.500), and (B) the Russian river (at Healdsburg) and the precipitation in Ukiah (633 ft, lat: 39.15, long: -123.20l).

4.3. Establishing Runoff Relationships

The next step after showing the strong linear relationships between runoff and precipitation was to apply the same procedures used for the rain gauge analysis in order to test the ratio between the annual river flows in the Sierra to the flows in the coastal rivers. The available database for this analysis was the full natural river-flow list provided by the California Department of Water Resources. Stream flow data is available for most of the Sierra Rivers since the beginning of the twentieth century but only a few coastal range rivers have such records. The pairs with the best correlations were chosen. Figure 13 displays a map of the locations of analyzed flows for the Sierra and coastal range rivers, and the main results of the trends of the ratio between them. Rivers pairs are marked by the blue circle for the coastal range rivers, red circle for the Sierra Rivers downwind and yellow for the eastern Sierra Rivers. The fractional change of the annual ratio of stream flow between the Sierra to the coastal range and Sierra to Sierra since about 1945–1950 is shown near each pair with green background.

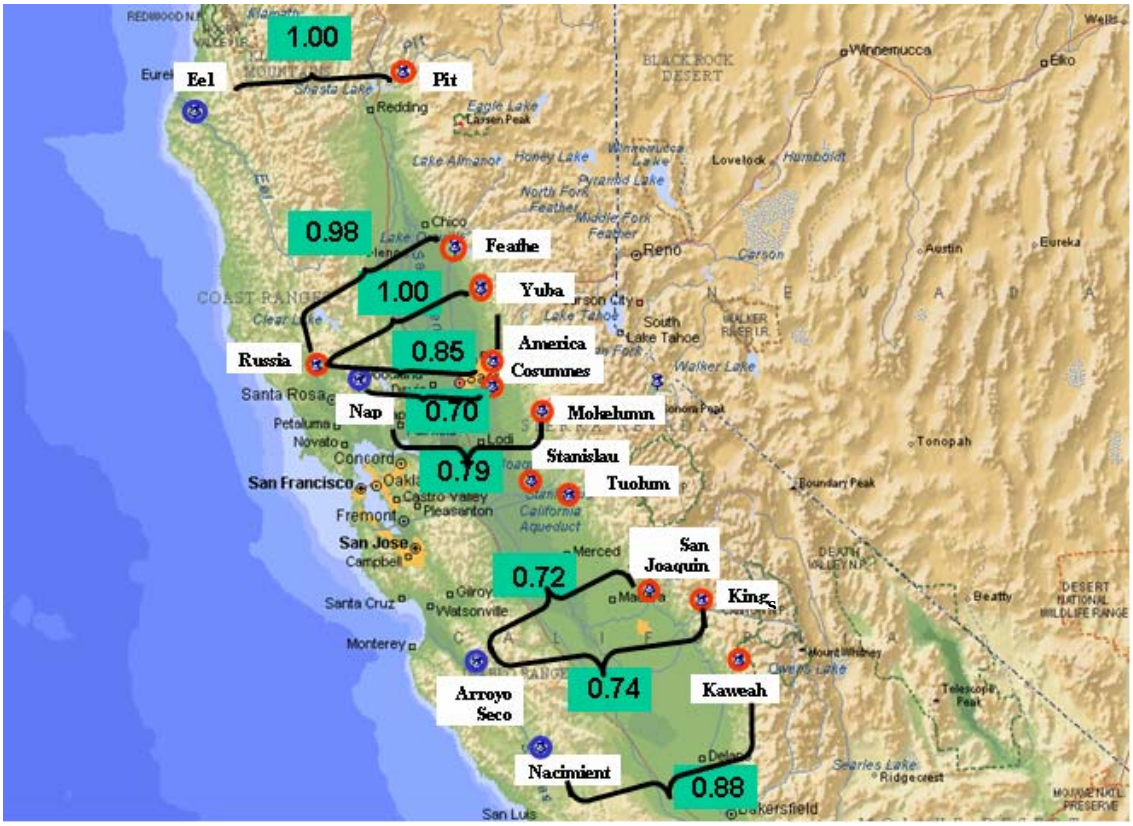

Figure 13. Map of the locations of analyzed flows for the Sierra and coastal range rivers, and the main results of the trends of the ratio between them. The methodology for calculating the trends between the Sierra to the coastal rivers is shown in Figure 14 for the pair of American and Russian Rivers, in the nine-panel graph below. Note the good precipitation-flow relationships, which make the response of the hilly river flow linearly related to the change in the orographic enhancement factor of the precipitation.

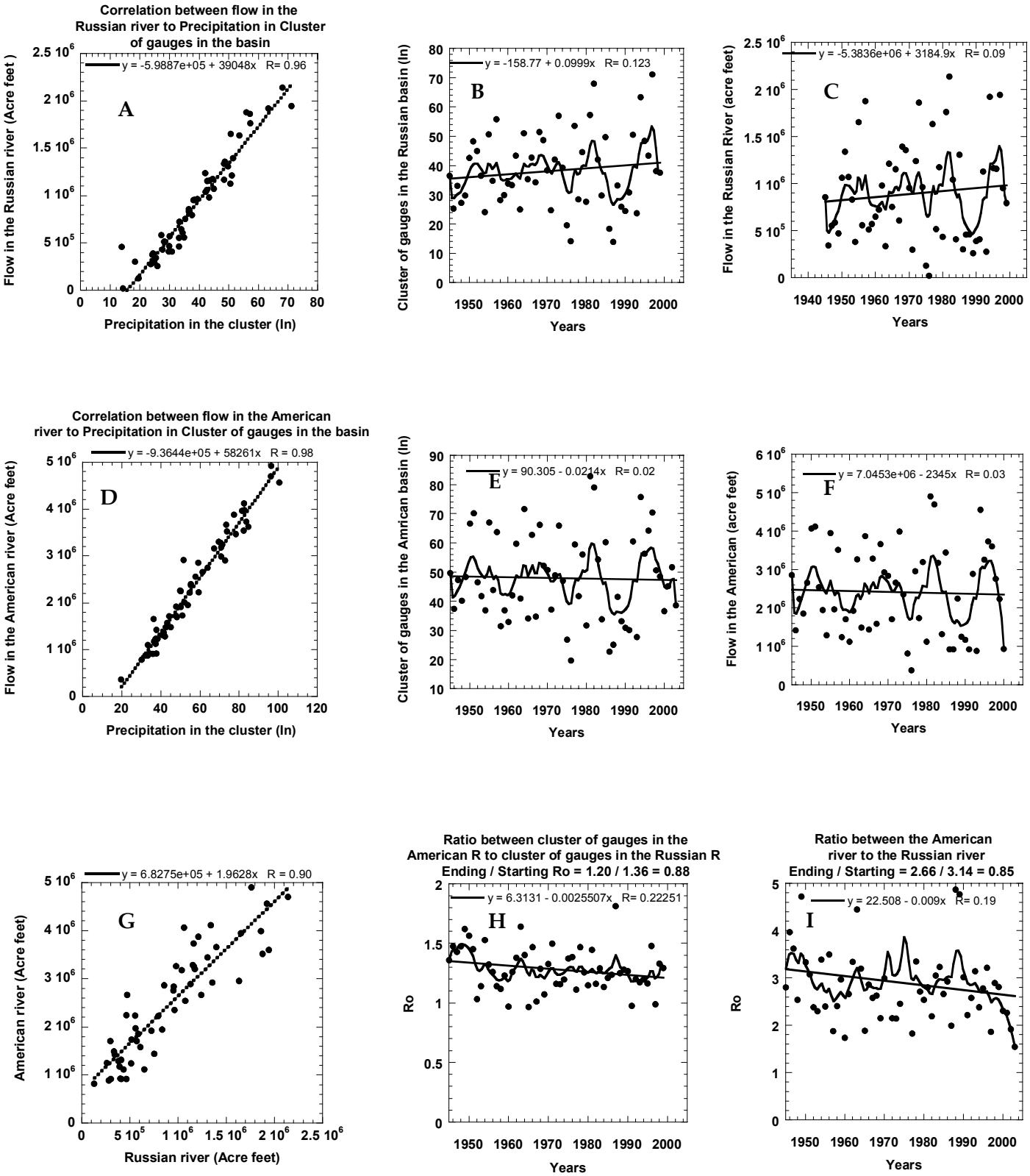

Figure 14. Correlation between (A) the Russian River and rain gauges in the basin, (D) the American River and rain gauges in the basin, and (G) the American vs. the Russian rivers. The middle columns of the panel display the annual precipitation at clusters of rain gauges at (B) the Russian basin, (E) the American river, and (H) the ratio between them. The right column displays the flow in (C) the Russian River, (F) the American River, and(I) the ratio between them.

Additional analyses of trends for the period of 1945–2000 rain gauges and river flows in the Sierra Nevada are presented in Table B1 in Appendix B.

Anther way for detecting the loss of water in the Sierra rivers due to the decrease in orographic precipitation, is to measure the relative trend between the ratio of Sierra rivers to plains rain gauges. The research team already showed the high correlation between annual volumes of stream flow to precipitation (hilly and plains rain gauges). Figure 15 displays the ratio between stream flow volumes in: (A) Merced (at Merced Falls) to precipitation in Merced, (B) San Joaquin River to precipitation at Big Sur, and (C) San Joaquin River to precipitation at Fresno.

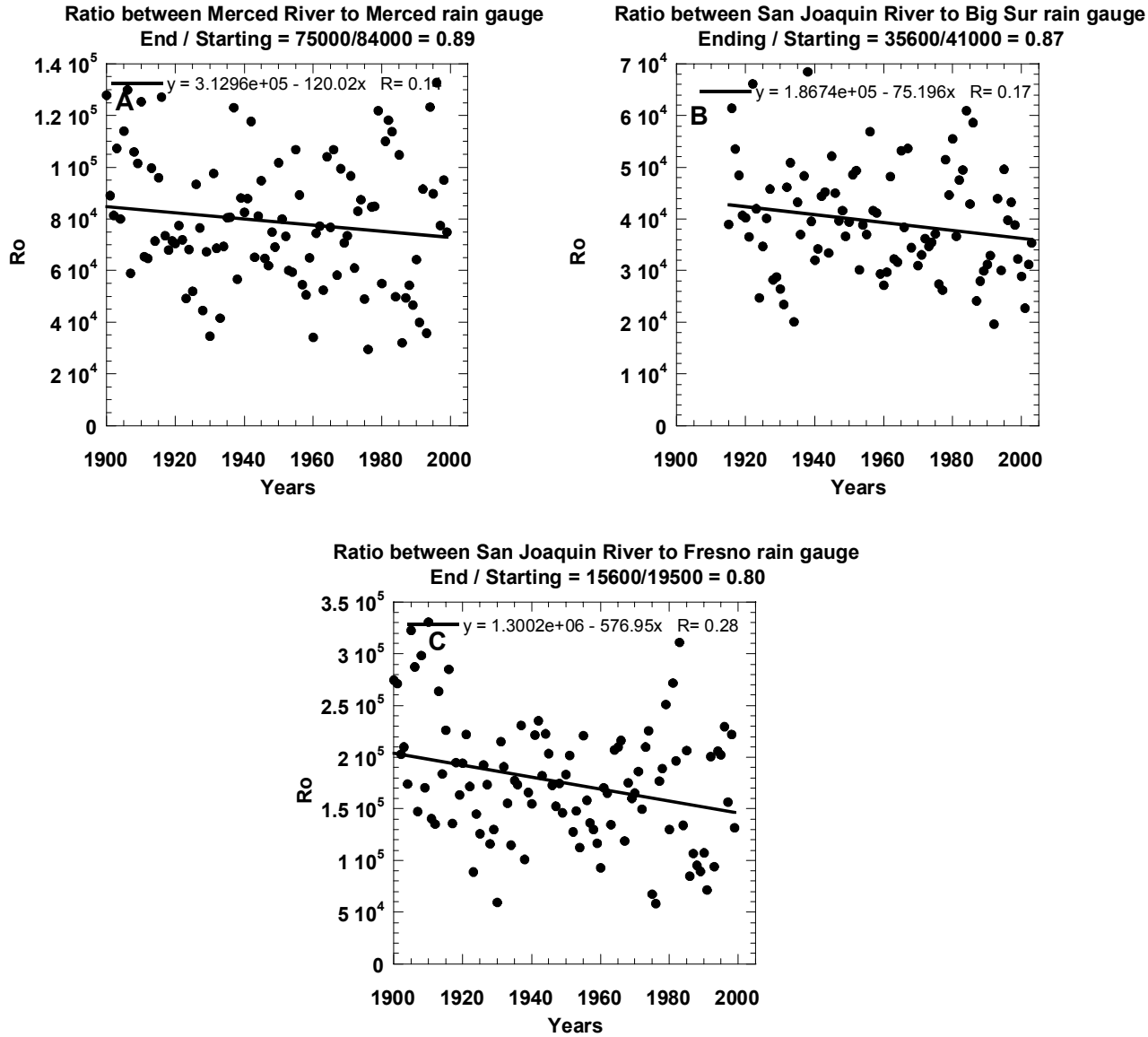

Figure 15. The ratio between (A) Merced to precipitation in Merced, (B) San Joaquin River to precipitation at Big Sur, and (C) San Joaquin River to precipitation at Fresno

The analysis for the 1945–2003 period shows decreasing trends for the ratio between the Sierra to the coastal range rivers, while a stable trend is noted for the ratios in the northern rivers (the Pit versus the Eel, and the Feather and the Yuba versus the Russian River). Only two rivers in the coastal range have a measurement record since the beginning of the twentieth century: the Arroyo Seco and the Nacimiento rivers. The results for the 100-year trend analysis for the San Joaquin and Kings Rivers (Sierra) versus the Arroyo Seco (coastal), and for the Kaweah River (Sierra) versus the Nacimiento River (coastal), showed a stable trend for the complete 100-year period (Figure 16A). The ratio for the first half of the century was found to be stable (Figure 16B) but the ratio in the second half showed a decreasing trend (Figure 16C).

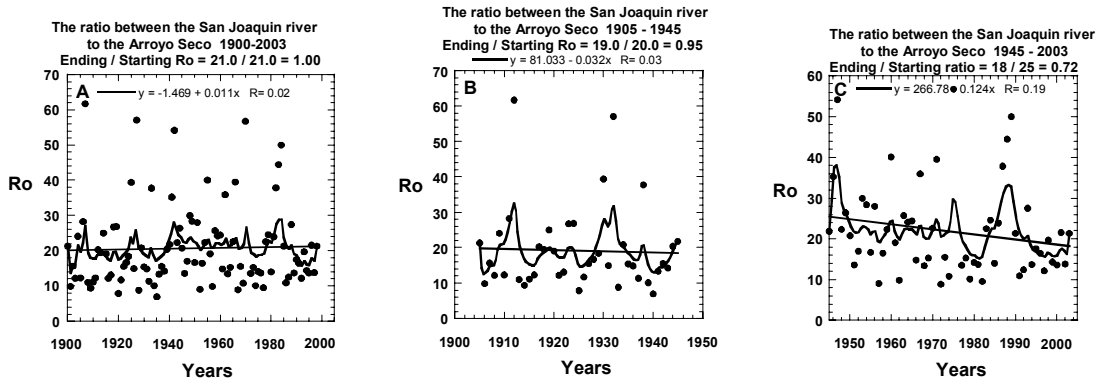

Figure 16. Stable trend for the 100-year ratio between (A) the San Joaquin river to the Arroyo Seco, and also for (B) the period 1905–1945, and (C) the decreasing trend for the period between 1945–2003.

To better understand the differences between the first half and the second half of the century, the research team examined runoff/precipitation ratios through the twentieth century for Sierra (San Joaquin, Kings and the Kaweah rivers) and coastal range basins (Arroyo Seco and Nacimiento rivers). The ratio and the correlation between the Arroyo Seco versus precipitation at Big Sur for three periods: 1916–2000, 1916–1945, and 1945–2000 are presented in Appendix B, Figure B8. It can be seen that the decrease in the runoff/precipitation ratio occurred in the first half of the century while in the second half the ratio increased. This trend means that during the first half of the century there was less water in the Arroyo Seco for the same amount of precipitation. Such a trend is not natural because runoff is not expected to decrease while the precipitation is stable. This casts doubt on the quality of the stream flow records in the coastal rivers during the first half of the twentieth century.

4.4. Downwind versus Upwind Sierra Runoff Relationships

Next, the research team explored the question of what happens downwind of the ridgeline to the excess cloud water that was not converted into precipitation due to the suppression of precipitation on the upslope side. Apparently the added cloud water and newly formed precipitation particles that pass over the divide cause enhancement of the precipitation on the downslope side (see example from Givati and Rosenfeld [2004] in Figure 17). This phenomenon occurs in all areas with available data where suppression was observed on the upslope side. No trends in the ratio were found at the upslope and downslope of hills downwind of relatively pristine areas.

Figure 17. The ratio of annual precipitation between rain gauges on the eastern vs. the western Sierra slopes in a relatively polluted area (Woodfords vs. Pacific House gauges) and in a relatively pristine area in Northern California (Boca vs. Bowman gauges)
Source: Givati and Rosenfeld (2004)

Another step forward was to analyze the ratio between rivers that drain from the western slopes to rivers that drain from the eastern Sierra slopes. Figure 18 displays the Ro between the Stanislaus River on the western slopes versus the West Walker River, located on the eastern slopes. The analysis is for the periods 1905–2003 (18A) and 1945–2003 (18B), and the same for the ratio between the Mokelumne River versus the West Walker for the same periods (18C and 18D). The figure that the ratio between the western to the eastern rivers decreased by about 10%–15% over the years. This is consistent with the rain gauge ratio results from the same areas, as shown previously by Givati and Rosenfeld (2004).

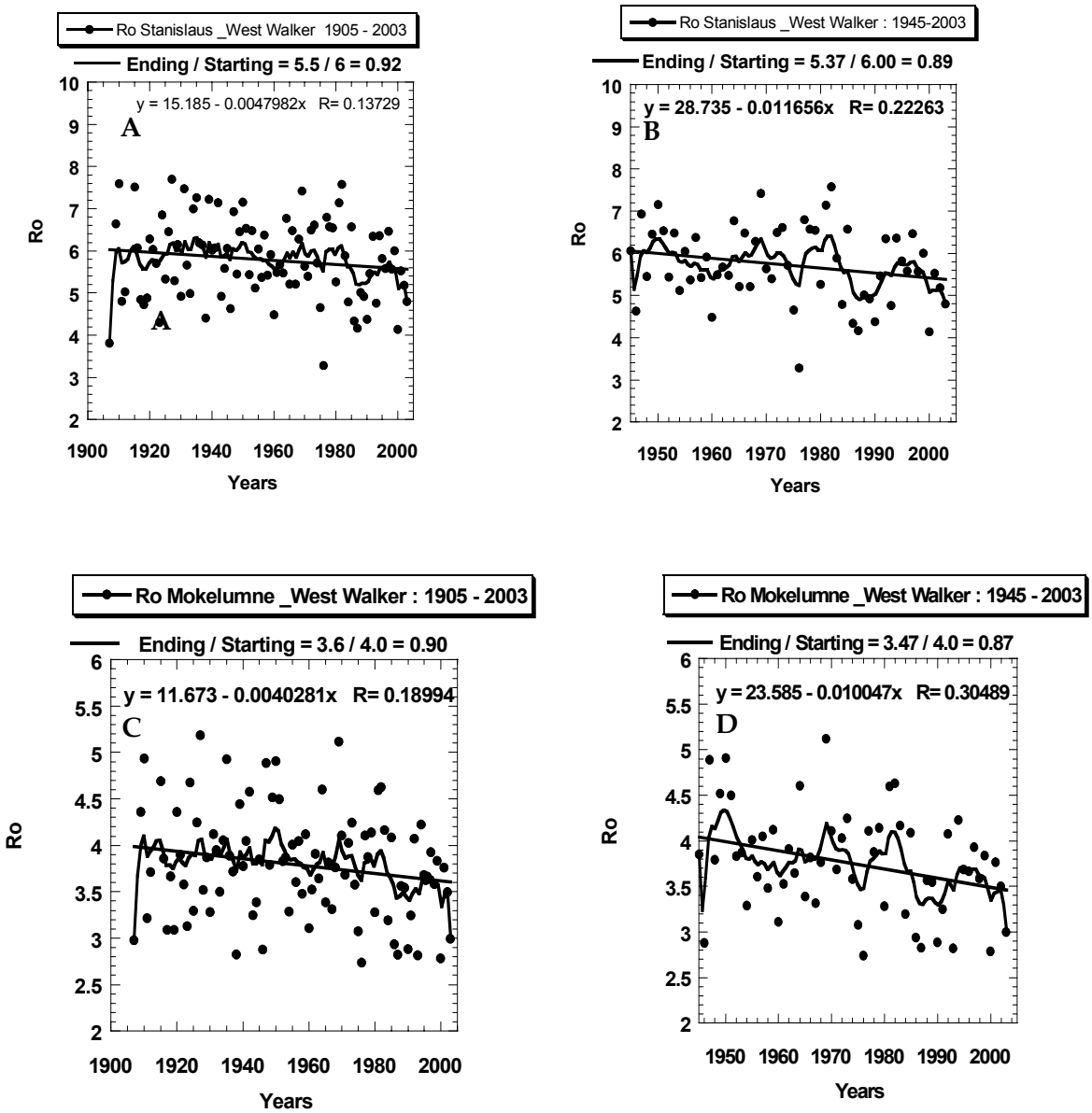

Figure 18. The ratio between western vs. eastern Sierra slopes for the periods of 1905–2003 (panels A and C) and 1945–2003 (panels B and D) for the Stanislaus River vs. the West Walker River,(A and B) and the Mokelumne River vs. the West Walker River (C and D)

Figure 19 presents the main results for the ratio trends analysis for Western versus Eastern slopes in the central Sierra. It can be seen that the ratio between the American river, the Cosumnes and the Mokelumne rivers (western slopes) versus the West Walker River (eastern slopes) has decreased by 15%–20%. Additional information regarding individual trends for the eastern and western rivers, the correlations and the Ro between them (western versus eastern slopes) for the periods 1905–2003, and 1945–2003 is presented in Appendix B, Figures B9–B13.

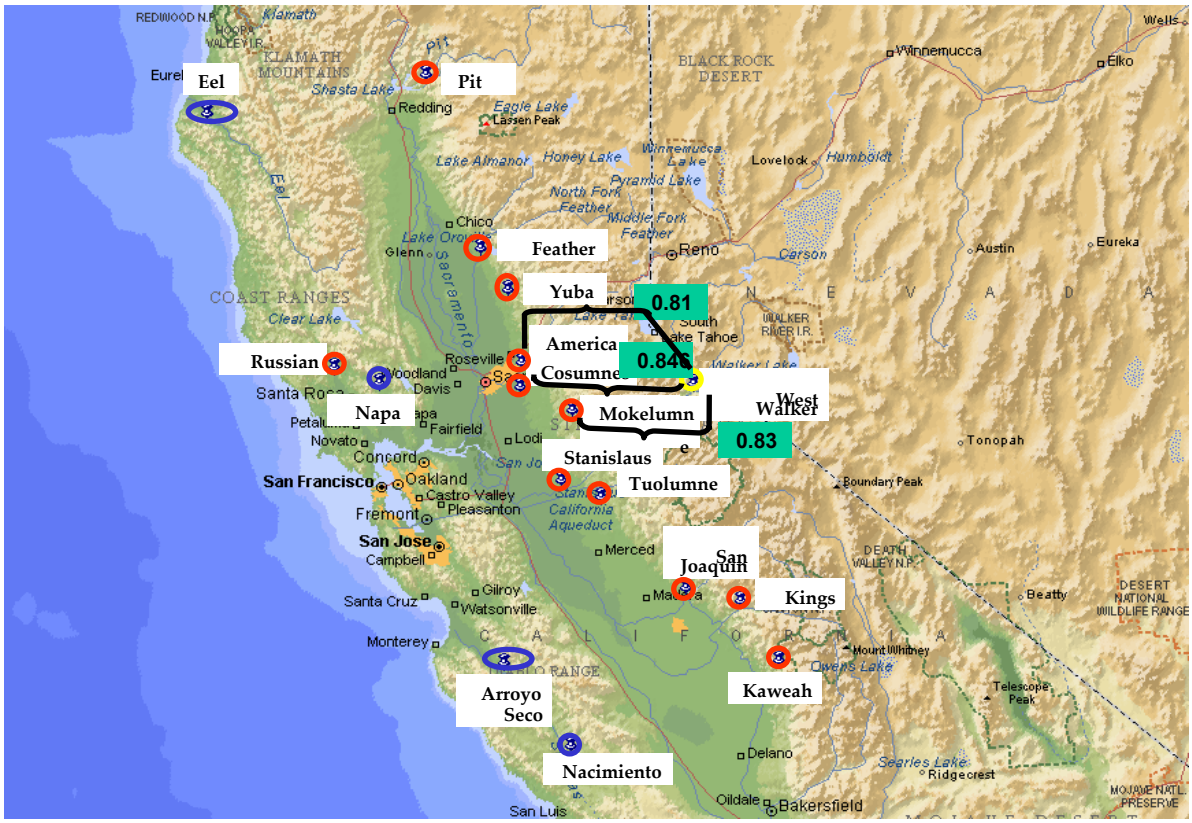

Figure 19. The ratio between the American river, the Cosumnes and the Mokelumne rivers (western slopes) vs. the West Walker River (eastern slopes)

4.5. Runoff Relationships in Relatively Pristine vs. Polluted Areas

It was informative to examine the ratios between rivers in relatively polluted areas versus rivers in relatively pristine areas. Figure 20 presents individual trends for two western slope rivers: (A) the Feather river and (B) the American river; (C) the correlations; and the ratio between them for the period (D) 1905–2003, and (E) 1945–2003. The Feather River is located in Northern California in a relatively pristine area. The figure illustrates that the ratio between the American river (a relatively polluted area) and the Feather (a relatively pristine area) has decreased over the years.

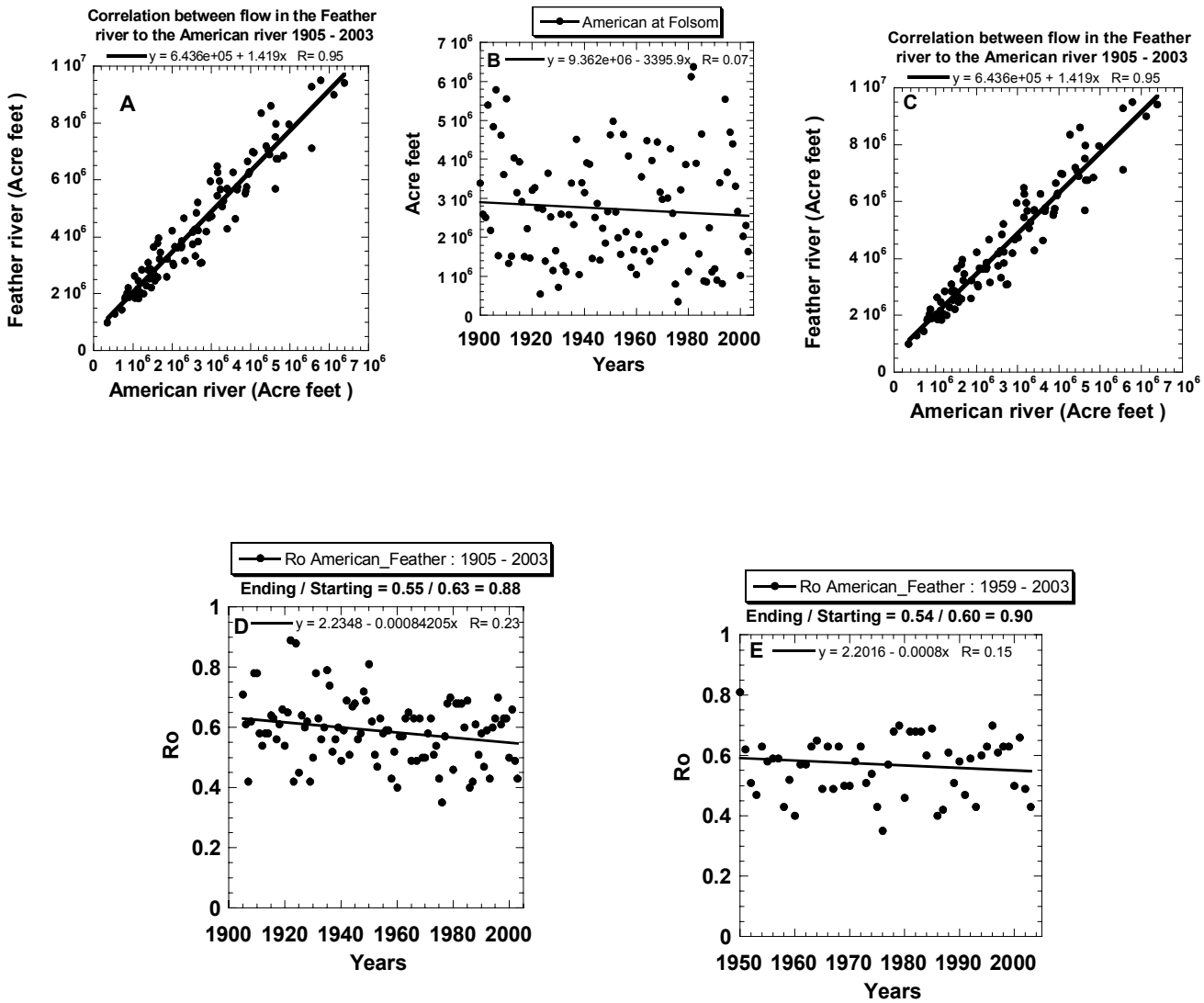

Figure 20. Trends, correlation, and the ratio between the American and the Feather rivers

4.6. Precipitation and Runoff Relationships in Washington State

To buttress the case for the apparent effect of pollutants on precipitation and runoff in California, the State of Washington was examined for similar effects. Washington State, which also has polluted orographic areas (such as downwind of Seattle) and relatively pristine orographic areas (such as the Olympic peninsula), provided the opportunity to repeat the gauge and stream-flow trend analyses. Figure 21 displays the locations of hilly and plains rain gauges in the relatively pristine Olympic peninsula: Wishka, hilly relatively pristine gauge, (440 ft, lat: 47.16, long: 123.42) versus Aberdeen, plains gauge, (10 ft, lat: 46.59, long: 123.49); and the hilly and plains gauges in the relatively polluted Seattle area: Palmer, a hilly polluted gauge, (900 ft, lat: 47.18, long: 121.50) versus a cluster of gauges in the Seattle area (20 ft, lat: 47.39, long: 122.18).

Figure 21. The locations of hilly (red) and plains (blue) rain gauges in a relatively pristine area and a polluted area in Washington state

Figure 22 displays the ratio of annual precipitation between (A) Wishka versus Aberdeen (a relatively pristine area in the Olympic peninsula) and in a relatively polluted area between (B) Palmer (a hilly area downwind of Seattle) versus Seattle. The orographic factor increased over the years in the more pristine area but decreased in the polluted region.

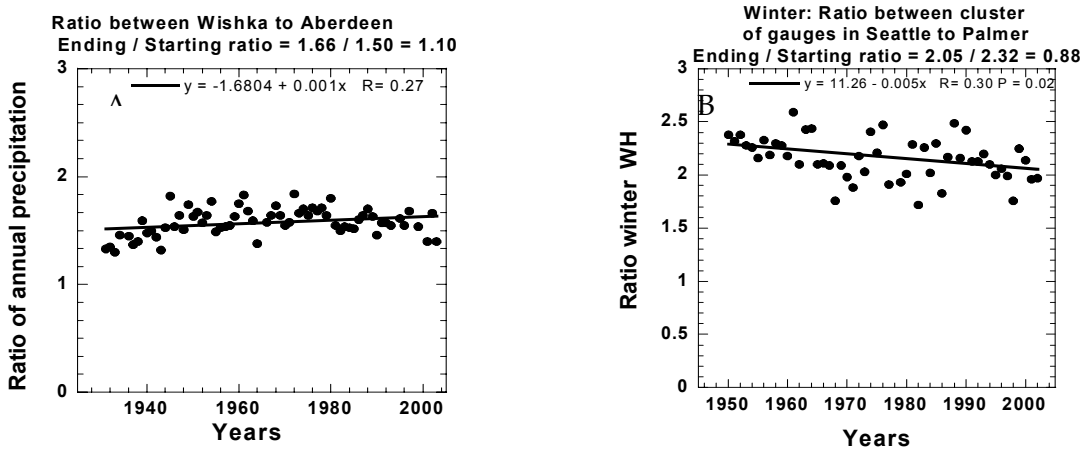

Figure 22. The ratio of annual precipitation in a relatively pristine area, the Olympic peninsula, Washington : (A) Wishka versus Aberdeen, and the ratio in a relatively polluted area between (B): Palmer versus Seattle

Figure 23 displays the location of the Quinault River, in a more pristine area of the Olympic peninsula, and the Cedar river, a relatively polluted hilly area downwind of the Seattle area. The correlation (A) and the ratio (B) between the annual stream flow of the Cedar river (downwind to Seattle) to the Quinault River (in the relatively pristine Olympic peninsula) is presented in Figure 24. As was presented for the Sierra Nevada, California, there is a decrease in the ratio of river flows in the polluted area to the river flows in the pristine areas in Washington. This similarity of result makes the case being made for California a little more credible and persuasive.

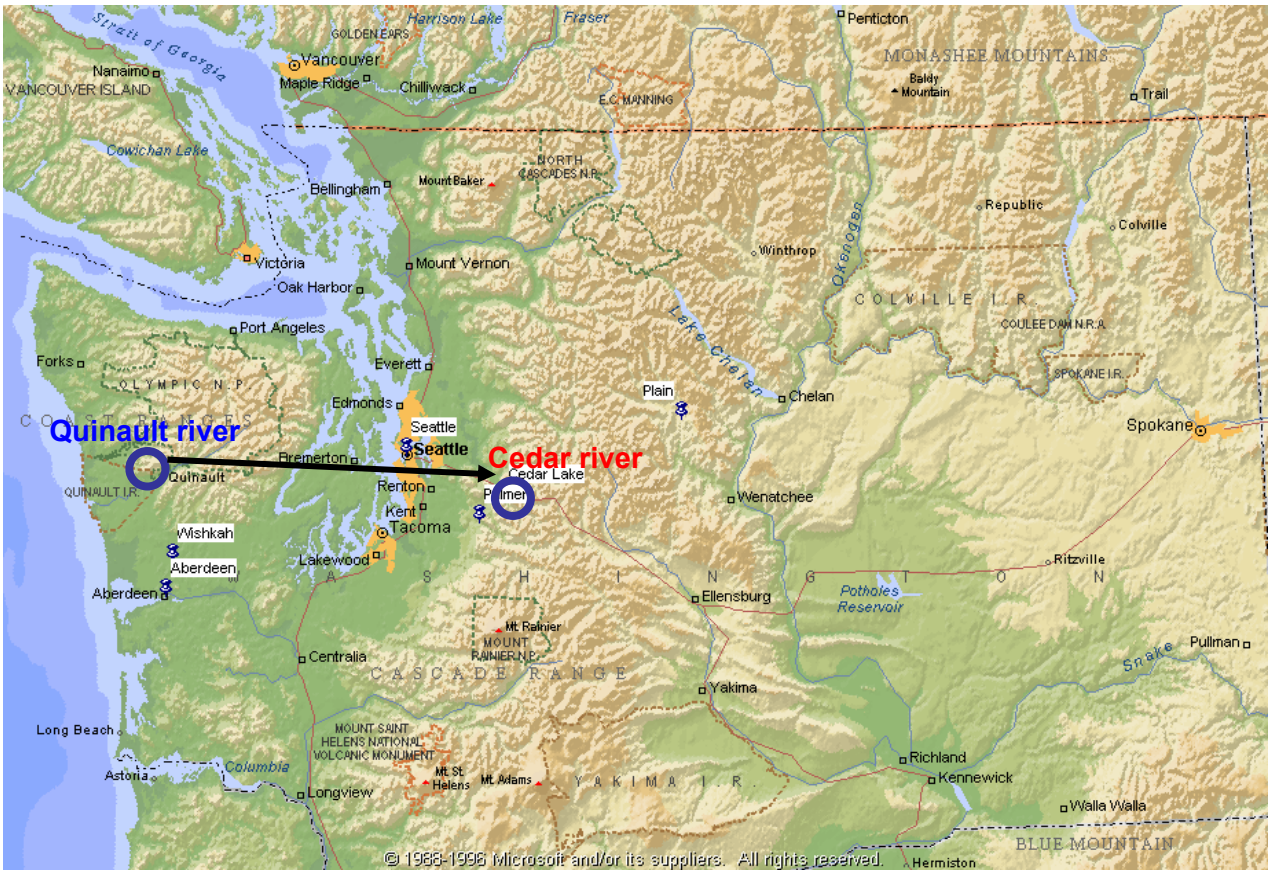

Figure 23. The locations of Quinault River (in the Olympic peninsula), and the Cedar River (downwind of Seattle, Washington)

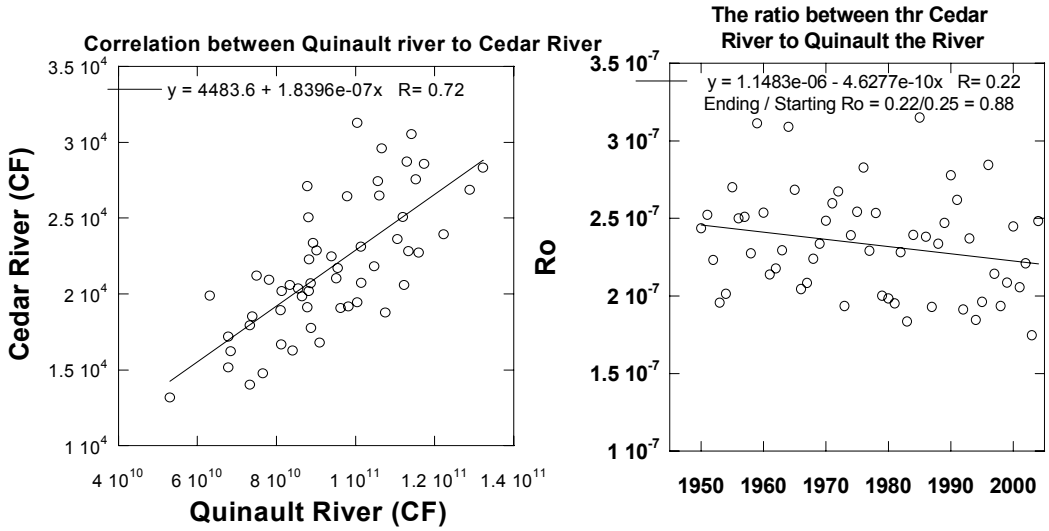

Figure 24. The correlation (A) and ratio (B) between the annual stream flow in the Cedar River downwind of Seattle to the annual stream flow in the Quinault River in the relatively pristine Olympic peninsula

4.7. Climate Indices as an Alternative Explanation for the Decreasing Ro

A possible alternative explanation for the reduction in Ro is a decreasing trend in the cross-mountain component of the low tropospheric winds and attendant moisture flux during rain events. Givati and Rosenfeld (2004) applied a radiosonde regression model and found that the relevant meteorological conditions during rain days did not change systematically over the years, and the observed trends in Ro likely have other causes such as anthropogenic air pollution. Precipitation in the western United States may also be subject to climatic fluctuations like the SOI (Allan et al. 1991) and its multi-decadal counterpart, the PDO (Zhang et al. 1996; Mantua et al. 1997). The PDO Index is defined as the leading principal component of the North Pacific monthly sea surface temperature variability. The PDO is a long-lived El Niño-like pattern of Pacific climate variability. The SOI is defined as the normalized pressure difference between Tahiti and Darwin, Australia (Ropelewski and Jones 1987). Figure 25 displays the winter values (October–April) of (A) the PDO (Mantua et al. 1997) and (B) SOI from 1900 to 2003. During this period the PDO had three phases: a positive (warm) phase from 1900–1944, a negative (cold) phase from 1945–1975, and another positive phase since 1976.

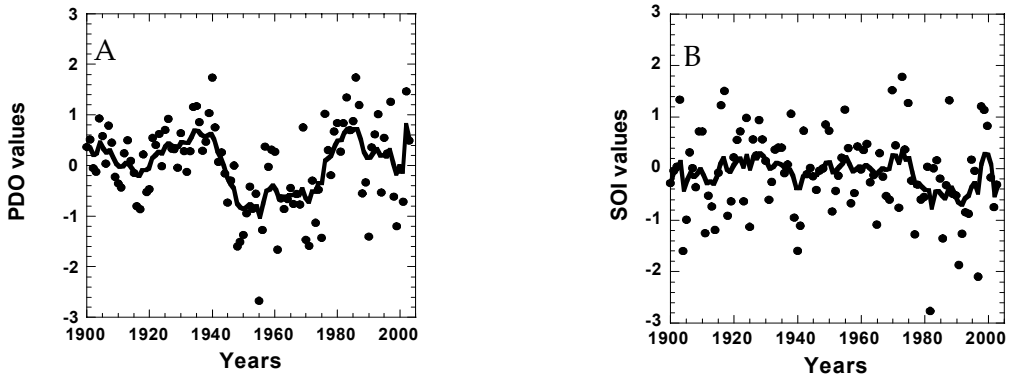

Figure 25. Winter values (October–April) of the PDO and SOI indexes. Note the three phases of the PDO: a positive phase from 1900–1944, a negative phase from 1945–1975, and another positive phase since 1976.

Dettinger et al. (2004) characterized the effects of the PDO and the SOI on the ratio of precipitation between mountains and plains areas in the California Sierra Nevada. During negative PDO and positive SOI the westerly wind component is stronger, so that the mountain/plains orographic factor is higher than in the positive PDO phase—that is, El Niño like. There is less overall precipitation in the negative PDO than in the positive PDO phase (Dettinger et al. 2004). Tables 2 and 3 contain results for linear multiple regression models, where the annual precipitation and the hilly/plains Ro are explained by variability in PDO, SOI, and year as the three independent regression parameters. The rain gauges are San Diego and Cuyamaca, in Southern California (due to its 100-year measurement record) and Sacramento and Pacific House in Northern California. The dependent variables in the regressions were first the individual precipitation measurements made by the hilly and plains rain gauges (see Table 2), and second, the Ro of precipitation between those hilly to plains gauges (see Table 3). Table 2 shows that the PDO and the SOI do affect the precipitation amounts. For example, the P values for the PDO effect on precipitation in San Diego and in Cuyamaca are 0.004 and 0.005, respectively. Nonetheless when the effect of the PDO and SOI is tested not on the absolute precipitation amounts but on the ratio between them, no significant effect is found. The only variable that has a significant effect on the ratio is the years for which Ro is calculated. The Ro decreases significantly over the years, even when the variability in PDO and SOI is taken into account by the multiple regression model. The ”years“ variable represents another change (e.g., increasing aerosol emissions) that occurs with time and affects Ro. It appears, therefore, that the decreasing Ro with the years is likely the result of the increasing small CCN aerosols over the same period of time.

Table 2. Multiple linear regression results showing the significances of three independent variables: The PDO, the SOI, and the years over which Ro is calculated vs. the dependent variable—individual precipitation of rain gauges in California.

Station Name	San Diego	Cuyamaca	Sacramento	Pacific House
PDO P value	0.004	0.005	0.642	0.358
SOI P value	0.43	0.175	0.247	0.972
Years P value	0.522	0.287	0.580	0.835

Table 3. Multiple linear regression results showing the significances of three independent variables: The PDO, the SOI and years, vs. the dependent variable, the ratio of precipitation between the rain gauge pairs, which is the orographic enhancement factor.

Pairs of stations	Cuyamaca/ San Diego	Pacific House/ Sacramento
PDO P value	0.816	0.431
SOI P value	0.670	0.703
Years P value	0.003	0.012

4.8. The Effects of the PDO on the Runoff / Precipitation Ratio

To examine the effects of the PDO on the runoff/precipitation ratio and on hilly/plains ratio, the research team analyzed the time series with respect to the winter positive values of the PDO. Figure 26 shows the runoff/precipitation ratio in the San Joaquin basin versus the PDO for the period 1914–2000. It can be seen that the trend is stable, and there is no effect of the PDO on the ratio.

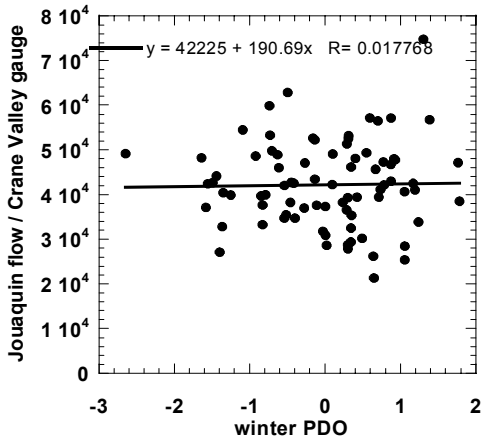

Figure 26. The ratio between runoff at the San Joaquin River and precipitation in Crane Valley versus the PDO winter positive values

To analyze the effect of the PDO on the mountain/coast precipitation, the research team separated the PDO phases into negative and positive phases and examined the mountain/coast ratio of precipitation in both phases. Figure 27 A and B show the ratio between the Sierra rain gauge in Crane Valley to the coastal rain gauge in Big Sur, in (A) negative and(B) positive PDO. The ratio between the hilly to the coastal rain gauges decreases in both PDO phases--that is, there is a higher decrease during the negative phase. Absolute precipitation amounts are affected by fluctuations in the atmospheric circulation patterns, such as those associated with the PDO and SOI (Rosenfeld and Givati 2006). However, these climatic fluctuations cannot explain the observed trends in the ratio of annual precipitation.

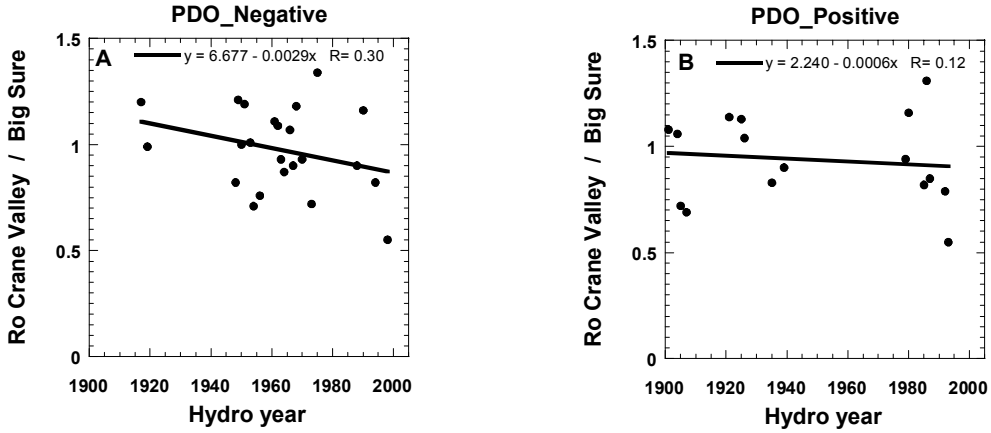

Figure 27. The ratio between precipitation at Crane Valley (Sierra) to precipitation at Big Sur (coastal range) during negative and positive PDO phases

4.9. Conclusions

The findings in this study, as in the authors' previous work, suggest that anthropogenic air pollution has had a major impact on orographic precipitation and, as a result, on stream flow volumes, which are responsible for most of the water resources in California. Several studies had already shown the effect of air pollution on precipitation in California, Israel, Colorado, Utah, New Mexico, Arizona, and Washington (Borys 2003; Givati and Rosenfeld 2004, 2005; Rosenfeld and Givati 2006; Griffith et al. 2005; Jirak and Cotton 2006), but this study is the first to quantify this effect on mountain stream flow volumes. The absolute precipitation amounts and stream flow volumes did not decrease in California and even showed some increase during the last 50 years, but the ratio between mountain to coastal rain gauges and rivers, downwind of pollution sources, showed a decrease of 15%–30%. A decreasing trend was also found during the last 50 years for the ratio between Sierra river flows in relatively polluted areas to Sierra river flows in relatively pristine areas. The decreases occurred on the western slopes of the Sierra, where new orographic clouds are generated over the slopes. Such decreases were not found for rain gauges and rivers in relatively pristine areas in Northern California. The rivers on the eastern slopes of the Sierra showed increasing flows relative to the river flows on the Sierra western slopes. This is consistent with the rain gauge ratio results in the same areas, as the authors showed in previous studies. Both absolute precipitation amounts and Ro are affected by fluctuations in the atmospheric circulation patterns such as those associated with the PDO and SOI. However, these climatic fluctuations cannot explain the observed trends in Ro.

5.0 Determining the Relationship between Air Pollution and Cloud Structure and Precipitation-Forming Processes

5.1. Satellite-Inference of Cloud Effective Radius in California

This task attempted to determine whether there is a relationship between pollution aerosols and cloud structure and precipitation-forming processes, beginning with a much larger sample of multi-spectral satellite images than was used in the initial research, which found the negative relationship between air pollution and orographic precipitation. On each day with a satellite overpass, the multi-spectral imagery was processed to infer the r_e of cloud particles for the clouds within selected areas within the field of view. This was done because previous studies have shown that areas with small r_e are slow to develop precipitation. After the satellite inferences had been made they were composited geographically.

The r_e of cloud particles increases with height or with decreasing cloud top temperature (T) at a rate that is indicative of the precipitation-forming processes. The cloud base temperature during winter westerly flow in California is determined to a large extent by sea surface temperature, and therefore the effective radius at a given T is indicative of the rate of increase of r_e with height. The r_e in the T range of -5°C to -10°C is particularly indicative of the precipitation processes. A cloud with significant precipitation processes glaciates quickly at the -5°C to -10°C isotherms, so that the indicated r_e would appear much larger in this T range than a cloud with suppressed precipitation having large concentrations of CCN aerosols, for example.

The research to this point, involving observations and modeling, supports the view that pollution aerosols decrease orographic precipitation downwind of aerosol pollution sources in central and southern California. Satellite case studies have provided examples of obvious "pollution tracks" in the field of cloud tops, in the form of reduced cloud-top particle effective radii downwind of well-defined pollution sources. The second contract objective was to test whether the areas in which decreasing trends of the orographic precipitation have been documented are also areas where the cloud-top particle size has been reduced spatially and temporally during winter orographic weather events. The conditions thought to be most susceptible to the suppressive effects of pollution aerosols are orographic clouds growing over the Sierra in a cold post-frontal air mass. Under these conditions relatively pristine air from the ocean picks up pollutants as it traverses the heavily urbanized and industrial areas before it reaches the Sierra range, where clouds are formed as the air is lifted orographically. The wind flow during such conditions is southwesterly to northwesterly. With a given emission rate of the aerosols, their concentrations in the air are expected to be inversely proportional to the wind speed. Consequently, the r_e of the cloud-top particles is expected to be smaller with light winds. However, the orographic precipitation amounts are expected to be proportional to the cross-mountain wind component. Thus, for a given cross-mountain wind component at light winds a strong suppression of small amounts of precipitation are expected; whereas with strong winds giving stronger orographic lift, smaller suppression of large amounts of precipitation is expected. This disparity might not be as great as implied, because with light winds there is more time for the precipitation to occur, whereas with strong winds there is more limited time

for the orographic clouds to convert their cloud water to precipitation. This increases their susceptibility to precipitation suppression by even smaller concentrations of pollution aerosols.

The following analysis documents the spatial dependence of cloud top satellite-retrieved effective radii on wind direction, wind speed, and cloud top temperatures.

5.1.1. Methodology

The analyzed period includes all the available AVHRR overpasses for the following months in each listed year:

- 1995: January through April
- 1995: October through December
- 1996: October
- 2003: November through December
- 2004: January through April
- 2004: October through December
- 2005: January through March

Each AVHRR overpass with clouds that were identified as feeding from the boundary layer was analyzed the following way:

1. Homogeneous geographic areas with similar cloud top properties were manually identified and enclosed by a rectangle. In all, 2284 suitable rectangles were identified over California, the adjacent ocean, and in some cases farther north along the west coast.
2. The T-r_e dependence of the clouds within each rectangle was analyzed and saved. These two first stages were the most time consuming.
3. The vertical profile of winds and temperatures for the central point of each rectangle were taken from the NCEP reanalysis data and associated with the satellite-retrieved cloud properties.
4. California and its coastal water areas were divided into homogeneous geographic quadrilateral areas with respect to the topography and density of population to the west of them.
5. The T-r_e profiles in (3) that fell into each geographic area in (4) during selected wind conditions were averaged, and the mean r_e for a selected T was displayed on the map of the geographic areas for (4). The map is shown in Figure 28.
6. The results of (5) were assessed in the context of the conceptual model described in the background section. This step constitutes the next section.

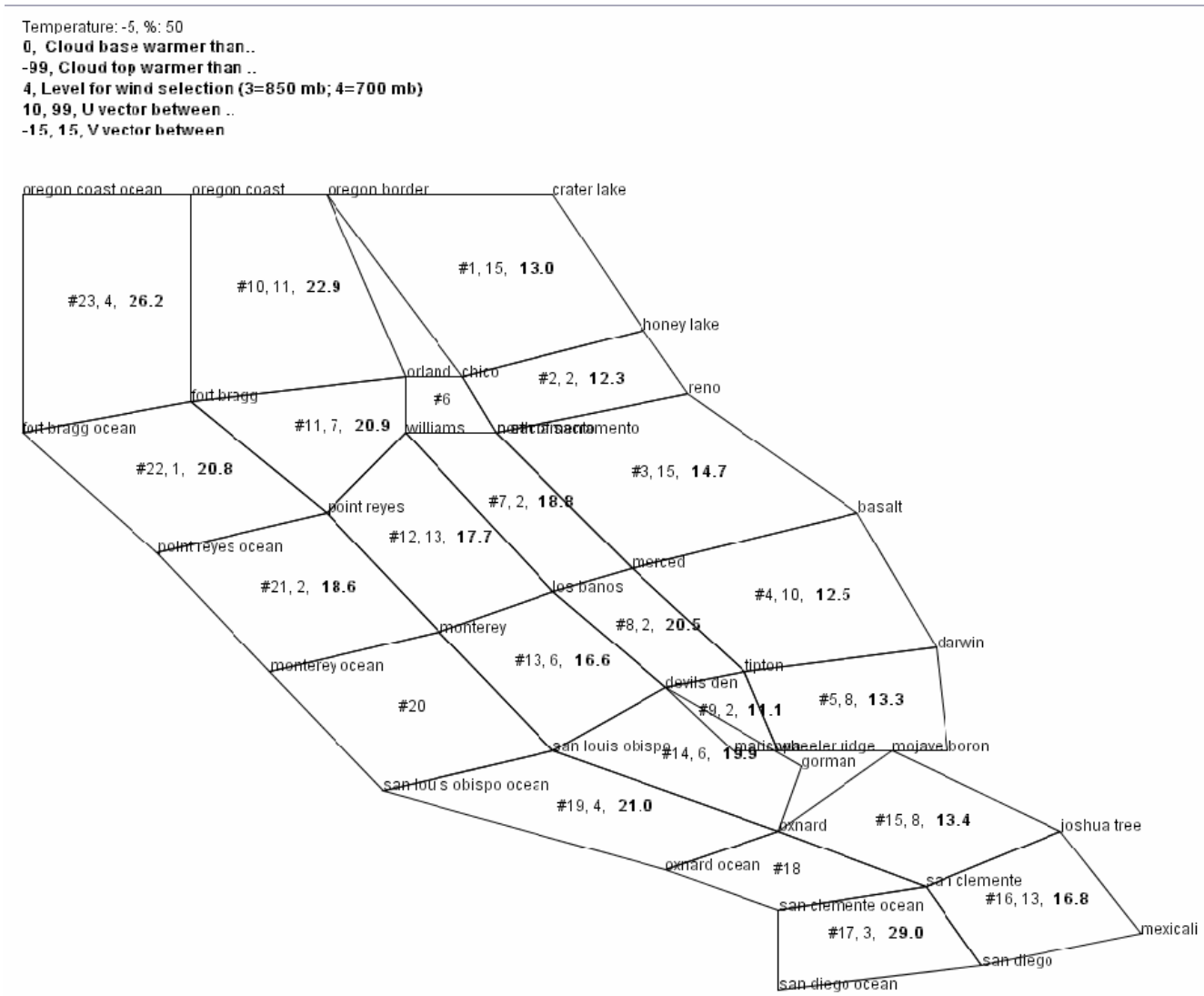

Figure 28. A map of the regions in which the cloud properties were characterized. The area numbers appear with a # sign before them. The corners of the regions are denoted by the name of the nearest geographical landmark. The middle number denotes the number of cases meeting the selection criteria in each region, and the averaged r_e of these cases is the right number within each area.

5.1.2. Results

In Table 4 the geographical distribution of the r_e along the Sierra Nevada is given as a function of the wind directions and speeds. Table 5 provides the same for the coastal range, and Table 6 for the coastal ocean. All three tables incorporate 700 millibar (mb) winds. Tables 7 and 8 are the same as Tables 5 and 6, except they incorporate 850 mb winds. Areas 6 through 9 are not represented in the tables because they lacked enough observations to make significant findings.

According to the tables, the following generalizations can be made:

A. The effective radius over the Sierra Nevada:

1. The smallest r_e occurs in near-stagnant conditions along all the Sierra Nevada with winds with $U < 5$ meters per second (m s^{-1}) at 700 mb (where U represents the westerly wind component and -U represents the easterly wind component). This is consistent with local pollution not being replaced with more pristine maritime air even in the northern Sierra during these conditions.
2. With increasing U, r_e increases to 12–13 micrometers (μm) at T = -5°C in the northern Sierra when $V > 0$ (where V represents the southerly wind component—therefore, where a southerly component of the wind exists—and -V represents the northerly wind component), but becomes 14.1 μm when the wind has no southerly component ($V < 0$). This is consistent with pollution aerosols reaching the northern Sierra under southerly winds.
3. The increase of r_e with U is evident most strongly in the central Sierra. This is consistent with this area being downwind of major sources of aerosol emissions that get more diluted as the wind increases.
4. The southern Sierra has lower r_e than the central Sierra during moderate and strong winds. The northern Sierra also has smaller r_e than the central Sierra under moderate winds, but larger than the southern Sierra.
5. The r_e increases more slowly with decreasing T in the central and southern Sierra, compared to the northern Sierra. The slower increase of r_e with elevation is the most robust indicator for the slower development with height of precipitation in the clouds. This finding is consistent with the gauge and stream-flow analyses that show that the greatest losses of water occur in the central and southern Sierra. These new satellite analyses indicate that these losses are tied to the release of pollutants from the urbanized areas.

B. The effective radius in the coastal range:

1. The r_e is much larger over the coastal range than over the Sierra Nevada for all conditions.
2. Generally, r_e increases with stronger westerly winds.
3. The largest r_e is observed in Northern California. A decrease is evident to the east of the San Francisco and Los Angeles areas. The r_e between Los Angeles and San Francisco is smaller than in Northern California.

C. The effective radius over the coastal waters:

1. The r_e is much larger yet over the coastal waters than over the coastal range. The r_e, therefore, decreases from ocean inland to the Sierras, as expected.
2. The r_e is reduced over the ocean during conditions of weak winds, which indicates the advection of pollution from land to sea.

Some of the results are illustrated in the figures that follow. The first graph (Figure 29) for conditions of light and variable winds at 700 mb gives a bar plot of the median effective radius at temperatures of 0°C, -5°C, and -10°C for the five paired Sierra/Coast areas shown in Figure 28, starting in the north and moving southward from there. Plotted above each bar is the number of observations, which are small in some cases. By referring to the ordinate scale, one can determine at what temperature the clouds in the various areas reached the precipitation threshold of 14 μm.

The most obvious feature of Figure 29 is that the effective radii are greater for the coastal area than for the paired Sierra area to its east. This makes sense because the clouds in the coastal zone would not have been as affected by pollutants as the clouds farther inland. Under light variable winds there is not much difference among the various Sierra areas. Certainly no north to south difference is evident. Note that the clouds in the coastal zone reach the precipitation threshold of 14 μm by -10°C in all cases and at -5°C in the south-central and south-coastal zones.

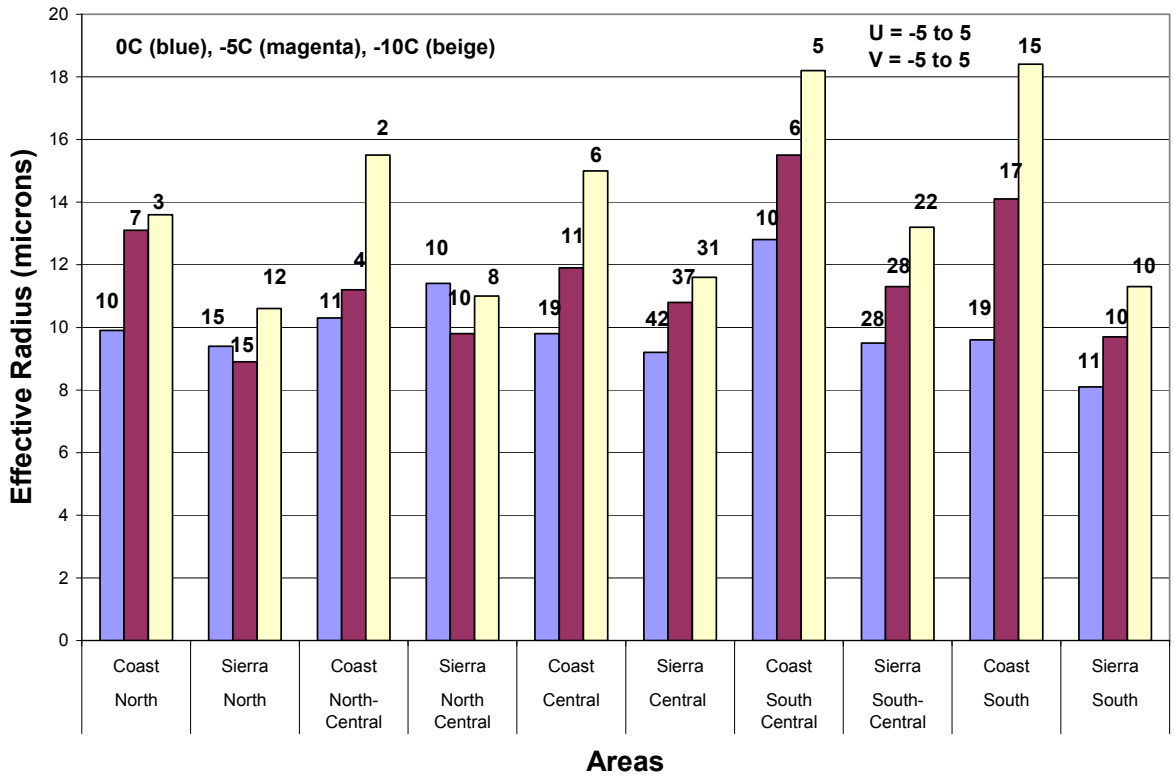

Figure 29. Median effective radii vs. temperature under light and variable 700 mb winds for five coast and five Sierra areas as shown in Figure 28. The number of cases appears above each bar.

Table 4. Summary of the median effective radius calculations for areas in the Sierra Nevada, with 700 mb winds. The first and second rows show wind vectors U (eastward) and V (northward) and their wind velocities (upper number to lower number), in m s-1. The next five rows represent the five ranges of the Sierra Nevada from north to south, with the area numbers corresponding to the areas in Figure 28. The first number in each wind/temperature block is the number of cases that met the selection criteria for each region, and the number to its immediate right is the effective radius of all the cases at the listed T, for cloud base warmer than 0°C.

		U	-5 5	5 10	5 10	10 30	5 15	5 15	5 15	10 99	15 99
	T	V	-5 5	-5 5	-5 10	-5 10	-15 0	0 15	-15 15	-15 15	-15 15
1. Oregon Chico	0		15 9.4	5 9.7	7 9.7	14 10.6	5 11.1	14 10.1	19 10.3	15 10.6	4 9.6
	-5		15 8.9	5 12.8	6 11.9	14 12.9	5 14.1	13 12.0	18 12.6	15 13.0	4 12.4
	-10		12 10.6	4 14.9	5 13.9	10 15.6	4 20.0	11 13.6	15 15.3	11 16.3	2 16.2
2. Chico Sacramento	0		10 11.4	0	1	2 12.9	3 13.2	1	4 13.1	2 12.9	0
	-5		10 9.8	0	0	2 12.3	3 14.7	1	4 15.4	2 12.3	0
	-10		8 11.0	0	0	2 16.3	2 16.3	0	2 16.3	2 16.3	0
3.Sacramento Merced	0		42 9.2	14 8.2	14 8.2	14 11.9	17 10.9	16 11.0	33 10.9	15 11.8	0
	-5		37 10.8	12 8.1	12 8.1	14 14.6	14 12.7	16 14.2	30 13.5	15 14.7	0
	-10		31 11.6	12 9.3	12 9.3	11 16.1	12 15.1	13 13.4	25 14.2	11 16.1	0
4. Merced Tipton	0		28 9.5	19 7.9	21 7.9	8 13.2	14 9.6	18 8.8	32 9.1	11 12.1	2 8.6
	-5		28 11.3	19 10.4	21 10.6	7 13.4	14 11.2	17 10.8	31 11.0	10 12.5	2 11.8
	-10		22 13.2	11 11.4	12 12.6	6 13.5	7 11.9	13 12.8	20 12.4	8 13.3	1
5. Tipton Gorman	0		11 8.1	5 8.5	6 9.0	6 7.7	4 8.9	8 8.5	12 8.6	9 8.8	3 9.9
	-5		10 9.7	5 10.0	6 10.9	5 11.6	4 11.7	7 11.4	11 11.5	8 13.3	3 15.1
	-10		10 11.3	2 9.8	2 9.8	3 14.5	3 13.5	2 8.6	5 11.5	5 15.1	2 18.6

Table 5. The same as Table 4, but for the coastal range, 700 mb winds. Areas are listed from north to south.

		U	-5 5	5 10	5 10	10 30	5 15	5 15	5 15	10 99	15 99
	T	V	-5 5	-5 5	-5 10	-5 10	-15 0	0 15	-15 15	-15 15	-15 15
10. Oregon Fort Bragg	0		10 9.9	8 14.5	11 14.2	6 19.5	7 16.1	16 17.0	23 16.7	15 17.4	5 14.0
	-5		7 13.1	7 19.6	10 19.2	5 21.2	5 23.3	13 20.8	18 21.5	11 22.9	4 20.6
	-10		3 13.6	3 30.9	5 27.8	3 25.3	2 34.2	8 29.1	10 30.1	8 28.7	3 22.4
11. Ft Bragg Point Reyes	0		11 10.3	5 14.5	6 15.2	5 14.8	4 16.1	8 14.4	12 15.0	9 15.5	5 16.3
	-5		4 11.2	4 14.2	5 15.7	4 17.7	3 19.8	7 16.2	10 17.3	7 20.9	4 22.7
	-10		2 15.5	2 17.9	2 17.9	4 21.0	0	5 17.5	5 17.5	4 21.0	2 25.0
12. Pt Reyes Monterey	0		19 9.8	13 11.4	15 12.3	20 13.6	17 12.3	27 12.6	44 12.4	22 14.1	7 16.0
	-5		11 11.9	9 17.6	10 17.8	12 16.6	9 17.7	18 17.2	27 17.4	13 17.7	3 22.7
	-10		6 15.0	6 18.1	7 18.7	10 21.7	3 17.9	14 20.4	17 19.9	11 22.9	2 31.2
13. Monterey S. L. Obispo	0		10 12.8	9 11.0	14 13.6	9 16.0	12 14.6	14 14.3	26 14.4	10 15.6	4 14.5
	-5		6 15.5	6 14.7	9 18.1	5 17.3	9 15.7	8 18.6	17 17.0	6 16.6	2 15.4
	-10		5 18.2	4 16.4	5 18.0	2 22.7	6 15.3	2 24.2	8 17.5	2 22.7	1
14. S.L.Obispo Oxnard	0		19 9.6	12 8.6	13 9.8	9 13.5	17 9.9	10 12.1	27 10.7	13 13.6	5 14.5
	-5		17 14.1	11 11.3	12 12.6	2 20.3	13 15.0	7 13.7	20 14.6	6 19.9	2 16.2
	-10		15 18.4	7 12.1	8 13.9	1	3 14.0	6 14.5	9 14.3	2 21.2	1
15.Oxnard San Clemente	0		17 11.0	13 9.7	16 10.3	21 13.1	23 10.4	12 12.5	35 11.1	22 12.9	8 12.2
	-5		15 12.9	9 13.7	12 14.2	7 13.9	9 11.0	10 16.7	19 14.0	8 13.4	3 9.0
	-10		14 18.2	3 17.0	4 21.3	5 16.3	3 12.3	5 23.3	8 19.2	5 16.3	2 10.6
16.S.Clemente San Diego	0		16 11.1	3 12.4	7 10.3	21 13.5	9 9.4	12 11.7	21 10.7	24 13.3	12 5.5
	-5		14 15.2	3 16.7	6 13.8	12 17.1	5 13.0	10 16.4	15 15.3	13 16.8	4 18.0
	-10		11 17.4	2 24.6	2 24.6	5 20.4	0	5 19.1	5 19.1	5 20.4	2 27.8

Table 6. The same as Table 4, but for the coastal ocean, 700 mb winds. Areas are listed from north to south.

		U	-5 5	5 10	5 10	10 30	5 15	5 15	5 15	10 99	15 99
	T	**V**	**-5 5**	**-5 5**	**-5 10**	**-5 10**	**-15 0**	**0 15**	**-15 15**	**-15 15**	**-15 15**
23. Oregon Fort Bragg	**0**		3 17.1	2 17.3	3 15.2	3 21.6	2 25.3	3 15.2	5 19.2	4 22.0	2 18.7
	-5		1	1	2 23.0	3 25.2	2 28.3	2 23.0	4 25.6	4 26.2	2 24.1
	-10		0	0	1		2 34.1	1	3 32.2	4 32.6	2 31.0
22. Ft Bragg Point Reyes	**0**		2 11.6	1	1	1	0	1	1	1	1
	-5		0	1	1	1	0	1	1	1	1
	-10		0	1	1		0	1	1	1	1
21. Pt Reyes Monterey	**0**		1	0	0	3 16.0	2 17.1	0	2 17.1	3 16.0	2 14.3
	-5		0	0	0	2 18.6	1	0	1	2 18.6	2 18.6
	-10		0	0	0		0	0	0	1	1
20. Monterey S.L.Obispo	**0**		1	2 16.0	4 20.2	1	2 10.9	4 24.8	6 20.1	1	0
	-5		0	2 21.5	4 27.8	0	1	3 33.8	4 27.8	0	0
	-10		0	1	3 27.7		1	2 34.6	3 27.7	0	0
19.S.L.Obispo Oxnard	**0**		4 13.0	0	0	3 14.0	2 18.8	2 18.5	19 18.6	4 18.2	2 22.5
	-5		3 14.4	0	0	3 17.7	1	2 23.8	3 19.6	4 21.0	2 23.1
	-10		2 15.1	0	0		0	1	1	2 31.2	2 31.2
18.Oxnard San Clemente	**0**		0	0	1	1	1	1	2 17.3	1	0
	-5		0	0	1	0	0	1	1	0	0
	-10		0	0	0		0	0	0	0	0
17.S.Clemente San Diego	**0**		1	0	1	5 23.0	1	5 22.2	6 22.6	6 23.2	1
	-5		1	0	1	2 28.1	1	2 21.8	3 24.7	3 29.0	1
	-10		**0**	**0**	**1**		**0**	**2 25.7**	**2 25.7**	**1**	**0**

Table 7. The same as Table 5, but for the coastal range with 850 mb winds. Areas are listed from north to south.

		U	-5 5	5 10	5 10	10 30	5 15	5 15	5 15	10 99	15 99
	T	**V**	**-5 5**	**-5 5**	**-5 10**	**-5 10**	**-15 0**	**0 15**	**-15 15**	**-15 15**	**-15 15**
10. Oregon Fort Bragg	**0**		16 11.7	7 17.8	16 17.6	0	10 16.0	10 17.2	20 16.6	0	0
	-5		13 15.7	6 25.3	13 23.6	0	7 23.3	8 22.0	15 22.6	0	0
	-10		5 21.5	6 28.8	10 28.8	0	5 28.4	5 29.3	10 28.8	0	0
11. Ft Bragg Point Reyes	**0**		11 10.6	8 15.2	9 15.5	2 16.0	5 16.3	6 15.1	11 15.6	2 16.0	0
	-5		8 13.0	7 20.7	8 20.9	1	3 25.3	6 18.6	9 20.9	1	0
	-10		4 16.2	4 21.2	4 21.2	1	1	5 21.5	5 21.5	1	0
12. Pt Reyes Monterey	**0**		30 10.8	17 12.9	24 13.5	0	9 12.6	20 14.3	29 13.8	1	0
	-5		20 16.5	12 15.9	16 17.1	0	4 15.3	14 18.3	18 17.6	1	0
	-10		10 16.5	9 21.2	12 22.5	0	2 21.1	11 23.4	13 23.1	1	0
13. Monterey S.L.Obispo	**0**		28 12.7	9 15.4	9 15.4	1	7 15.0	4 14.1	11 14.7	1	0
	-5		17 14.9	6 16.6	6 16.6	1	6 15.7	2 17.1	8 16.1	1	0
	-10		10 19.0	4 14.4	4 14.4	1	3 12.0	2 22.7	5 16.3	1	0
14.S.L.Obispo Oxnard	**0**		33 9.6	15 12.9	17 13.3	1	13 11.2	7 17.3	20 13.3	2 13.6	0
	-5		26 12.6	10 16.9	11 17.9	1	12 16.7	2 22.7	14 17.6	2 16.2	0
	-10		21 16.0	4 17.4	5 19.2	0	4 19.4	2 22.0	6 20.2	1	0
15.Oxnard San Clemente	**0**		41 9.8	17 13.1	18 13.8	5 12.7	15 12.6	10 15.7	25 13.8	5 12.7	0
	-5		33 12.9	5 16.1	6 17.9	3 9.0	6 10.4	5 22.3	11 15.8	3 9.0	0
	-10		19 18.1	4 18.9	5 21.9	2 10.6	3 12.1	5 25.8	8 20.6	2 10.6	0
16.S.Clemente San Diego	**0**		28 10.4	16 12.7	16 13.4	5 13.5	12 12.2	12 14.6	24 13.4	5 13.5	0
	-5		20 14.5	9 17.3	11 16.6	3 19.8	6 17.0	8 17.5	14 17.3	3 19.8	0
	-10		11 17.4	4 19.8	5 19.1	2 27.8	2 29.0	5 18.6	7 21.6	2 27.8	0

Table 8. The same as Table 6, but for the coastal ocean, 850 mb winds. Areas are listed from north to south.

		U	-5 5	5 10	5 10	10 30	5 15	5 15	5 15	10 99	15 99
	T	**V**	**-5 5**	**-5 5**	**-5 10**	**-5 10**	**-15 0**	**0 15**	**-15 15**	**-15 15**	**-15 15**
23. Oregon Fort Bragg	**0**		5 17.6	3 23.9	4 20.6	1	2 25.3	4 18.5	6 20.8	1	0
	-5		2 24.0	3 26.8	4 25.2	1	2 28.3	4 24.8	6 25.9	1	0
	-10		1	3 32.3	4 31.4	1	2 34.1	4 29.9	6 31.3	1	0
22. Ft Bragg Point Reyes	**0**		1	0	1	0	0	1	1	0	0
	-5		0	0	1	0	0	1	1	0	0
	-10		0	0	1	0	0	1	1	0	0
21. Pt Reyes Monterey	**0**		1	2 17.1	3 15.5	1	2 17.1	2 14.3	4 15.7	1	0
	-5		0	1	2 16.0	1	1	2 18.6	3 17.9	1	0
	-10		0	0	0	1	0	1	1	1	0
20. Monterey S.L.Obispo	**0**		4 13.0	0	0	0	0	1	1	1	0
	-5		2 21.5	0	0	0	0	1	1	1	0
	-10		1	0	0	0	0	1	1	1	0
19.S.L.Obispo Oxnard	**0**		4 13.0	2 18.8	3 18.4	1	3 17.1	2 24.2	5 20.1	1	0
	-5		3 14.4	1	2 18.9	1	2 13.3	2 28.8	4 21.0	1	0
	-10		2 15.1	0	0	1	1	1	2 31.2	1	0
18.Oxnard San Clemente	**0**		1	1	1	0	1	1	1	0	0
	-5		1	0	0	0	0	2	0	0	0
	-10		0	0	0	0	0	0	0	0	0
17.S.Clemente San Diego	**0**		1	4 23.3	5 22.2	2 23.0	2 23.0	5 22.2	7 22.4	2 23.0	0
	-5		1	1	2 21.8	2 30.2	2 30.2	2 21.8	4 26.0	2 30.2	0
	-10		0	1	2 25.7	0	0	2 25.7	2 25.7	0	0

The next plot (Figure 30) gives the median effective radii for the ten areas under moderate southwest winds at 700 mb. Again, the coastal areas have much larger effective radii and precipitation than their paired Sierra areas. Note the enormous difference between the effective radii in the northernmost two coast and Sierra areas. All of the coastal clouds reached the precipitation threshold of 14 μm, even at cloud top temperatures of 0°C. On the other hand, none of the clouds in the paired northern Sierra area reached the precipitation threshold, probably due to the advection of pollutants from the heavily urbanized areas to the southwest. The other Sierra areas do not differ much from the northernmost Sierra area under moderate southwesterly flow.

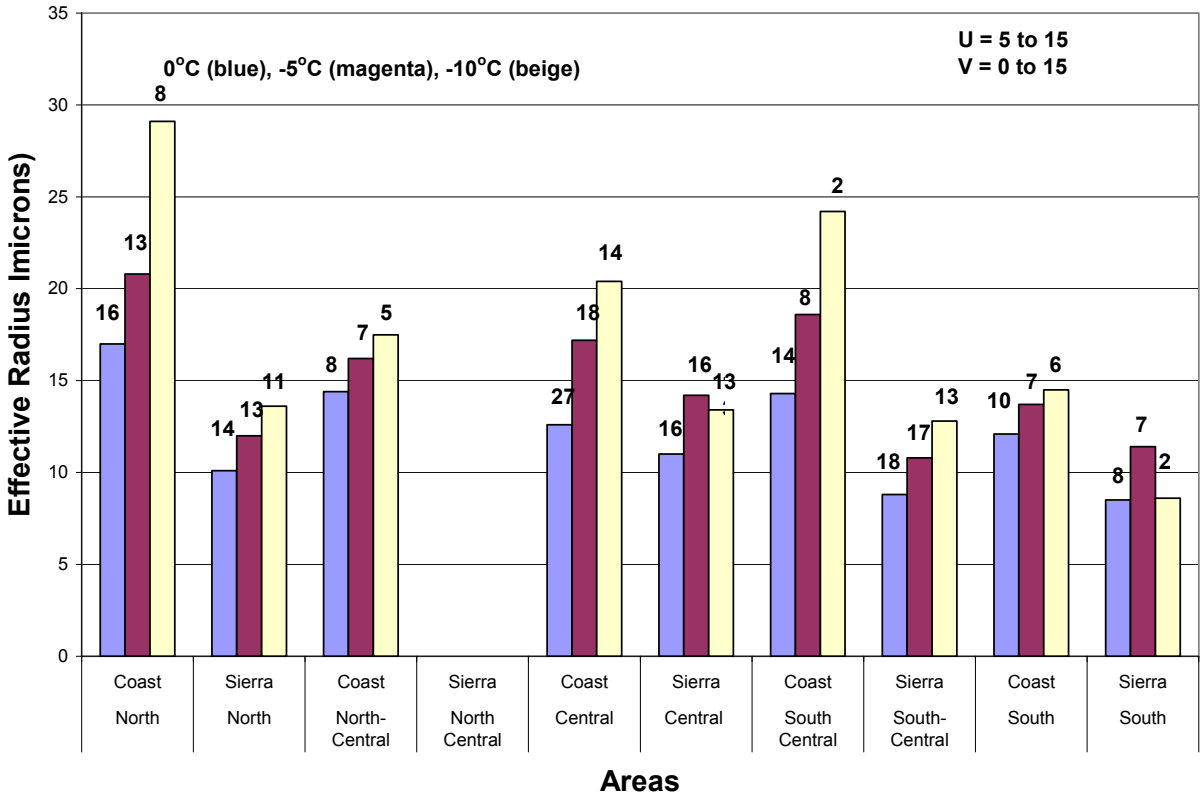

Figure 30. Median effective radii vs. temperature under moderate 700 mb southwest winds for five coast and five Sierra areas as shown in Figure 28. The number of cases appears above each bar.

The mean conditions under moderate 700 mb northwesterly flow (Figure 31) are an interesting contrast to the conditions under southwesterly flow. The effective radii are largest in the north for both the coast and Sierra areas, because this flow should be least contaminated by pollutants. From there, the mean r_e decrease progressively to the south as pollutants generated in the urbanized coastal areas move southeastward into the Sierra areas. The main shortcoming here, however, is sample size, which is very small for some of the areas.

The last depiction of the median effective radii is for strong westerly winds up to 30 m s^{-1} (Figure 32). As with the other depictions, the median effective radii are larger in the coastal areas than they are in the paired Sierra areas. Although the differences are not large, the effective radii are somewhat greater in the northern Sierra areas than in the southern Sierra areas.

These results are consistent with, but not proof of, the claimed linkage between pollution and altered cloud microphysics and precipitation. The main study limitation was sample size. Despite the enormous effort that was put into the study, the sample is still too small in some instances to be certain that the differences have been quantified with high confidence. Even so, it appears that the areas with documented precipitation losses are those areas that have the smallest satellite-inferred effective radii. The remaining uncertainties are whether the satellite inferences of cloud structure are real and, if so, whether the regional differences in cloud structure can be explained by the ingestion of pollution aerosols. These issues are addressed next.

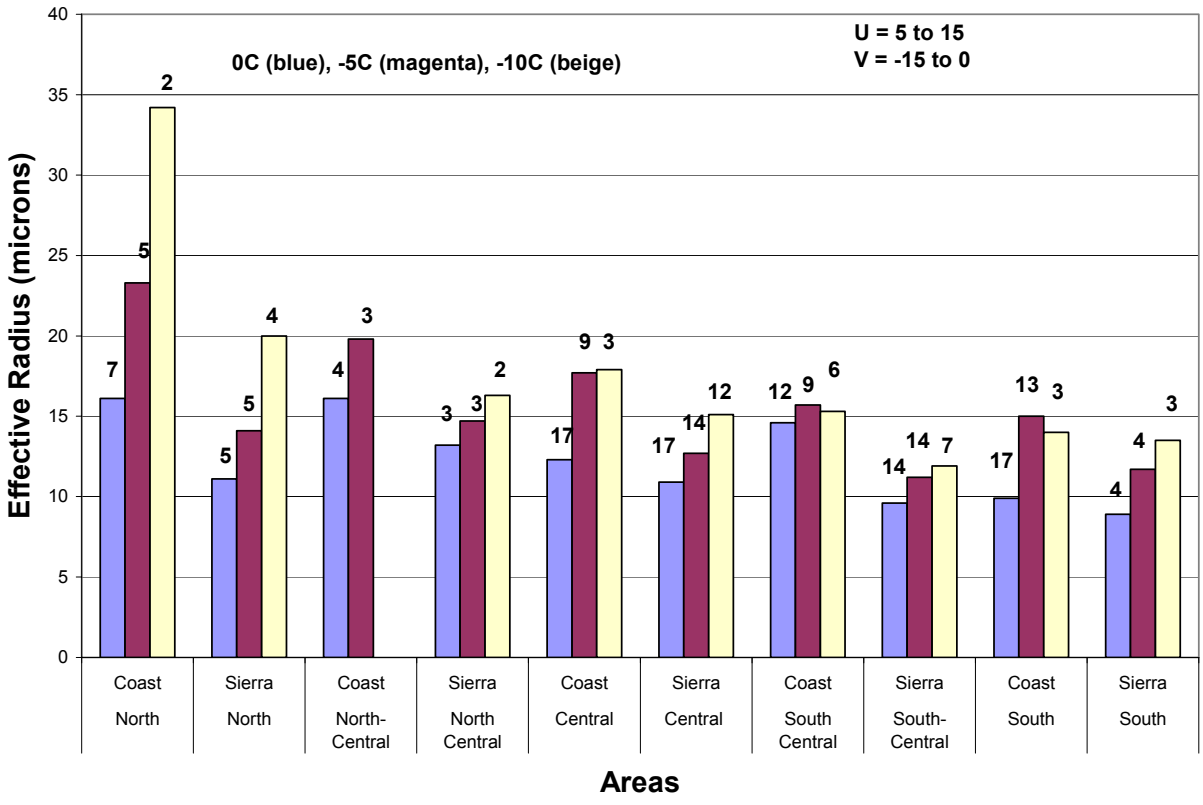

Figure 31. Median effective radii vs. temperature under moderate northwesterly winds at 700 mb for the five coastal and five Sierra areas shown in Figure 28. The number of cases appears above each bar.

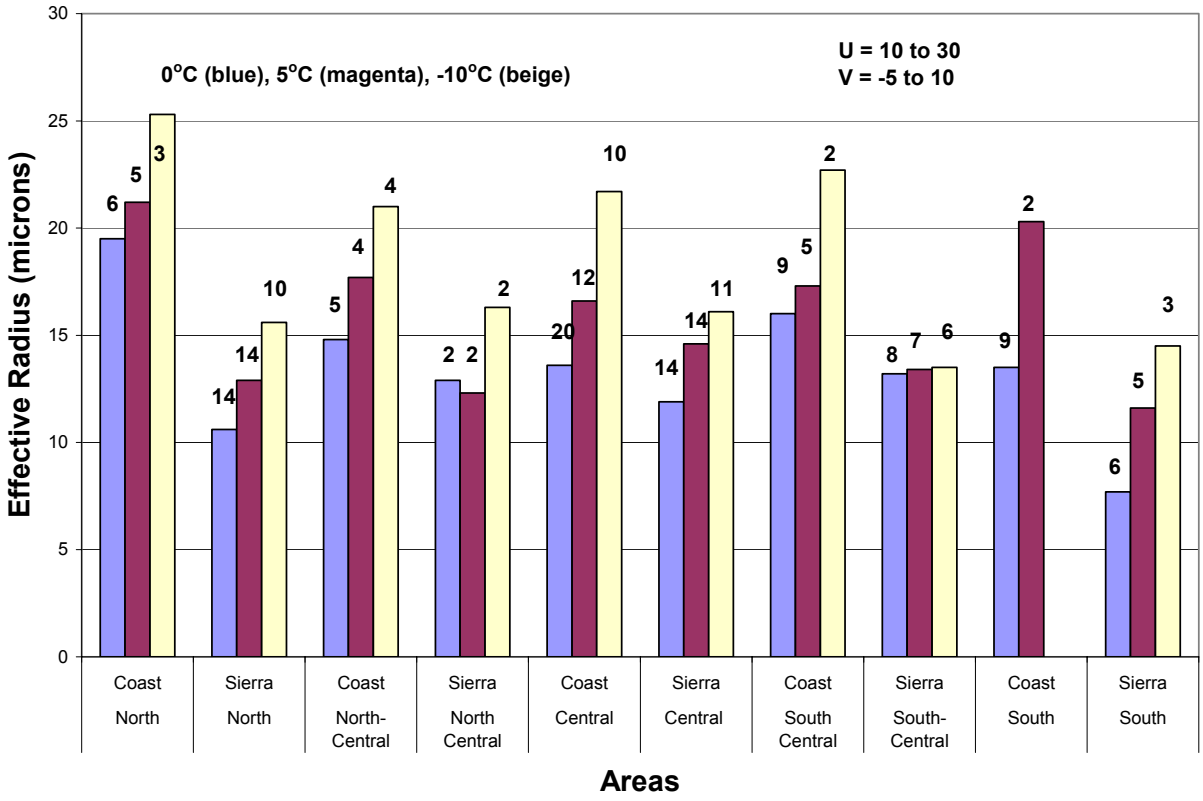

Figure 32. Median effective radii vs. temperature for strong westerly winds at 700 mb for the five paired coast and Sierra areas, as shown in Figure 28. The number of cases appears above each bar.

5.2. Aircraft Validation of the Satellite Inferences of Cloud Microstructure

The overall investigation of pollution effects on Sierra Nevada winter precipitation ultimately must focus on the nature and source of the pollutants that the satellite study indicates are decreasing the precipitation's orographic component. They apparently are tiny cloud CCN that result in a very narrow spectrum of small drops that inhibits precipitation-forming coalescence processes and ultimately the riming of ice crystals in the clouds. According to the satellite inferences, the decreases in cloud r_e are taking place over the central and southern Sierra, where the losses in precipitation and stream flows were documented, but not in the northern Sierra, where no such changes were noted. The next step in the overall investigation was to determine whether the satellite-inferred cloud properties, especially the effective radius, could be validated by actual measurements by a cloud physics aircraft in the subject clouds. A program, called the Suppression of Precipitation (SUPRECIP) Experiment was designed by WWC and funded separately by the California Energy Commission (Energy Commission) to provide the needed documentation. SUPRECIP-1 and SUPRECIP-2 were conducted from Sacramento, California, during February and March in 2005 and 2006, respectively. A Cheyenne II, turbo-

prop, cloud physics research aircraft was used in SUPRECIP-1 and both the Cheyenne and an additional Cessna 340 aerosol aircraft were flown in SUPRECIP-2. The number, sizes and concentrations of ingested aerosols and the resulting internal cloud microphysical structure were documented. Even though the SUPRECIP effort was not funded under the original Energy Commission contract with WWC, it is crucial to the understanding of the overall research effort. Consequently, the key SUPRECIP results to date are summarized here.

As presented in the SUPRECIP-1 final report (Woodley et al. 2005), the use of the Cheyenne II, turbo-prop, cloud-physics aircraft made possible the documentation of differences in cloud microstructure associated with differences in CCN that were visibly related to air pollution. It was determined further that these differences were consistent with the satellite retrievals, which were validated by the aircraft measurements. This is crucial since, previously, only the satellite retrievals were available as indicators of the apparent negative effect of pollution on Sierra precipitation. Thus, the new aircraft measurements have validated the satellite inferences of cloud microstructure by showing the negative impact of pollutants on cloud processes and precipitation, thereby making the linkages much more credible. Through the aircraft and satellite measurements in SUPRECIP it has been noted that some of the Sierra precipitation was produced by surprisingly shallow relatively pristine clouds. This suggests that pollution will act detrimentally on such clouds and may help explain the long-term losses in Sierra orographic precipitation.

In comparing the satellite and aircraft inferences of cloud r_e, the satellite inferences of r_e were made for all of the cloud pixels within a series of boxes along the aircraft flight track. Each box was defined such that it encompassed some of the individual aircraft cloud passes. This made it possible to compare the median effective radii for the cloud passes at the height and temperature of the pass with the satellite inferences of the effective radii at the 50th percentile for the composite cloud for all clouds in the box. The results are given in Figure 33, which shows a scatter plot of the cloud microphysical effective radii as measured by the cloud physics aircraft (Aircraft r_e, or effective radius) versus the inferences from the satellite imagery (Satellite median r_e) for two days of study in SUPRECIP-1. Considering the differences in scale (i.e., individual cloud passes versus the composite cloud within a box that contains the cloud passes) and time, the agreement is remarkably good (linear correlation = 0.73), giving increased credibility to the satellite inferences of r_e. Thus, the regions in California having experienced losses in precipitation and stream flow over the years had decreased r_e values when compared to those inferred for more pristine areas of California. Because the satellite inferences of r_e agree generally with the aircraft measurements of r_e, albeit with a rather limited sample, one is led to the conclusion that the clouds in the areas of precipitation loss and stream flow actually had smaller drop sizes and more inefficient precipitation-forming processes. Although it seemed reasonable to the researchers to ascribe the decreased droplet sizes to the ingestion of pollution aerosols, not everyone was persuaded because of the small sample. More had to be done.

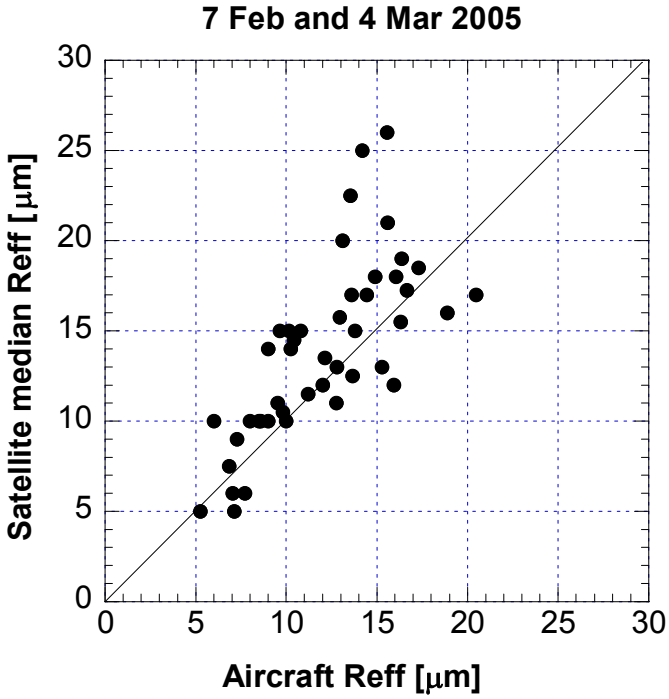

Figure 33. Scatter plot of the median effective radii determined by aircraft (Aircraft r_e) for individual cloud passes vs. the median effective radii inferred from the multi-spectral satellite imagery (Satellite median r_e) for the altitudes and temperatures of the aircraft cloud passes for clouds within boxes that contain the cloud passes. The comparisons were made for data obtained on February 7 and March 4, 2005.

Additional analyses were made for those days having complete cloud microphysical data sets, including time, the altitude and temperature of the cloud pass, the cloud droplet probe (CDP) liquid water contents (LWC), mean and maximum droplet concentrations, and the median r_e for each cloud pass. The cloud imaging probe (CIP) instrument provided an estimate of the cloud precipitation water. Aerosol information was supplied by the CCN counter operated at 0.5% supersaturation. The total aerosols as a function of size were provided by the dual mobility analyzer (DMA). For information about the aircraft instrumentation, the reader is referred to Appendix B of the SUPRECIP-1 final report (Woodley et al. 2005).

The SUPRECIP-1 data were used to show an association between the CCN concentrations evident before and after each cloud pass and the in-cloud droplet concentrations. This is shown in Figure 34, which is a scatter plot and regression analysis relating the aircraft-measured droplet concentrations (mean and maximum) to the observed CCN concentrations before and after the cloud penetrations. The figure shows that the greater the CCN around the cloud at the level of its penetration, the greater the in-cloud droplet concentrations. Thus, aerosols would appear to have a direct effect on in-cloud structure, suggesting a connection between pollution aerosols and altered cloud processes.

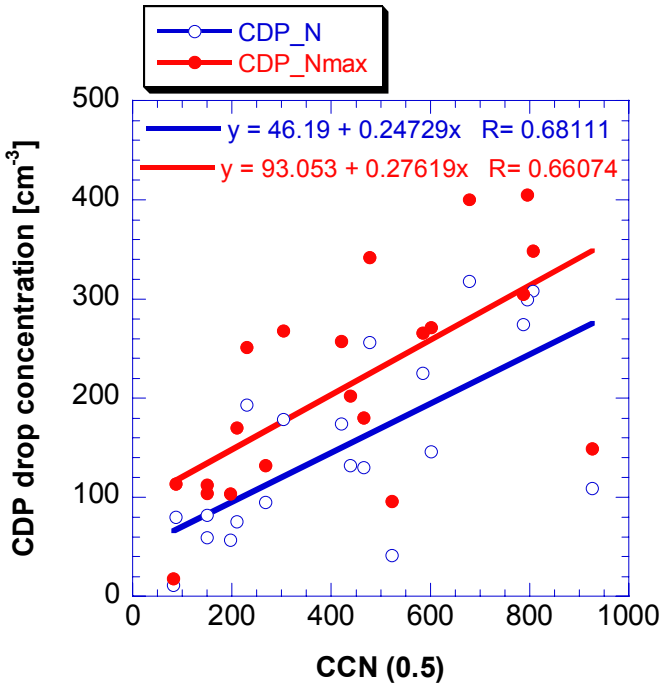

Figure 34. Cloud drop number concentrations as a function of the CCN concentration at a supersaturation of 0.5%. Each point represents the median (blue) and maximum (red) droplet concentrations for one cloud pass. The best-fit equations and corresponding correlations are as shown.

The next step in the analysis was to relate the effective diameter of the cloud drops, normalized for the cloud liquid water content by the expression Deff / $LWC^{0.333}$, to the CCN concentrations for each cloud pass, where Deff is the effective diameter. In developing this correction one must understand that for the same CCN, the effective diameter would increase with height above cloud base, as would the LWC. The variable cloud-penetration heights above cloud base cause a random variability that might mask the relationships between the CCN and the effective diameter. Because the cloud base height is unknown, it is necessary to normalize with the next best thing, which is the LWC. Because droplet diameter depends linearly on the cube root of the volume, the correct normalization form is as used here (i.e., Deff / $LWC^{0.333}$). The CCN concentrations were taken from the immediate clear air vicinity of the pass. The averaging is just for the cloud drops throughout the pass. Note that the correlation is denoted as unsigned. The negative relation is given by the regression equation. Upon examining the plot in Figure 35 it can be seen that the effective diameter decreases as the CCN aerosol concentration increases. This is the aerosol connection to the drop-size distribution. Thus, as the CCN pollution aerosols increase, the drop sizes decrease. From the perspective of the researchers, this should have settled the matter; however, a reviewer of the SUPRECIP-1 final report did not agree with this conclusion, and admittedly, the results were based on a very small sample. Further, a connection between the aerosols and precipitation had not been shown. One of several motivations for conducting the SUPRECIP-2 research was to address these deficiencies.

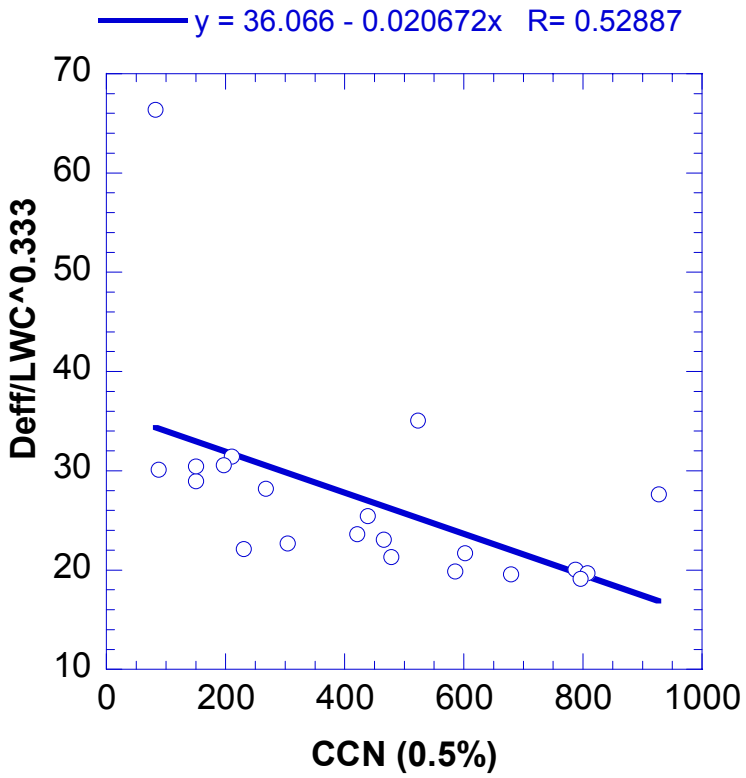

Figure 35. The effective diameter of the cloud drops normalized for the cloud liquid water content by the expression Deff / $LWC^{0.333}$, as a function of the CCN concentrations for each cloud pass

The addition of the aerosol aircraft during SUPRECIP-2 made it possible to measure the CCN below the bases of clouds being studied by the Cheyenne II cloud physics aircraft. This made it possible to associate the subcloud CCN to the in-cloud measured parameters. As of this writing, 6 of 19 flights when both aircraft flew together had been analyzed. For portions of the 6 flights the depth of cloud needed for the droplet mean effective diameters to reach the precipitation threshold of 24 μm in each studied cloud was determined along with the corresponding subcloud CCN values. The scatter plot relating the two is given in Figure 36. The two are well correlated (i.e., R = 0.90). That is, the higher the CCN counts, the greater the cloud depth needed for the cloud to develop precipitation. Thus, clouds that ingest pollution aerosols will have smaller satellite-inferred effective radii, smaller aircraft measured cloud drops, and higher droplet concentrations, requiring greater cloud depths for the drops to reach precipitation size. Although the SUPRECIP-2 analyses are continuing, it appears that a direct link between pollution and the loss of Sierra precipitation and stream flows has been established.

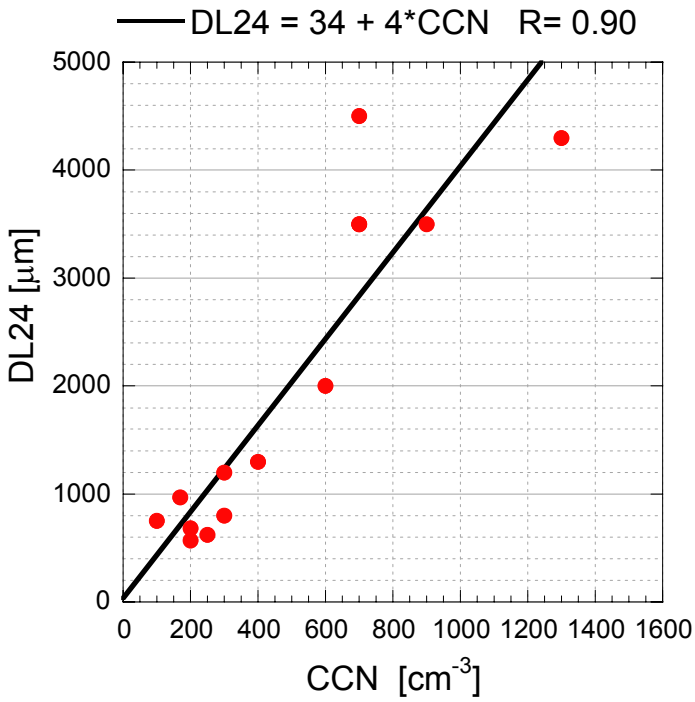

Based on the flights from:

2006 02 28a

2006 02 28b

2006 03 01

2006 03 02a

2006 03 02b

2006 03 02c

Yet unanalyzed data exists for up to 13 additional flights

Figure 36. Scatter plot of the cloud depth (in meters) necessary for the in-cloud droplet sizes to reach the precipitation threshold of 24 μm versus the maximum CCN concentrations measured beneath each subject cloud

6.0 Numerical Simulation of Cloud Processes Under Polluted and Non-Polluted Conditions

6.1. Objectives of the Numerical Study

Statistical analysis performed by Givati and Rosenfeld (2004) and later by Jirak and Cotton (2006) showed persistent decreases in precipitation over the Sierra Nevada Mountains (California) during at least the past 50 years. These decreases were found downwind (eastward) from urban zones located in the vicinity of the coastline. Givati and Rosenfeld hypothesized that these decreases in precipitation were caused by anthropogenic aerosols, whose production has been increasing progressively during this period. As was observed in many field experiments, as well as in numerical simulations, an increase in the aerosol concentration leads to an increase in droplet concentration and a corresponding decrease in droplet size. Collisions between small droplets are inefficient, so that these droplets ascend to higher levels without the production of large raindrops—that is, without production of warm rain.

It should be mentioned that the aerosol hypothesis as a cause of the precipitation decrease is not very obvious. First, some works have shown precipitation enhancement around heavily polluted urban areas such as Houston (Shepherd and Burian 2003) and Tokyo (Ohashi and Kida 2002). Second, the time delay in the raindrop formation does not mean that the accumulated rain at the surface will also automatically decrease. There are occasions when the delay in the raindrop formation (and the decrease in warm rain) leads to the production of a larger amount of ice, which should grow faster by water vapor deposition and may produce a larger mass of precipitating particles as a result of ice-ice or ice-water collisions.

Consequently, the main objectives of the numerical simulations were:

1. To verify (justify or disprove) the aerosol hypotheses of the persistent decrease of precipitation over the upwind slopes of the Sierra Nevada Mountains.
2. To reveal the mechanisms and conditions under which aerosols lead to the decrease in precipitation amount.

The structure of the rest of this chapter includes four additional sections. Section 6.2 discusses the problem of the initial choice of the numerical model. Section 6.3 discusses the results and conclusions made from three-dimensional simulations. Section 6.4 discusses results obtained in 2-D simulations. The discussion and conclusions can be found in Section 6.5.

6.2. The Choice of Numerical Model

Most existent mesoscale cloud-resolving models use so-called bulk-parameterization of microphysical processes. The bulk parameterization schemes preset the shape of the size distributions of cloud hydrometeors (for example, the Gamma distribution and Marshall-Palmer distribution). As a result, the equation system describing microphysical processes is reduced to a relatively small number of equations for integral values, such as mass contents (in so-called *one-moment schemes*). A comparatively small amount of microphysical variables makes

the bulk-parameterization models effective from a computational point of view. At the same time, these models are not suitable for investigation of aerosol effects, because, as was mentioned above, the aerosols affect droplet sizes—that is, make droplet size distributions (DSD) narrower. This key aerosol effect cannot be taken into account in the models with prescribed DSD.

There are two types of numerical cloud-resolving models that claim that they are sensitive to aerosols: (1) two-moment bulk parameterization schemes, and (2) spectral (bin) microphysics schemes. Two-moment bulk parameterization schemes (or some versions of them) calculate two moments of DSD (two integral parameters), namely: total concentration and total mass contents of hydrometeors. This means that two-moment bulk parameterization schemes are able to calculate the mean volume size of hydrometeors of different types. The effect of aerosols is taken into account in this scheme by changing this mean droplet size (via changing the droplet concentration). The utilization of two-moment bulk-parameterization schemes is often considered to be a dramatic improvement of the bulk-parameterization models. Note, however, that the main assumptions of the bulk-parameterizations remain with the two-moment schemes, namely, the shape of size distributions is preset. Moreover, the advantages related to the implementation of an additional variable (concentration) are often accompanied by serious disadvantages. For instance, the mean mass sedimentation velocity and the mean concentration sedimentation velocity are different. Consequently, water mass sediments faster than concentration does. This procedure leads, sometimes, to unpredictable large or small values of particle size, and other factors. The problems become even more serious when the processes of drop freezing, collisions, and riming are considered. For instance, freezing should be proportional to drop mass—that is, the freezing probability of 1000-micron-radius drops is 10^6 times higher than that of 10-micron-radius drops. Consequently, freezing should cut off mainly the tail of the DSD. At the same time, it is impossible in the bulk parameterization, where a Marshall-Palmer distribution (with an infinitely long tail) is always assumed. These examples do not exhaust the limitations of bulk parameterizations from the physical point of view.

Another type of microphysical scheme is the spectral (bin) microphysics (SBM). A detailed SBM model of deep convective clouds has been developed at the Hebrew University of Jerusalem (HUCM). The details of model microphysics are presented in studies by Khain and Sednev (1996); Khain et al. (1999); Khain et al. (2001, 2004); and Phillips et al. (2006). The SBM model is based on solving the equation system for size distribution functions of drops, ice particles, and aerosols. The model is unique as concerns sophistication of the description of ice microphysics. It calculates three size distribution functions for ice crystals (columns, plates, and dendrites), as well as three size distributions for snow, graupel, and hail. In addition, it includes the size distribution for aerosol particles allowing for the simulation of the budget of aerosols and for the investigation of aerosol effects on cloud microphysics and dynamics. In the current version of the model, each size distribution is described using 33 mass (size) bins. The model takes into account the changes of the particle density with both particle size and temperature. The aspect ratios of ice crystals and snowflakes are calculated as a function of their size according to the observed data and laboratory measurements (Pruppacher and Klett 1997 ; Khain and Sednev 1996). The SBM scheme includes the main microphysical processes, such as nucleation of drops

and ice crystals; diffusion growth/evaporation; drop-drop, drop-ice, and ice-ice collisions; differential sedimentation depending on mass and shape of particles and air density; breakup of large raindrops, and others. Melting is accurately treated (Phillips et al. 2006), so water fraction in melting graupel, hail, and snow particles of different size is calculated. Thus, size distributions of water mass (liquid water fraction) within ice particles of different type and mass is also calculated. Both processes of suction and formation of surface water skin are taken into account, as are the differences in the processes of melting of graupel and snowflakes. As soon as the depth of the water skin on graupel or hail exceeds some critical value, shedding takes place with the formation of small raindrops.

The model is specially designed to take into account cloud–aerosol interaction and effects of aerosols on cloud microphysics and precipitation. The main mechanism by means of which cloud-aerosol interaction takes place is the droplet nucleation (CCN activation). As a result of this process, CCN with sizes exceeding the critical values (determined by the Kohler theory) turn out to be droplets. Respectively, corresponding bins of the aerosol mass grid become empty. This process is known as *nucleation scavenging.* Aerosols with sizes below the critical one remain non-activated and are advected by the wind. According to many studies, nucleation scavenging is responsible for about 90% of the aerosol decrease in the atmosphere.

The chemical properties of the aerosols were taken into account only for the calculation of the critical size. The amount of aerosols within droplets was not calculated in this study. These calculations are time consuming. At the same time, the amount of "aerosols" within drops does not affect precipitation formation. Note that the microphysical scheme allows one to take these effects into account. This could be done for the calculation of the chemical composition of precipitation.

It was assumed in the calculations that the aerosols consisted of sodium chloride (NaCl). In case the chemical composition of aerosol particles differs from NaCl, one can easily calculate the "effective" size distribution of the NaCl particles having nucleation properties similar to those of the non-NaCl particles (Mazin and Shmeter 1983). Indeed, the nucleation properties of aerosols are determined by the "chemistry" term in the equation for diffusion growth, which contains the product Br_N^3, where B is the coefficient responsible for the chemical properties of aerosols (it includes the van 't Hoff factor, the molecular weight, and the dry bulk density), and r_N is the radius of a dry aerosol particle. The radius of the equivalent NaCl particle can be calculated as $r_{N\,NaCl} = r_N (B / B_{NaCl})^{1/3}$. Note that the ratio $(B / B_{NaCl})^{1/3}$ is often quite close to one because of the power (1/3). It means that size distribution of CCN is actually insensitive to the chemical composition of aerosols.

The main criteria for the choice of the aerosol concentration were the relevant droplet concentrations typical of continental (polluted) and maritime conditions.

The SBM model has been used for the simulation of deep convective clouds and cloud ensembles. The model was used for investigation of aerosol effects on dynamics and precipitation of continental and maritime deep convective clouds (Khain et al. 2004; Khain and

Pokrovsky 2004; Khain et al. 2005) and for the investigation of the effects of ice melting on cloud dynamics (Phillips et al. 2006). The SBM of HUCM has been implemented into the MM5 model. Using MM5-SBM model, the rain events over Florida accompanied by squall line formation (Lynn et al. 2005a, 2005b) were simulated successfully. The comparison with observations and with the results of bulk parameterizations applied within the same dynamical frameworks indicated that the SBM represents the cloud structure and precipitation much more accurately. This is why the MM5-SBM model was chosen for the performance of the simulations within the project's framework.

This choice was risky to some extent, because three-dimensional (3-D) simulations with SBM models require about 20 times more computer time than the models using bulk parameterizations. Besides, the SBM scheme also requires an accurate description of model dynamics and, first of all, vertical velocities, which determine the value of supersaturation and droplet concentration. This approach requires utilization of high model resolution. In studies by Lynn et al. (2005a, 2005b) 3-km resolution was used to simulate deep convective clouds and squall lines. As was mentioned, reasonable results were obtained and the research team believed that this model with similar or even better resolution would allow the case studies to be simulated.

6.3. Simulations with the 3-D MM5-SBM Model

The orographic clouds observed on 7 December 2003 (local sidereal time, or LST) over the Sierra Nevada Mountains were chosen for simulations. Figure 37 shows a visible satellite picture showing the observed cloud structure. This case is addressed in more detail in Figures 9–11 and in their discussion.

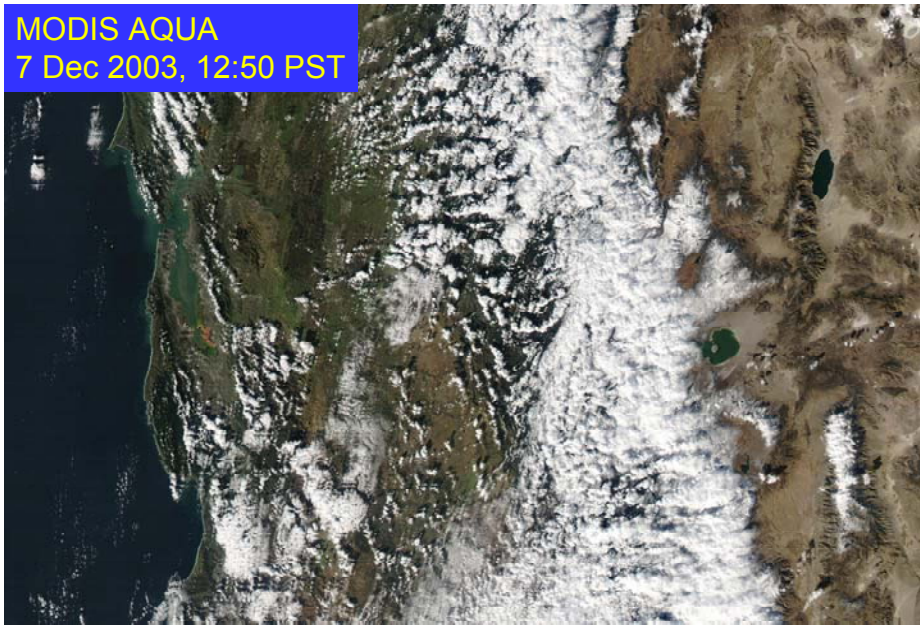

Figure 37. Satellite picture of cloudiness observed on 7 December 2003

To choose the area where the SBM would be used to reveal the effects of urban pollutants on precipitation (California region), the research team started to simulate the evolution of the meteorological fields over the large area centered at about 37.0 N and -117.5W. A triple-nested grid system was used in the simulations (Figure 38A). The resolution and sizes of the grids were as follows:

- Outermost grid: resolution of 27 km; 192 x 240 grid points.
- Intermediate grid: resolution of 9 km; 337 x 337 grid points.
- Finest grid: resolution of 3 km; 226 x 226 grid points.

Spectral (bin) microphysics was used on the finest grid only. Bulk-parameterizations were used on the outer grids. This approach significantly decreased the computational time.

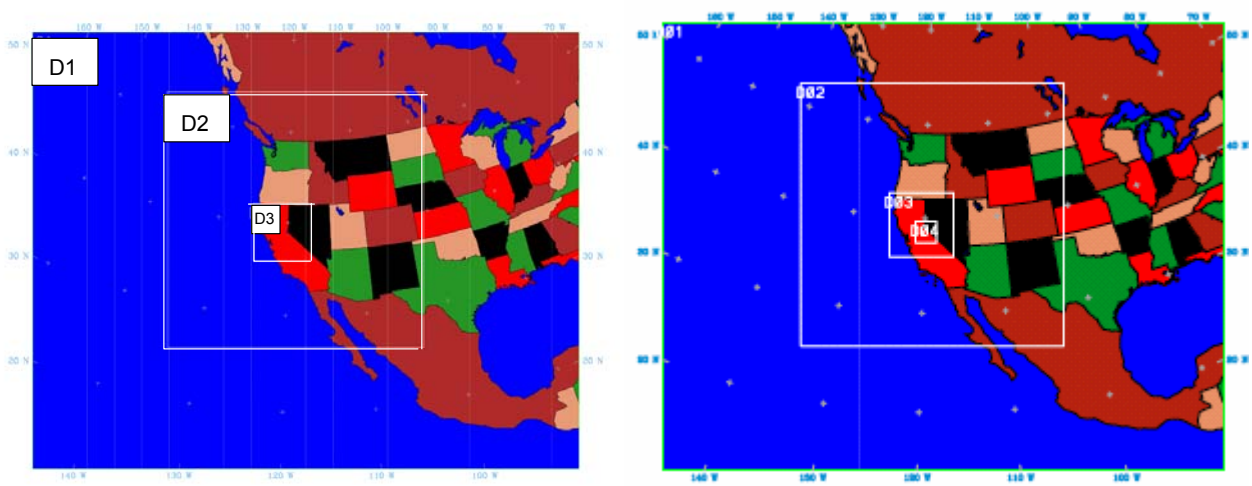

(A) (B)

Figure 38. The nested grid system used in the simulations with the MM5-SBM model. (A) the triply nested grid system with the finest grid resolution at 3 km; (B) the nested grid system consisting of four grids, with the finest grid resolution at 1 km.

A great number of simulations were carried out using the configuration shown (left panel) in Figure 38. These simulations were performed for different aerosol concentrations: low concentration (~100 cubic centimeters, or cm^{-3}) typical of maritime aerosols (M-cases) and high concentration (~ 1500 cm^{-3}) typical of polluted continental aerosols (C-cases). The simulations were performed in versions ranging from only warm-cloud microphysics to the full range of mixed-phase cloud microphysics.

The simulations were performed for about 12 hours. After some modifications of the topographical representation and an increase in the vertical model resolution the cloudiness structure had been simulated realistically (Figure 39a). One can see that the cloudiness structure and its location were simulated with high accuracy. The difference in precipitation amounts in millimeters in the M- and C-cases is shown in Figure 39b. One can see that

precipitation in the C-case is somewhat smaller than in M-case over the upwind slope, in agreement with the results reported by Givati and Rosenfeld (2004). At the same time the analysis of the fields of vertical velocity, as well as of cloud structure, showed that the horizontal resolution of 3 km was too crude to resolve these fields with the necessary accuracy. Underestimation of the vertical velocity led to the underestimation of aerosol effects in the C-case. Consequently, it was decided to increase the resolution of the finest grid to 1 km. A new grid was implemented, as shown in Figure 38B).

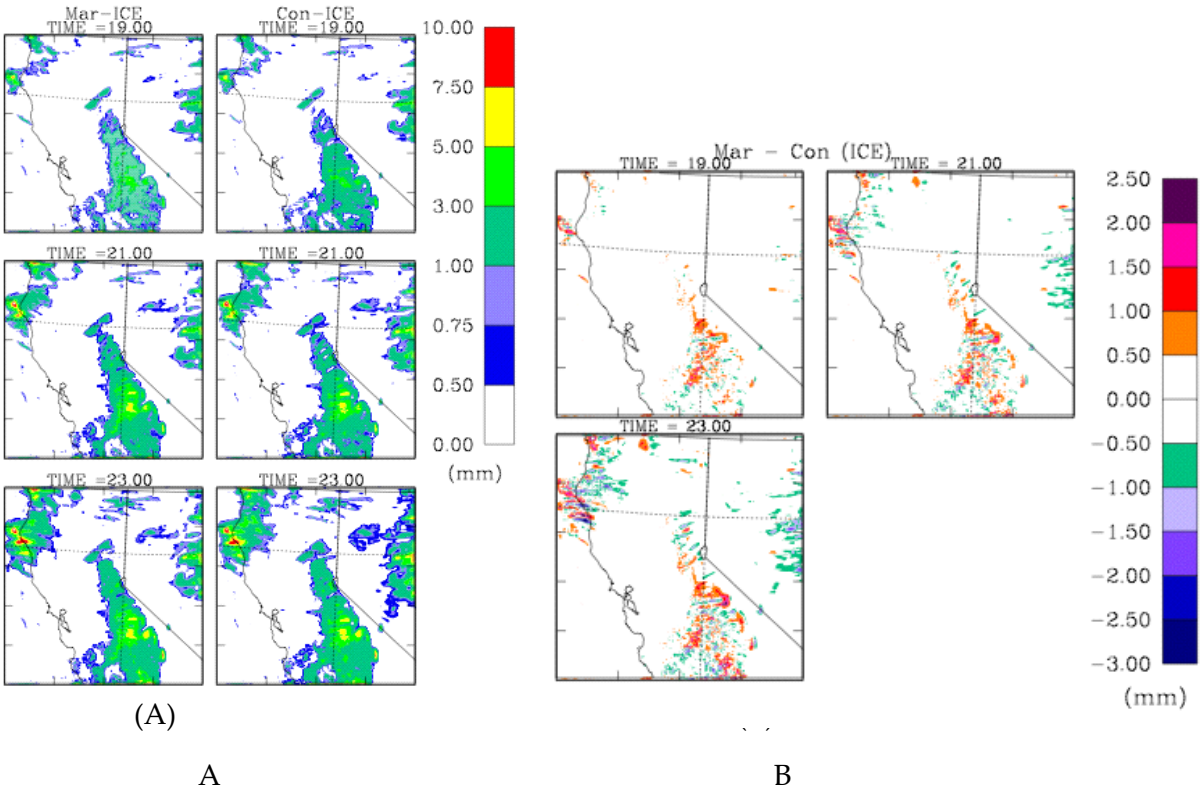

Figure 39. (A) Accumulated rain amounts in mm in the M- and C-runs, (B) difference in millimeters

Figure 40 shows the accumulated precipitation in the M- and C-cases in simulations with 1-km resolution for the finest grid. One can see that 1-km resolution simulations provided much better detailed reproduction of the precipitation structure. In spite of the fact that the general precipitation structure in the M- and C-cases is similar, there are significant differences in precipitation, as is shown in Figure 41.

The dramatic improvement of the precipitation representation with the increase in the model resolution can be seen from comparison of Figure 39 (B) and Figure 41. While the results obtained with the 3-km resolution do not reveal any spatial redistribution of the precipitation caused by an increase in the aerosol concentration, the 1-km resolution simulations clearly indicate this redistribution.

One can see that the increase in the aerosol concentration decreased precipitation over the upwind (western) slope by 20% to 40% and increased the precipitation on the ridge peak and over the downwind slope up to 20%.

These results agree well with those obtained by Givati and Rosenfeld (2004). The M-C differences in accumulated precipitation (in %) in the 1 km resolution simulations are shown in Figure 41.

Accumulated precipitation in M- and C-cases, full microphysics

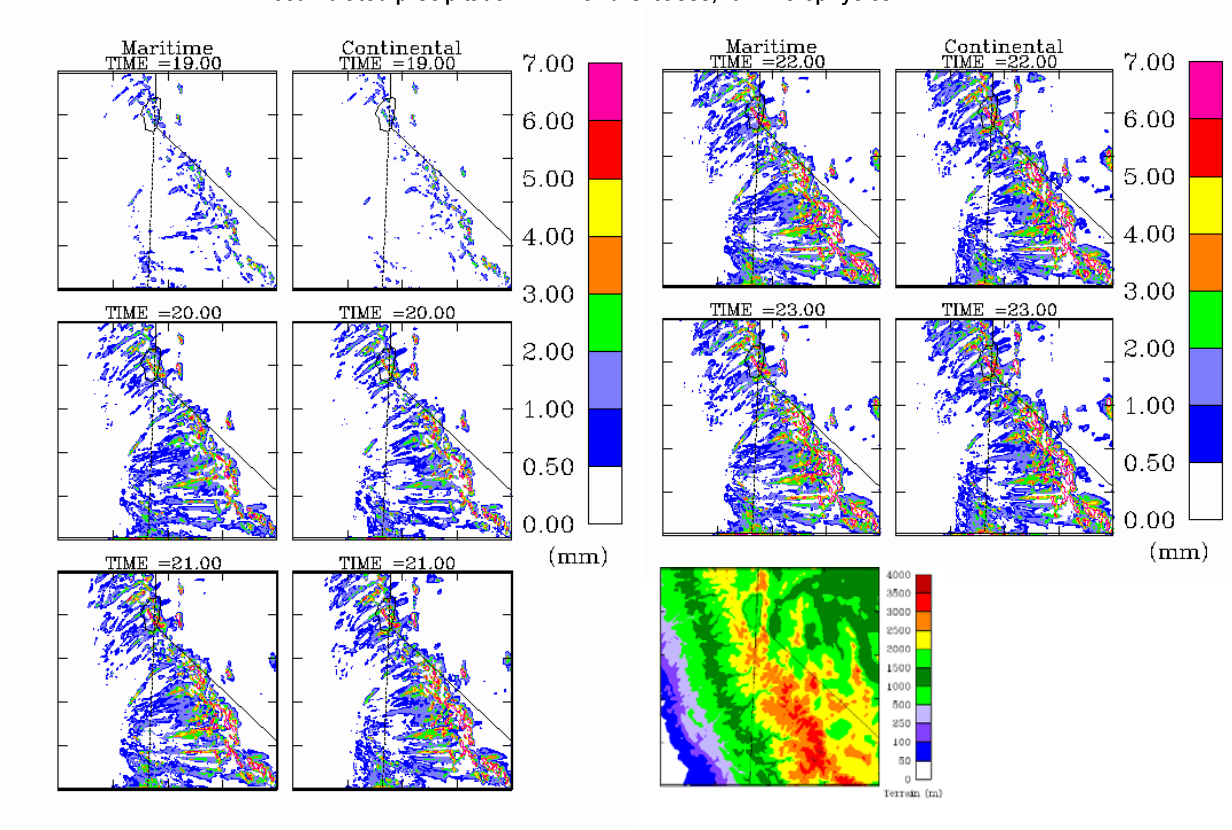

Figure 40. Accumulated precipitation in the M- and C-cases in simulations with "full microphysics" included within the time period 19–23 hours into the simulation

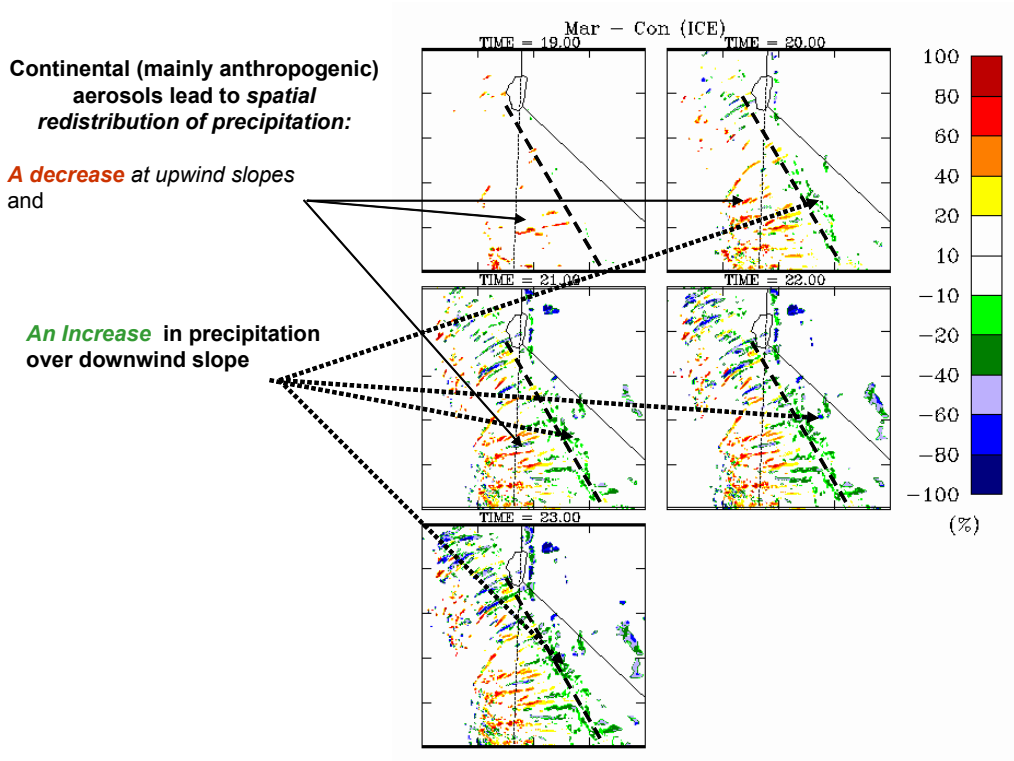

Figure 41. The ratio (PM-PC)/PM (in %) obtained in the 1-km resolution simulation at different time instances. PM-accumulated precipitation under maritime (clean) air; PC-accumulated rain in C-case (polluted air). The dashed line shows the location of the main ridge.

The physical interpretation of this spatial redistribution of precipitation is as follows. An increase in the aerosol concentration leads to a decrease in droplet size and slows raindrop formation. Consequently, the residence time increases for the droplets located within cloud. In addition, it leads to a larger production of cloud ice that has slower sedimentation velocity. The background wind transports these hydrometeors downwind toward the mountain ridge and the downwind slope. However, the evaporation of hydrometeors over the downwind slope leads to a net decrease in the total precipitation over the whole mountain area, due to the increase in the aerosol concentration. These results agree with those obtained by Givati and Rosenfeld (2004) as well.

These detailed comparisons of the numerical results with the observations indicates a good agreement between them. In the simulated case the decrease in the accumulated rain due to the aerosol effects was 20%–30%. Sensitivity studies indicate that the aerosol effects depend on environmental conditions, for instance, on the air humidity. It means that the contribution of aerosols to the precipitation change may vary from season to season, and even from day to day.

These numerical results are further justification for the view that the increase in the concentration of anthropogenic aerosol can be the reason for the observed decrease in precipitation.

To illustrate further the effect of aerosols on cloud processes Figure 42 presents examples of cross-sections in the fields of liquid water content, rain water, graupel, and snow contents obtained in the 1-km resolution simulation at 20 hours into the simulation.

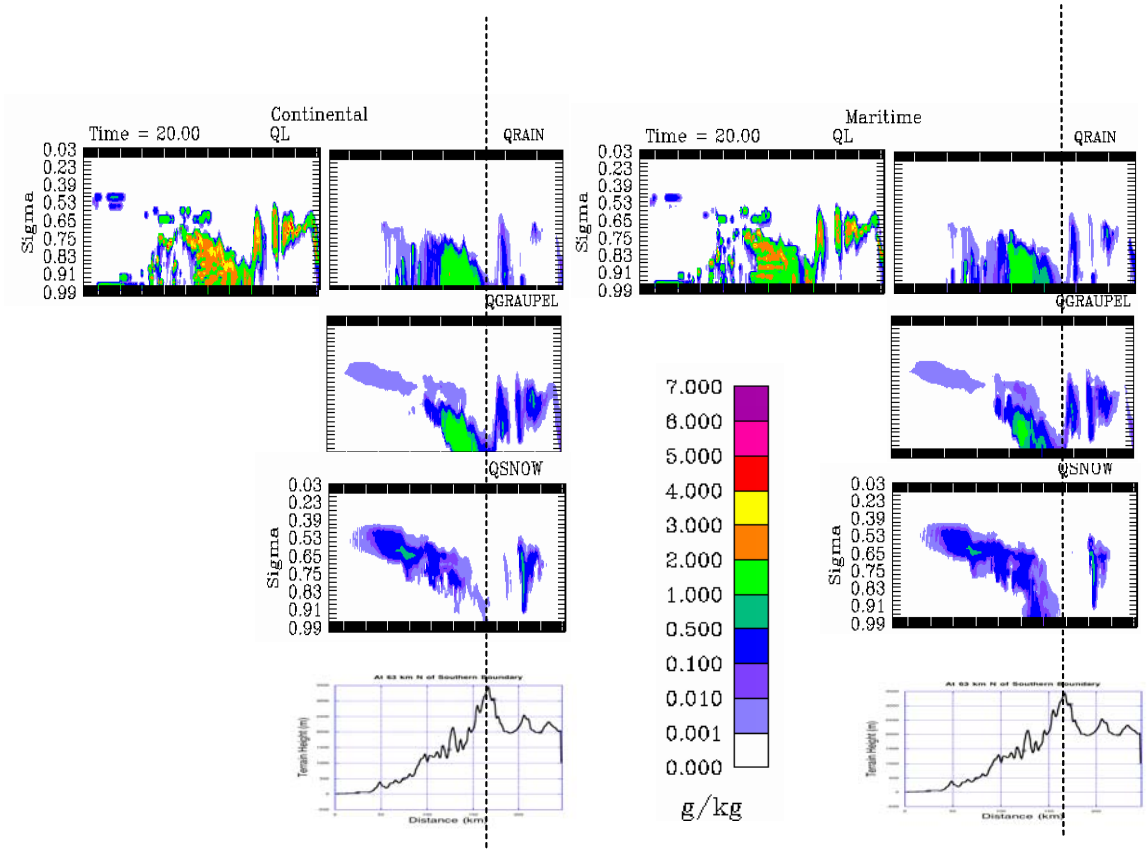

Figure 42. Cross-sections in the fields of liquid water content (QL), rain water (QRAIN), graupel (QGRAUPEL) and snow (QSNOW) contents obtained in the 1-km resolution simulation at 20 h into the simulation. The topography profile is presented for the sake of convenience.

One can see that an increase in the aerosol concentration leads to an increase in cloud mass content and to an increase in mass of ice over the mountain ridge and over the downwind slope. Thus, 3-D simulations using the MM5-SBM with the 1-km resolution support the results of observations and show that the increase in the production of anthropogenic aerosols can be the reason for precipitation decreases over the upwind slope of the mountains.

It should be noted in concluding this section that supplemental simulations of this case study using bulk-parameterization models were not able to reproduce the structure of the cloudiness and the fine effects caused by the aerosols.

6.4. Two-Dimensional Simulations with Spectral (bin) Microphysics (SBM)

6.4.1. Modification of Model Microphysics

Despite the reasonable results that have been obtained using the MM5-SBM model as concerns general aerosol effects, the simulations indicated that this model has some problems with accurate reproduction of meteorological fields at high resolution over complex terrain. It underestimates the vertical velocities, which leads to faster development of rain over upwind slopes. In addition, the analysis of the 3-D results, as well as the detailed analysis of the shape of DSD in deep convective clouds simulated by the Hebrew University cloud model also indicated that the SBM scheme regularly overestimated the rate of raindrop formation. Because 3-D simulations are time consuming, the research team decided to perform the detailed investigation of these effects using 2-D simulations.

To account for orographic effects and to be able to possibly perform 3-D simulations with high resolution in the future, the novel Weather Research Forecast (WRF) model was chosen as the dynamical framework. As a result of significant efforts, the SBM was implemented into this model. The WRF model has both 2-D and 3-D versions.

Below are described the results obtained using the 2-D WRF with the spectral (bin) microphysics. The coupled model was used to simulate the development of orographic clouds observed during 7 December 2003 (LST) over the Sierra Nevada Mountains. All simulations were performed using a single (non-nested) two-dimensional domain, oriented west to east. The simulations were run for three hours, which was sufficient time for clouds to form on the upslope side of the mountain and to advect over the far mountain peak downwind. The model was run at 6 second dynamical time steps (as compared to 12 seconds in the MM5 simulation) using 1 km grid resolution in the horizontal and about 200 m grid resolution in the vertical. The simulation domain extended over 494 km, but results are presented here for only the inner part of the domain, which was defined as beginning at 150 km and ending at 350 km. Radiation and surface model physics were not included. The clouds were generated by the vertical winds that resulted from the strong upslope (westerly) winds. Moreover, the turbulent kinetic energy (TKE) boundary layer scheme artificially included a TKE drag coefficient of 0.003 and ground sensible heat flux of 100 watts per square meter (W m^{-2}).

It should be noted that a modification of the SBM scheme has been performed within the framework of the project to allow simulation of narrow DSD in the continental case. The scheme modification is described in detail by Khain et al. (2006). The idea of the modification is described below. It is well known (see, for example, Khain et al. 2000) that SBM models face the problem of artificial (numerical) DSD broadening. The broadening is caused by remapping of drop masses and concentrations obtained as a result of diffusion growth and collisions on the regular mass (bin) grid. This broadening accelerates raindrop formation, which introduces errors into simulations of microphysics and precipitation, especially in cases of continental and "smoky" clouds.

The widely used method of the remapping proposed by Kovetz and Olund (1969) (hereafter, K-O) induces a significant droplet spectrum broadening (see, for example, Khain et al. 2000). Some improvement of this algorithm by Khain et al. (2004) does not eliminate this problem for highly polluted clouds. The K-O remapping scheme conserves two moments of size distributions (concentration and mass). The research team has developed a new remapping scheme that conserves three moments of size distributions: concentration, mass, and radar reflectivity (the sixth moment). Figure 43 compares DSDs calculated using the traditional K-O scheme and the new one.

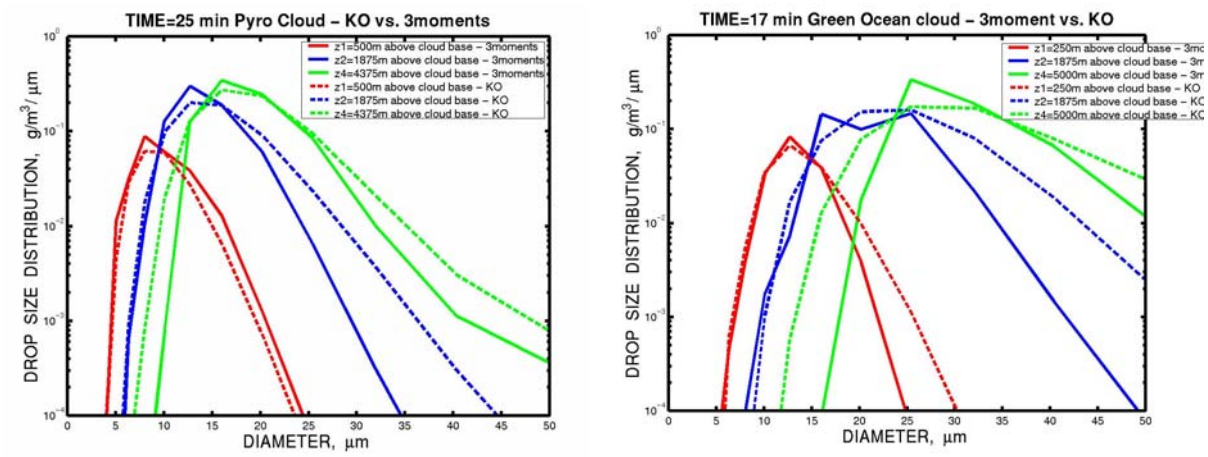

Figure 43. DSDs obtained using the traditional K-O scheme and a new three-moment scheme along the axis of the simulated pyro-cloud (left) and the green-ocean cloud (right). The DSDs calculated using the three-moment scheme are narrower than those calculated using the K-O scheme.

One can see that DSDs calculated using the new scheme are narrower and broaden with height slower than those calculated using the K-O scheme. The utilization of the new three-moment scheme (referred to hereafter as the *three-point scheme*) significantly improved the representation of the DSD in the simulated cases. As is shown below, the new scheme allowed the reproduction of in situ-measured DSDs in convective clouds (Khain et al. 2006). Figures 44–46 demonstrate the significant improvement in the accuracy of the representation of orographic cloud structure.

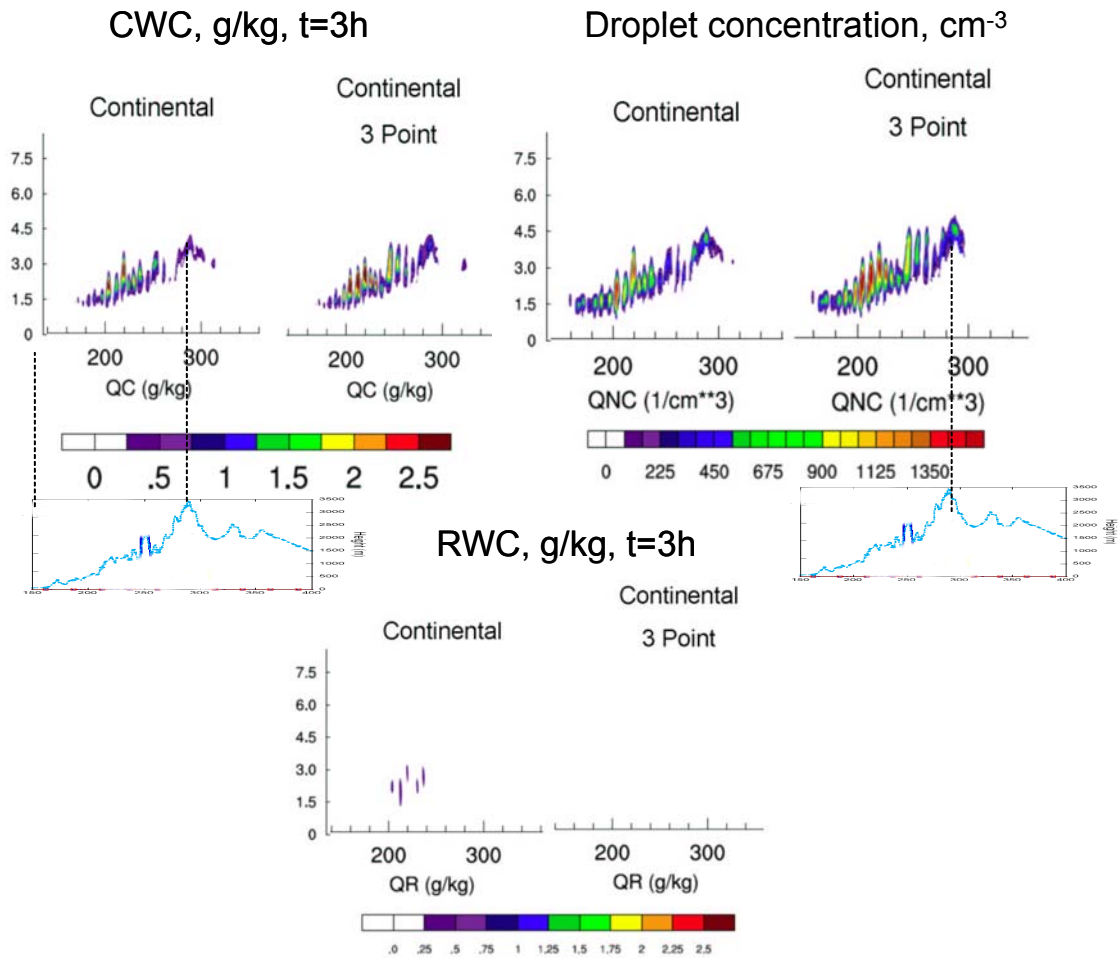

Figure 44. East to west cross sections of droplet concentration, CWC, and rainwater contents (RWC) simulated with the old (two-point) and a new (three-point) remapping schemes

Figure 44 compares fields of droplet concentration, cloud water content (CWC) and rainwater contents (RWC) simulated using the old (two-point) and the new (three-point) remapping schemes. One can see that the new scheme leads to a higher droplet concentration and CWC, lower RWC (it actually excluded the formation of raindrops) in this particular case. Another comparison between the 2-point and 3-point schemes is given in Figure 45, where contents of ice hydrometeors are presented. One can see that the new 3-point scheme increases ice-crystal and snow formation.

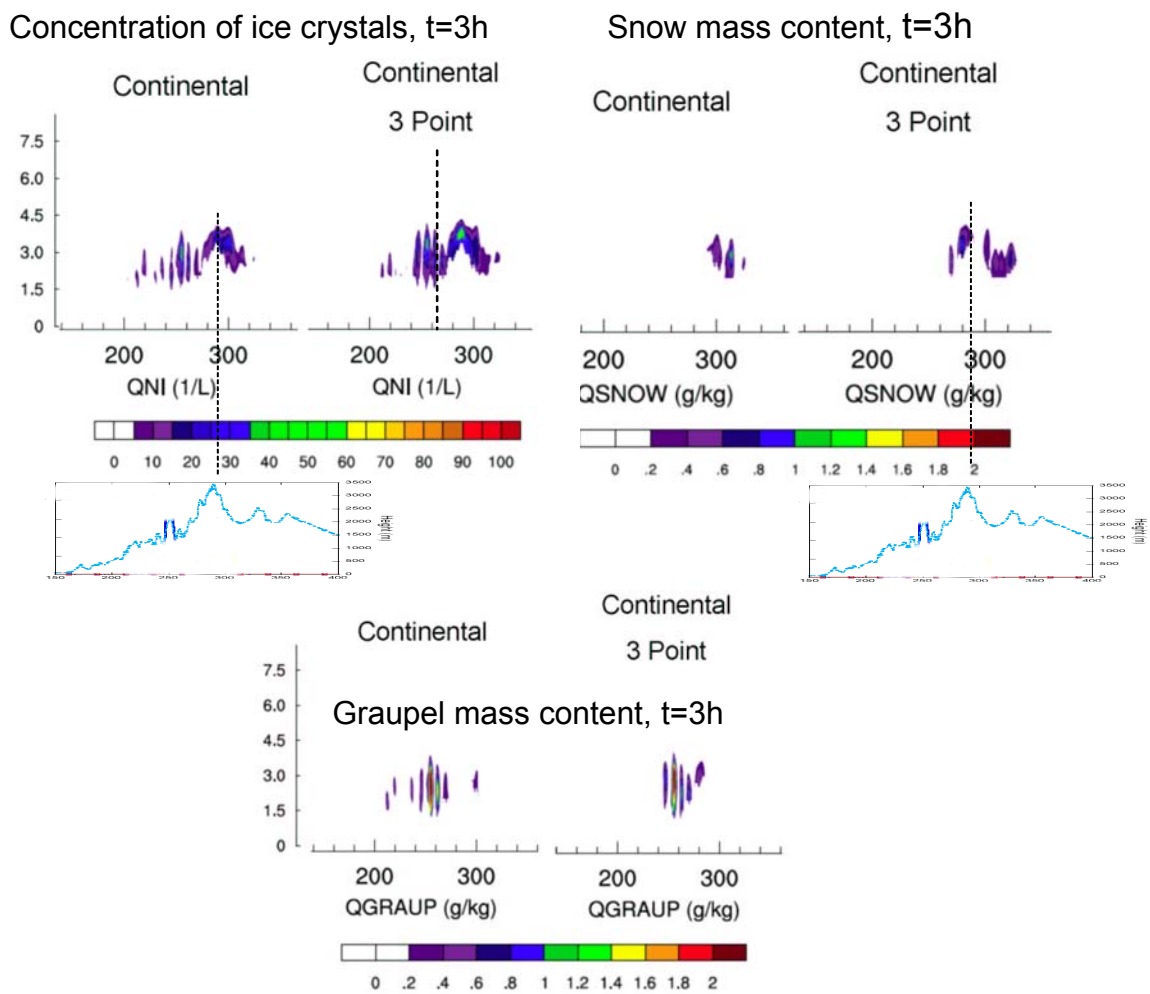

Figure 45. The same as Figure 44, but for ice hydrometeors

These effects are of crucial importance for revealing the fine effects of aerosols on precipitation. Figure 46 shows the accumulated rain amounts in M- and C-cases calculated using the old two-point and new three-point remapping schemes. One can see that the new scheme indicates a significant decrease in precipitation over the upwind slope in the case of high aerosol concentrations. At the same time, there was no effect in the case of low aerosol concentrations, because the new scheme cannot prevent the realistic formation of raindrops in the case of low aerosol (= low droplet) concentrations.

It should be stressed that this modification of the SBM scheme is novel. The strong necessity to develop such an accurate scheme became apparent when the research team started simulations of stratocumulus clouds, which require especially accurate schemes.

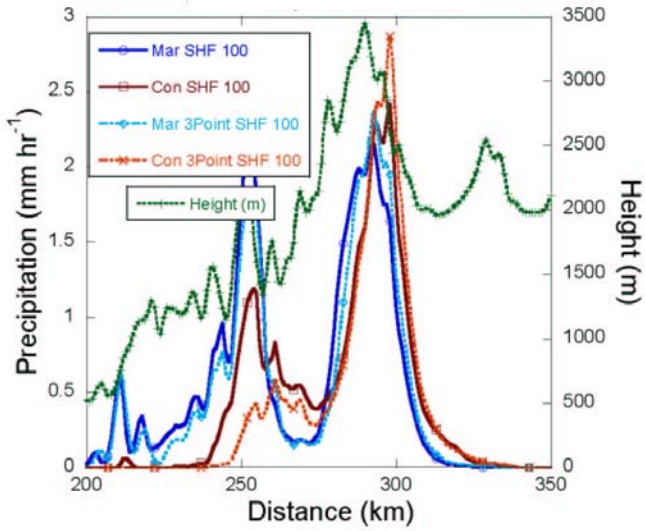

Figure 46. Spatial distributions of accumulated precipitation in M- and C-cases when the old (two-point) and new (three-point) schemes were used.

6.4.2. Results of Basic 2-D Simulations

The results obtained from the 2-D simulations are described in detail by Lynn et al. (2006) and presented in Appendix C, so they will be discussed only briefly here. Initially, two simulations were conducted, referred to here as Mar (maritime)-Control and Con (continental)-Control. They used the full-microphysics (liquid and ice processes). The differences in aerosol concentration led to important differences in the microphysics of the simulated orographic clouds. Figure 47 shows that maximum droplet concentration in Con-Control reached greater than 1000 cm^{-3}, while in Mar-Control the droplet concentration did not exceed 100 cm^{-3}. Figure 48 shows that Con-Control produced much more cloud LWC on the upwind slope, but less RWC than Mar-Control (Figure 49**)**. One can see that, in agreement with expectations, an increase in aerosol concentration leads to an increase in droplet concentration and LWC, but dramatically decreases the RWC.

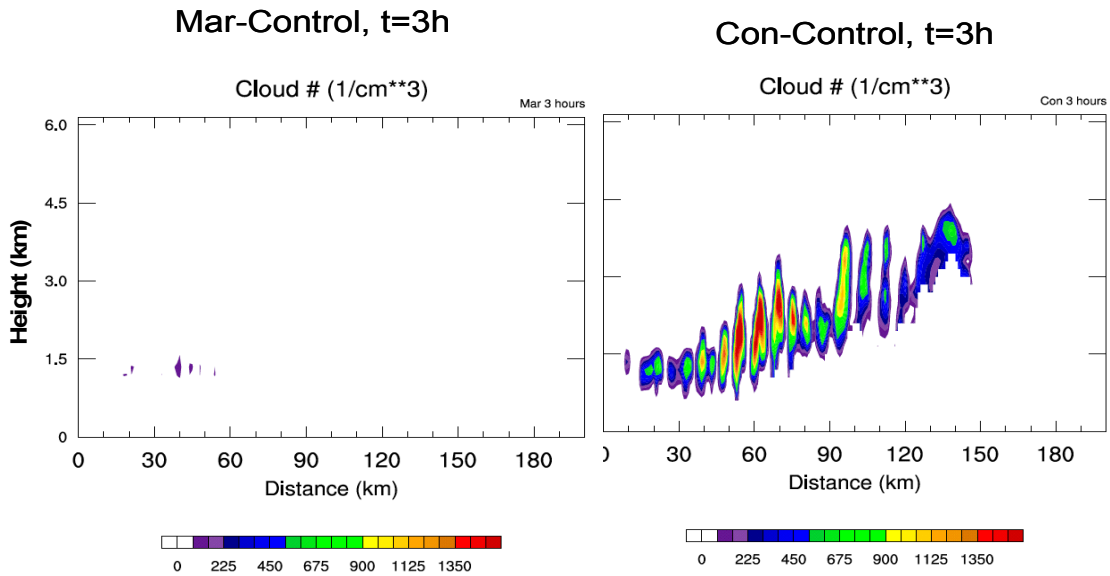

Figure 47. West-to-east cross-sections of cloud droplet concentrations simulated with MAR-Control (left) and Con-Control (right) at 3 hours

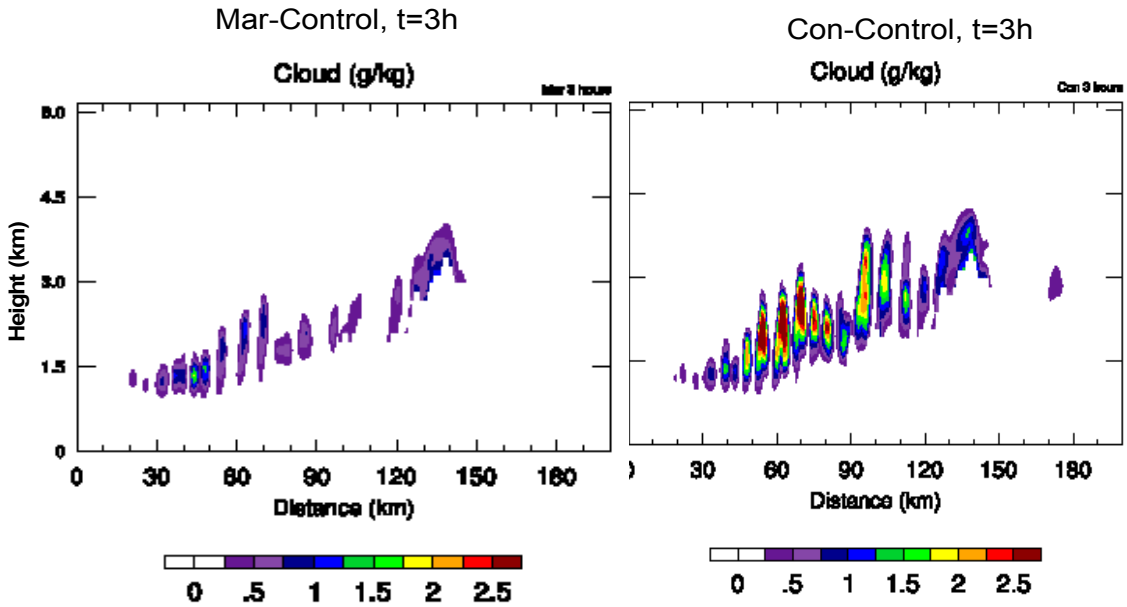

Figure 48. West-to-east cross-sections of CWC simulated with MAR-Control (left) and Con-Control (right) at 3 hours

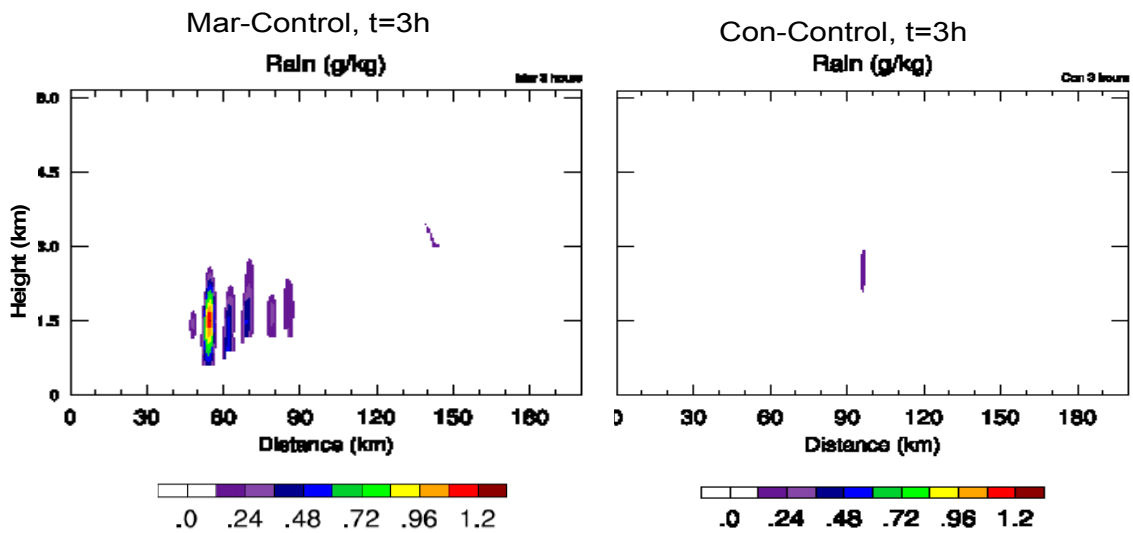

Figure 49. Same as Figure 48, but for rain water mass

The Con-Control produced more ice crystals (Figure 50) and snow (Figure 51) than Mar-Control, especially downwind on the mountain slope (and even beyond the highest peak).

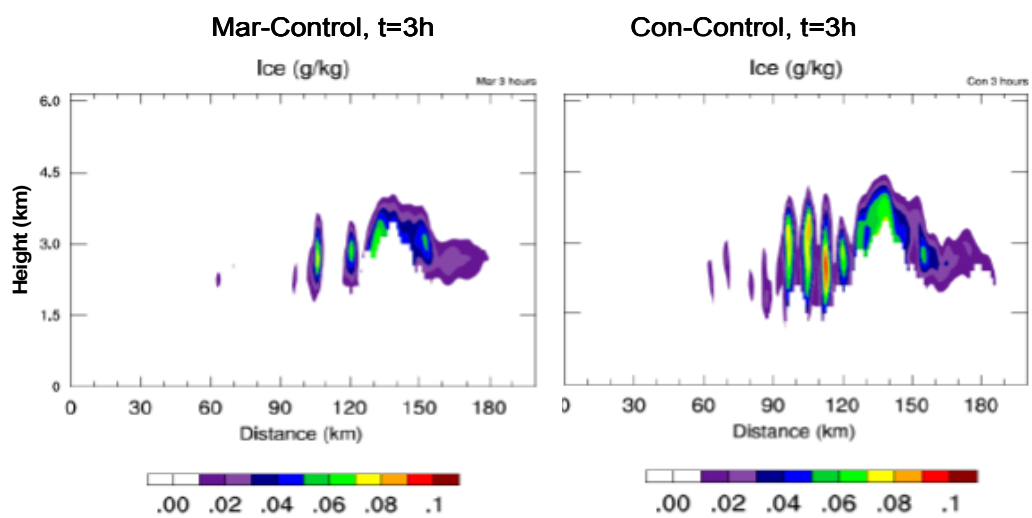

Figure 50. Same as Figure 48, but for ice crystal mass (dendrites, columns, and plates)

Figure 52 shows the accumulated precipitation from warm and cold cloud processes obtained from the Mar-Control and Con-Control for the three-hour simulation period. The figure shows that the maritime simulations produce more precipitation upwind (toward the western boundary, or sea) than the simulations with continental aerosols. In fact, the precipitation accumulated in the Mar-Control experiment began about 40 km upwind of the starting point

of accumulation in Con-Control. Also, the highest amount of precipitation in the Mar-Control experiment fell to just west of the highest peak, while in Con-Control the largest amount of precipitation fell downwind of the highest peak.

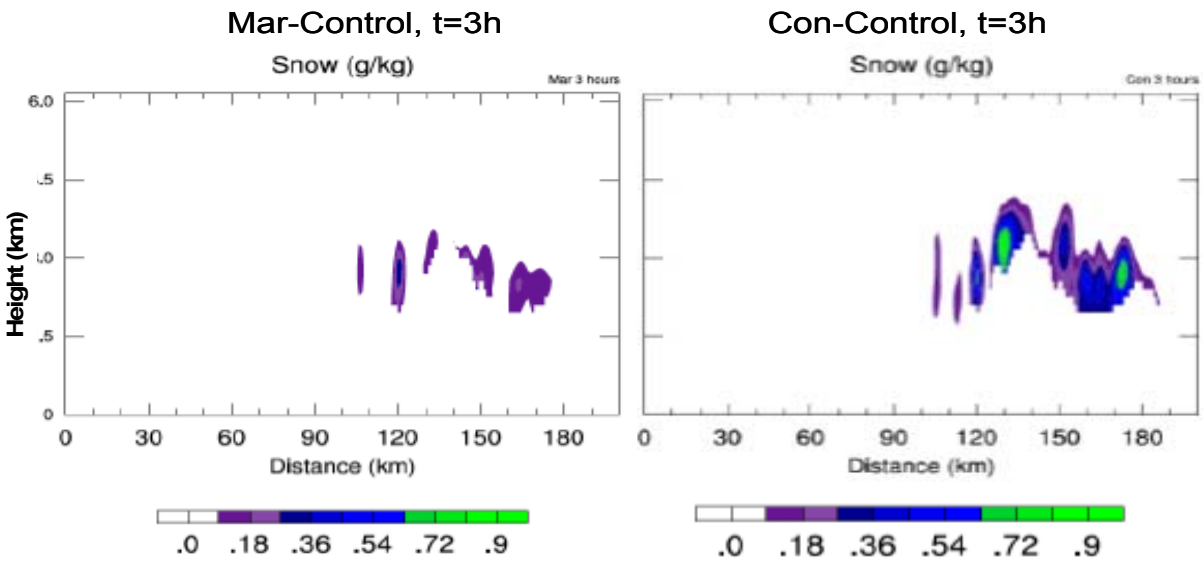

Figure 51. Same as Figure 48, but for snow mass

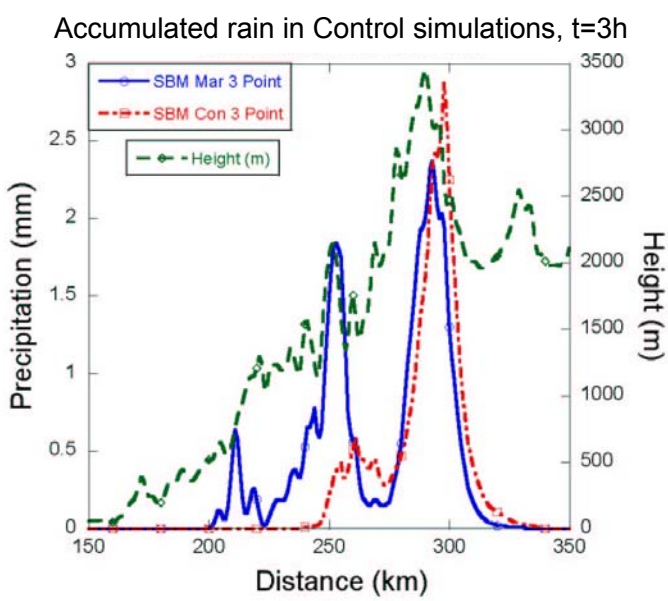

Figure 52. Accumulated precipitation on the mountain slope for three hours, for both Mar-Control and Con-Control The green line is the height of the terrain.

The first maximum in Mar-Control's precipitation peak occurred because of warm rain processes. The second maximum in the peak occurred mainly because of graupel. Ice crystals and snow induced the third maximum in the precipitation peak. In Con-Control, warm rain processes did not contribute to precipitation. Rather, the first maximum in the precipitation peak was formed by graupel, but the amount of graupel in Con-Control was apparently less than in Mar-Control. Both ice and snow processes led to the formation of the second maximum over the highest peak, which was somewhat larger than that obtained in Mar-Control. Note that for the third peak, there was sedimentation of crystals, graupel, and snow in downdrafts over the eastern side of the peak from stratocumulus-like clouds with the cloud base located at or near the surface. Further, the masses of snow and ice crystals in the Con-Control case are larger and advected farther eastwards than in the Mar-Control case; thus the precipitation peak is larger in the Con-Control case and is shifted farther downwind than in the Mar-Control case. As a result, at a distance of 150 km from the west edge of the cross section the precipitation in the Con-Control case is larger than in the Mar-Control case. The value of the excess is, however, significantly smaller than the deficit in the precipitation in the Con-Control case over the upwind slope. As a result, the accumulated precipitation in the Mar-Control case turns out to be larger than in the Con-Control case by about 30% (see Table 9), which corresponds well to the observations by Givati and Rosenfeld (2004) and Jirak and Cotton (2006).

The west-to-east cloud structure obtained in both simulations is punctuated by convective elements west of the highest topographical peak, with stratiform cloud over the peak and downwind. This type of cloud structure is similar to that observed and shown in Figure 37. Moreover, both simulations produced a sharp cutoff in precipitation amount and cloud mass downwind of the highest peak. Also, the Con-Control simulation produced many super-cooled droplets at cloud top, with most ice particles present in the maximum amount below this level (about 3 km). According to aircraft observations on the same type of day as these simulations, the cloud tops of smoky clouds contain a large amount of super-cooled droplets with a large amount of ice particles located below.

The difference in the accumulated rain is related to a higher precipitation loss in the Con-Control simulation. For instance, ice crystals and snow penetrating eastward to 180 km contribute to precipitation only slightly because of high evaporation within the range $150 \text{ km} < x < 180 \text{ km}$ along the east-west cross section, where relative humidity is low because of downdrafts leading to air heating. Thus, the important factor in the Con-Control simulation's accumulated precipitation decrease is the higher loss of precipitating mass by ice sublimation in the dry air farther eastward beyond the highest peak and over the downward slope. The loss of precipitating ice mass to sublimation also explains the higher loss of precipitating mass in clouds developing in smoky air by which aerosols can decrease precipitation from deep clouds (as discussed in detail by Khain et al. [2005]).

The fields of supercooled water and ice crystals and snow indicate that cloud tops in the Con-Control case are higher than in the Mar-Control case, so that aerosols invigorate the orographic clouds. This result corresponds to findings by Khain et al. (2004, 2005) and by Lynn et al. (2005a, 2005b) obtained in simulations of deep convective clouds, and it reflects the dynamical aerosol effects of aerosols. In the Con-Control case, droplets continue growing by diffusion leading to

higher latent heat release as compared to the Mar-Control case. The formation of larger amounts of ice also leads to higher latent heat releases, which leads to higher vertical updraft velocities in the Con-Control case, as compared to the Mar-Control case. Another reason for higher cloud tops in the Con-Control case is that both droplets and ice particles are smaller and, having lower sedimentation velocity, are able to ascend to higher levels than in the Mar-Control case.

6.4.3. Sensitivity Studies

Aerosol effects on precipitation are closely related to thermodynamic factors. Many sensitivity studies have been conducted to figure out this relationship and to understand better the physical mechanism of aerosol effects (see Appendix C for more detail). Sensitivity tests demonstrated the crucial importance of relative humidity. An increase in humidity leads to a decrease in the base-heights of all clouds (including those formed under high aerosol concentrations), leading to clouds resting on the mountain surfaces and precipitation. Moreover, the increase in air humidity decreases droplet evaporation and ice sublimation, which is especially important for the C-cases. Consequently, in cases of very high humidity the precipitation in the C-case turned out to be larger than that in the M-case (see Table 9).

Other variables had to be considered. Another factor of crucial importance is the wind speed. Weak horizontal winds lead to weak vertical velocities, and consequently, to very weak clouds. Ice processes increase the effects of aerosols on precipitation from orographic clouds. An increase in aerosol concentration leads to an increase in the formation of ice with small density and shifts the precipitation downwind. If the air humidity is relatively low, these ice particles evaporate rapidly, decreasing the precipitation in the C-cases. According to simulations and analytical estimations, heat fluxes from the surface are of the secondary importance (see Table 9).

Table 9. Accumulated precipitation (in mm) obtained up to the hour shown. The data were averaged from 150 to 350 km in the simulation domain.

Model run	Mar	Con
	3 hours	3 hours
Control runs	0.44	0.32
Surface Heating Function (SHF) 10 W m^{-2}	0.53	0.34
3/4 Wind	0.158	0.04
Relative Humidity (RH)=90%	3.62	3.78

6.5. Comparison of the SBM Results with Those from Bulk Parameterization

As was mentioned above, the results of simulations obtained using the MM5-SBM model have been compared to those obtained using the Risner2 parameterization, which is included into the MM5 model. A couple of years ago this parameterization was considered to be the best and the most sophisticated bulk–parameterization scheme available (see Lynn et al. 2005b). The model with this bulk parameterization was not able even to reproduce the cloud structure shown in Figure 37. Similar results about the abilities of this bulk parameterization scheme have been obtained by Lynn et al. (2005a) in simulations of a rain event in Florida accompanied by the formation of a squall line. This is the reason that the research team did not use this bulk parameterization in its later simulations.

At the same time, the research team has been collaborating with Dr. Greg Thompson, who actively worked on the improvement of his new bulk-parameterization scheme. Different versions of this scheme were successively tested using the MM5 model in simulations of both deep convection and stratocumulus clouds. The comparisons showed, as a rule, some new problems with the bulk scheme, so each new iteration required an improvement in the scheme. Recently, a final version of this scheme developed for use with the WRF was completed (Thompson et al. 2006). This was used in this study with parameters recommended by Dr. Thompson to simulate the effects of aerosols on orographic clouds. This new method incorporates a large number of improvements to both the physical processes and computer coding that are unique to it. For instance, the assumed snow size distribution depends on both ice water content and temperature and is represented as a sum of exponential and gamma distributions. The new snow treatment reduces ice supersaturation at high altitudes (low temperatures) and within deep glaciated clouds but enhances supercooled liquid water in shallow, relatively warm clouds. This aspect, combined with a rain size distribution intended to mimic classical and non-classical precipitation-formation mechanisms result in improved forecasts of freezing drizzle and aircraft icing.

The new bulk microphysical parameterizations (BMP) depart from other BMPs by assuming each hydrometeor species (except snow) conforms to a generalized gamma distribution. Moreover, the rain size distribution significantly shifts depending on whether the rain appears to originate from melted ice versus rain produced by collision/coalescence. Improvements have also been made to better simulate sedimentation. The scheme mimics the melting of snow in which the smallest flakes melt into small drops first, followed by the larger flakes. More realistic melting of snow implies that it will take longer for the overall melted snow mass to reach the ground. The new BMP graupel species also contains a variable intercept parameter in order to capture graupel-like snow and higher density (and faster falling) hail. The model is designed to mimic many processes currently only described using SBM type schemes. For instance, the new scheme uses a look-up table generated from 100 size bins of rain and snow. In the case of rain-collecting snow (and snow-collecting rain) the scheme transverses the snow size bins. If the mass of the water drop exceeds the mass of the snow particle, it is assumed that the two particles join as one, thus freezing the drop into graupel (hail in reality). If, on the other

hand, the water drop mass is less than the snow particle mass, the snow simply accretes the water drop, thus increasing the snow mass and decreasing the rain mass. The Thompson BMP also has a cloud number parameter (CNP; now referred to as Nt c) that can be set to simulate "maritime" or "continental" type clouds. Currently, one sets the CNP as a constant in space and time. The most immediate plan for the scheme is to include the prediction of cloud water and rain number concentrations. Cloud water will activate on an assumed aerosol distribution that, at minimum, will differentiate the continental versus maritime horizontal model points, as well as vary aerosol amounts in the vertical, based on points being within or above the boundary layer.

Figure 53 summarizes the results of the comparison of precipitation amount calculated by SBM and BMP for M- and C-cases. Parameters Nt_c are related to droplet concentration in clouds, which is prescribed depending on the expectations concerning aerosol concentration. While Nt_c = 25 cm^{-3} corresponds to maritime aerosols (maritime clouds), Nt_c = 300 cm^{-3} corresponds in this scheme to very continental (i.e., > 1,000 aerosol particles cm^{-3}) cases.

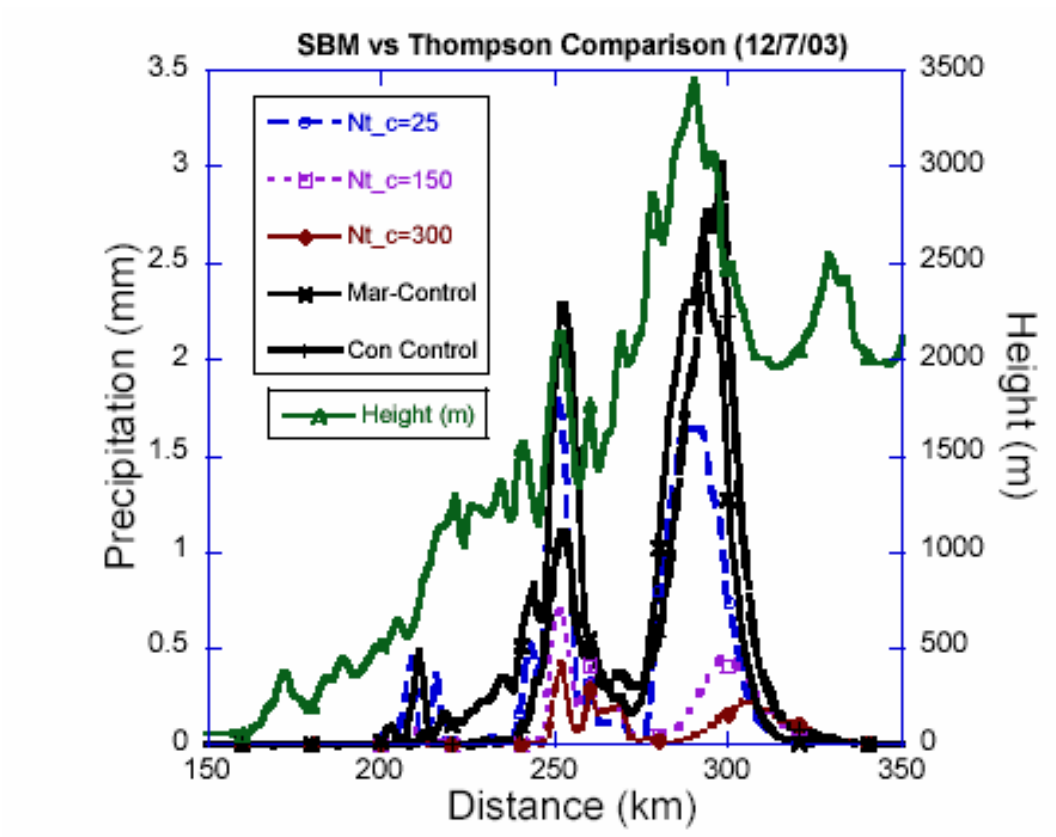

Figure 53. Accumulated precipitation in simulations with spectral bin microphysics and bulk microphysics parameterization developed by Thompson et al. (2006) The units for the Nt c values are cm^{-3}.

One can see that the BMP has the tendency to predict a dramatic decrease in precipitation under an increase in aerosol concentration. Overall, the BMP underestimates the precipitation amount, especially under continental conditions. Moreover, the WRF-BMP does not simulate the shift (downwind) in precipitation obtained with the WRF-SBM and found in observations. Analysis of hydrometeor fields indicates that the BMP simulates too little ice, snow, and graupel on the upwind slope. Thus, this BMP, which is considered the most advanced bulk-parameterization scheme in existence, is unable to respond to aerosol effects properly.

6.6. Discussion and Conclusions

During the course of the numerical component of the overall research effort, mesoscale models (MM5-SBM) and (WRF-SBM) have been developed and used (in 3-D and 2-D configurations, respectively) for investigation of the effect of aerosols on orographic clouds over the California Sierra Nevada Mountains downwind from the urban areas. The main uncertainty to be resolved by the study was whether the production of anthropogenic aerosols near the western coast of the United States can decrease precipitation over the mountain ridges downwind of the urban areas, as has been documented by Givati and Rosenfeld (2004, 2005) and by Rosenfeld and Givati (2006) using gauge and stream flow data. The simulations both with the 3-D and 2-D models definitely show that the answer is in the affirmative, namely, the *production of the anthropogenic aerosols and their incorporation into orographic clouds are the likely reason for the documented precipitation decreases.*

This model-based conclusion was strengthened observationally by Rosenfeld and Givati (2006) who provided evidence of orographic precipitation suppression by air pollution aerosols in the western United States (see Appendix D). The areas experiencing the greatest loss in orographic precipitation were those with the highest concentrations of fine (< 2.5 microns diameter) pollution aerosols. On the other hand, relatively pristine areas with no changes in orographic precipitation also were those areas having no systematic changes in the aerosols and small overall concentrations of fine pollution aerosols.

In the case study chosen for simulation (7 December 2003) the cloudiness of the orographic type was dominant. In this case, aerosols were shown to decrease the precipitation over the upwind mountain slopes by about 30% and shift it eastwards to the peak and to the downwind (eastern) slope of the mountains. Thus, some increase in snow precipitation occurs on the mountain peak and immediately downwind under high aerosol concentrations. However, the net effect of the aerosols is a decrease in the precipitation on the mountain range.

Detailed analysis performed using 2-D WRF-SBM showed that the mechanism of aerosol effects on precipitation is not as simple as was thought initially. It was found that the magnitude and even sign of precipitation change due to the aerosol effects depends on thermodynamic conditions, for instance, on air humidity. Because air humidity is different in different areas, the aerosol effects also should be different. For instance, the simulations predicted a precipitation increase in polluted urban areas such as Houston (Shepherd and Burian 2003) and Tokyo (Ohashi and Kida 2002) under conditions of high humidity in these areas.

Because air humidity can change during a month or even a day, the magnitude of aerosol effects can also change respectively. Actually, this result was found in the WRF-SBM simulations of a second California case study (2 March 2005) not reported here. The smallest effect of aerosols was noted during the morning hours, when the relative humidity was high, and the maximum aerosol effect (50% decrease in precipitation) was found in the afternoon, when the humidity reached its minimum value.

Supplemental simulations showed that the effect of aerosols on precipitation also depends on temperature, because temperature affects the type of precipitation (warm, graupel, or snow) as well as its spatial distribution. These precipitating particles have different sedimentation speeds and are transferred by a background wind to different distances. The results reported by Givati and Rosenfeld (2004, 2005) reflect a 50-year tendency of precipitation (in the 40 most recent years) and represent the averaged climatic features of California. In this context, it was fortunate that the simulations were of 7 December 2007, because this case represents typical climatic characteristics of the area.

Some comments concerning the "technical" aspect of the project are warranted. It should be stressed first of all that *the decision to use a more accurate (but time consuming) spectral bin microphysics model proved to be correct*. The existent bulk parameterizations are unable to describe the fine effects of aerosols. From the theoretical point of view this follows from the fact that aerosols affect the shape of the hydrometeor size distributions. Precipitation depends on the tail of these distributions (larger particles). It is impossible to describe aerosol effects accurately using only one moment (mass contents) or even two moments (mass and concentrations) of these distributions. In an attempt to be practical in terms of computer time , several bulk parameterization schemes were tested, including the very new ones, but they were unable to respond to the changes produced by the aerosols. Thus, had a bulk parameterization model been chosen as a numerical tool, the project would have been doomed to failure.

It also should be noted that the research team faced several technical and theoretical problems in the course of the project performance. First, the team had planned to use a 64 processor TC-cluster for the 3-D simulations. Unfortunately, the cluster did not work in the required configuration. This significantly limited this study's computational abilities for 3-D simulations. As a result, 3-D simulations with WRF–SBM model were not carried out.

Second, the research team did not expect that the widely used non-hydrostatic MM5 model would lose its accuracy at high-grid resolution. The team was forced to implement SBM into the novel WRF model, which allows utilization of very high grid resolution.

Third, the team had to improve the SBM scheme to eliminate artificial droplet spectrum broadening. The development of the new SBM scheme and its testing was carried out in parallel with the MM5-SBM simulations. The new scheme was used only at the stage when the WRF-SBM model was used. The authors suppose, therefore, that the aerosol effects on precipitation found in the 3-D MM5-SBM model are underestimated (in spite of the fact that this effect is quite obvious even when the previous SBM version was used).

Last, in the initial simulations of the second case study (March 2, 2005), there were certain times that the absolute humidity became negative, which is physically unrealistic. Detailed analysis showed that the problem was in the advection scheme of the WRF model. The correction of this model mistake took some time and slowed the analysis of the second case study's results. Note however, that the simulations did not reveal any new significant results as compared to the simulations of the first case. As was mentioned above, it was found that aerosol effects were different at different periods of day time, which is attributed to the effects of air humidity discussed in detail previously.

Despite these problems, the authors believe that *the main goals of this project's numerical section have been achieved successfully*. The aerosol effects were found to be a substantial factor that can decrease the precipitation from orographic clouds and spatially redistribute it on the mountain. The utilization of advanced SBM models has allowed us to evaluate the aerosol effects quantitatively. The results may be important for business planning (for example, agriculture). For instance, an increase in aerosol concentration leads to a decrease in warm precipitation over the mountain slope, but to an increase in snow precipitation over the mountain peak. The extra melted water during summertime might be an important factor.

The results are consistent with those of Jacobson (2004) and those of Jacobson and Kaufman (2006), who modeled the effects of aerosols on precipitation and wind, respectively. In the former paper, anthropogenic aerosol particles and their precursor gases (AAPPG) were modeled to reduce precipitation in the Sierra-Nevada Mountains and the Central Valley in February and August. Slight increases in precipitation in some locations beyond the mountains were also seen in both months, but the net effect was a precipitation reduction over land. Similarly, AAPPG were modeled to reduce precipitation in February and August over most of the SCAB grid, including in mountainous regions. Increases in precipitation occurred beyond the mountains in both months. Again, the net effect of particles was to reduce precipitation.

The simulation results also show the ways to find places where pronounced aerosol effects on precipitation can be expected. They provide the explanation of the differences (and even contradictions) between the results reported by different authors. A scientific paper detailing these simulation results has been submitted and accepted for publication in the *Journal of Geophysical Research*. It appears herein as Appendix C. Both reviewers of this report found these results to be novel and contributed significantly to the understanding of aerosol effects on clouds and precipitation.

To this end, the authors believe that the results can be used in choosing a strategy of cloud seeding for precipitation enhancement. For instance, glaciogenic seeding of orographic clouds over upwind slopes should lead to the increase and larger storage of ice precipitation on the mountain peak. These are related problems that can be addressed further during the course of future projects.

7.0 Overall Report Summary

The totality of the research effort by Woodley Weather Consultants (WWC) for the California Energy Commission to date has produced the following overall results:

- Strong evidence from aircraft and satellite platform observations suggest that cloud microstructures have been altered, the net orographic component of Sierra Nevada precipitation has been diminished and the resulting stream flows have been reduced in mountainous terrain, primarily downwind of major urban and industrial areas. These changes have been most pronounced since 1945 and continue to the present. Little change in cloud structures, precipitation, and stream flows have been noted in more pristine areas, especially over the northern Sierra.
- The above changes have been noted over much of the Western United States in ancillary studies conducted by the principal investigators.
- These changes apparently have been produced by the ingestion of fine (< 1 μm diameter) particles, acting as hygroscopic cloud condensation nuclei (CCN) produced in the urban/industrial areas, which make the clouds microphysically inefficient in the formation of precipitation-sized drops and ice particles.
- Model simulations support the relationship between the pollutants and the suppressed net precipitation and runoff.
- This study demonstrated that the apparent changes in cloud microphysical properties and precipitation as noted in the processed satellite imagery correspond to "real" changes in cloud structure, as documented by aircraft measurements.
- The documented changes in cloud properties are apparently due to anthropogenic pollutants generated locally in California.
- The ancillary SUPRECIP-1 and SUPRECIP-2 field efforts that made use of aircraft cloud physics aircraft to make measurements of cloud properties under polluted and non-polluted conditions were crucial to establishing a direct link between the pollution aerosols and altered cloud properties, making the overall linkages between pollution and decreased mountain precipitation much more credible.

Although the results from the initial year of the ancillary SUPRECIP effort (SUPRECIP-1) supported the view that pollution is suppressing California orographic precipitation, further investigation was needed, because it was impossible to characterize the problem in only a five-week measurement program. SUPRECIP was continued for a second year as SUPRECIP-2 in order to focus on the orographic storm events in the Sierra Nevada that were lacking in 2005. Specifically, it was crucial to document the ingestion of the pollution aerosols by the orographic clouds as they formed and moved uphill. The satellite imagery already indicates that this is taking place and the precipitation and stream flow measurements show the long-term effects of the pollution. It was nearly impossible in 2005 to systematically "map" the pollution aerosols at low to mid levels in urban and downwind areas with the Cheyenne II cloud physics aircraft while it was in instrument flight rules (IFR) flight. Because of this, a second aircraft (a Cessna

340 II) was used in SUPRECIP 2 to carry cloud nucleus (CN) and cloud condensation nuclei (CCN) counters for the mapping of the aerosols during visual flight rules (VFR) flight. More attention was focused on the details of the pollution "footprint" as to the sources, kinds, and concentrations of the pollution aerosols and on what portions of the Sierra should be most affected by them. With this plan the Cessna 340 low-level aircraft mapped the pollution aerosols upwind of the coast, over the urban/industrial areas and downwind while the Cheyenne II cloud physics aircraft flew above to document their effects on the clouds ingesting them. The results from this program buttressed the overall results presented in this final report.

The issues addressed by this research effort are at the cutting edge of societal concerns. It appears that aerosols have been having an effect in California and in regions with a similar climate and topography (such as Israel, Australia, South Africa, and others) over at least the last 50 years due to the suppressive effect of pollution on precipitation. In California, such changes, if validated by further research, would mean diminished water resources, less hydroelectric power, and a degraded environment.

8.0 References

Allan, R. J., N. Nicholls, P. D. Jones, and I. J Butterworth. 1991: "A further extension of the Tahiti-Darwin SOI, early SOI results and Darwin pressure." *J. Climate* 4: 743–749.

Albrecht, B. S. 1989: "Aerosols, cloud microphysics and fractional cloudiness." *Science* 245: 1227.

Alpert, P., and H. Shafir. 1991: "On the role of the wind vector interaction with high-resolution topography in orographic rainfall modeling." *Quart. J.R. Meteor. Soc*. 117: 421–426.

Andreae, M. O., D. Rosenfeld, P. Artaxo, A. A. Costa, G. P. Frank, K. M. Longo, and M. A. F. Silva-Dias. 2004: "Smoking rain clouds over the Amazon." *Science* 303: 1337–1342.

Borys, R. D., D. H. Lowenthal, S. A. Cohn, and W. O. J. Brown. 2003: "Mountain and radar measurements of anthropogenic aerosol effects on snow growth and snowfall rate." *Geophys. Res. Lett.* 30(10): 1538, doi: 10.1029 /2002GL016855.

Braham, Roscoe R., Jr. 1981: "Summary of urban effects on clouds and rain." *Meteorological Monographs* 18(40): 141–152.

Cerveny, R. S., and R. C. Balling Jr. 1998: Weekly cycles of air pollutants, precipitation and tropical in the coastal NW Atlantic region (Letter to Nature). *Nature* 394, 6693: 561–563.

Changnon, S. A. 1979: "Rainfall changes in summer caused by St. Louis." *Science* 205: 402–404.

Changnon, S. A., R. T. Shealy, and R. W. Scott. 1991: "Precipitation changes in fall, winter, and spring caused by St. Louis." *J. Appl. Meteor*. 30: 126–134.

Coakley, J. A., Jr., R. L. Bernstein, and P. A. Durkee. 1987: "Effect of ship-stack effluents on cloud reflectivity." *Science* 237(4818): 1020–1022.

Dettinger, M., K. Redmond, and D. Cayan. 2004: "Winter Orographic Precipitation Ratios in the Sierra Nevada – Large-Scale Atmospheric Circulations and Hydrologic Consequences." *J. Hydromet.* 5: 1102–1116.

Dusek, U., G. P. Frank, L. Hildebrandt, J. Curtius, J. Schneider, S. Walter, D. Chand, F. Drewnick, S. Hings, D. Jung, S. Borrmann, and M. O.Andreae. 2006. "Size matters more than chemistry for cloud nucleating ability of aerosol particles." *Science* 312: 1375–1378.

Duus, A. L. 1992: "Estimation and analysis of snow cover in the Snowy Mountains between 1910 and 1991." *Aust. Meteorol. Mag.* 40: 195.

Eagen, R. C., P. V. Hobbs, and L. F. Radke. 1974: Particle emissions from a large Kraft paper mill and their effects on the microstructure of warm clouds. *Journal of Applied Meteorology* 13(5): 535–552.

Gatz, Donald F. 1979: "Investigation of pollutant source strength rainfall relationships at St. Louis." *Journal of Applied Meteorology* 18(10): 1245–1251.

Givati, A., and D. Rosenfeld. 2004: "Quantifying precipitation suppression due to air pollution." *Journal of Applied Meteorology* 43: 1038–1056.

Givati, A., and D. Rosenfeld. 2005: "Separation between Cloud Seeding and Air Pollution Effects." *Journal of Applied Meteorology* 44: 1298–1314.

Griffith, D. A., M. E. Solak, and D. P. Yorty. 2005: "Is air pollution impacting winter orographic precipitation in Utah? Weather modification association." *J. Wea. Modif.* 37: 14–20.

Gunn, R., and B. B. Phillips. 1957: "An experimental investigation of the effect of air pollution on the initiation of rain." *J. Meteor*. 14; 272–280.

Hallett, J., and S. C. Mossop. 1974: "Production of secondary ice crystals during the riming process." *Nature* 249: 26–28.

Harasymiw, B., and J. McGee. 1993: *Snowy precipitation enhancement project: A proposal to evaluate feasibility of increasing snow precipitation over the Snowy Mountains area. Appendix B.* Snowy Mountains Hydroelectric Authority, Cooma NSW, Australia.

Hobbs P. V., and L. F. Radke. 1969: "Cloud condensation nuclei from a simulated forest fire." *Science* 163, 279–280.

Jacobson, M. Z. 2004. *Effects of Anthropogenic Aerosol Particles and their Precursor Gases on California and South Coast Climate. California Energy Commission.* PIER Energy-Related Environmental Research. CEC-500-2005-003.

Jacobson, M. Z., and Y. J. Kaufman. 2006: "Wind reduction by aerosol particles." *Geophysical Research Letters* 33, L24814, doi:10.1029/2006GL027838.

Jauregui, E., and E. Romales. 1996: "Urban effects on convective precipitation in Mexico City." *Atmos. Environ.* 30: 3383–3389.

Jirak, I. L., and W. R. Cotton. 2006: "Effect of air pollution on precipitation along the Front Range of the Rocky Mountains." *J. Appl. Meteor.* 45: 236–245.

Johnson, D. B. 1982: "Role of giant and ultragiant aerosol particles in warm rain initiation." *Journal of the Atmospheric Sciences* 39(2): 448–460.

Jonas, P. R., and B. J. Mason. 1974: "Evolution of droplet spectra by condensation and coalescence in cumulus clouds." *Quarterly Journal of the Royal Meteorological Society* 100(425): 286–295.

Kaufman, Y. J., and R. S. Fraser. 1997: "The effect of smoke particles on clouds and climate forcing." *Science* 277: 1636–1639.

Kaufman, Y. J., I. Koren, L. A. Remer, D. Rosenfeld, Y. Rudich. 2005: "Smoke, Dust and Pollution Aerosol Clouding the Atlantic Atmosphere." *Proceedings of the National Academy of Sciences* 102: 11207–11212.

Khain, A. P., and I. Sednev. 1996: "Simulation of precipitation formation in the Eastern Mediterranean coastal zone using a spectral microphysics cloud ensemble model." *Atmospheric Research* 43: 77–110.

Khain, A. P., A. Pokrovsky, and I. Sednev. 1999: "Effects of cloud-aerosol interaction on cloud microphysics, precipitation formation and size distribution of atmospheric aerosol particles: Numerical experiments with a spectral microphysics cloud model." *Atmos. Res.* 52: 195–220.

Khain, A. P., M. Ovtchinnikov, M. Pinsky, A. Pokrovsky, and H. Krugliak. 2000: "Notes on the state-of-the-art numerical modeling of cloud microphysics." *Atmos. Res.* 55: 159–224.

Khain A. P., D. Rosenfeld, and A. Pokrovsky. 2001: "Simulation of deep convective clouds with sustained supercooled liquid water down to -37.5°C using a spectral microphysics model. *Geophysical Research Letters* 3887–3890.

Khain A., A. Pokrovsky and M. Pinsky, A. Seifert, and V. Phillips. 2004: "Effects of atmospheric aerosols on deep convective clouds as seen from simulations using a spectral microphysics mixed-phase cumulus cloud model Part 1: Model description." *J. Atmos. Sci* 61: 2963–2982.

Khain A., and A. Pokrovsky. 2004: "Effects of atmospheric aerosols on deep convective clouds as seen from simulations using a spectral microphysics mixed-phase cumulus cloud model Part 2: Sensitivity study." *J. Atmos. Sci.* 61: 2983–3001.

Khain, A., D. Rosenfeld, and A. Pokrovsky. 2005: "Aerosol impact on the dynamics and microphysics of convective clouds." *The Quarterly Journal of the Royal Meteorological Society* 131: 1–25.

Khain A., N. Benmoshe, and A. Pokrovsky. 2006: "Simulation of deep clouds with warm cloud base using spectral (bin) microphysics." *J. Atmos. Sci.* (in revision).

Koren, I., Y. J. Kaufman, L. A. Remer, and J. V. Martins. 2004. "Measurement of the effect of Amazon smoke on inhibition of cloud formation." *Science* 303: 1342–1345.

Kovetz, A., and B. Olund. 1969: "The effect of coalescence and condensation on rain formation in a cloud of finite vertical extent." *J. Atmos. Sci.* 26: 1060–1065.

Lammel, G., and T. Novakov. 1995: "Water nucleation properties of carbon black and diesel soot particles." *Atmos. Environ.* 29: 813–823.

Lensky I. M., and D. Rosenfeld. 1997: "Estimation of precipitation area and rain intensity based on the microphisical properties retrieved from NOAA AVHRR data." *Journal of Applied Meteorology* 36: 234–242.

Levin, Z., E. Ganor, V. Gladstein. 1996: "The Effects of Desert Particles Coated with Sulfate on Rain Formation in the Eastern Mediterranean." *J. Appl. Meteor*. 35: 1511–1523.

Lowenthal, D. H , B. Zielnska, J. C. Chow, J. G. Watson, M. Gautam, D. H. Ferguson, G. R. Neuroth, and K. D. Stevens. 1994: "Characterization of heavy-duty diesel vehicle emissions." *Atmos. Environ.* 28: 731–743.

Lynn, B. H., A. P. Khain, J. Dudhia, A. Pokrovsky, D. Rosenfeld, and A. Seifert. 2005: "Simulating a CaPe Convective Squall Line Using MM5 Coupled with Spectral (Bin) Microphysics. Part 1. Model Description and Preliminary Results." *Monthly Weather Review* 133: 44–58.

Lynn, B., A. Khain, J. Dudhia, D. Rosenfeld, A. Pokrovsky, and A. Seifert. 2005: Spectral (bin) microphysics coupled with a mesoscale model (MM5). Part 2: Simulation of a CaPe rain event with squall line. *Mon. Wea. Rev.* 133: 59–71.

Lynn, B., A. Khain, D. Rosenfeld, and W. L. Woodley. 2006: "Effects of aerosols on precipitation from orographic clouds." *Journal of Geophysical Research* In press.

Mantua, N. J., S. R. Hare, Y. Zhang, J. M. Wallace, and R. C. Francis. 1997: A Pacific interdecadal climate oscillation with impacts on salmon production. *Bull. Amer. Meteor. Soc*. 78: 1069–1079.

Maricq, M. M., R. E. Chase, D. H. Podsiadlik, and R. Vogt. 1999: "Vehicle Exhaust Particle Size Distributions: A Comparison of Tailpipe and Dilution Tunnel Measurements." SAE Paper No. 1999-01-1461, *Society of Automotive Engineers*, Warrendale, Pennsylvania.

Mazin, I. P., and S. M. Shmeter. 1983: *Clouds, their structure and formation*. Leningrad: Gidrometeoizdat. 279p.

Mossop, S. C., and J. Hallett. 1974: "Ice crystal concentration in cumulus clouds: Influence of the drop spectrum. *Science* 186(4164): 632–634.

Novakov, T., V. Ramanathan, J. E. Hansen, T. W. Kirchstetter, M. Sato, J. E. Sinton, and J. A. Sathaye. 2003: "Large historical changes of fossil-fuel black carbon aerosols." *Geophys. Res. Lett.* 30(6): 1324, doi:10.1029/2002GL016345.

Ohashi, Y., and H. Kida. 2002: "Local Circulations Developed in the Vicinity of Both Coastal and Inland Urban Areas: A Numerical Study with a Mesoscale Atmospheric Model." J. Appl. Meteorol 41: 30–45.

Oki, R., K. Furukawa, S. Shimizu, Y. Suzuki, S. Saton, H. Hanado, K. Okamoto, and K. Nakamura. 1999: "Preliminary Results of TRMM: Part 1, A Comparison of PR with Ground Observations." *Marine Technology Society Journal* 32(4): 13.

Pierson, W. R., and W. W. Brachaczek. 1983: "Particulate Matter Associated with Vehicles on the Road II." *Aerosol Sci. Technol*. 2: 1–40.

Phillips V., A. Khain, and A. Pokrovsky. 2007: "The Influence of Melting on the Dynamics and Precipitation Production in Maritime and Continental Storm-Clouds." *J. Atmos. Sci.* 64 (2): 338–359.

Pruppacher, H. R., and J. D. Klett. 1997: *Microphysics of clouds and precipitation.* 2nd edition, Oxford Press. 914 p.

Radke, L. F., J. A. Coakley, and M. D. King. 1989: "Direct and remote sensing observations of the effects of ships on clouds." *Science* 246: 1146–1149.

Ramanathan, V., P. Crutzen, J. Kiehl, and D. Rosenfeld. 2001: "Aerosols, Climate, and the Hydrological Cycle." *Science* 294: 2119–2124.

Rangno, A., and P. V. Hobbs. 1994: "Ice particle concentrations and precipitation development in small continental cumuliform clouds." *Quarterly Journal of the Royal Meteorological Society* 120(517): 573–601.

Ropelewski, C. F., and P. D. Jones. 1987: "An extension of the Tahiti-Darwin Southern Oscillation Index." *Monthly Weather Review* 115: 2161–2165.

Rosenfeld, D., and G. Gutman. 1994: "Retrieving microphysical properties near the tops of potential rain clouds by multispectral analysis of AVHRR data." *J. Atmos. Res.* 34: 259–283.

Rosenfeld, D., and I. Lensky. 1998: Spaceborne sensed insights into precipitation formation processes in continental and maritime clouds. *Bulletin of the American Meteorological Society* 79 (11): 2457–2476.

Rosenfeld, D. 1999: "TRMM observed first direct evidence of smoke from forest fires inhibiting rainfall." *Geophys. Res. Lett*. 26: 3105–3108.

Rosenfeld, D. 2000: "Suppression of rain and snow by urban air pollution." *Science* 287: 1793–1796.

Rosenfeld, D., and W. L. Woodley. 2000: "Deep Convective Clouds with Sustained Supercooled Liquid Water Down to -37.5°C." *Nature* 405: 440–442.

Rosenfeld D., R. Lahav, A. P. Khain, and M. Pinsky. 2002: "The role of sea-spray in cleansing air pollution over ocean via cloud processes." *Science* 297: 1667–1670.

Rosenfeld, D., and W. L. Woodley. 2003: Closing the 50-year circle: From cloud seeding to space and back to climate change through precipitation physics. Chapter 6 of *Cloud Systems, Hurricanes, and the Tropical Rainfall Measuring Mission (TRMM)* edited by Drs. Wei-Kuo Tao and Robert Adler. Meteorological Monographs. American Meteorological Society. p. 59–80.

Rosenfeld, D., I. M. Lensky, J. Peterson, and A. Gingis. 2006: "Potential impacts of air pollution aerosols on precipitation in Australia." *Clean Air and Environmental Quality* 40(2): 43–49.

Rosenfeld D. 2006: Aerosols Suppressing Precipitation in the Sierra Nevada: Results of the 2006 Winter Field Campaign. Presented at the *Third Climate Change Research Conference.* California Energy Commission. Sacramento, California, 13–15 September 2006. Presentation available at

www.climatechange.ca.gov/events/2006_conference/presentations/2006-09-14/2006-09-14_ROSENFELD.PDF.

Rosenfeld, D., and A. Givati. 2006: "Evidence of orographic precipitation suppression by air pollution induced aerosols in the western U.S." *J. Applied Meteorology and Climatology* 45: 893–911.

Skamarock, W., J. B. Klemp, J. Dudhia, D. O. Gill, D. M. Barker, W. Wang, and J. G. Powers. 2005: A description of the Advanced Research WRF Version 2. NCAR Technical Note. Mesoscale and Microscale Meteorology Division, NCAR. Boulder, Colorado. June.

Shepherd, J. M., H. Pierce, and A. J. Negri. 2002: "Rainfall modification by major urban areas: Observations from spaceborne rain radar on the TRMM satellite." *J. Appl. Metor*. 41: 689–701.

Shepherd, J. M., and S. J. Burian. 2003: "Detection of urban-induced rainfall anomalies in a major coastal city." *Earth Interactions* 7: 1–14.

Squires, P. 1958: "The microstructure and colloidal stability of warm clouds." *Tellus* 10: 256–271.

Takemoto, B. K., B. E. Croes, S. M. Brown, N. Motallebi, F. D. Westerdahl, H. G. Margolis, B. T. Cahill, M. D. Mueller, and J. R. Holmes. 1995: "Acidic deposition in California: Findings from a program of monitoring and effects research." *Water, Air & Soil Pollution* 85: 261–272.

Thompson, G., P. R. Field, W. D. Hall, and R. Rasmussen. 2006: "A new bulk microphysical parameterization for WRF (& MM5)." Presented at WRF conference, June 2006.

TRMM. 1997: TRMM (Tropical Rainfall Measuring Mission) was launched on 28 November 1997 as a cooperative project of the National Aeronautics and Space and Administration (NASA) and the National Space Development Agency of Japan (NASDA). The TRMM data are available at http://daac.gsfc.nasa.gov/CAMPAIGN_DOCS/hydrology/hd_trmm_intro.html.

Warner, J. 1968: "A reduction in rainfall associated with smoke from sugar cane fires—an inadvertent weather modification?" *J. Appl. Meteor.* 7: 247.

Weingartner, E., H. Burtscher, and U. Baltensperger. 1997: "Hygroscopic properties of carbon and diesel soot particles." *Atmos. Environ.* 31: 2311–2327.

Williams, D. J., J. W. Milne, S. M. Quigley, D. B. Roberts. 1989: "Particulate-emissions from in-use motor vehicles." *Atmos. Environ.* 23: 2647–2661.

Woodley Weather Consultants. 2005. *The Use of a Cloud Physics Aircraft for the Mapping of Pollution Aerosols Detrimental to Winter Orographic Precipitation over the California Sierra Nevada.* California Energy Commission, PIER Energy-Related Environmental Research. CEC-500-2005-205.

Zhang, Y., J. M. Wallace, and D. S. Battisti. 1997: "ENSO-like interdecadal variability: 1900–93." *J. Climate* 10: 1004–1020.

9.0 Glossary

AVHRR	Advanced very high resolution radiometer onboard NOAA satellites
BMP	bulk microphysical parameterizations
CALIPSO	Cloud-Aerosol Lidar and Infrared Pathfinder Satellite Observation satellite
CCN	cloud condensation nuclei
CDP	cloud droplet probe
CIP	cloud imaging probe
cm	centimeter
cm^{-3}	cubic centimeter
CN	cloud nucleus
CNP	cloud number parameter
CWC	cloud water content
dBZ	The radar precipitation reflectivity [mm^6m^{-3}] measured in decibels
D_L	Modal liquid water diameter. The droplet diameter corresponding to the modal liquid water content measured by the CDP during a cloud pass
DMA	dual mobility analyzer
DSD	droplet size distributions
GHz	gigahertz
HUCM	Hebrew University Cloud Model from the Hebrew University of Jerusalem
IFR	instrument flight rules
IMPROVE	Interagency Monitoring of Protected Visual Environments
IN	ice nuclei
IR	infrared
kg	kilogram
kg hr^{-1}	kilograms per hour
LST	local sidereal time
LWC	liquid water content
m	meter

mb	millibar
mm	millimeter
m s^{-1}	meters per second
NOAA	National Oceanographic and Atmospheric Administration
PDO	Pacific Decadal Oscillation
PIER	Public Interest Energy Research Program
PR	precipitation radar
r_e	The effective radius ($r_e = \langle r^3 \rangle / \langle r^2 \rangle$), where r is the radius of the cloud droplets in the measurement volume
Ro	The orographic enhancement factor, defined as the ratio of precipitation in a hill or mountainous region to the precipitation in plains or valley locations upwind
RWC	rainwater contents
SBM	spectral (bin) microphysics
SOI	Southern Oscillation Index
SUPRECIP	Suppression of Precipitation Program Experiment
T	temperature
TMI	TRMM (passive) Microwave Imager
TRMM	Refers to the orbiting satellite of the Tropical Rain Measuring Mission
μ	micron
μm	micrometer
UT	Universal Time, which is the same as Greenwich Mean Time
VFR	visual flight rules
VIRS	Visible and Infra Red Sensor onboard TRMM satellite
WRF	Weather Research Forecast model
WWC	Woodley Weather Consultants

Appendix A

The Satellite Methodology Used in the Research Effort

APPENDIX A

THE SATELLITE METHODOLOGY USED IN THE RESEARCH EFFORT

Background

The method of Rosenfeld and Lensky (1998) makes use of AVHRR multi-spectral data from polar orbiting satellites to infer the evolution of convective cloud particles and precipitation at various heights within the clouds. The method can be applied also to orographic clouds such as those occurring in California during the winter season in order to determine whether pollution is affecting these clouds. The very high resolution (that is, 1 kilometer [km]) of the AVHRR imagery provided by the polar-orbiting NOAA-14 and NOAA-16 satellites will even make it possible to bring the focus down to specific areas of interest in California. That this can be done is demonstrated by Rosenfeld and Lensky (1998) and Rosenfeld (1999) for forest fires in Indonesia and by Rosenfeld (2000) for individual pollution sources in southeastern Australia.

How the Method Works

The method to deduce the microphysical structure of clouds from space makes use of data from the Advanced Very High Resolution Radiometer (AVHRR) onboard the National Aeronautic and Atmospheric Administration (NOAA) operational weather satellites, which provide sub-satellite 1.1 km data in five channels centered at 0.65, 0.9, 3.7. 10.8, and 12.0 micrometers (μm). The visible wave band (0.65 μm) is used to select points with visibly bright clouds for the analyses. The thermal infrared (0.9 μm) is used to obtain cloud-top temperatures. Cloud-top particle size is inferred from the solar radiation component of the 3.7-micron wave band.

In making the inferences of cloud microphysical structure, the effective radius (r_e) of fully cloudy pixels is retrieved in the manner described by Rosenfeld and Gutman (1994) and Lensky and Rosenfeld (1997). This is done by inverting a radiative transfer model developed by Nakajima and King (1990) using the solar reflectance component of the 3.7 μm channel and the viewing geometry as inputs. Retrieval of particle size at cloud top is based on the fact that water absorbs part of the solar radiation at the 3.7 μm wave band. While the back-scattered solar radiation is determined mainly by the surface area of the particles, the amount of absorption is determined by the volume of the particles. Therefore, larger particles absorb more and reflect less, so clouds that are made of larger droplets are seen darker in the reflected 3.7 μm radiation.

Knowing the energy radiated from the sun and the portion of that energy reflected back to the satellite sensor, the fraction of the solar energy absorbed can be retrieved. This provides the basis for calculating the ratio between the integral volume and integral surface area of cloud particles in the satellite measurement volume. Conventionally, this ratio has been defined as the *particle effective radius*, r_e.

The initial research suggests that a r_e of 14 μm is a threshold value above which clouds contain precipitation-size particles that can be detected by weather radar (Rosenfeld and Gutman 1994). The maximum value of r_e that can be retrieved by this method is 30 μm.

The evolution of r_e as a function of cloud-top height or temperature (T) of growing convective elements can reveal the microphysical evolution of the clouds as they grow vertically and undergo the various microphysical process that lead to the formation of precipitation. However, the satellites carrying high-resolution AVHRR sensors typically provide only a twice-daily snapshot image of a specific portion of the earth. Thus, a single cloud cannot be viewed continuously in the imagery. This difficulty is overcome by observing an area containing a convective cloud cluster composed of cloud elements at various stages of vertical growth. This allows compositing of the r_e calculations for many clouds as if they represented a single cloud at different times in its lifetime.

The actual composite is done in the following steps:

1. Define a window, typically of several thousand pixels, encompassing convective cloud clusters with growing elements at various stages of development.
2. Calculate the median and other percentiles of the r_e for pixels within each 1°C interval of cloud top T.
3. Display graphically the T versus r_e curves of the 10th, 25th, 50th, 75th, and 90th percentiles.
4. Analyze the shape of the median (50th percentile) to find the microphysical zones as discussed below.

The shape of the T versus r_e diagrams contain much information on the microphysical processes in the clouds. It is known that droplets grow by diffusion a small distance above the base of convective clouds, while higher up in the clouds the hydrometeor growth rate is often accelerated by coalescence and ice processes. Because nearly all cloud droplets are nucleated at cloud base and cloud water-mass increases less than linearly with depth, it is found that the r_e in clouds with mostly diffusional growth increases by a power law of less than $D^{1/3}$, where D is depth above cloud base. D can be approximated using Tb-T, where T and Tb are cloud top and base temperatures, respectively. It can then be seen that r_e is proportional to $(Tb-T)^{1/3}$ and a plot of r_e versus temperature will look like an upward convexed curve. Therefore, a deviation from such a curve (that is, an upward concave curve) indicates the existence of amplification mechanisms for the cloud-particle growth rate, such as coalescence and ice formation processes, which lead ultimately to precipitation.

Based on about a hundred analyzed cases well distributed over the globe, the evolution of convective cloud-top particles as a function of depth above cloud base and cloud-top temperature can be characterized into five distinct vertical zones, not all necessarily appearing in a given cloud system:

1. *Diffusional droplet growth zone:* Very slow growth of cloud droplets with depth above cloud base, indicated by shallow slope of dr_e/dT.

2. *Droplet coalescence growth zone:* Large increase of the droplet growth rate dr_e/dT at $T > 0^oC$, indicating rapid growth of the cloud droplets with depth above cloud base. This can only occur by drop coalescence.
3. *Rainout zone:* A zone where r_e remains stable at about 20 μm, probably determined by the maximum drop size that can be sustained by rising air near the cloud top, where the larger drops are precipitated to lower elevations and may eventually fall as rain from the cloud base. This zone is so named, because the clouds seem to be raining out much of their water while growing. The radius of the drops that actually rain out from cloud tops is much larger than the indicated r_e of 20 μm, being at the upper end of the drop size distribution.
4. *Mixed phase zone:* The large growth rate that may occur at $T < 0^oC$ can be attributed to coalescence as well as to mixed phase precipitation formation processes. Therefore, the mixed phase and coalescence zones are ambiguous at temperatures below freezing. Because the first ice phase in growing continental clouds appears typically at $T < -10^oC$, the zones are separated arbitrarily at -10^oC.
5. *Glaciated zone:* A nearly stable r_e zone at below freezing temperatures at a value greater than that of the rainout zone. The value is probably determined by the maximum ice particle size that can be sustained near cloud top, where the larger particles are precipitated to lower elevations while aggregating and forming snowflakes. Several examples of the above cloud-microphysical zones as inferred from the AVHRR imagery are provided in the following case studies. Plotted are the 25th, 50th, 75th, and 90th percentiles of the r_e for each 1^oC interval. The median is indicated by the thick line. The numbers in the plots refer to the growth zones as numbered above.

The first two examples are from continental situations in Israel, where it can be seen that there was a deep diffusional growth zone capped by a zone of mixed-phase growth Figures 1a and 3b). In the second example a glaciated zone lay above the mixed-phase zone (Figure 1b).

In contrast to the first two examples are plots of r_e versus temperature for two AVHRR windows in an image covering the Bay of Bengal (Figure 2a) and Thailand (Figure 2b). In these plots the diffusional growth zone is virtually nonexistent in clouds over the Bay of Bengal, where the droplet coalescence growth zone is already well developed a small distance above the bases of the maritime clouds. Even in the interior of Thailand (Figure 2b) the diffusional growth zone is shallower than in the examples shown for Israel above which there is a zone of droplet growth by coalescence.

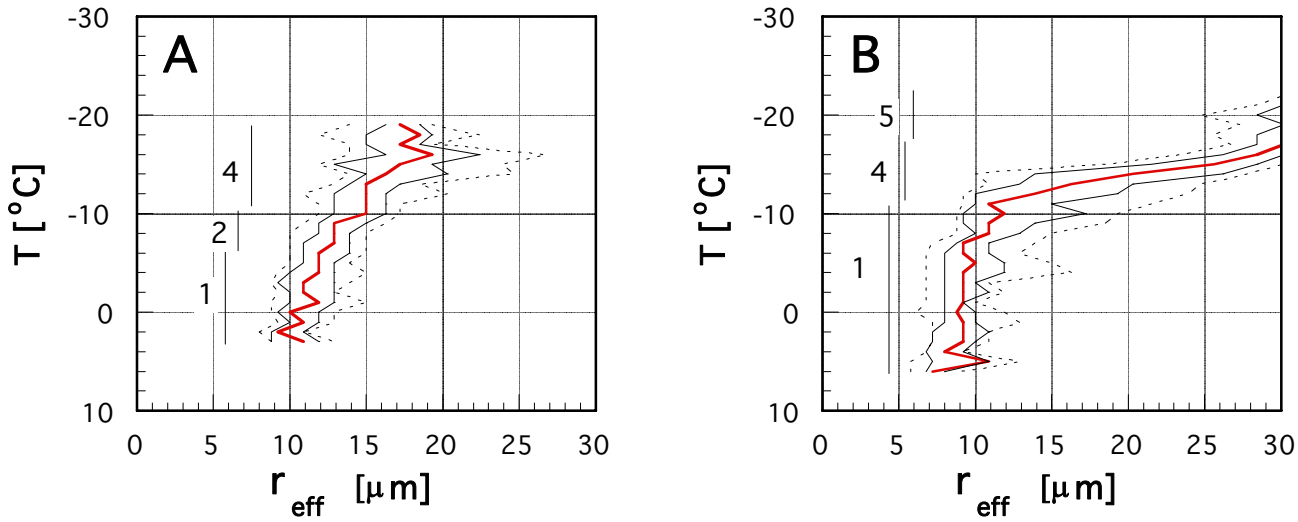

Figure 1. The effective radius as a function of cloud-top temperature for two AVHRR windows over Israel on 25 March (A) and 3 April 1995 (B). Plotted are the 10%, 25%, 50%, 75%, and 90% percentiles of the r_e for each 1°C interval. The thick line indicates the median. The vertical bars denote the different microphysical zones as numbered in the text.

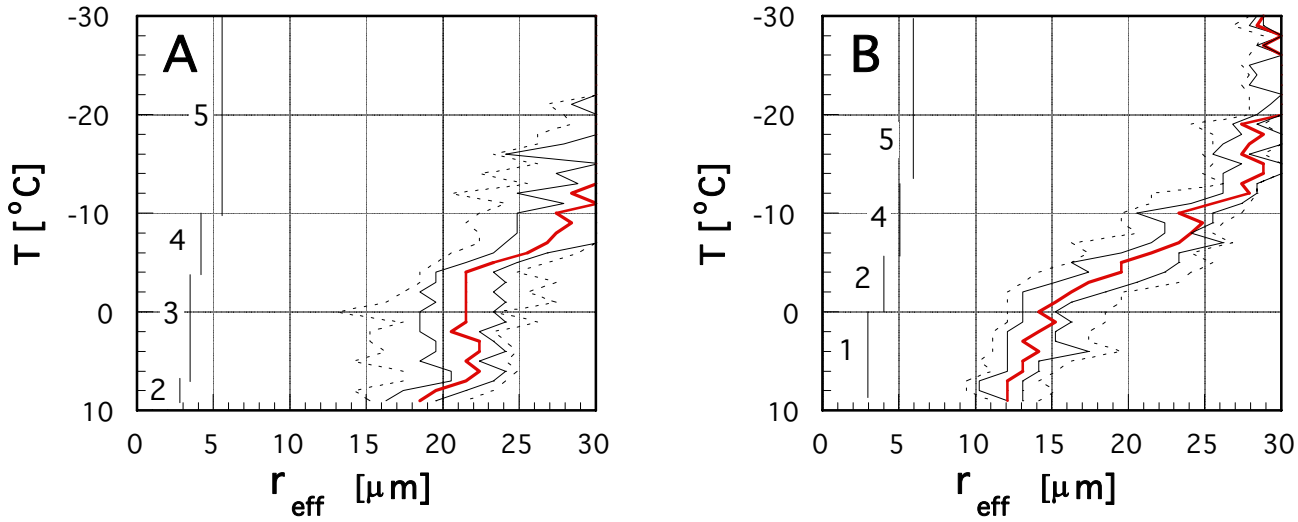

Figure 2. The same as Figure 3, but for two AVHRR windows containing clouds growing in monsoon flow on 12 November 1992. Window A covers a portion of the Bay of Bengal to the Burmese coastal areas and window B is in the interior of Thailand.

The rainout zone can exist only in clouds with well-developed coalescence that has progressed to the extent that further increase of drop size is compensated by the large drop fallout from the

cloud tops. Therefore, the rainout zone exists just above the droplet coalescence growth zone. As can be seen (Figure 2a), the rainout zone is well-developed in maritime clouds, but its extent is reduced in less maritime clouds (Figure 2b) and completely vanishes in continental clouds (Figure 1a and 1b).

The mixed-phase zone exists above the glaciated zone. Often the coalescence and mixed phase zones overlap to one continuous region of rapid growth of r_e through the 0°C isotherm. In such cases the separation between the zones is set arbitrarily to -6°C (Figure 2b). The transition from the rainout zone to the glaciated zone (Figure 2a) is also defined as a mixed-phase zone.

A glaciated cloud is one in which practically all of its water has turned into ice particles. Cloud-top glaciation occurs at temperatures of about -5°C to -10°C for clouds with well-developed coalescence, typical of maritime clouds (Figure 2a), in agreement with the laboratory experiments of Hallett and Mossop (1974). Glaciation occurs typically at about -15°C for continental clouds with some coalescence (Figure 2b) or -20°C for more continental clouds. In the extreme, glaciation can occur at temperatures as cold as -38°C for highly continental clouds (Rosenfeld and Woodley 2000).

References

Hallett, J., and S. C. Mossop. 1974: "Production of secondary ice crystals during the riming process." *Nature* **249**: 26–28.

Lensky I. M., and D. Rosenfeld. 1997: "Estimation of precipitation area and rain intensity based on the microphisical properties retrieved from NOAA AVHRR data." *Journal of Applied Meteorology* **36**: 234–242.

Nakajima, T., and M. D. King, 1990: Determination of the optical thickness and effective particle radius of clouds from reflected solar radiation measurements. Part I: Theory. *J. Atmos. Sci.,* **47,** 1878-1893.

Rosenfeld, D., and G. Gutman. 1994: "Retrieving microphysical properties near the tops of potential rain clouds by multispectral analysis of AVHRR data." *J. Atmos. Res.* **34**: 259–283.

Rosenfeld, D., and I. Lensky. 1998: Spaceborne sensed insights into precipitation formation processes in continental and maritime clouds. *Bulletin of the American Meteorological Society* **79** (11): 2457–2476.

Rosenfeld, D. 1999: "TRMM observed first direct evidence of smoke from forest fires inhibiting rainfall." *Geophys. Res. Lett*. **26**: 3105–3108.

Rosenfeld, D. 2000: "Suppression of rain and snow by urban air pollution." *Science* **287**: 1793–1796.

Rosenfeld, D., and W. L. Woodley. 2000: "Deep Convective Clouds with Sustained Supercooled Liquid Water Down to -37.5°C." *Nature* **405**: 440–442.

Appendix B

Results of Supplemental Analyses for Objective 1: Hydrological Stream Flow Analysis

Appendix B

Results of Supplemental Analyses for Objective 1: Hydrological Stream Flow Analysis

This appendix, containing 1 table and 12 figures, provides additional information for the graphs that are presented in this report. In addition, more cases and results are brought forth here to show that the results presented in the body of the report are examples of the general situation.

Table B1. Examination of trends (1945–2000) in the orographic component of California Sierra Nevada precipitation using precipitation rain gauges and river flows for 10 Sierra river basins and their highly correlated upwind control river basins

Sierra basin	Coastal basin	Correlation of basin gauges	Correlation of river flows	Trend derived from basin precip. gauges	Trend derived from river flows
Pitt	**Eel**	**0.87**	**0.92**	**1.05**	**1.09**
Feather	**Russian**	**0.94**	**0.94**	**1**	**1**
Yuba	**Russian**	**0.91**	**0.91**	**1.02**	**1**
American	**Russian**	**0.92**	**0.9**	**0.85**	**0.88**
Cosumnes	**Napa**	**0.9**	**0.88**	**0.83**	**0.69**
Mokelumne	**Napa**	**0.89**	**0.88**	**0.84**	**0.79**
San Joaquin	**Arroyo Seco**	**0.94**	**0.83**	**0.87**	**0.72**
Kaweah	**Nacimiento**	**0.93**	**0.81**	**0.83**	**0.87**
King	**Arroyo Seco**	**0.93**	**0.93**	**0.87**	**0.73**
Merced	**Arroyo Seco**	**0.88**	**0.9**	**0.82**	**0.77**

Figures B1–B6 show the absolute trends of the annual stream flow volumes, annual trends of the precipitation, the correlation, and the ratio between coastal rivers to coastal rain gauges. The locations of the coastal rivers and rain gauges are presented in Figure B7.

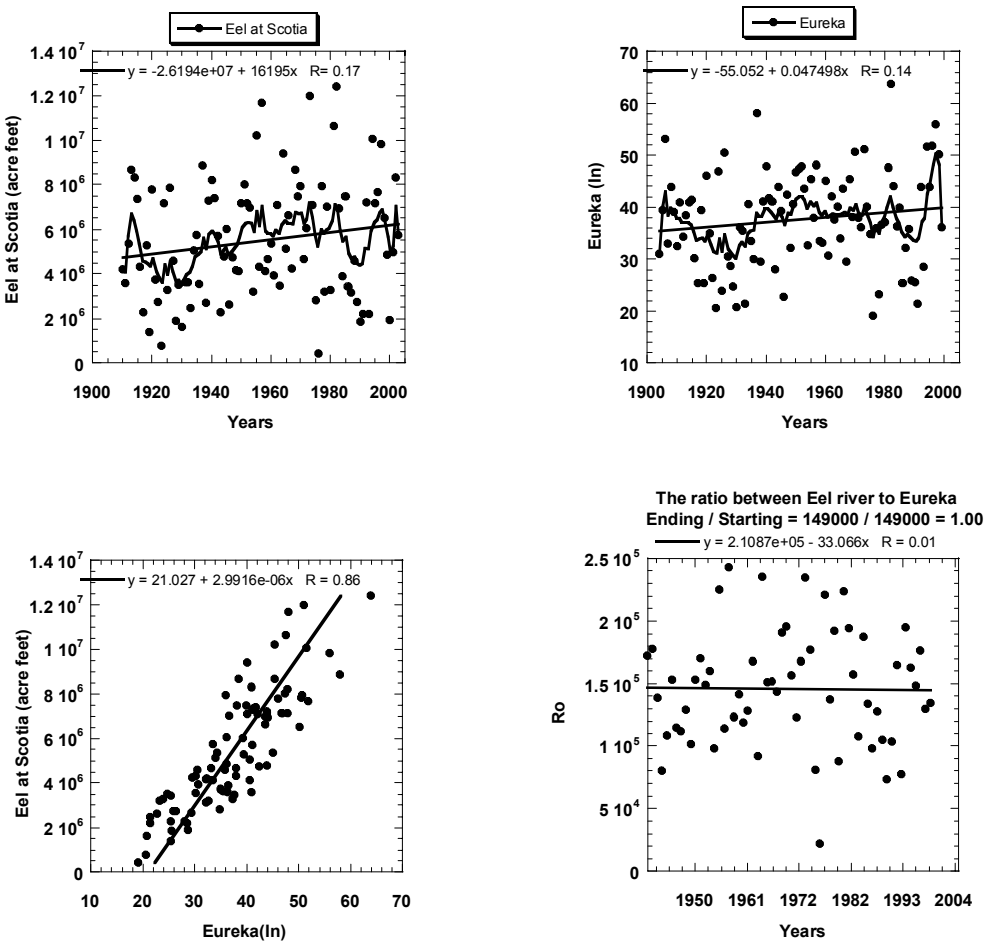

Figure B1. The annual flow in the Eel River, the annual precipitation at Eureka, the correlation, and the ratio between them

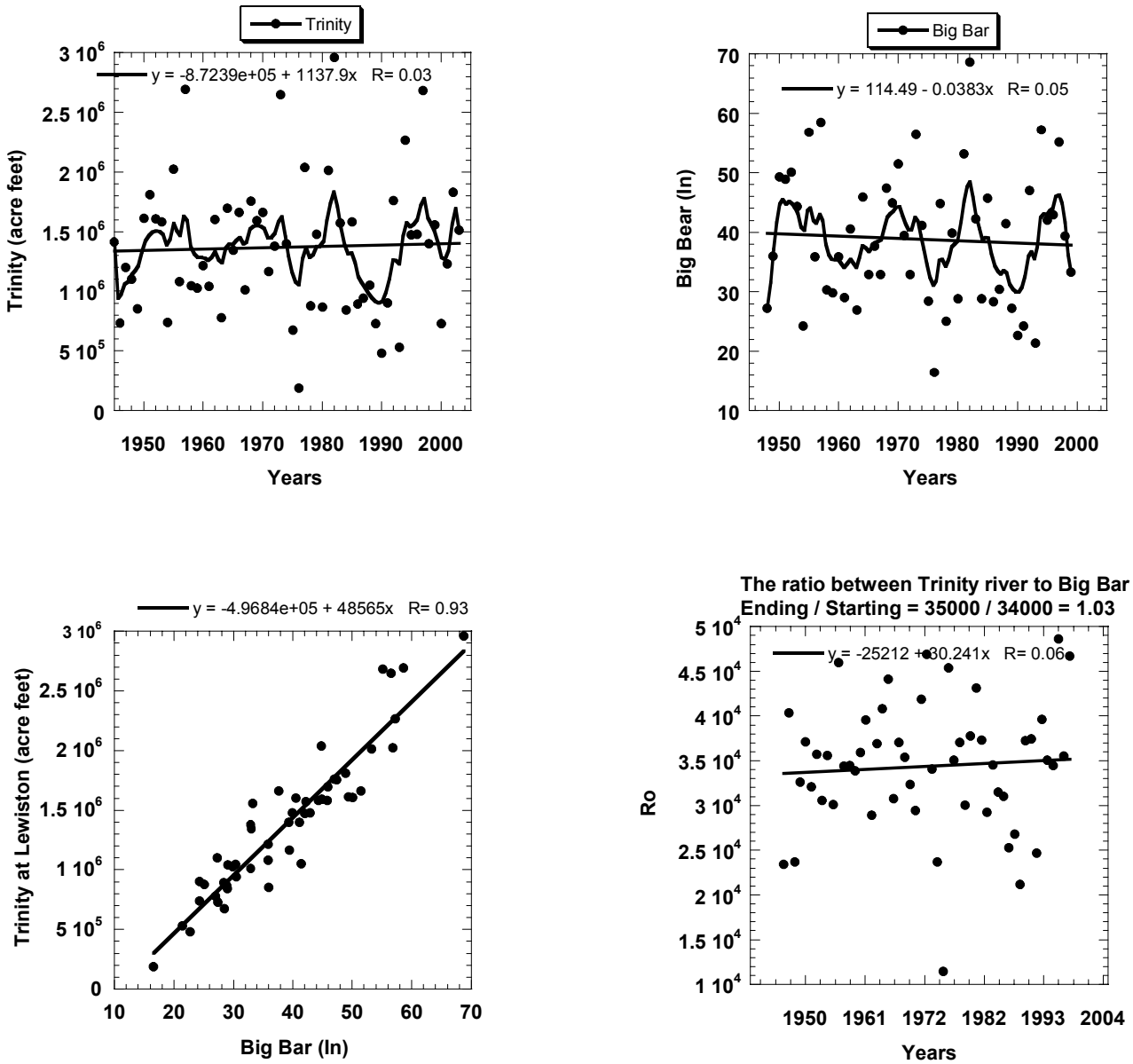

Figure B2. The annual flow in the Trinity River, the precipitation at Big Bar, the correlation, and the ratio between them

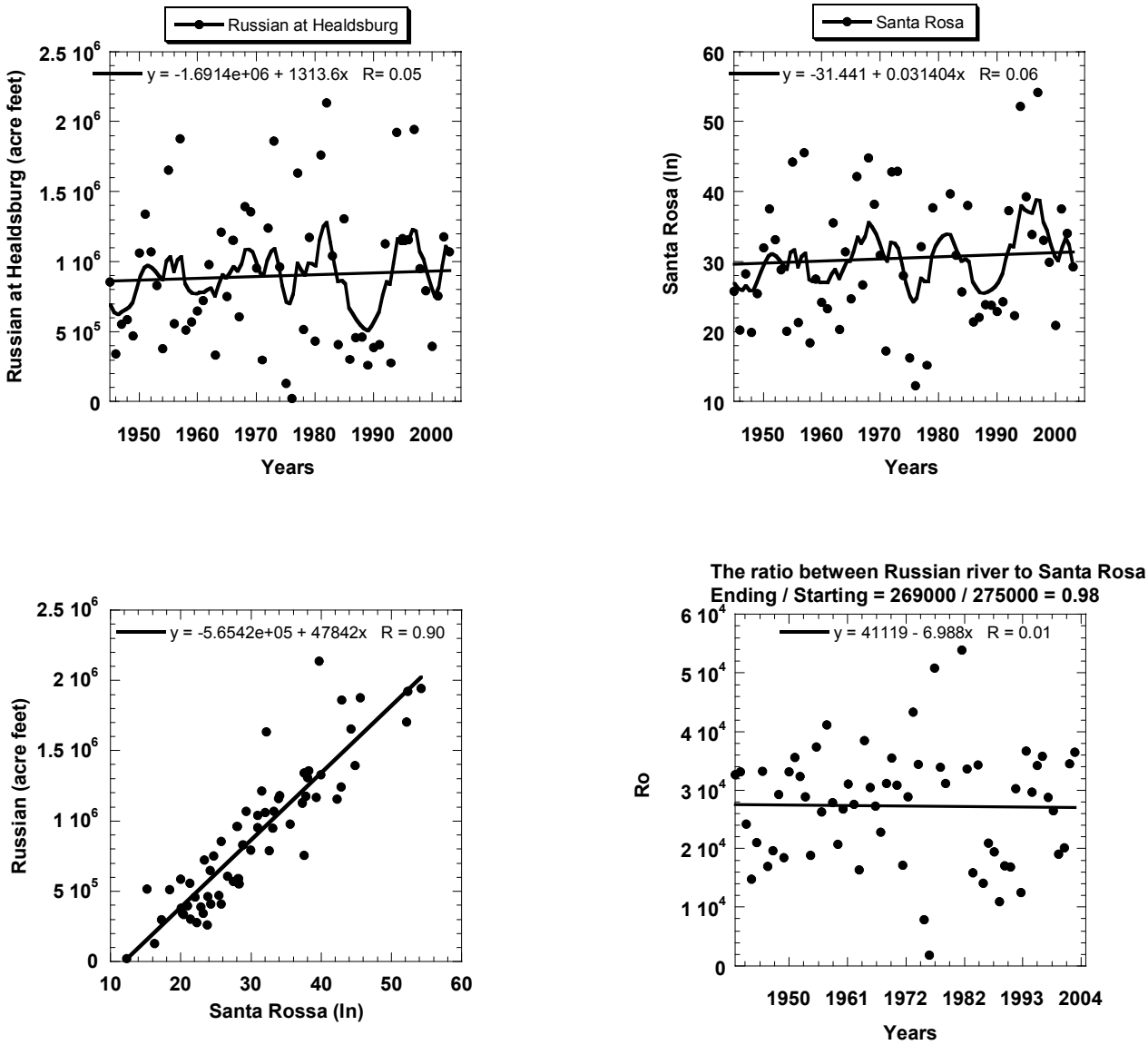

Figure B3. The annual flow in the Russian River, the precipitation at Santa Rosa, the correlation, and the ratio between them

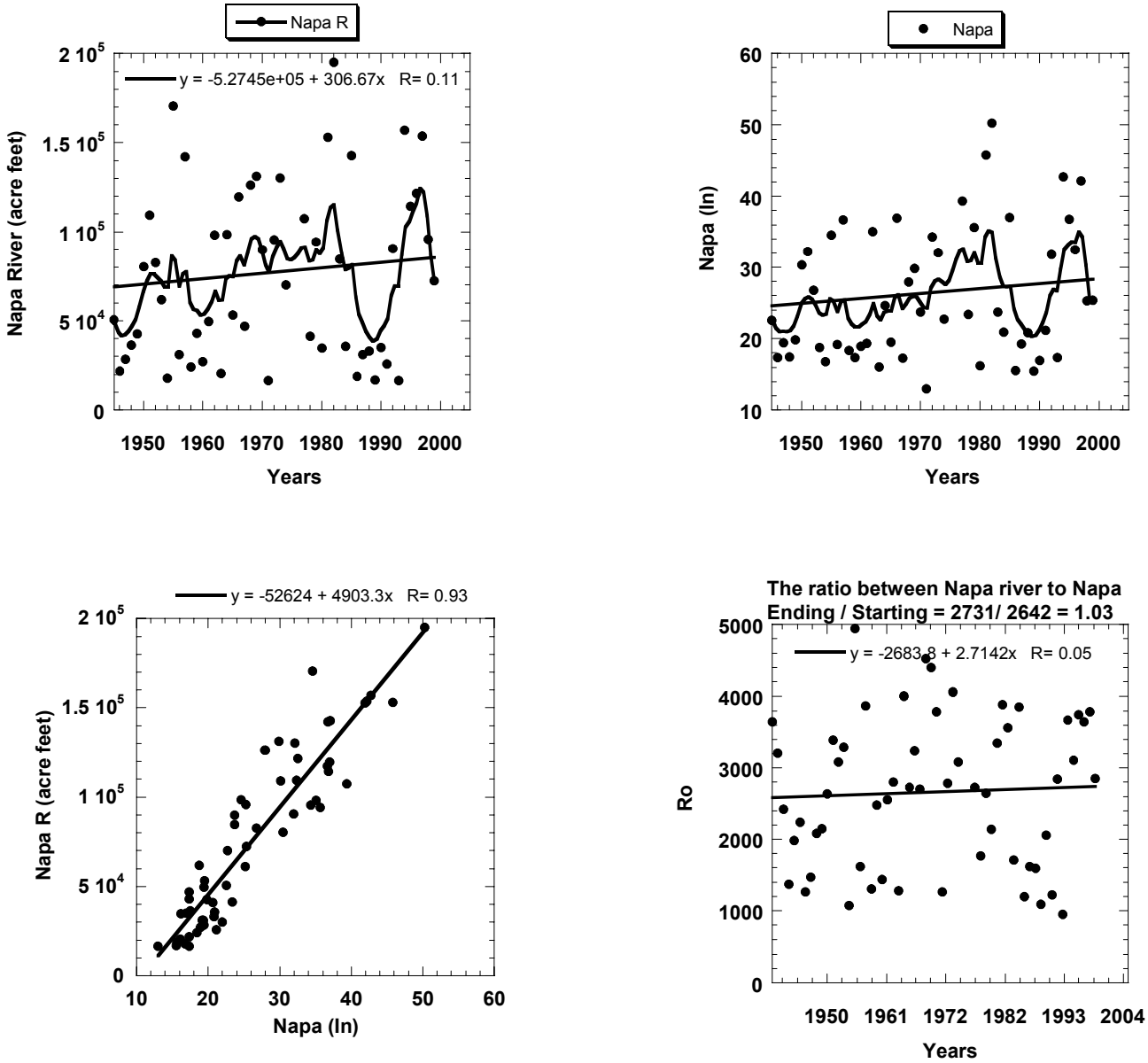

Figure B4. The annual flow in the Napa River, the precipitation at Napa, the correlation, and the ratio between them

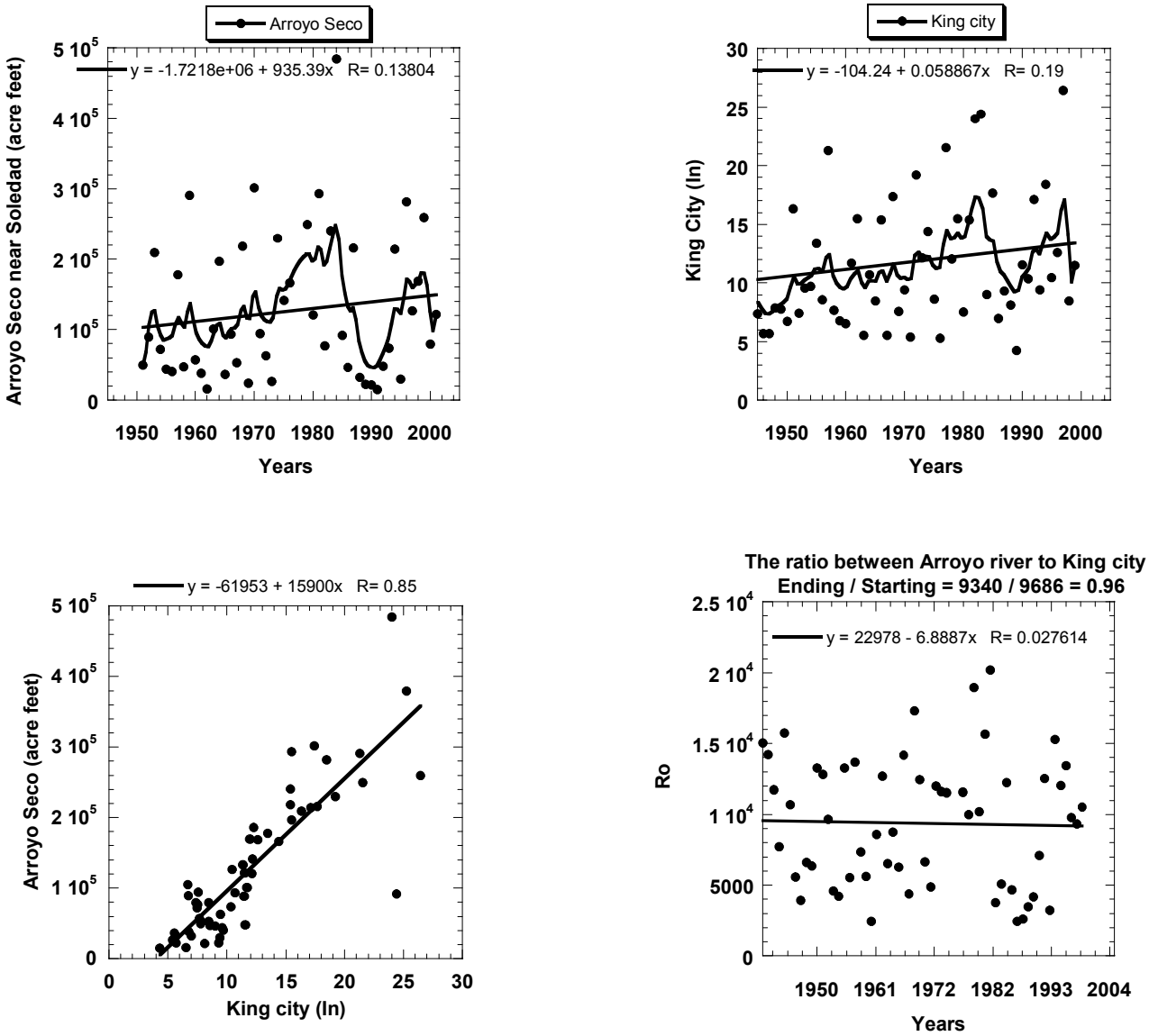

Figure B5. The annual flow in the Arroyo River, the precipitation at King City, the correlation, and the ratio between them

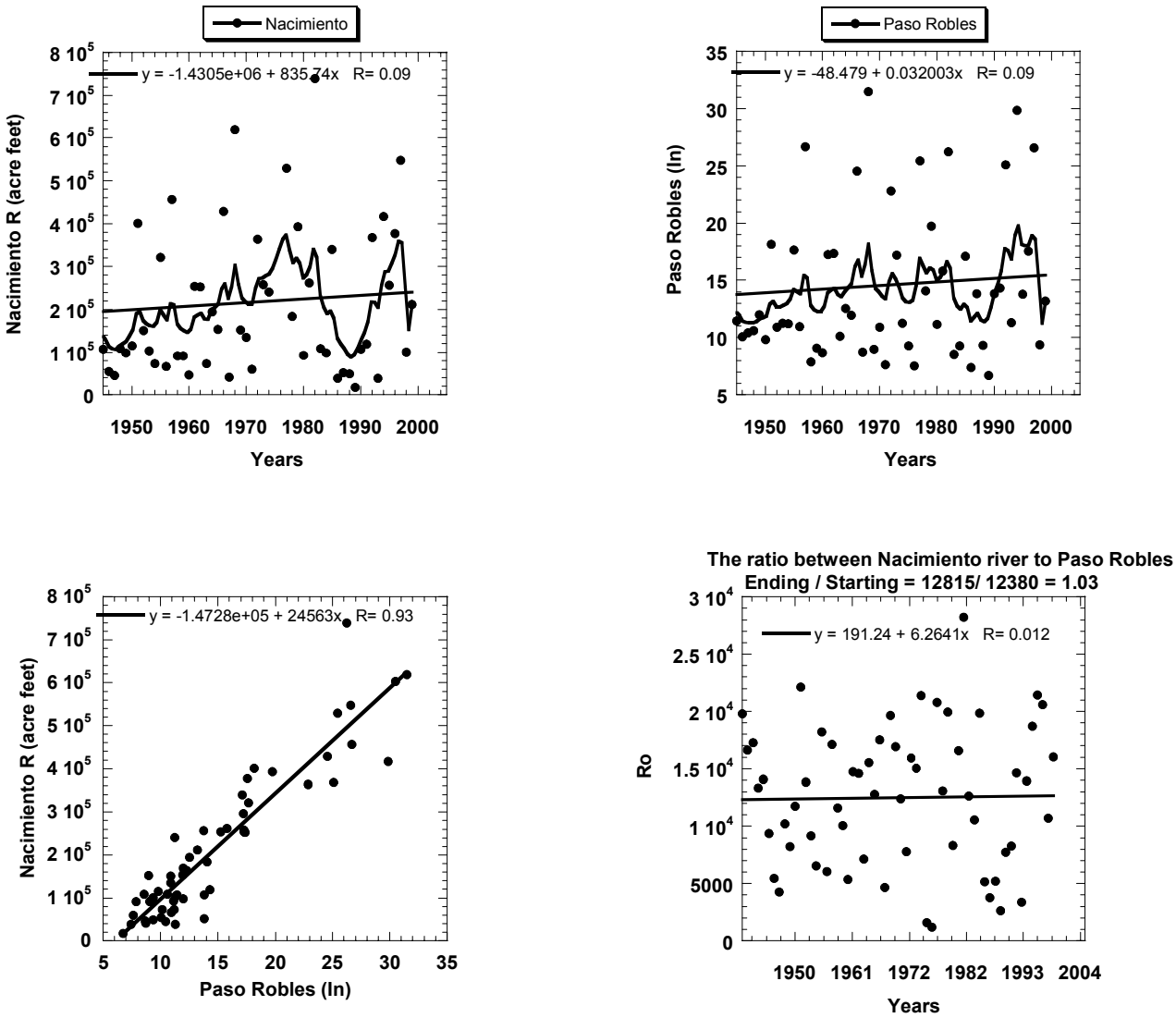

Figure B6. The annual flow in the Nacimiento River, the precipitation at Paso Robles, the correlation, and the ratio between them

Figure B7. Pairs of coastal rivers and highly correlated rain gauges located at their drainage basin: The Eel River (at Scotia) vs. Eureka; Trinity River (at Lewiston) vs. Big Bar; Russian river (at Healdsburg) vs. Santa Rosa; Napa River (near St. Helena) vs. Napa; Arroyo River (near Soledad) vs. King City; and Nacimiento River (below Nacimiento Dam) vs. Paso Robles. All the rivers and the hydrometric stations are from the California Department of Water Resources snow course list.

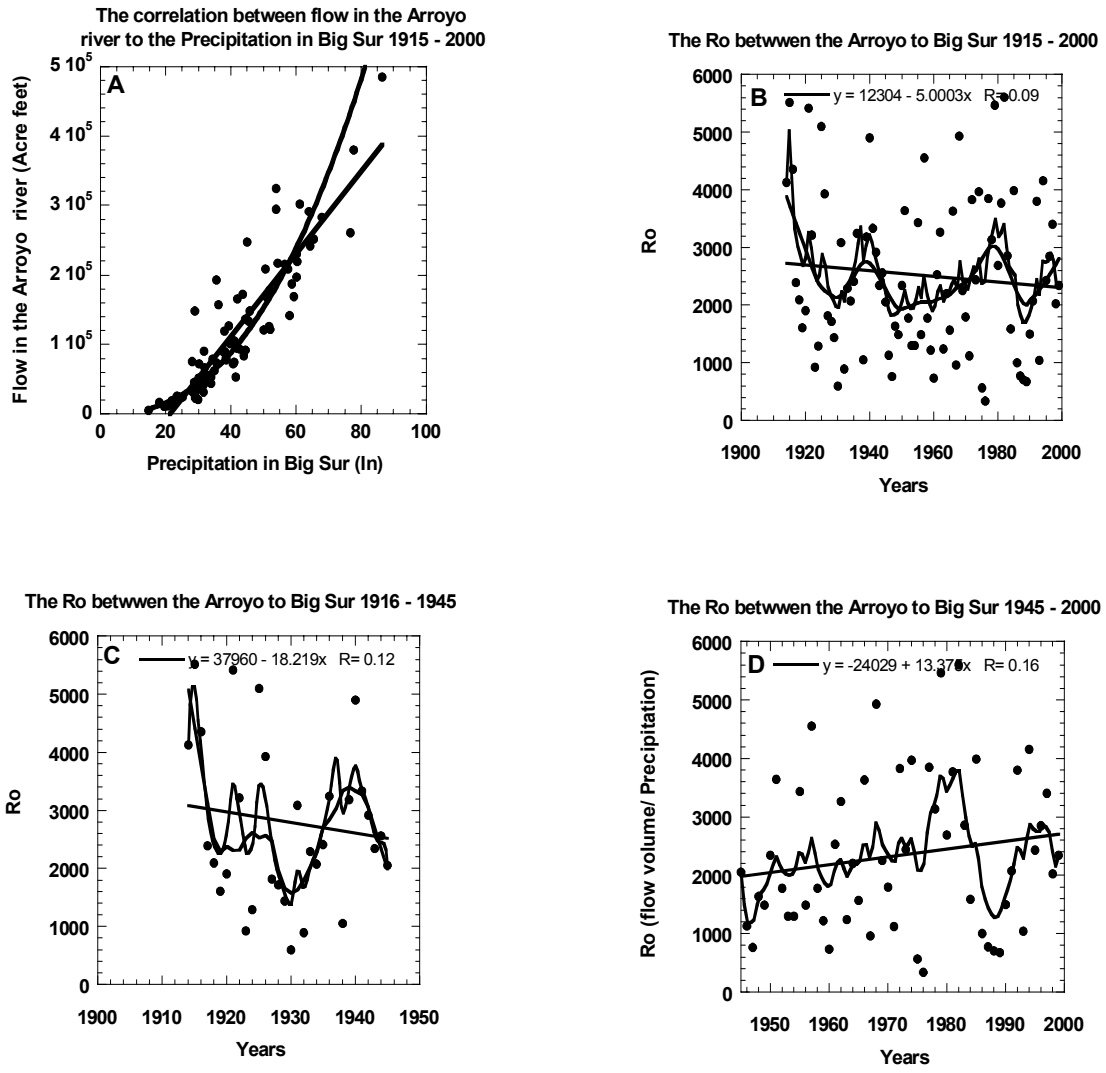

Figure B8. The correlation (A) and the ratio between the stream flow in the Arroyo River to the precipitation at Big Sur for the periods: (B) 1916–2000, (C) 1916–1945, and (D) 1945–2000

Figures B9–B13 present individual trends for the eastern and western rivers in the Sierra Nevada, the correlations and the Ro between them (western versus eastern slopes) for the periods 1905–2003, and 1945–2003.

Stanislaus at Goodwin (western slopes) vs. West Walker near Coleville (eastern slopes)

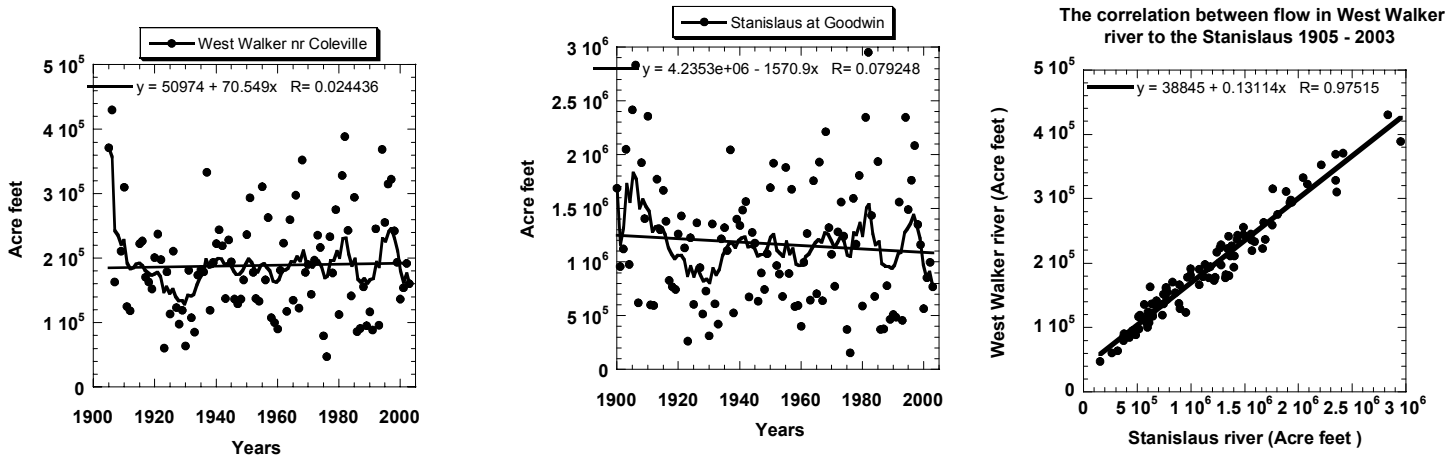

The ratio between the Stanislaus vs. the West Walker

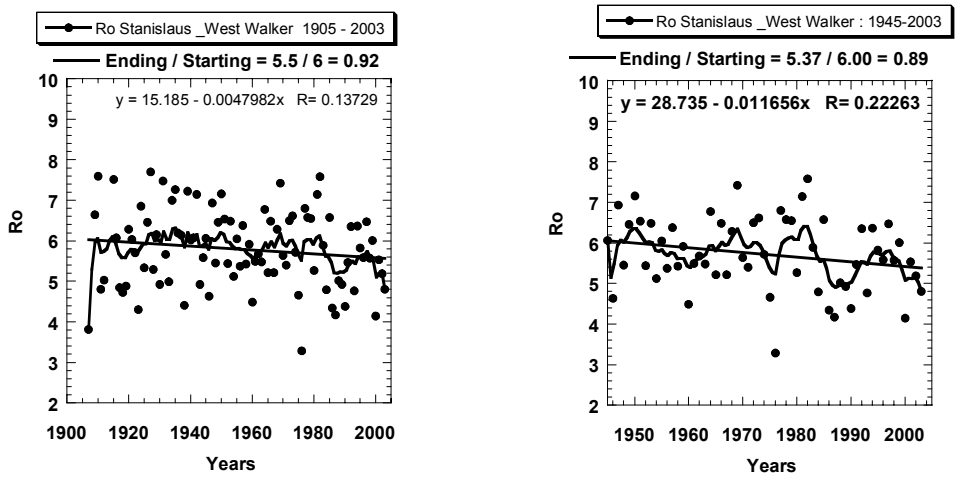

Figure B9. Trends for the West Walker and Stanislaus Rivers, the correlation, and the ratio between them. Note the decreasing trend between the Stanislaus to the West Walker River.

Mokelumne at Mokelumne hill (western slopes) vs. West Walker near Coleville (eastern slopes)

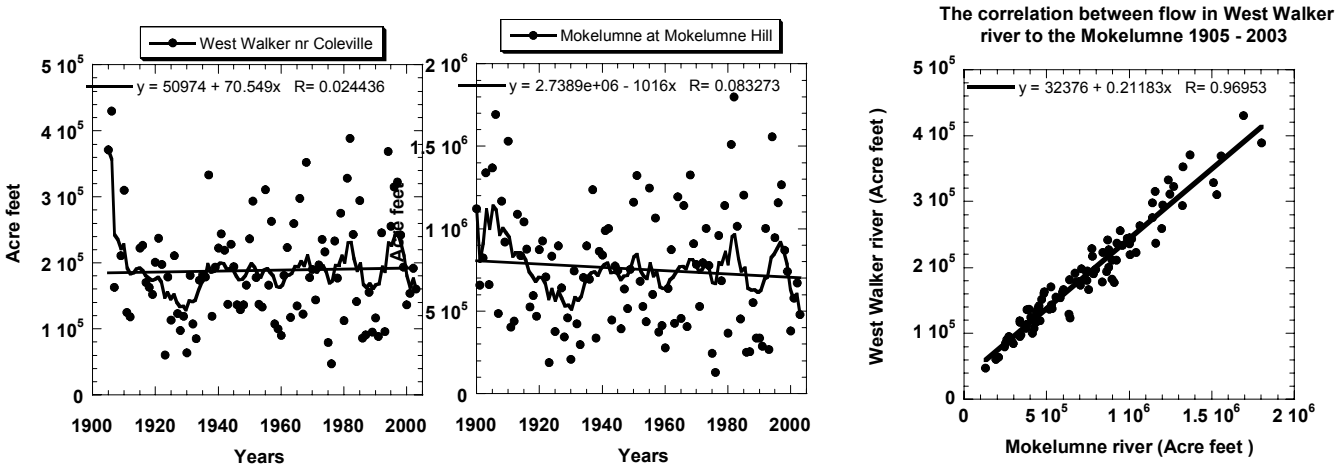

The ratio between the Mokelumne (western slopes) vs. the West Walker (eastern slops)

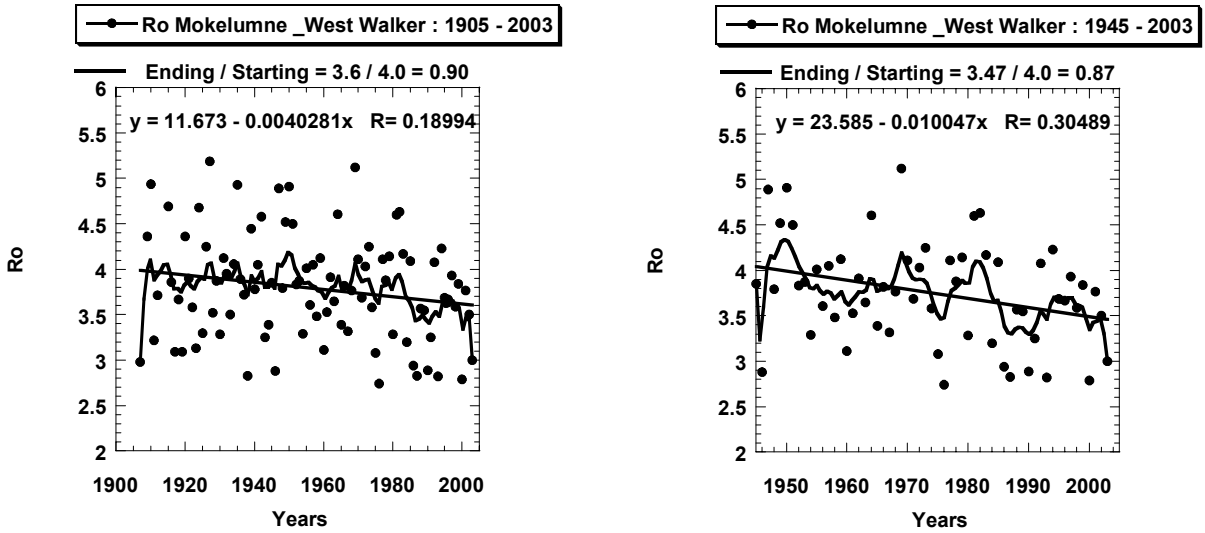

Figure B10. Same as Figure B8, but for the Mokelumne vs. the Walker River

Cosumnes at Michigan Bar (western slopes) vs. West Walker near Coleville (eastern slopes)

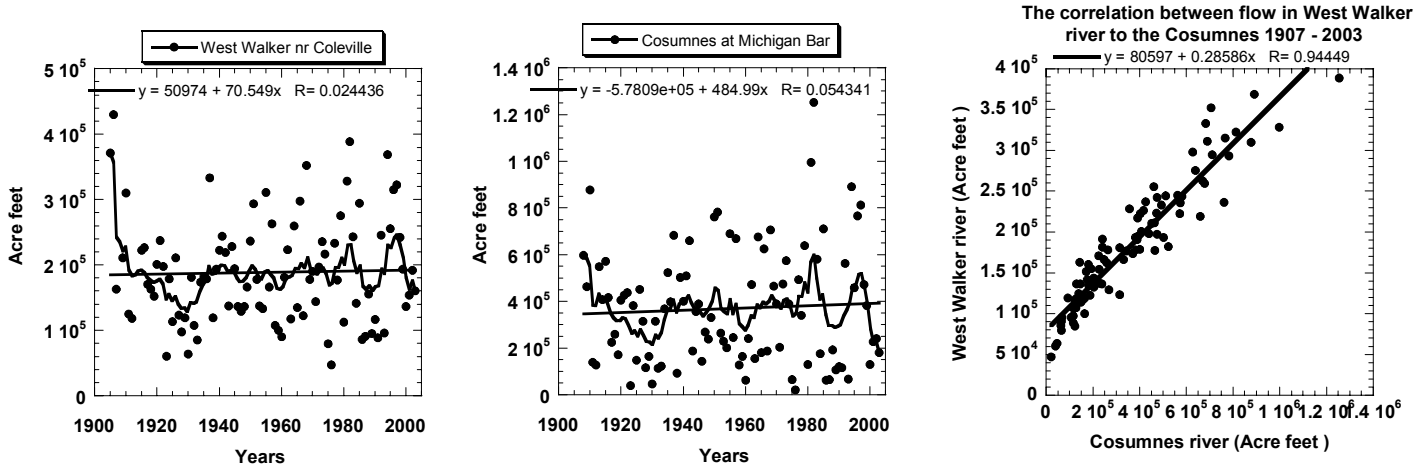

The ratio between the Cosumnes (western slopes) vs. the West Walker (eastern slopes)

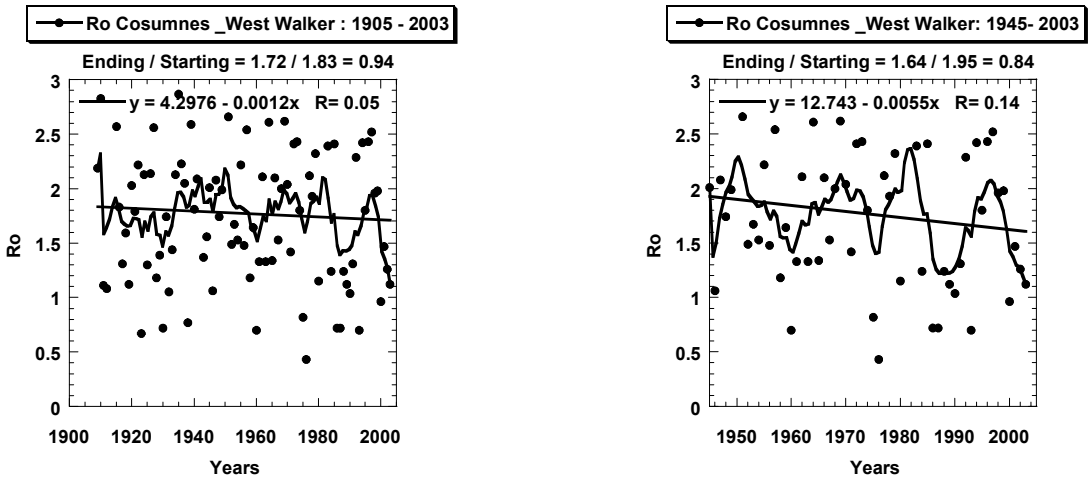

Figure B11. Same as Figure B9, but for the Cosumnes vs. the Walker River

American at Folsom (western slopes) vs. West Walker nr Coleville (eastern slopes)

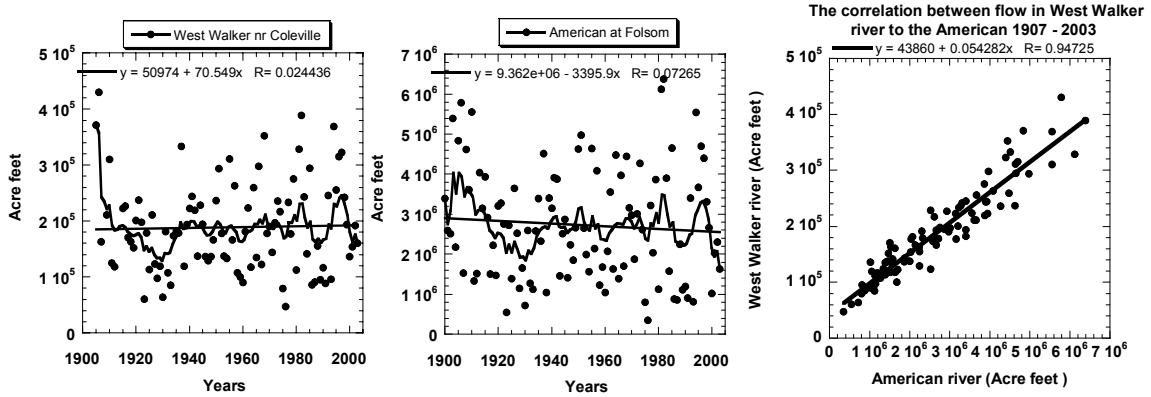

The ratio between the American vs. the West Walker

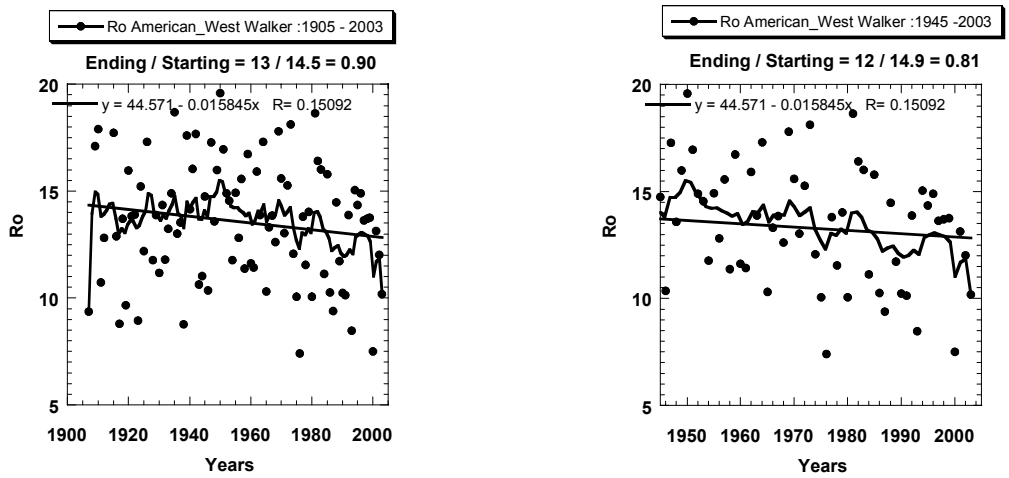

Figure B12. Same as Figure B10, but for the American vs. the West Walker River

American at Folsom (western slopes) vs. West Carson near Woodfords(eastern slopes)

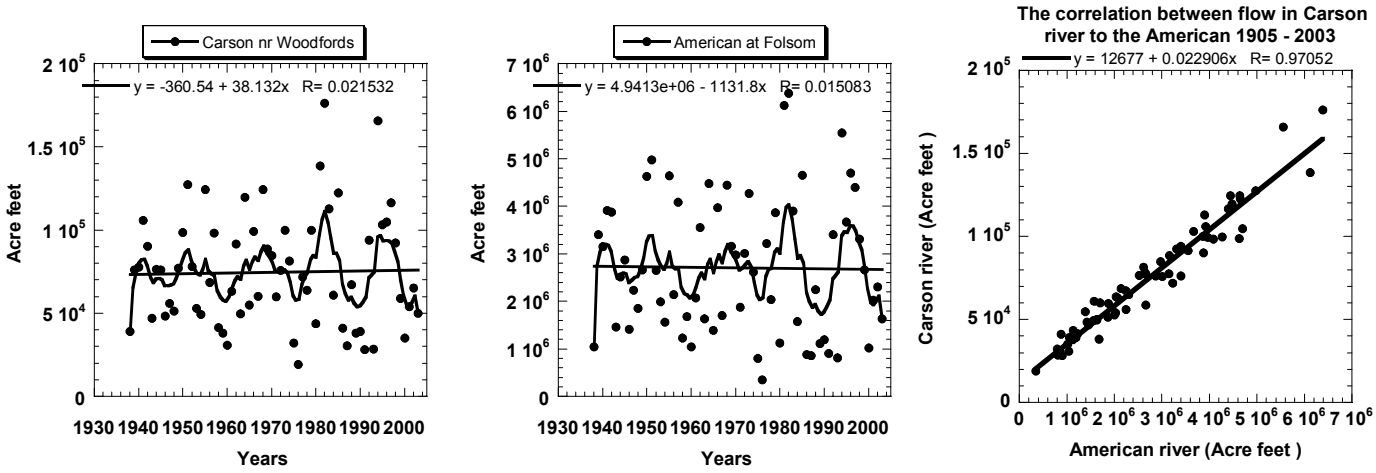

The ratio between the American vs. the West Carson

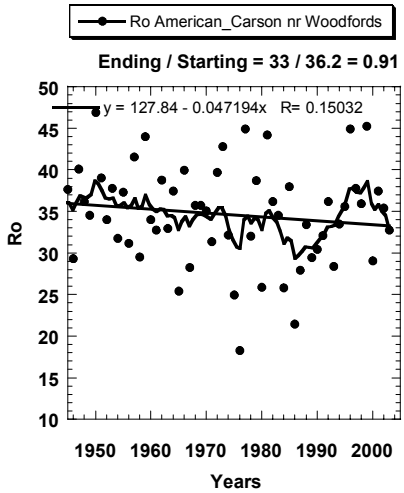

Figure B13. Same as Figure B11 but for the American vs. Eastern Carson River

Appendix C

Effects of Aerosols on Precipitation from Orographic Clouds

Appendix C

Effects of aerosols on precipitation from orographic clouds

Barry Lynn (1,2), Alexander Khain (1), Daniel Rosenfeld (1)

and William L. Woodley (3)

(1) Department of the Atmospheric Sciences, The Hebrew University of Jerusalem, Israel

(2) Columbia University, Center for Climate Systems Research, New York, New York

(3) Woodley Weather Consultants, Littleton, Colorado

Submitted to Journal of Geophysical Research

April 2006

Accepted on August 21, 2006

Communicating address

Prof. Alexander Khain, Department of the Atmospheric Sciences, The Hebrew University of Jerusalem, Givat Ram, 91904, Jerusalem, Israel

Tel: 972-2-6585822

Email: khain@vms.huji.ac.il

Abstract

Spectral (bin) microphysics (SBM) was coupled to the Weather Research Forecast (WRF) model to investigate the effect of aerosols (i.e., air pollution) on precipitation in the Sierra Nevada Mountains. Two-dimensional simulations were produced using either maritime ("clear-air") or continental ("dirty-air") aerosols. The simulation with clean air produced more precipitation on the upwind mountain slope than the simulation with continental aerosols. After three hours of simulation time, the simulation with maritime aerosols produced about 30% more precipitation over the length of the mountain slope than the simulation with continental aerosols. Sensitivity tests demonstrated the importance of relative humidity and vertical velocity on cloud microphysical structure and precipitation amount. Greater differences in precipitation amounts between simulations with clean and dirty air were obtained when ice microphysical processes were included in the model simulations.

Keywords: Cloud-aerosol interaction, aerosol effects on precipitation, orographic clouds, Numerical modeling, spectral bin microphysics, weather forecast model

1. Introduction

Recent observational and numerical studies demonstrate a significant effect of aerosol particles on precipitation amount and spatial distribution (e.g., Rosenfeld 1999; Ramanathan et al. 2001; Andreae 2004; Givati and Rosenfeld 2004; Khain et al. 2005; Lynn et al. 2005a, 2005b; Jirak and Cotton 2006). Effects of anthropogenic aerosols produced in urban areas on precipitation are of special interest. Studies have found that air pollution from industrial and urban areas can act to suppress precipitation (Rosenfeld 2000; Borys et al. 2000). Yet, some work has shown precipitation enhancement around heavily polluted urban areas such as Houston (Shepherd and Burian 2003) and Tokyo (Ohashi and Kida 2002). The difference in the results is possibly related to different environmental conditions in the zones investigated in the studies. As shown by Khain et al. (2005), aerosol effects on precipitation from deep convective clouds strongly depend on the thermal stability of the atmosphere, air humidity, and the magnitude of the dominating wind shear. Since urban zones affect both thermal stability and aerosol concentration, the aerosol effects on precipitation can change from location to location. Moreover, since many factors affect precipitation formation in urban areas, it is difficult to reveal and to quantitatively evaluate effect of aerosols in these areas.

In this sense, investigation of precipitation from topographically produced clouds located downwind of urban areas could provide better opportunity to reveal and evaluate aerosol effects. For instance, Givati and Rosenfeld (2004) examined the effects of air pollution on short-lived shallow clouds, forming over the mountains of California (and Israel) during the cold season. Jirak and Cotton (2006) focused their study on warm-season clouds forming at elevated sites downwind of urban areas along the Front Range of California. Each study found decreases in precipitation associated with polluted air relative to stations in more pristine air of around 30%. Urban areas affect many meteorological parameters in zones located downwind (such as temperature, atmospheric stability, and wind speed) that can affect precipitation regime. The main question addressed in the study is, whether production of anthropogenic aerosol can be the mechanism of the decrease in precipitation reported by Givati and Rosenfeld (2004) and Jirak and Cotton (2006).

This paper uses a spectral (bin) microphysics model (SBM) coupled with the Weather Research Forecast (WRF) model to reveal the sensitivity of precipitation from orographic clouds over the Sierra Nevada Mountains to aerosol concentration. Section 2 presents the conditions of numerical experiments, while Section 3 examines the results. Section 4 presents the discussion and conclusions.

2. Design of Numerical Experiments

To investigate aerosol effects on precipitation, an SBM scheme has been used that is based on solving an equation system for size distribution functions of drops, three types of ice crystals (dendrites, columns, and plates), snow, graupel, and hail/frozen drops—as well as aerosol particles. This scheme has been described in detail in Khain et al. (2004). It has been used for investigation of aerosols effects on precipitation from single clouds under continental and maritime conditions using the Hebrew University cloud model (HUCM) (e.g., Khain et al. 2001;

2004; Khain and Pokrovsky 2004). A modified version of this scheme was coupled to a mesoscale model, MM5, and used for simulation of a rain event accompanied by squall line formation (Lynn et al. 2005a, 2005b). It was found that SBM allows better prediction of both spatial distribution and amount of precipitation as compared to commonly used bulk-parameterization schemes. Here, the full SBM scheme has been coupled to WRF (Skamarock et al. 2005) using the same approach for embedding the microphysics within the model dynamic time step as in Lynn et. al (2005a, 2005b).

A significant advantage of the SBM is that it simulates cloud-aerosol interaction through the calculation of aerosol effects on size distribution of cloud hydrometeors and hence, on precipitation. At the same time, many SBM schemes artificially broaden the droplet size distribution (DSD) during the process of diffusional growth by remapping of the DSD on a regular mass grid at each time step (Khain et al. 2000, 2004). This broadening can mask the effect of aerosols on the DSD, especially in the case of high aerosol concentration, when, in fact, a quite narrow DSD should form. In the present study, a new scheme of remapping has been used that conserves three moments of the hydrometeor size distributions (concentration, mass, and radar reflectivity) as compared to the commonly used Kovetz and Olund (1969) scheme that conserves only concentration and mass during the remapping. The conservation of the radar reflectivity (6th moment) leads to the simulation of a more narrow spectrum, more consistent with in situ formation of clouds under both low and high aerosol concentrations. In fact, supplemental simulations of well documented convective clouds measured in SMOCC (Andreae et al. 2004) indicate that DSD produced with the new scheme provided better agreement than the original scheme with observed DSD at all levels of measurements (BenMoshe et al. 2006).

The coupled model was used to simulate the development of orographic clouds observed during 7 December 2003 over the Sierra Nevada Mountains located a few hundred kilometers (km) inland from the California (Pacific) coastline. They are nearly parallel to the coastline. All simulations were produced using a single (non-nested) two-dimensional domain, oriented west to east. Simulations were run for three hours, which was sufficient time for clouds to form on the upslope side of the mountain and to advect over the far mountain peak. The model was run at 6-second time steps using 1 km grid resolution in the horizontal and about 200 m grid resolution in the vertical. The simulation domain extended over 494 km, but results are presented only the inner part of the domain, which was defined as beginning at 150 km and ending at 350 km. Radiation and surface model physics were not included. The clouds were generated by the vertical winds that resulted from the strong upslope (westerly) winds. Moreover, the turbulent kinetic energy (TKE) boundary layer scheme that was employed artificially included a TKE drag coefficient of 0.003, and ground sensible heat flux of 100 watts per square meter (W m^{-2}). The temperature, humidity, and wind are constant at the left boundary. There is a flux of temperature, humidity, and wind velocity from the left boundary into the domain. Within the domain, these fields are modified by the development of precipitation along the mountain ridge. At the right boundary, open boundary conditions were used, that is, zero horizontal gradients of these quantities were assumed.

A satellite picture showing observed clouds is shown in **Figure 1**.

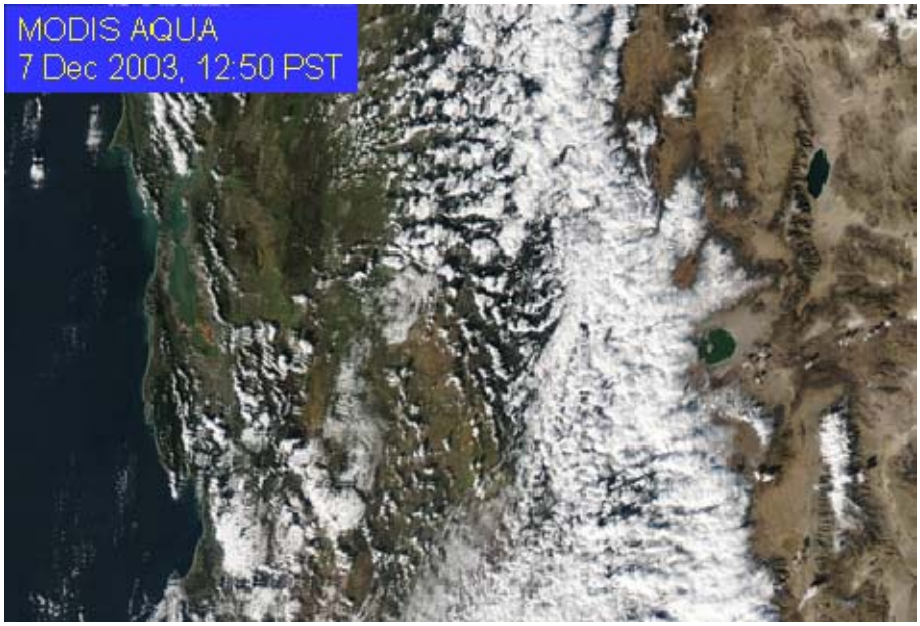

Figure 1. Satellite picture of the cloudiness during polluted conditions (7 December 2003). One main peak of cloudiness and sharp eastern boundary of cloudiness is seen. Clouds are small convective or stratocumulus clouds.

Initial atmospheric conditions were obtained from a sounding at Oakland, California, (16 LST 07 December 2003), and then interpolated to the WRF grid domain using the WRF standard interpolation program. **Figure 2 shows t**he initial atmospheric conditions prior to the formation of clouds within the model domain (obtained from a "control" simulation at 30 minutes). The component of the vector wind perpendicular to the mountain ridge was used, and specified as the u component in the west-to-east WRF domain. The vertical velocity generally increased as the strong westerly winds transverse the highest mountain peaks, ranging from about ½ meter per second (m s^{-1}) to greater than 2.5 m s^{-1} (upper panel). Local topography peaks led to concentration of positive vertical velocities at western slopes of these peaks and negative velocities over eastern slopes. This structure of the vertical velocities fosters the formation of cumulus and stratocumulus orographic clouds. The temperatures (middle) ranges from about 284 kelvin (K) at the base of the mountain slope to about 260 K at the mountaintop at 3.3 km, with the freezing level located at a height just less than 1.5 km. The relative humidity was a minimum of between 50% and 60% at the base of the mountain slope but generally increased as the moist air ascended and cooled on the mountain slope (bottom).

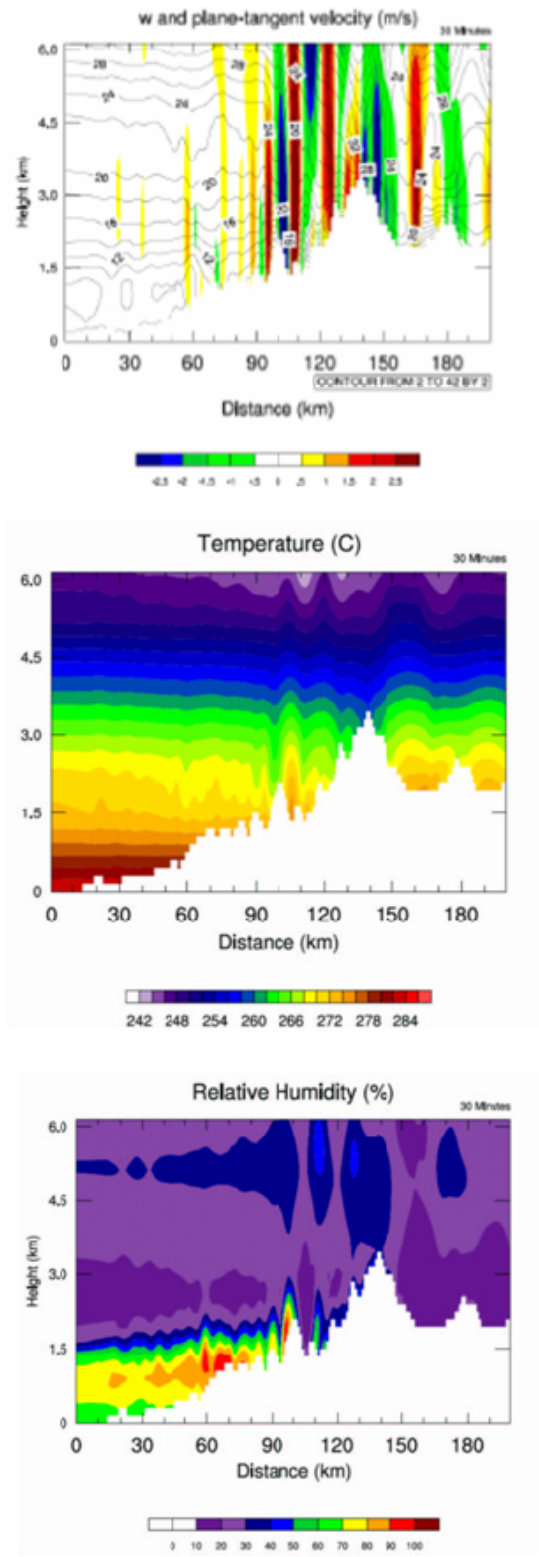

Figure 2. West to east cross-sections of vertical velocity and horizontal wind (upper panel), temperature (middle panel), and relative humidity (lower panel) 30 minutes after the start of the simulations. The figures show 201 grid elements, stretching from X=150 to X=350 km.

The sensitivity of simulated precipitation to aerosols was tested using two distinct aerosol concentrations, referred to as either "maritime" (Mar) or "continental" (Con). The first represents "clean" air while the second represents "dirty" air. The fields of cloud condensational nuclei (CCN) were initially (time [t] = 0) assumed to be spatially homogeneous. The initial size distribution of CCN was calculated using the method described by Khain et al. (2000). Initial dependence of cloud nuclei of super saturation was given by a well-known expression: $N_{CCN} = N_0 S^k$, where S is the super saturation in % (maritime: N_0 = 250 cm^{-3}, k = 0.462; continental: N_0 = 1250 cm^{-3}, k = 0.308). The maximum size of dry CCN particles in the continental case was 0.4 micrometers (μm), which roughly corresponds to a 2 μm radius nucleated droplet. The maximum size of dry aerosol particles in maritime air was assumed equal to 2 μm, which can produce nucleated droplets with radius of about 10 μm. Coefficients N_0 chosen for the experiments provide realistic droplet concentrations in "continental" (several hundred to thousand cm^{-3}) and maritime (~100 cubic centimeters [cm^{-3}]) conditions. At t > 0, the size distribution of aerosols was modified through nucleation scavenging and advection.

The size distributions of aerosol particles reaching the mountains most likely form as a result of a mixture of maritime aerosol (coming from the sea) and anthropogenic aerosols produced near the coast-line. The maritime air contains small aerosol concentration, but the size distribution is wider (with larger aerosol particles than in continental). The question arises, what is the effect of the tail of large maritime aerosols in the aerosol size distribution on precipitation? To clarify this problem, the research team performed a simulation referred to as (M+C), in which aerosol size distribution was obtained as a sum of the maritime and continental size distributions.

Sensitivity tests were produced that included increasing the relative humidity from the surface to 2 km to 90%, and from 2 to 5 km to 50%. These were referred to as *Mar-RH90* and *Con-RH90*, respectively. Two more simulations were produced using a reduced value for the sensible heat flux of 10 W m^{-2}, referred to as *Mar-SHF10* and *Con-SHF10*. Finally, simulations were done to simulate the effect of background wind on precipitation under both maritime and continental aerosol conditions, referred to as *Mar-3/4* and *Con-3/4.* In these last simulations, the profile of the horizontal wind speed was set equal to ¾ of its initial value in the control.

3. Results

a. Comparison of Mar-Control with Con-Control

The differences in aerosol concentration led to important differences in the microphysics of the simulated orographic clouds. **Figure 3** shows that maximum droplet concentration in Con-Control reached greater than 1000 cm^{-3}, while in Mar-Control the droplet concentration did not exceed 100 cm^{-3}. **Figures 4** shows that Con-Control produced much more cloud liquid water (LWC) on the upwind slope, but less rain water content (RWC) than Mar-Control (**Figure 5)**.

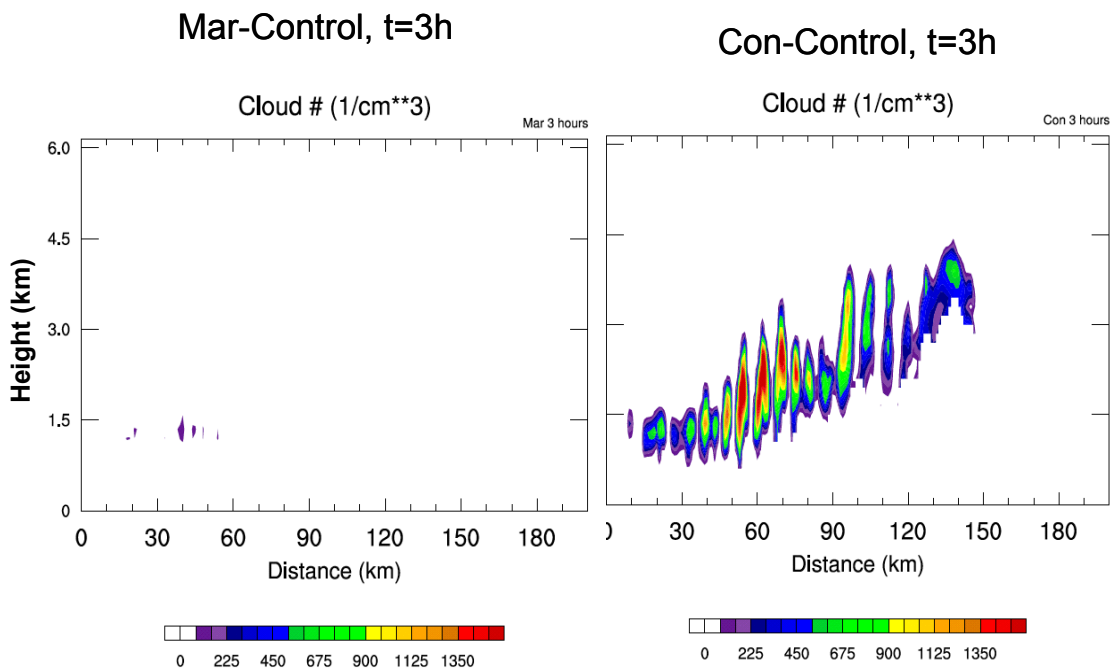

Figure 3. West to east cross-sections of cloud droplet concentration simulated with MAR-Control (left) and Con-Control (right) at 3 hours

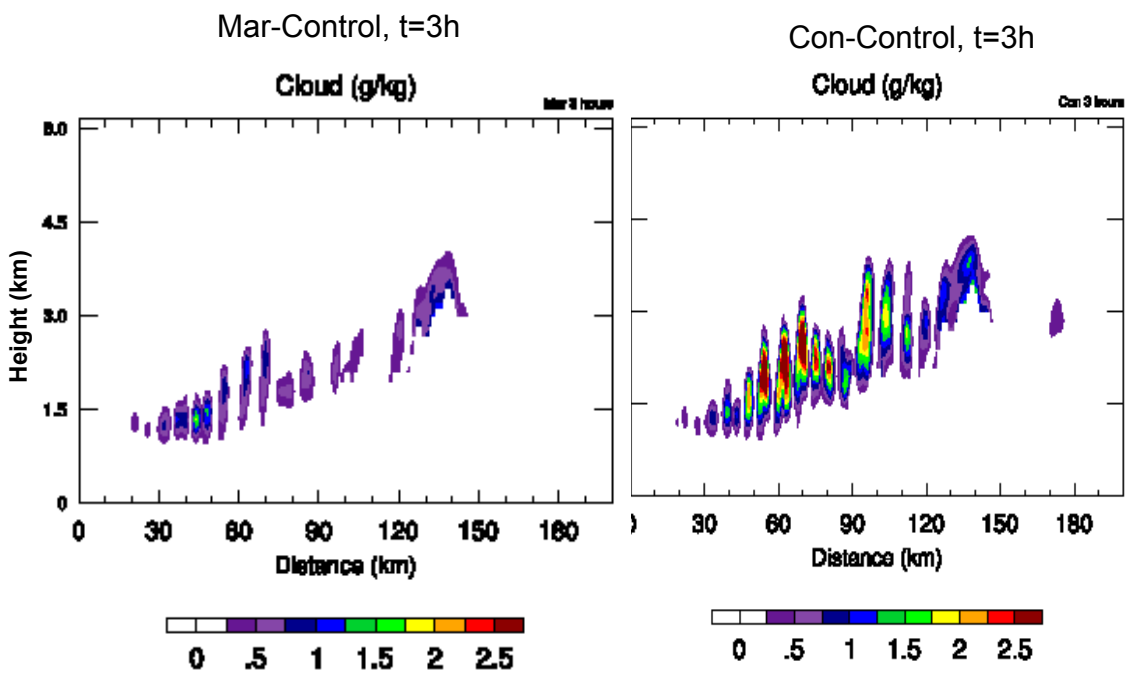

Figure 4. West to east cross-sections of cloud water content simulated with MAR-Control (left) and Con-Control (right) at 3 hours

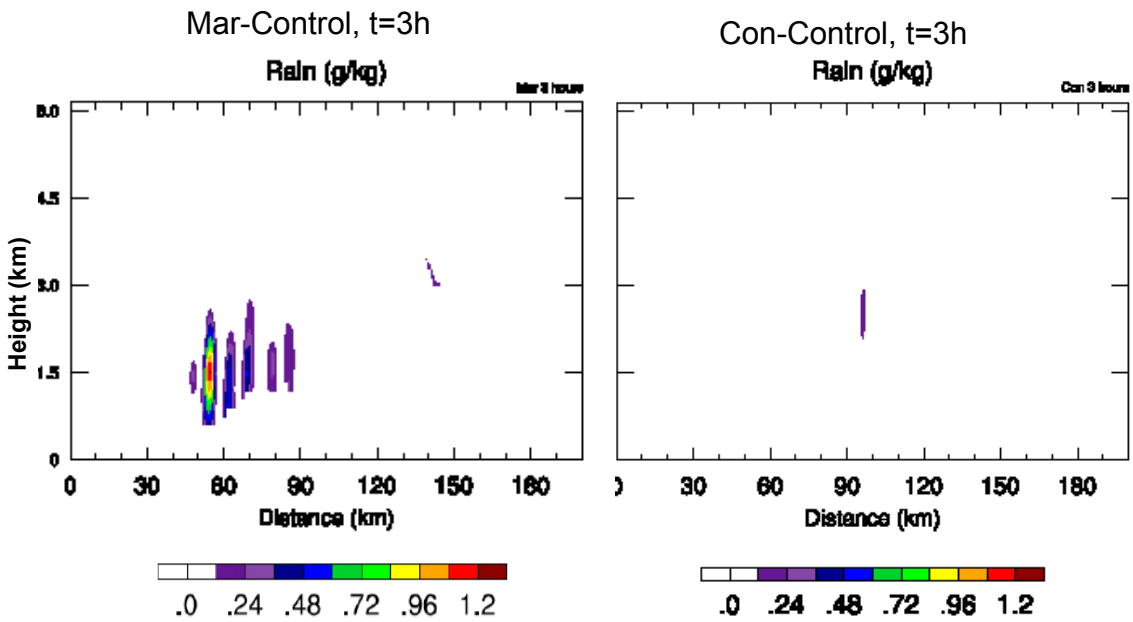

Figure 5. Same as Figure 3, but for rain water mass.

Khain et al. (2004, 2005) and Lynn et al. (2005a, 2005b) simulated deep convective clouds and obtained larger LWC in "polluted" clouds. As explained in these papers, the number of droplets forming in continental air masses is quite large, but because these droplets are relatively small they do not fall as precipitation, but remained suspended in large numbers in clouds and continue growing by diffusion. The same mechanism appears to be effective for relatively shallow orographic clouds as well. Note that cloud droplets in the Con-Control reach higher heights than in Mar-Control because the smaller size of the droplets in the Con-Control allows them to escape accretion onto precipitation. In comparison, large raindrops formed in Mar-Control fall down before reaching even 1.5 km above the surface.

The Con-Control produced more ice crystals (**Figure 6**) and snow (**Figure 7**) then Mar-Control, especially downwind on the mountain slope (and even beyond the highest peak). The higher production of ice crystals and snow content in the Con-Control can be attributed to several factors. First, the process of droplet freezing is not efficient, as stated, in the Con-Control case, because most liquid droplets remain quite small. Thus, in Con-Control most droplets ascend to levels of ~-10°C to -20°C temperatures. Here, they reach sizes large enough (larger than 10 microns in radius) to be collected by ice crystals (formed by primary ice nucleation, which at these heights reach sizes exceeding ~50 microns through depositional grown). Collision of ice crystals then leads to formation of snow.

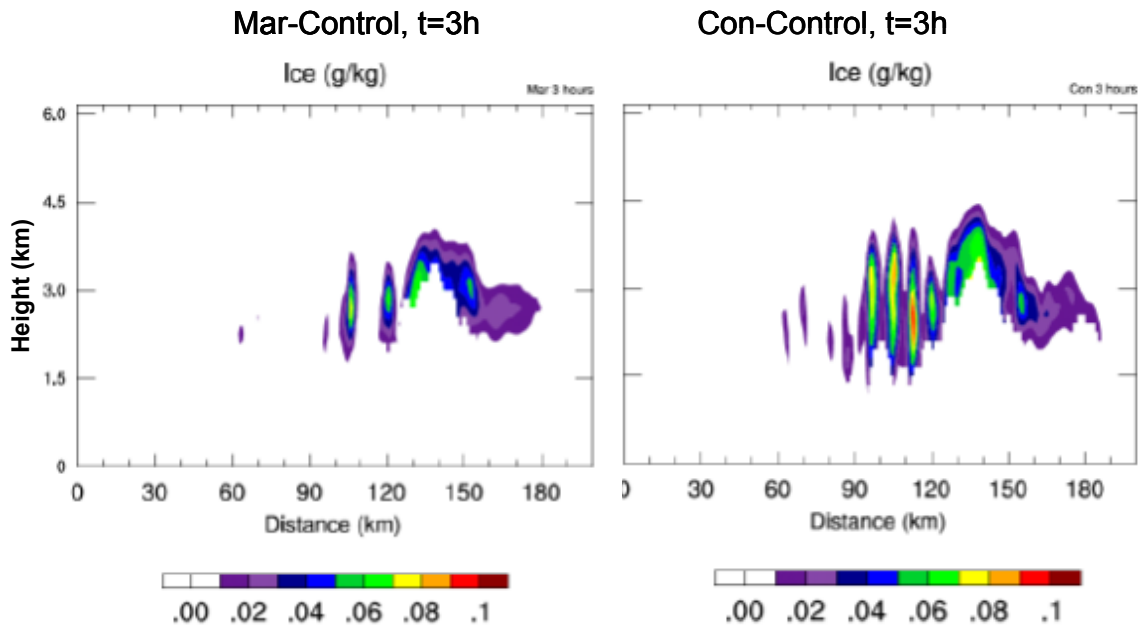

Figure 6. Same as Figure 3, but for ice crystal mass (dendrites, columns, and plates)

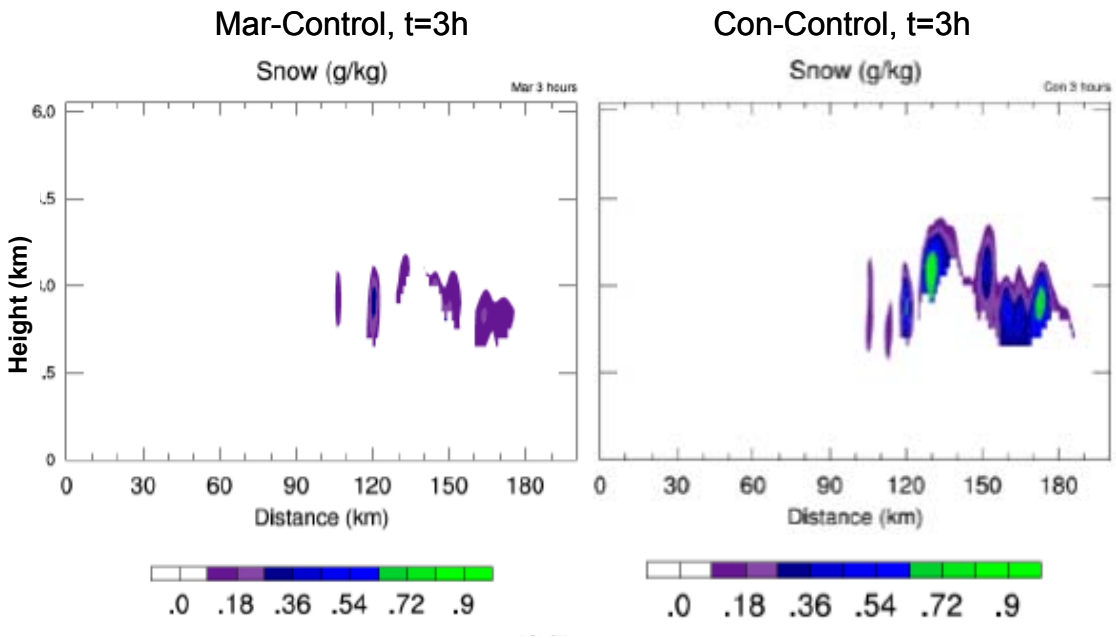

Figure 7. Same as Figure 3, but for snow mass

In contrast, the Mar-Control simulation produced much more graupel mass (and large frozen drops, not shown) on the first half of the upwind side of the slope than Con-Control (**Figure 8**). The formation of graupel in the Mar-Control at between x~50 to x~90 km (where x is the distance from west to east along the cross-section) is related to freezing of raindrops at comparatively high temperatures (-5°C to -8°C). In the Con-Control, drops are small and their freezing is ineffective. At the same time, these drops are collected by large crystals to produce graupel. Thus, the production of graupel in the Con-Control is caused mainly by process of riming of ice crystals and snow and is concentrated in the area of the high LWC, snow, and ice contents. In both cases, graupel falls on the upwind slope because of significant sedimentation velocity, but it forms and falls further upwind in Mar-Control than Con-Control.

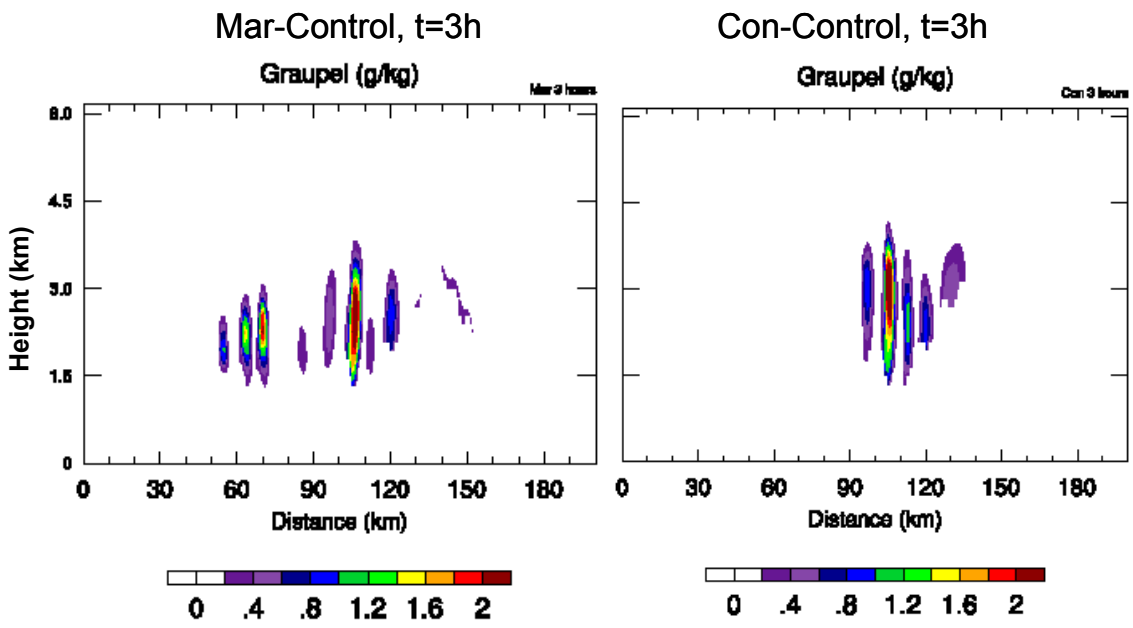

Figure 8. Same as Figure 3, but for graupel

Figure 9 shows the accumulated precipitation from warm and ice processes obtained from the Mar-Control and Con-Control, for the three-hour simulation period. The figure shows that the maritime simulation produced more precipitation upwind (towards the western boundary or sea) than the simulations with continental aerosols. In fact, the precipitation accumulated in Mar-Control experiment began about 40 km upwind of the starting point of accumulation in Con-Control. Also, the highest amount of precipitation in Mar-Control fell to just to the west of the highest peak, while in Con-Control the largest amount of precipitation fell downwind of the highest peak.

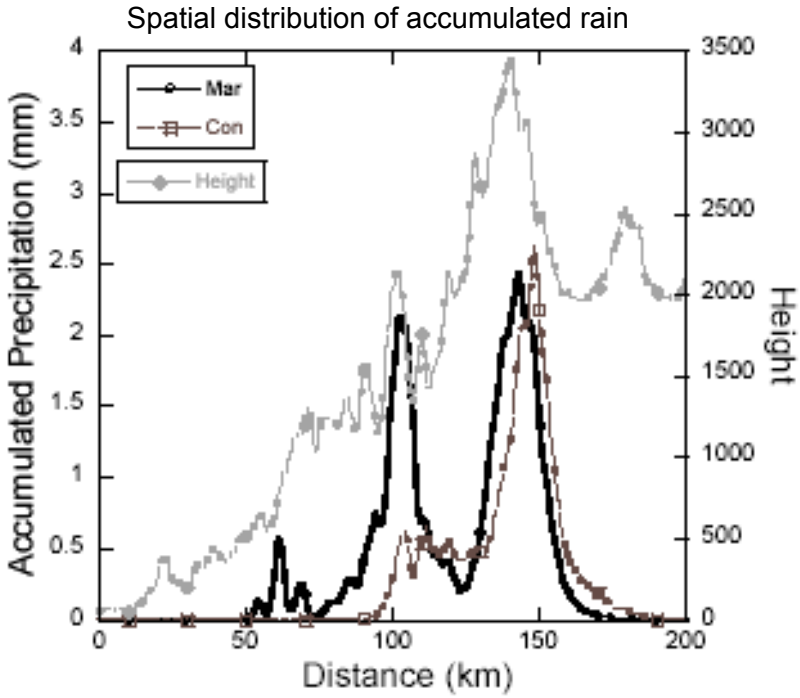

Figure 9. Accumulated precipitation on the mountain slope for 3 hours for both Mar-Control and Con-Control

In total, there are three maxima in the precipitation distribution in Mar-Control, while there are two peaks in the precipitation distribution in Con-Control. Each occurred near local maximum in topography. Based on the analysis of the figures above, the first maximum in Mar-Control's precipitation peak occurred because of warm rain processes. The second maximum occurred mainly because of graupel. Ice crystals and snow induced the third maximum in the precipitation peak. In Con-Control, warm rain processes did not contribute to precipitation. Rather, the first maximum was formed by graupel, but the amount of graupel in Con-Control was apparently less than in Mar-Control. Both cloud ice and snow processes led to the formation of the second maximum over the highest peak, which was somewhat larger than obtained in Mar-Control.

In both simulations in the third peak, there was sedimentation of crystals, graupel, and snow in downdrafts over the eastern side of the peak from stratocumulus-like clouds with cloud base located at or near the surface. Yet, the masses of snow and ice crystals in the Con-Control case were larger and advected further eastwards than in the Mar-Control; thus the precipitation peak is larger in the Con-Control and was shifted further downwind than in the Mar-Control case. The value of the excess was, however, significantly smaller than the deficit in the precipitation in Con-Control over the upwind slope. As a result, the accumulated precipitation in the Mar-Control case turned out to be larger than in the Con-Control case by about 30% (see Table 1), which corresponds well to the observations by Givati and Rosenfeld (2004) and Jirak and Cotton (2006).

Table 1. Accumulated precipitation (mm) obtained during 3 hours of simulations. The data were averaged from 150 to 350 km in the simulation domain.

Model run	Mar-Control	Con-Control
	3 hours	3 hours
Control runs	0.44	0.32
Surface heating function = 10 W m^{-2}	0.53	0.34
3/4 Wind	0.158	0.04
Relative humidity=90%	3.62	3.78

The west-to-east cloud structure obtained in both simulations was punctuated by convective elements west of the highest topographical peak, with stratiform cloud over the peak and downwind. This type of cloud structure is similar to that observed and shown in Figure 1. Moreover, both simulations produced a sharp cutoff in precipitation amount and cloud mass downwind of the highest peak (as implied by the satellite observation). Also, the Con-Control simulation produced many super-cooled droplets at cloud top, with ice particles present in maximum amount below this level (about 3 km). According to aircraft observations on the same day of these simulations, cloud tops of polluted clouds contained a large amount of super-cooled droplets, with large amount of ice particles was located below.

The difference in the accumulated rain is related to higher precipitation loss in the Con-Control. For instance, ice crystals and snow penetrating eastward to 180 km contributed to precipitation only slightly, as noted, because of high evaporation within the range 150 km < x < 180 km, where relative humidity is low (see Figure 10) because of downdrafts leading to air heating. Thus, the important factor in the decrease in the accumulated precipitation in the Con-Control is the higher loss of precipitating mass by ice sublimation in the dry air farther eastward beyond the highest peak and over the downward slope. The concept that the higher loss of precipitating mass in clouds developing in dirty air was also the major mechanism by means of which aerosols can decrease precipitation from deep clouds (as discussed by Khain et al. [2005] in detail).

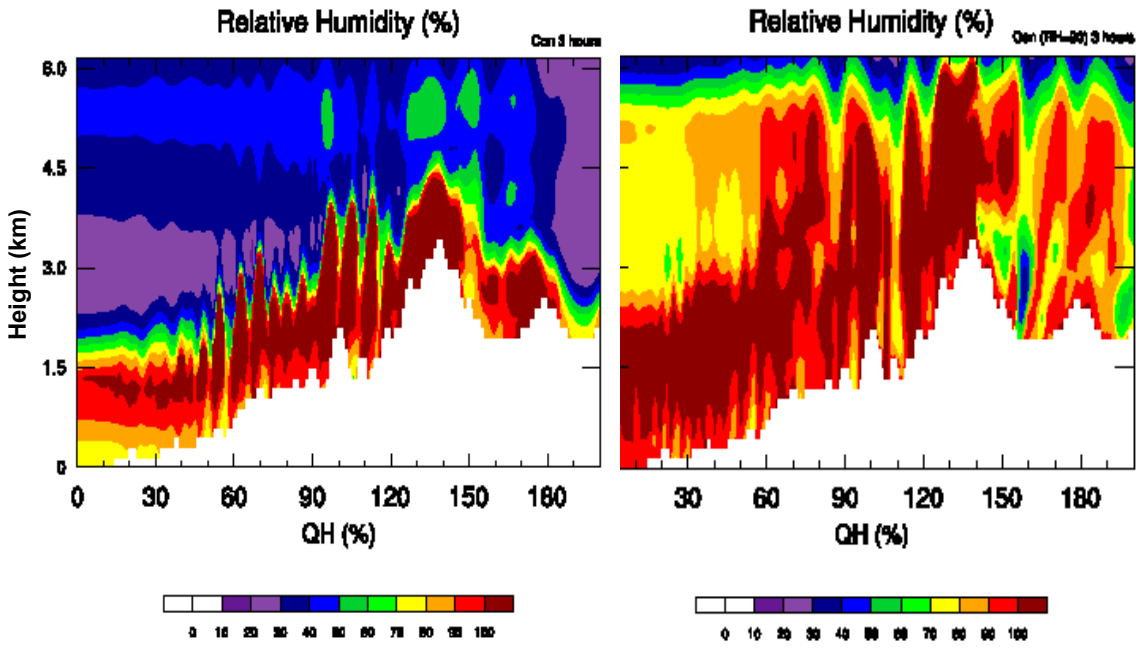

Figure 10. Relative humidity fields in simulations Con-Control (left) and Con-RH (right)

The fields of supercooled water and ice crystals and snow indicate that cloud tops in the Con-Control are higher that in the Mar-Control, so that aerosols invigorate the orographic clouds. This result corresponds to the finding by Khain et al. (2004, 2005) and Lynn et al. (2005a, 2005b) obtained in simulations of deep convective clouds, and reflects the dynamical effects of aerosols. In the Con-Control case, droplets continue growing by diffusion leading to higher latent heat release as compared to the Mar-Control. Formation of a larger amount of ice also leads to higher latent heat release, which leads to higher vertical updraft velocities in the Con-Control case as compared to the Mar-Control case (Figure 11). Another reason for higher cloud tops in the Con-Control case is that both droplets and ice particles are small and escape accretion onto precipitating particles. Therefore, having low sedimentation velocity, they are able to ascend to higher levels than in the Mar-Control case.

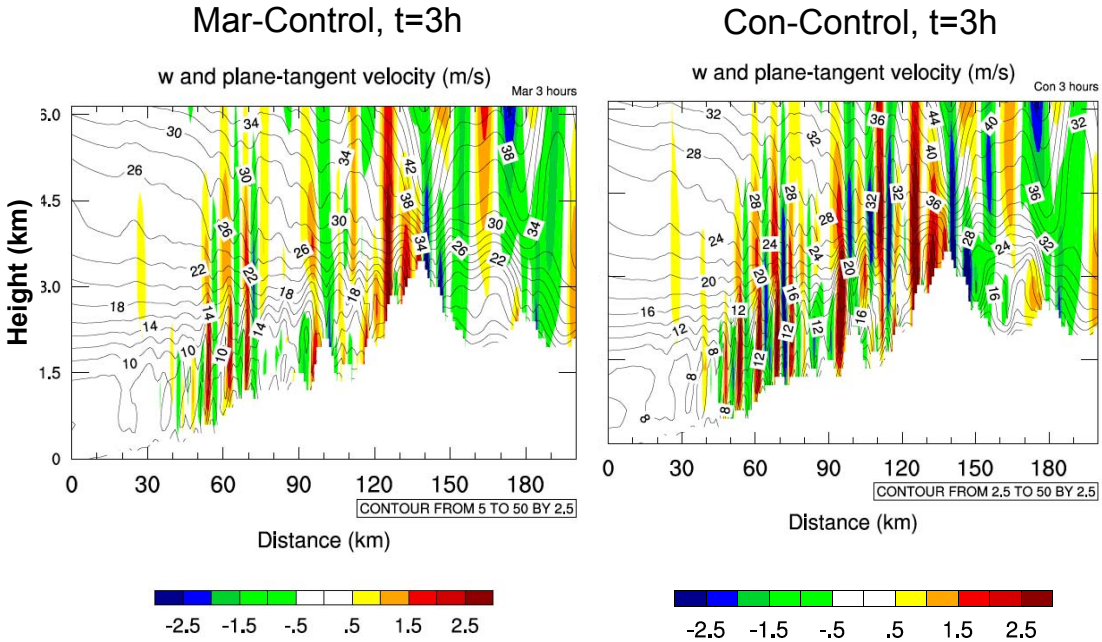

Figure 11. Vertical velocities in the Con-Control and Mar-Control cases

There was a very high similarity of the results obtained in the new Mar-Control + Con-Control (M+C) simulation and the Con-Control performed earlier. The differences both in the amount and spatial distribution of precipitation turned out to be negligible. The accumulated rain was 0.34 millimeters (mm) in the (M+C) simulation as compared to 0.32 mm in the Con-Control case. This effect is attributed to the compensation of the effects of a general increase in concentration of aerosols compared to the increase in the possible effect on precipitation of the amount of large aerosols. Thus, the results of the (M+C) simulation indicate that the existence of a relatively small amount of large maritime aerosols cannot change the effect of anthropogenic aerosols. Note that no ultra-giant CCN were assumed in the aerosol spectrum, either in the M and (M+C) runs.

b. Comparison of Liquid-only and Mixed-phase Microphysics Simulations

Figure 12 shows rainfall obtained from Mar-Control-Liq and Con-Control-Liq. Comparing with the corresponding graph in Figure 9, one notes that the aerosol-induced differences in accumulated precipitation are much larger when ice processes are included. Significant difference in precipitation amounts in the liquid-only and mixed-phase microphysics with continental aerosols is seen at x~100 km (local topography maximum). Figure 5b indicates that at x~100 km a small amount of warm rain occurred in Con-Control, even when ice microphysics was included. This indicates that collisions between drops start to be efficient to produce warm rain over the first large topographical peak. However, the formation of ice particles by drop-ice collisions actually eliminated warm rain in the Con-Control when ice microphysics was included. Since the graupel particles formed do not collect any ice particles (as assumed in the microphysical scheme), the ice particles, including graupel, remain comparatively small and

have lower sedimentation velocity and are advected downwind. Thus, simulation of liquid-only processes (without liquid/ice interaction) increases precipitation over the upwind slope and decreases it over downwind slope. Thus, aerosols leading to narrowing the DSD affect significantly not only warm, but also ice cloud microphysics and, accordingly, precipitation distribution and amount.

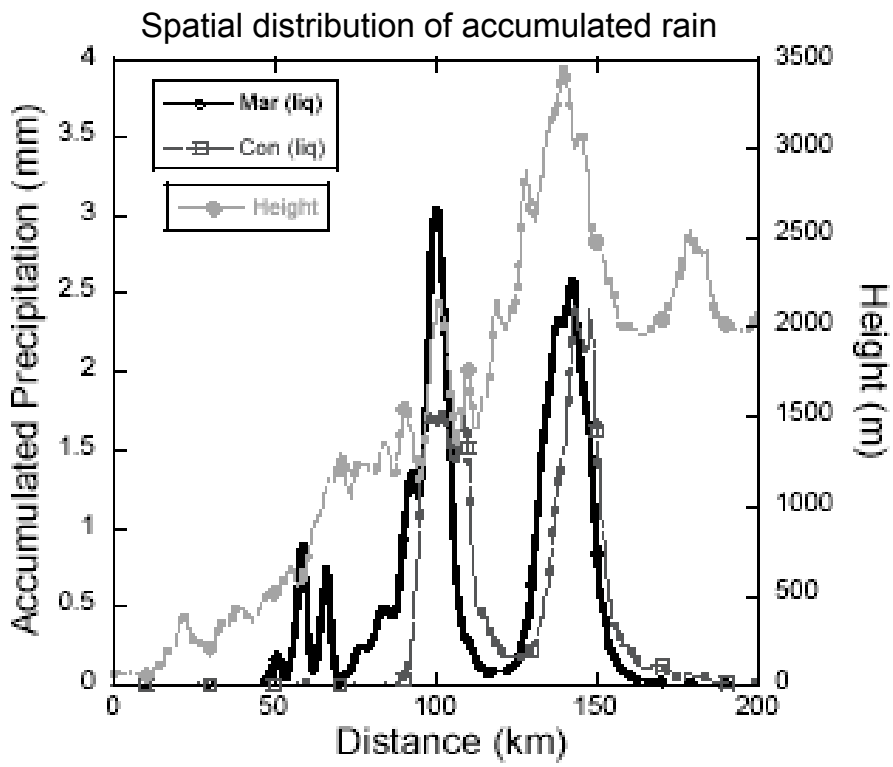

Figure 12. Same as Figure 8, but for simulations with liquid only microphysical processes

c. Sensitivity Tests

To investigate the effects of air humidity on orographic precipitation sensitivity tests were produced that included increasing the relative humidity from the surface to 2 km to 90%, and from 2 to 5 km to 50%. These were referred to as Mar-RH90 and Con-RH90. Cloud microstructure also depends on vertical velocities and wind speed. Consequently researchers conducted the sensitivity experiments in which were studied the effects of air humidity, surface heat fluxes, and background wind speed.

Effects of air humidity. Increasing the relative humidity led to a decrease in the height of cloud base and to a shift of cloud formation westward (Figure 13) to x~15 km. Clouds formed near the underlying surface (Figures 10 [right] and 13 [left)]. Since the slope was quite gentle at x ranged from 0 to 30 km, the vertical velocity at cloud base was less than ~1 m/s. This led to a relatively low droplet concentration even in Con-RH90, that varied from several tens near cloud base to

several hundred at 1-1.5 km above the underlying surface (Figure 13a). Thus, high air humidity led to large LWC (Figure 13 [right]). Such cloud structure fosters droplet collisions, since the droplet concentration was not high and the DSD contained large droplets nucleated near the cloud base. Moreover, high humidity dramatically decreased evaporation of falling droplets. As a result, the increase in the air humidity led to warm rain formation in Con-RH90. In Mar-RH90 warm rain also started at smaller x (Figure 14).

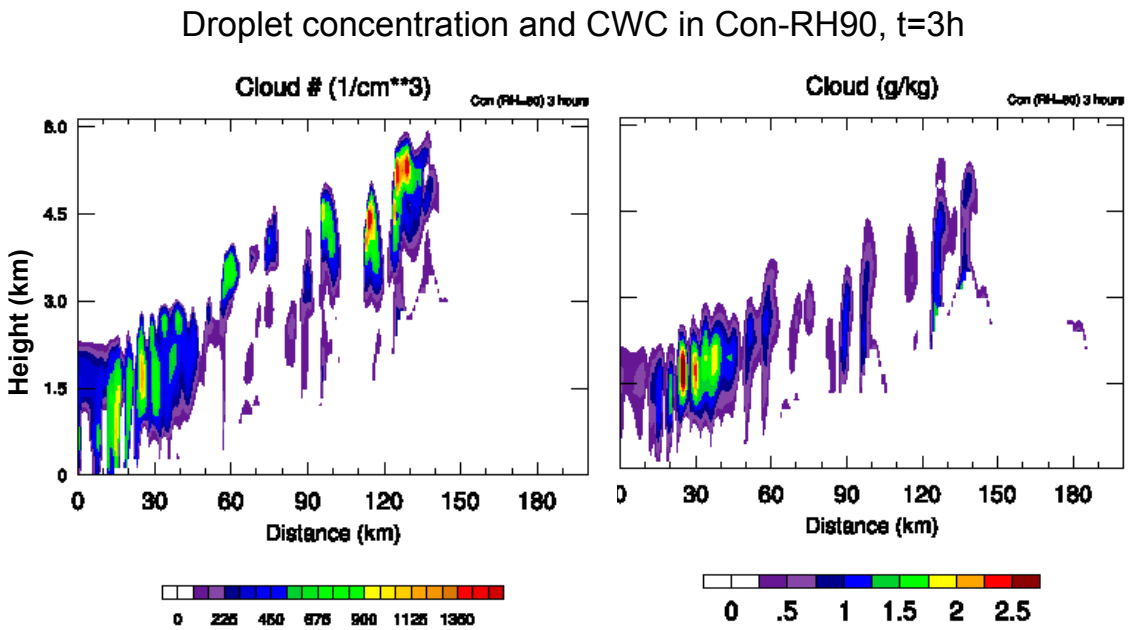

Figure 13. Droplet concentration and CWC in simulation Con-RH90 at t=3h

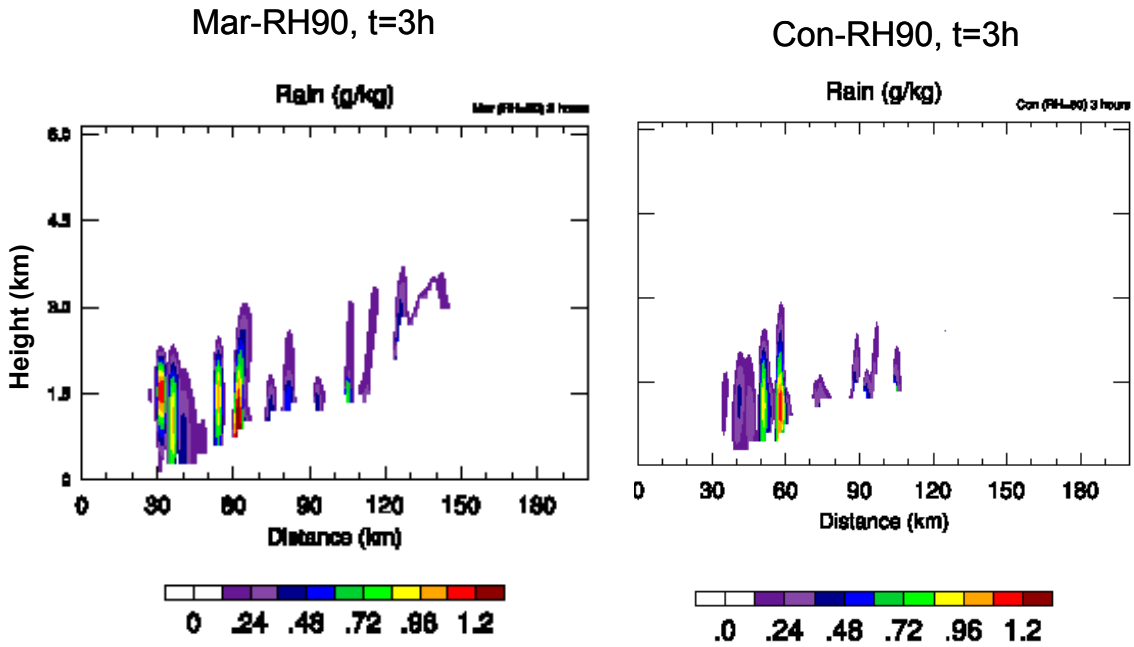

Figure 14. Fields of RWC in simulations Mar-RH90 and Con-RH90 at t=3 h

However, this spatial difference in the initiation of precipitation was not accompanied by the decrease in accumulated rain in Con-RH90, as compared to Mar-RH90. The production of larger ice precipitation in the Con-RH90 case (not shown) fully compensated for the decrease in the warm precipitation. As seen in Figure 15 the increase in humidity that is assumed in these sensitivity simulations largely eliminated the aerosol effects on precipitation amount. Moreover, the accumulated rain in Con-RH90 was even larger than in Mar-RH90 (See Table 1). The authors suppose that the situations with so high air humidity is relatively rare, so that they do not contribute significantly to the statistics presented by Givati and Rosenfeld (2004) and Jirak and Cotton (2006).

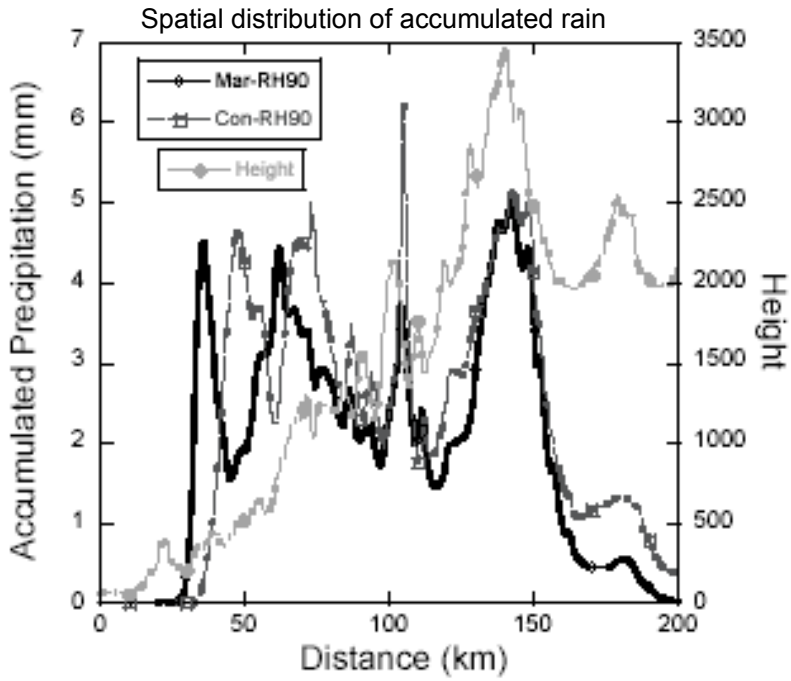

Figure 15. Same as Figure 8, but for simulations Mar-RH90 and Con-RH90 at t=3 h

Effects of surface heat fluxes. Figure 16 (left) shows results from the Mar-SHF10 and Con-SHF10. When comparing to the appropriate graph in Figure 9, one sees that the 90% decrease in sensible heat flux led to a small decrease in accumulated precipitation, while increasing somewhat the difference between Mar-SHF10 and Con-SHF10 on the upwind slope. In general, the effects of surface heat fluxes turned out to be not very important as concerns the precipitation amount and distribution. The authors attribute this effect to the fact that the characteristic time scale of the air heating due to the fluxes is of several hours, so the fluxes could not change temperature and relative humidity significantly during the 3-hour period of simulations.

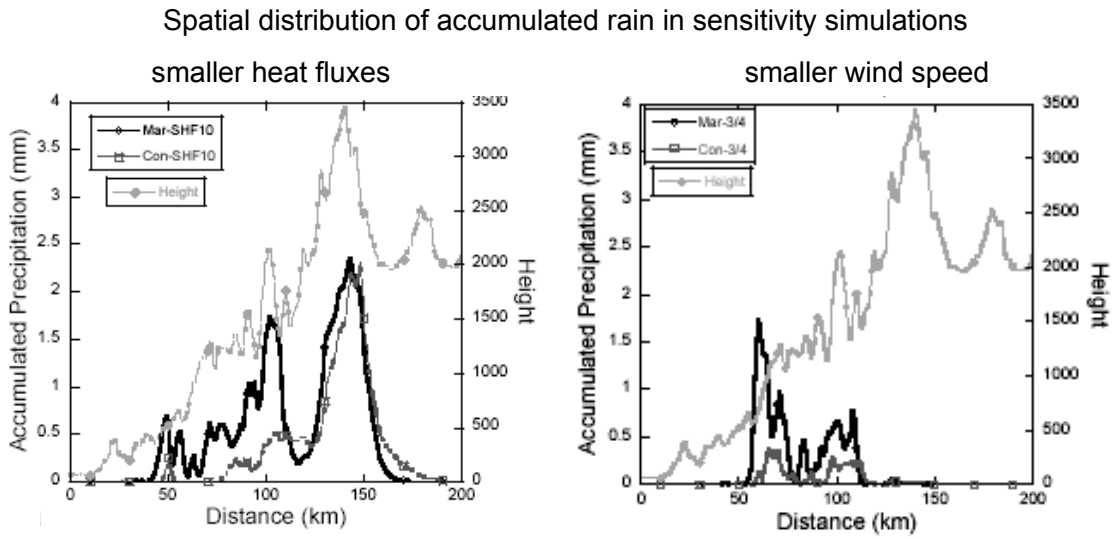

Figure 16. Same as in Figure 15, but for simulations with a sensible heat flux of 10 W m^{-2} (left), and smaller (3/4) background wind speed (right)

Effects of wind speed. Decreasing the wind to 3/4 of its initial value reduced the amount of precipitation in both Mar-3/4 and Con-3/4 (Figure 16 (right panel)). This is because a decrease in the horizontal velocity led to a corresponding decrease in the vertical velocity over upwind slopes. Small vertical velocities produce very weak and shallow clouds at upwind slopes. Because of low cloud depths, ice processes are ineffective. Each simulation produced two peaks in precipitation, and Con-3/4 produced precipitation even near the beginning of the upwind slope. Because there were smaller vertical velocities, the droplet concentration was smaller in Con-3/4 than in Con-Control (not shown). However, because of small vertical velocities and low supersaturation, droplets grow slowly. Respectively, precipitation at the surface forms via cloud "sedimentation" (drizzling) on upwind mountain slope.

4. Conclusions

Spectral (bin) Microphysics was coupled with a two-dimensional version of the Weather Research Forecast model and used to investigate aerosol effects (pollution) on amount and spatial distribution of precipitation in the Sierra Nevada Mountains. Two microphysical situations were simulated: the first with low concentration maritime aerosols (clean air) and the second with high-concentration continental aerosols (dirty air), using initial sounding data from 7 December 2003. The continental aerosol simulation was designed to reproduce the effect of anthropogenic aerosols produced in upwind urban areas on downwind precipitation forming on the mountain slope. The maritime aerosol simulation reproduced precipitation forming in relatively pristine air. Simulations were performed with a relatively high grid resolution (1 km in the horizontal and 200 m in the vertical). After three hours of simulation, precipitation amount in the maritime simulation was about 30% larger on the upwind slope than in the simulation with continental aerosols.

The maritime simulation produced warm rain near the beginning of the upwind slope, while the continental simulation did not produce warm rain anywhere on the slope. The maritime simulation also produced graupel precipitation in a second maximum occurring further up the mountain slope above a topographical peak. The continental simulation produced less graupel in the same location and less precipitation. This simulation, however, produced more cloud ice and snow than the maritime simulation, which accumulated in larger amounts on the highest peak and downwind. Owing to the greater production of cloud ice and snow, the maximum amount of precipitation on the highest topographical peak was shifted downwind from the location of maximum precipitation in the maritime simulation. Both simulations had convective-type precipitation on the upwind slope, which transitioned to stratiform precipitation further up the mountain slope. Evaporation of cloud ice and snow in atmospheric downdrafts beyond the highest peak led to a sharp cutoff in precipitation downwind of this peak, similar to what was shown in an observed satellite photograph (the strong effect of ice sublimation on precipitation is discussed in more detail by Khain et al. 2005).

As noted, the simulation with continental aerosols produced more cloud ice and snow particles than the simulation with maritime aerosols, without producing warm rain. Clouds forming in the continental aerosol air turned out to be more vigorous and reached higher heights than those formed in clean air, with ice crystals and snow within that had lower sedimentation velocities than raindrops and graupel. These lower sedimentation velocities led to a shift of ice precipitation downwind in the simulation with continental aerosols, compared to warm rain precipitation and graupel-type precipitation in the maritime simulation. These cloud ice and snow particles were advected by the background wind, and, as noted, evaporated on the downwind side of the highest mountain peak. Because cloud ice and snow particles were evaporated, the simulation with continental aerosols produced less precipitation over the whole mountain slope, owing to the greater prevalence of these types of precipitation particles in this simulation than in the maritime simulation. The results obtained using the aerosol size distribution equal to the sum of maritime and continental aerosol size distributions indicate that the existence of relatively small amount of large maritime aerosols does not change the effect of anthropogenic aerosols.

According to statistical analysis (Givati and Rosenfeld 2004; Jirak and Cotton 2006) precipitation over the mountain regions located downwind from coastal urban areas decreased during past several decades by about 30%. The present study's simulations show that effects of anthropogenic aerosols can be the reason of such decrease. It is clear that the results of statistical analysis include wide range of meteorological situations. Partially, the possible variability is shown in this study's sensitivity tests. It is shown that anthropogenic aerosols decrease precipitation under specific conditions, for example, for comparatively dry environmental conditions. The authors believe that these conditions play a dominating role in the total statistics.

The mechanism of aerosol-induced convection invigoration was first analyzed in detail by Khain et al. (2004, 2005). Now the aerosol induced convection invigoration has been reported in many numerical studies (e.g., Lynn et al. 2005a, 2005b; Wang 2005; Teller and Levin 2006) and observations (Koren et al. 2005). It seems it is a common effect that clouds in environments

with higher aerosol concentrations become deeper and more vigorous, with more glaciation as a consequence.

Supplemental simulations with ice microphysics excluded revealed a crucial role of ice formation in the aerosol effects on precipitation. Without simulated ice processes, the simulation with continental aerosols produced more precipitation in the location of the first topographical peak than it did when ice processes were included. Yet, the precipitation amount in the maritime simulation did not show similar sensitivity to the inclusion or exclusion of ice processes. This further emphasizes the importance of drop size distribution on the size distribution and types of ice particles that formed in each simulation. Thus, ice formation significantly intensifies the effects of aerosols on the precipitation amount and spatial distribution.

In sensitivity tests, the authors identified relative humidity and wind speed as critical environmental factors that determined both precipitation amounts and relative differences between simulations in clean and dirty air. Higher humidity decreased the cloud base level and triggered the cloud formation further upwind on the mountain slope where vertical velocity was smaller than further downwind on the slope. As a result, droplet concentration turned out to be relatively small, and droplet spectra distributions were able to develop to produce raindrops. Effective warm rain formation that occurred even in the continental aerosol case (but with some time delay and spatial shift in the downwind direction). Also, high relative humidity reduces precipitation loss caused by drop and ice evaporation. Thus, the increase in air relative humidity decreased the difference in precipitation amounts between the clean- and dirty-air simulations, and even changed the sign of this difference. Regarding the authors' simulations with reduced sensible heat flux, it is possible that over a longer time period in which atmospheric humidity and temperature could be modified, or fluxes of larger magnitude or fluxes with spatial and non-uniform variability in time, could each have had a stronger effect on the precipitation.

A decrease in the speed of the background wind led to a decrease in the vertical velocity and to a delay in the cloud and precipitation formation. Even so, the maritime precipitation formed earlier, and in somewhat greater amounts than in the continental simulation. Low vertical velocities lead to formation of narrow clouds which precipitate by cloud "sedimentation" (drizzling) on upwind mountain slope.

These idealized simulations reveal the effect of aerosols on precipitation formation and distribution from orographic clouds, and also reveal the most important microphysical and environmental factors that can enhance or inhibit the aerosol effects.

Future studies will focus on the quantitative evaluation of aerosol with a three-dimensional version of the same model, and include forcing from radiation processes.

Acknowledgments

The authors express their deep gratitude to Dr. J. Dudhia for consulting related to utilization of the WRF model and implementation of the SBM in WRF, as well as to W. Woodley for the interest to the work and valuable advice. The study has been performed with support from the National Science Foundation (grant #0503152) and the Israel Water Company (grant 162/03).

References

Andreae, M. O., D. Rosenfeld, P. Artaxo, A. A. Costa, G. P. Frank, K. M. Longlo, and M. A. F. Silva-Dias. 2004: "Smoking rain clouds over the Amazon." *Science* 303: 1337–1342.

BenMoshe N., A. Pokrovsky, and A. P. Khain. 2006: Simulation of aerosol effects on precipitation from green-ocean, smoky and pyro-clouds using a spectral microphysics model with an accurate calculation of supersaturation and diffusion growth. 12th Conference on Cloud Physics, Madison, 9–14 July, 2006.

Borys, R. D., D. H. Lowenthal, and D. L. Mitchell. 2000: "The relationships among cloud microphysics, chemistry, and precipitation rate in cold mountain clouds." *Atmos. Environ.* **34**: 2593–2602.

Givati, A., and D. Rosenfeld. 2004: "Quantifying precipitation suppression due to air pollution." *J. Appl. Meteorol.* 43: 1038–1056.

Jirak, I. L., and W. R. Cotton. 2006: "Effect of Air Pollution on Precipitation along the Front Range of the Rocky Mountains." *J. Appl. Meteorol. and Climatol*. 45 (1): 236–245.

Khain, A. P., M. Ovtchinnikov, M. Pinsky, A. Pokrovsky, and H. Krugliak. 2000: "Notes on the state-of-the-art numerical modeling of cloud microphysics." *Atmos. Res.* 55: 159–224.

Khain A. P., D. Rosenfeld, and A. Pokrovsky. 2001: "Simulation of deep convective clouds with sustained supercooled liquid water down to -37.5°C using a spectral microphysics model." *Geophysical Research Letters* 3887–3890.

Khain A., A. Pokrovsky, M. Pinsky, A. Seifert, and V. Phillips. 2004: "Effects of atmospheric aerosols on deep convective clouds as seen from simulations using a spectral microphysics mixed-phase cumulus cloud model Part 1: Model description." *J. Atmos. Sci.* 61: 2963–2982.

Khain, A., and A. Pokrovsky. 2004: "Effects of atmospheric aerosols on deep convective clouds as seen from simulations using a spectral microphysics mixed-phase cumulus cloud model Part 2: Sensitivity study." *J. Atmos. Sci.* 61: 2983–3001.

Khain, A., D. Rosenfeld, and A. Pokrovsky. 2005: "Aerosol impact on the dynamics and microphysics of convective clouds." *Q. J. Roy. Meteor. Soc.* 131: 2639–2663.

Koren I., Y. J. Kaufmann, D. Rosenfeld, L. A. Remer, and Y. Rudich. 2005: "Aerosol invigoration and restructuring of Atlantic convective clouds." *Geophysical Research Letters* 32, L14828, doi:10.1029/2005GL023187.

Kovetz, A., and Olund, B. 1969: "The effect of coalescence and condensation on rain formation in a cloud of finite vertical extent." *J. Atmos. Sci.* 26: 1060–1065.

Lynn B., A. Khain, J. Dudhia, D. Rosenfeld, A. Pokrovsky, and A. Seifert. 2005a: "Spectral (bin) microphysics coupled with a mesoscale model (MM5). Part 1. Model description and first results." *Mon. Wea. Rev.* 133: 44–58.

Lynn B., A. Khain, J. Dudhia, D. Rosenfeld, A. Pokrovsky, and A. Seifert. 2005b: "Spectral (bin) microphysics coupled with a mesoscale model (MM5). Part 2: Simulation of a CaPe rain event with squall line." *Mon. Wea. Rev.* 133: 59–71.

Ohashi, Y., and H. Kida. 2002: "Local Circulations Developed in the Vicinity of Both Coastal and Inland Urban Areas: A Numerical Study with a Mesoscale Atmospheric Model." *J. Appl. Meteorol.* 41: 30–45.

Ramanathan, V., P. J. Crutzen, J. T. Kiehl, and D. Rosenfeld. 2001: "Aerosols, climate and the hydrological cycle." *Science* 294: 2119–2124.

Rosenfeld, D. 1999: "TRMM observed first direct evidence of smoke from forest fires inhibiting rainfall." Ge*ophys. Res. Lett.* 26(20): 3105.

Rosenfeld, D. 2000: Suppression of rain and snow by urban and industrial air pollution. *Science* 287(5459): 1793–1796.

Shepherd, J. M., and S. J. Burian. 2003: "Detection of urban-induced rainfall anomalies in a major coastal city." *Earth Interactions* **7**: 1–14.

Skamarock, W., J. B. Klemp, J. Dudhia, D. O. Gill, D. M. Barker, W. Wang, J. G. Powers. 2005: A description of the Advanced Research WRF Version 2, NCAR Technical Note, June 2005, Mesoscale and Microscale Meteorology Division, NCAR, Boulder, Colorado, U.S.

Teller A., Z. Levin. 2005: "The effects of aerosols on precipitation and dimensions of subtropical clouds: A sensitivity study using a numerical model." *Atmos. Chem. Phys. Discuss.* 5: 7211–7245.

Wang, C. "A modelling study of the response of tropical deep convection to the increase of cloud condensational nuclei concentration: 1. Dynamics and microphysics." *J. Geophys. Res.* v. 110; D21211, doi:10.1029/2004JD005720.

Appendix D

Aerosol Properties and Trends in Relation to Changes in Precipitation over Elevated Terrain in the Western United States

Appendix D

Aerosol Properties and Trends in Relation To Changes in Precipitation Over Elevated Terrain in the Western United States

The underlying assumption of previous studies (Givati and Rosenfeld 2004, 2005) was that the trend of Ro encompassed the period of main growth of the population, so that the overall emissions at the end of the period is larger than at the beginning of the measured period, not requiring necessarily a monotonic growth throughout the analysis period. Respectively, the overall precipitation suppression was evaluated as ending/starting values of Ro, as calculated using a simple linear regression line of Ro as a function of year. Air pollution indices showed recovery (a decreasing trend) in California after the Clean Air Act was legislated in 1977, but Ro continued to decrease, and certainly did not show any recovery since then. Givati and Rosenfeld (2004) suggested that the there has been no decrease in the concentrations of small CCN, which are responsible for the suppression of precipitation, and pointed out the large increase in diesel consumption as a possible source of increasing production of such aerosols.

The current study expands the scope to the whole western United States, to both relatively pristine and polluted areas. Analyses of aerosol properties and trends are expanded to be correlated with the observed trends of precipitation, based on the Interagency Monitoring of Protected Visual Environments (IMPROVE) monitoring program. Aerosol mass concentrations and composition during the winter months (October–March) were obtained for the areas of interest for the period 1988–2003 (Data are available from the program website at http://vista.cira.colostate.edu/improve/). The trends were calculated using the tool provided at the IMPROVE website at http://vista.cira.colostate.edu/views/web/AnnualSummaryDev/Trends.aspx.

This tool provides quarter yearly averaged values of the parameters. The annual "winter" value is the average of the first and last quarters for that year. The trends of the mass concentration of the particles smaller than 2.5 μm ($PM_{2.5}$) and of the particles with 2.5 < diameter < 10 μm (PM_{10}–$PM_{2.5}$) were calculated. In addition, the trends of the following components of the fine particles were plotted: combined ammonium nitrates and sulfates, combined elemental and organic carbon, and soil materials. It is assumed here that small CCN concentrations are correlated positively with the mass of the soluble fraction of the fine particles, and hence act to suppress precipitation. Small CCN concentrations are certainly positively correlated with the fine fraction of sulfates and nitrates, and likely so with the carbonaceous aerosols after having the time between emission and arrival over the mountain ranges to chemically mature and develop some solubility. Soil particles constitute a small fraction of the fine particles, but probably a larger fraction of the coarse particles. No information is available in the IMPROVE data about the composition of the coarse fraction. However, even insoluble mineral particles can become hygroscopic by interacting with air pollution and getting coated with soluble materials such as sulfates, and so act to enhance precipitation (Levin et al. 1996).

The analyzed IMPROVE stations were selected based on the availability of the longest possible time series of aerosol measurements that are the geographically closest to represent the conditions at the higher elevation gauge of the rain gauge pairs. The locations of the paired rain gauges and the selected IMPROVE stations are shown in Figure 1, and their details are summarized in Tables 1 and 2, respectively.

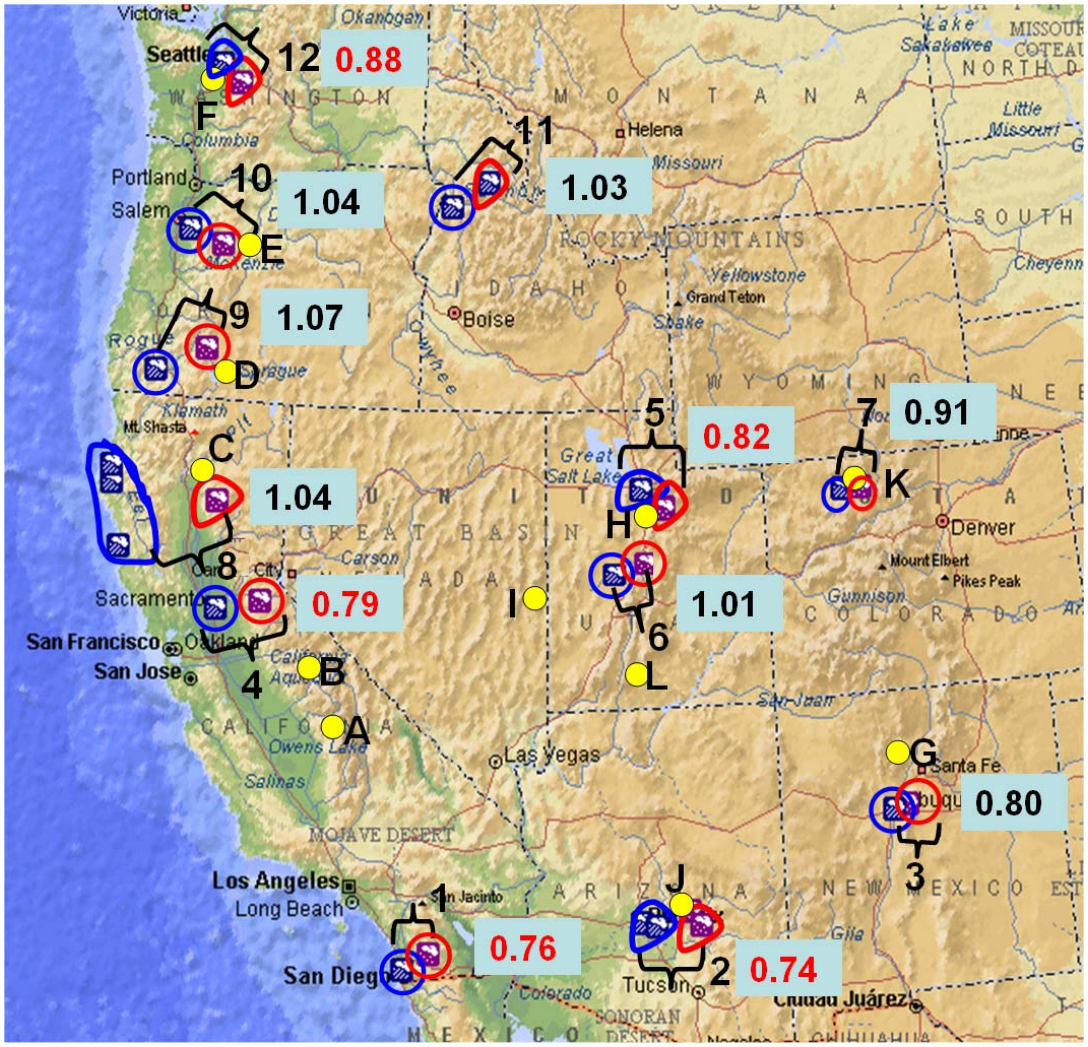

Figure 1. Summary map of the locations of the rain gauges and aerosol monitoring stations and the main results of the orographic precipitation. Rain gauge pairs are marked by the blue circle for the low station and red circle for the downwind hilly station. Clusters of gauges are shown by an irregular enclosure. The station pairs are numbered and the respective details are provided in Table 1. The fractional change of the winter (October–May) orographic enhancement factor of the high rain gauge(s) with respect to the low rain gauge(s) that was indicated during the measurement period is shown near each pair. The red numbers are smaller than 1.00 with statistical significance of $P < 0.05$. P is the statistical significance that corresponds to the t test statistic, which measures the probability that there is no trend. The locations of the IMPROVE aerosol monitoring stations are shown in the yellow circles and marked by characters respective to the reference in the text and the station details in Table 2.

Table 1. The locations and details of the plains and hilly rain gauge pairs and clusters, as numbered in Figure 1. Clusters of gauges appear under the same pair number.

Pair No.	Data since	State	Plains stations	Lat	Long	Elev(m)	Hilly stations	Lat	Long	Elev(m)
1	1888	CA	San Diego	32.44	-117.10	10	Cuyamaca	32.59	-116.35	1557
2	1914	AZ	Litchfield Park	33.30	-11.222	343	Miami	33.24	-110.53	1200
2		AZ	Sacaton	33.05	-111.45	427	Roosevelt	33.40	-111.09	733
2		AZ	Mesa	33.25	-111.52	410				
2		AZ	Goulds Ranch	33.23	-112.04	400				
3	1945	NM	Albuquerque	35.03	-106.37	1770	Sandia Crest	35.13	-106.27	3563
4	1945	CA	Sacramento	38.31	-121.30	8	Pacific House	38.75	-12.050	1147
5	1949	UT	Tooele	40.32	-112.18	1607	Silver Lake	40.36	-111.35	2903
5		UT	Salt Lake/Garfield	40.43	-112.12	1437	Alta	40.36	-111.38	2903
5		UT					Cottonwood	40.37	-111.47	1653
6	1945	UT	Delta	39.23	- 112.31	1587	Levan	39.33	-111.52	1770
7	1948	CO	Hayden	40.29	-107.15	2127	Steamboat Springs	40.30	-106.50	2257
8	1949	CA	Eureka	40.48	-124.10	3	Mineral	40.35	-121.600	1627
8		CA	Scotia	40.29	-124.06	5	De Sabla	39.52	-121.370	907
8		CA	Fort Bragg	39.27	-123.48	3				
9	1949	OR	Grant Pass	42.26	-123.19	310	Crater Lake	42.54	-122.08	2160
10	1954	OR	Stayton	44.48	-122.46	157	Marion Forks	44.37	-121.57	817
11	1958	ID	Riggins Ranger	45.25	-116.19	600	Elk City	45.49	-115.26	1327
							Headquarters	46.38	-115.48	1047
12	1949	WA	Seattle	47.36	-122.20	3	Palmer	47.18	-121.50	300
12		WA	Kent	47.23	-122.14	10				
12		WA	Puyallup	47.12	- 122.20	17				

Table 2. The locations of the IMPROVE aerosol monitoring stations used in this study

Station	State	ID code	Site Name	Latitude	Longitude	Elev (m)
A	CA	SEQU1	Sequoia	36.489	-118.829	519
B	CA	YOSE1	Yosemite	37.712	-119.704	1603
C	CA	LAVO1	Lassen	40.540	-121.578	1732
D	OR	CRLA1	Crater Lake	42.896	-122.136	1966
E	OR	THSI1	Three Sisters	44.291	-122.043	885
F	WA	PUSO1	Puget Sound	47.570	-122.312	97
G	NM	BAND1	Bandelier	35.78	-106.266	1988
H	UT	LOPE1	Lone Peak	40.445	-111.708	1768
I	NV	GRBA1	Great Basin	39.005	-114.216	2065
J	AZ	TONT1	Tonto	33.649	-111.109	775
K	CO	MOZI1	Mount Zirkel	40.538	-106.677	3243
L	UT	BRCA1	Bryce Canyon	37.618	-112.174	2481

The average aerosol concentrations probably differ considerably from those actually interacting with the clouds over the topographical barriers. However, it can be assumed that the levels and trends of the aerosol concentrations (Figure 2) that interact with the clouds are correlated those measured at the IMPROVE stations.

According to Figure 2, the central Sierra Nevada (Sequoia and Yosemite, panels A and B) are much more polluted than the northern Sierra (Lassen Volcano, panel C), in line with the strong decreasing trends of Ro in the central Sierra, but not in the north, as reported by Givati and Rosenfeld (2004). Furthermore, while the coarse particles show a decreasing trend, the fine particles are stable at very high levels of 8.5 $\mu g\ m^{-3}$ in Sequoia, mainly in the form of nitrates, sulfates and organic carbon. The fine particle mass is smaller in Yosemite, probably due to the higher elevation of the monitoring station, but still show a strong increasing trend, mainly due to organic carbon. The decreasing trend of coarse aerosols that can have an enhancing effect on precipitation also may have acted to decrease the mountain precipitation in much the same way that the increasing trend in the fine aerosols may have acted to suppress the mountain precipitation. Coarse aerosol mass concentrations are decreasing also in the relatively pristine areas in northern California and Oregon (panels C and E in Figure 2), but their concentrations are much smaller than in the central Sierra (Panels A and B in Figure 2). The concentrations of the fine aerosols in these relatively pristine areas is very small and yet slightly decreasing. These fine aerosols are primarily composed of organic carbon, probably from residential wood stove

combustion. Farther north, in the densely populated and industrial area of Puget Sound (Panel F of Figure 2), the air is polluted once more, with an increasing trend of the fine aerosols, mainly due to nitrates.

If these IMPROVE stations represent the conditions during orographic precipitation, it would be consistent with decreasing trends of orographic precipitation in central California, stability in northern California to central Oregon, and then decreasing trends again in Washington to the east of the densely populated area of Seattle, around Puget Sound.

Panel H of Figure 2 shows that Lone Peak, east of Salt Lake City, has high concentrations of fine aerosols, with a slightly increasing level due to nitrate and sulfate, along with decreasing trend of coarse aerosols. This is compatible with the reported strong decrease (-24% during 1949–2004) of orographic precipitation to the east of Salt Lake (Griffith et al. 2005). The much cleaner air to the west and to the south (Great Basin and Bryce Canyon, panels I and L in Figure 2) is consistent with the reported stability of the orographic precipitation in these regions (Griffith et al. 2005).

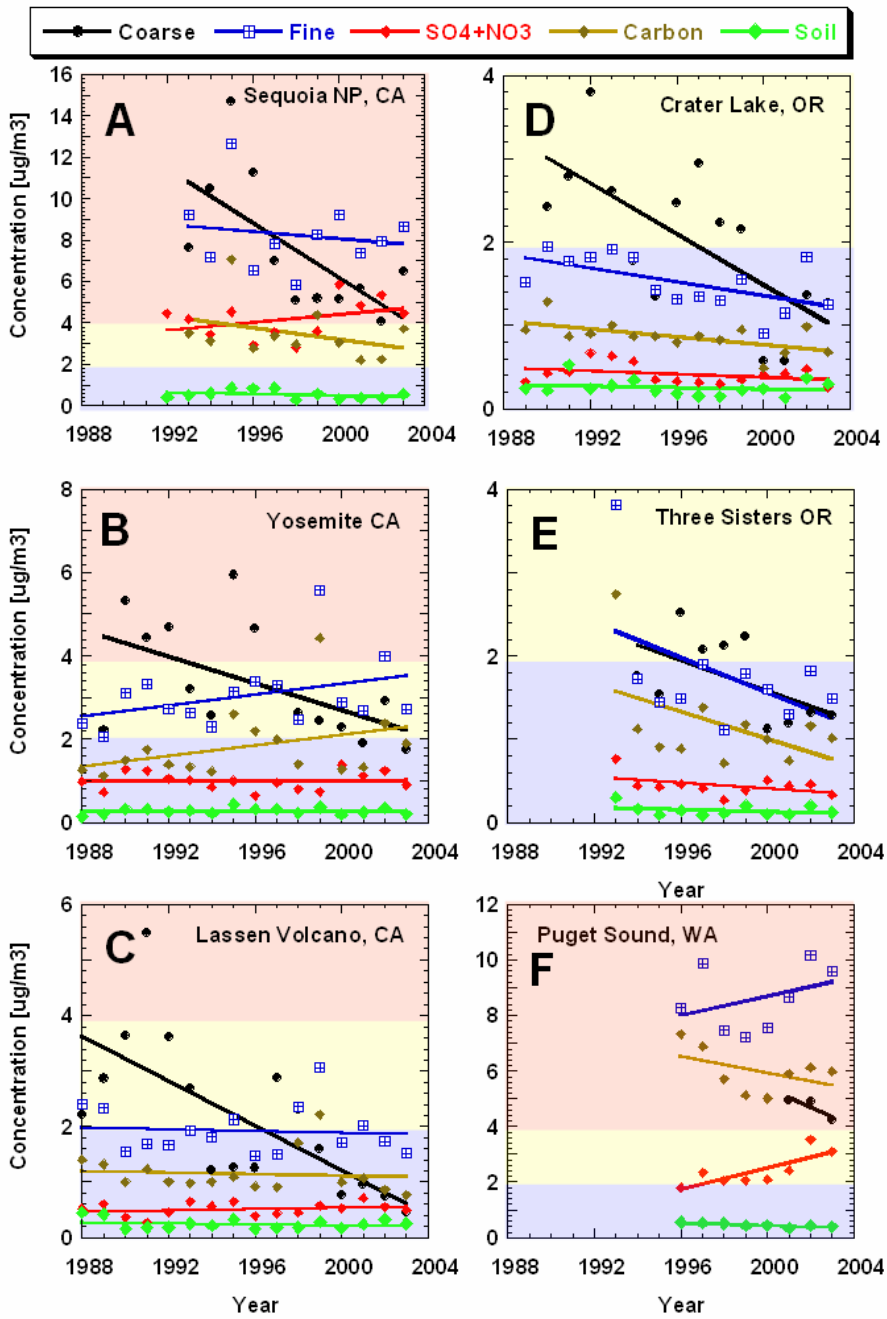

Figure 2. Trends of coarse (2.5 < diameter < 10 µm and fine (Diameter < 2.5 µm aerosols mass concentrations and compositions as measured during winter (October–March) by the IMPROVE monitoring program. The mass concentrations are given in µg m^{-3}. The composition of the fine aerosols is divided into mass of nitrates and sulfates (SO_4 and NO_3), organic and elemental carbon (Carbon), and crustal materials (Soil). The legend is provided at the top of the figure. The locations of the stations are marked with the respective letter on the map in Figure 1 and tabulated in Table 1.

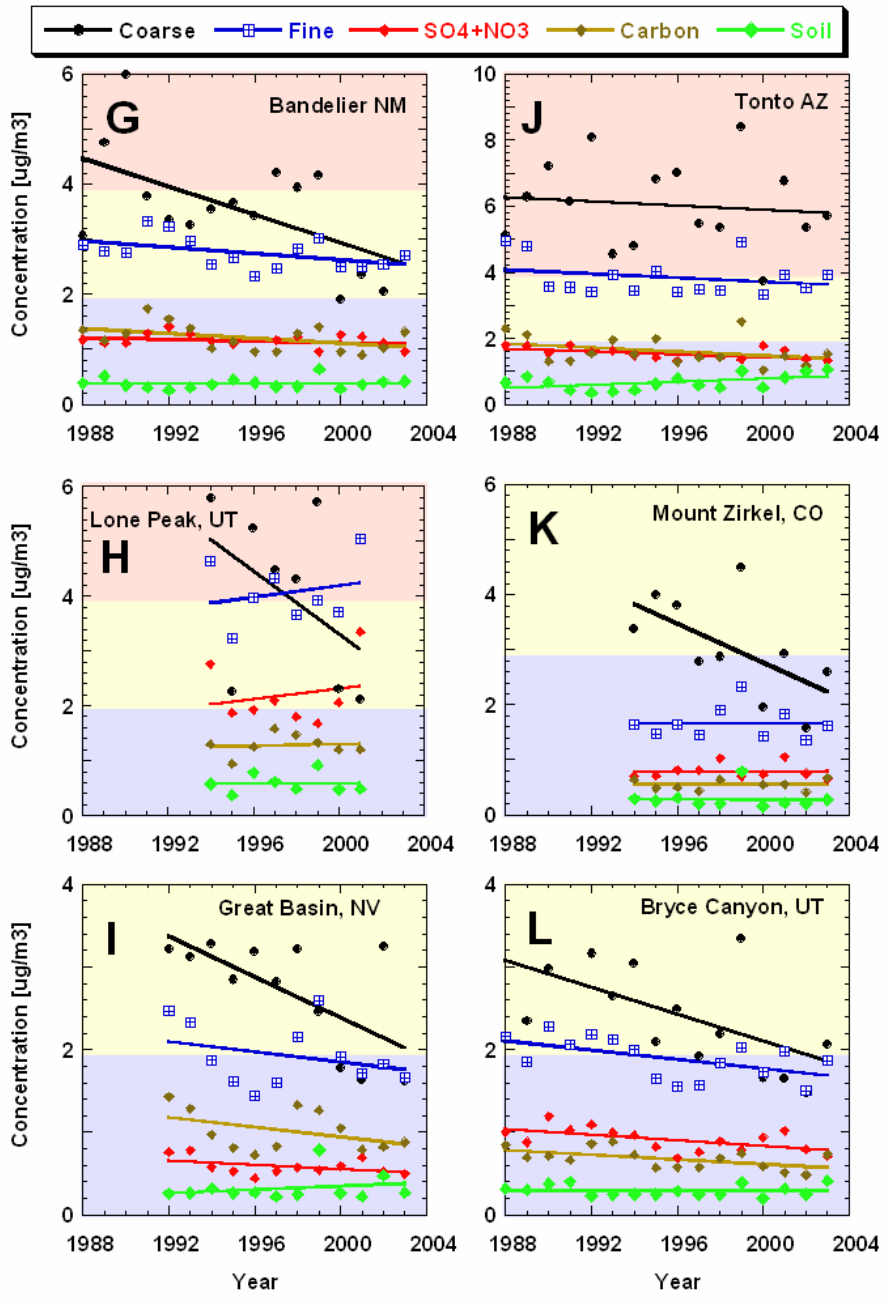

Figure 2. (continued)